


Doctoral Dissertation
Doctoral Program in Doctoral Program in Electrical, Electronic and Communications Engineering (33rd cycle)

Observing and Modeling the Physical Layer in Open and Disaggregated Optical Networks

Emanuele Virgillito

* * * * *

Supervisor
Prof. Vittorio Curri

Doctoral Examination Committee:
Prof. Paolo Serena, Referee, Università degli Studi di Parma
Prof. Luca Potì, Referee, Universitas Mercatorum
Dr. Rosanna Pastorelli, SM-Optics
Dr. Joao Pedro, Infinera Portugal
Dr. Annalisa Morea, Nokia

Politecnico di Torino
September 2021

I hereby declare that, the contents and organisation of this dissertation constitute my own original work and does not compromise in any way the rights of third parties, including those relating to the security of personal data.

. . . . . .

Emanuele Virgillito

Turin, September 2021

Summary

In this thesis we present our novel contributions in the field of open and disaggregated optical networks. Telecom operators are facing an increasing capacity demand due to the growing IP traffic pushed by the growing activation of IP based services, such as intensive media streaming or the upcoming 5G based services, especially in the post COVID-19 pandemic world. These trends will require an overhaul of the optical infrastructure in order to improve the network flexibility and capacity while keeping the infrastructure cost effective.

Thanks to the introduction of DSP-based receiver on coherent transmission, optical networks are becoming more and more *software-defined*, in order to automate the network orchestration. In this context, openness and disaggregation are becoming the keywords for the optical network evolution. With *open*, we refer to the need for open source software and network devices based on standardized data structures, allowing the network operation automation and interoperability between different vendor devices. The interoperability is linked to the concept of *disaggregation*. Traditional optical networks solutions are offered by vendors as monolithic blocks with proprietary orchestration tools. The disaggregation perspective aims to solve the vendor lock-in by treating at least the transceiver side and optical line system (OLS) as separate entities interfaced with open technologies, thus allowing for seamless and cost effective upgrades of specific network elements.

In this work we first propose a network abstraction based on the generalized signal-to-noise ratio GSNR as a general figure for the estimation of the quality-of-transmission (QoT) of a lightpath. Such abstraction has the aim to decouple the spectral content from the line system characteristics in order to simplify the optimizaton of the network working point with respect to the physical propagation impairments and develop effective tools for path computation in lightpath deploying. From this perspective, an effective abstraction of the complex mechanism behind the generation of non-linearities in optical fiber propagation is crucial. In this work, we observe non-linearities generation by means of extensive Split-Step Fourier method (SSFM) based simulation campaigns, which solve numerically the optical fiber propagation equation.

We first focus on dispersion-uncompensated (DU) OLSs populated with polarization multiplexed (PM) coherent channels, considering several symbol rate and

spectral grids scenarios, since the market is pushing towards the enlargement of symbol rate to improve capacity. Targeting the SNR as observable figure of performance, we show through a detailed set of SSFM simulations, that the overall non-linear interference (NLI) is composed of the self-channel interference (SCI) and the cross channel interference (XCI) originated by each of the interfering channels, thus allowing for a *spectrally disaggregated* modeling, opposed to the Four-Wave Mixing (FWM)-like aggregated approach. Furthermore, a worst-case, *spatially incoherent* estimation of the XCI can be accomplished, allowing for power and capacity optimizaton on a per fiber span basis.

We then consider the propagation of legacy intensity modulated-direct detected (IMDD) channels on dispersion-managed (DM) networks. In these networks, optical dispersion compensation was performed and optimized for specific trasmission scenarios, thus not allowing for dynamic and reconfigurable networking. We show that modern forward error correction (FEC) algorithms allow simpler modeling of non-linearities and we provide a QoT estimator enabling easier optimization and performance estimation in these systems.

As a further step, we consider the joint tranmission of coherent and IMDD lightpaths in DM OLSs. In such scenario, coherent channels are known to experience severe QoT degradation due to inline dispersion compensation and non-linear crosstalk originated by IMDD channels. We present an extensive SSFM simulation campaign to observe the non-linear phase noise (NLPN) originated by IMDD on coherent channels and we carry out Monte-Carlo observation to assess the impact of random birefringence on non-linearity generation. Then, a simple, conservative model for the QoT estimation of such degradations is presented and validated with experimental results.

As a final work, we consider multi-band systems, extending the available transmission bandwidth to the C+L band and beyond as a cheaper solution to enlarge the capacity of deployed systems. The extension of the transmission bandwith however triggers intense power transfer from higher frequencies to lower frequencies due to stimulated Raman scattering (SRS). This issue needs to be kept under control by means of power optimization strategies. Exploting SSFM simulations, we show here that disjoint power optimization between existing C-band traffic and newly deployed L-band channels delivers minimal penalties on the overall QoT, allowing easier multi-band upgrades of existing, online systems.

Acknowledgements

First, i would like to thank my supervisor Vittorio Curri for giving me the opportunity to start this PhD. His mentorship, experience and attention to get the general picture of the topics investigated have been fundamental to build an attitude to abstract the significant aspects of complex engineering problems.

I want also to thank all the people from Links Foundation, in particular Stefano Straullu for his competence and willingness in the experimental environment.

Special thanks go to all the PhD colleagues and team members, with which we shared inspiring research challenges or just endless coffee sessions: Alessio Ferrari, Mattia Cantono, Dario Pilori, Andrea D'Amico, Elliot London, Ihtesham Khan, Rasoul Sadeghi, Bruno Correia, Giacomo Borraccini and Marianna Hovsepyan.

I would like to acknowledge, among all the people from the industry I had the opportunity to met, Andrea Castoldi and Rosanna Pastorelli from SM-Optics. The weekly meetings going on since years now helped be to get awareness of the real problems and the effective solutions needed by the industry.

A heartfelt thank to my flatmate Attilio, for his unconditional friendship and for having cooked endless lunches and dinner for me during the hardest times of this experience.

Finally and most importantly, the biggest thanks goes to my family, for the constant support they gave me and for their unmatched support that let me cross the finish line.

Contents

List of Tables

List of Figures

Chapter 1

Introduction

Optical communication systems have become a crucial asset since they are the means through which digital end user services are deployed. In this thesis we report our novel contributions in the context of open and disaggregated networking. Specifically, we focus on the observation and convenient modeling of the propagation phenomena, which allow intelligent design and control of the network.

The thesis is organized as follows: In Chapter 1 we provide an introduction to the optical networks technologies and their current trends. In Chapter 2 we review the basic concepts of open and disaggregated optical networking together with the strategies to abstract it and perform software-defined management. Chapter 3 will introduce the simulation framework and methods based on the split-step Fourier method (SSFM), which has been used to observe the impairments arising due to propagation on an optical system. In Chapter 4, the results of a SSFM-based simulation campaign intercepting the significant phenomena arising in full-coherent systems on dispersion-uncompensated (DU) links are presented. Then, in chapter 5 we take a step back in time presenting a Quality of Transmission estimator (QoT-E) enabling softwarization of legacy intensity modulated-direct detected (IMDD)-based transmission on dispersion-managed (DM) links. In chapter 6 we first observe the generation of non-linearities arising from the mixed propagation of 10G IMDD channels together with coherent lightpaths in DM links and propose a simple model to evaluate the subsequent Quality of Transmission (QoT) degradation to enable mixed transmission and enhance network flexibility. In chapter 7 we present some SSFM results relatively to the power optimization strategies in multi-band optical systems exploiting C+L bands. Finally, in chapter 8 we draw some conclusions and propose future investigations.

1.1 Introduction to Optical Networks

In the last decades optical communications have seen a tremendous growth as the background infrastructure lying behind the countless telecommunications-based services which have become a fundamental part of the 21-th century people.

The first optical links were deployed in Italy back in 1977 dedicated to telephone traffic. In the following decade, the technological progress in fiber manufacturing and devices has reduced the propagation losses allowing for longer reach. However, electrical regeneration of the signal was needed at the end of each fiber segment; an extremely inconvenient operation, still today, due to the large electrical consumption and equipment needed. The introduction of Erbium-doped fiber amplifiers (EDFA) [109] greatly boosted the performance and reach of optical links, which could be then assembled in a *multi-span* configuration, since the amplification of the optical signal was done in the optical domain at the cost of amplified spontaneous emission (ASE) noise injection, which is still the most significant degradations of the transmission quality.

A further substantial capacity boost of optical systems has been determined by the introduction, during the 90s, of wavelength division multiplexed (WDM) systems, where several optical channels were arranged in a WDM comb by modulating them at non-overlapping frequencies, thus starting to more efficiently exploit the optical spectrum. Traditionally the C-band was used because of the fiber loss minimum ($\approx$ 0.2 dB/km) near the 1550 nm wavelength, which incidentally coincided with the maximum emission efficiency of Erbium for optical amplification.

The spectral occupation greatly increased year by year to around 100x WDM channel until dot-com bubble burst in 2000. For almost a decade no significant innovations were introduced, as the capacity offered by point-to-point optical links seemed to be more than enough to sustain the network traffic. At that time, optical channels were generated by intensity modulated-direct detected (IMDD) transceivers employing simple on-off keying (OOK) bit signaling scheme on the optical field intensity, then detected by simple photodiodes, thus losing all the optical field phase information. For this reason, the chromatic dispersion needed to be compensated optically by placing dispersion compensating units (DCU) periodically at the end of the fiber span, accordingly to complex *dispersion maps* schemes also balancing with respect to the dispersion impact on non-linear interference generation induced by Kerr effect [86]. Because of these limitations, these system where treated more like static point-to-point circuits as the dispersion map optimization prevented barely any dynamic adaptation of the transmission rate and/or spectral allocation. Consequently, IMDD systems net transmission rate was limited to 10 Gbps per wavelength.

Things radically changed around 2010, under the push of the first bandwidth-hungry multimedia streaming services, with the introduction of coherent transceivers. The ability of coherent transceivers to modulate and detect both amplitude and

phase of the optical field, paired with the development of fast analog-to-digital converter (ADC) and energy efficient electronic processors implementing digital signal processing (DSP) based algorithms was the game changer. First, it allowed to dramatically increase the spectral efficiency passing to quadrature amplitude modulation (QAM) schemes. Thanks to DSP-based receiver implementing adaptive equalization, linear effects as polarization mode dispersion (PMD) and chromatic dispersion could have been now compensated digitally at the receiver allowing to remove inline DCUs, which was also found to be beneficial for non-linearities [27]. The ability to distinguish and recover at the receiver between a pair of orthogonal polarization states allowed also a two-fold rate growth thanks to polarization multiplexing (PM), allowing to reach a net data rate of 100 Gbps per WDM wavelength. Soon, improved DSP techniques allowed the dynamic adaptation of symbol rate R_s and/or modulation formats, allowing to scale the delivered data rate to the reach and/or quality-of-transmission QoT offered by a lightpath [70]. In particular, the removal of inline DCU allowed the decoupling of the transceiver side from the line systems. Furthermore, the introduction of reconfigurable optical add-drop multiplexers (ROADM), took a step further enabling the add, drop and forward of single wavelengths directly at the optical level. Consequently the optical layer has evolved from single point-to-point communication to fully-meshed topologies where optical channel can added and dropped at any node or backhauled to the upper IP layer, enabling *transparent all-optical networking* [130].

1.2 Current Trends in Optical Networking

The transparent and flexible scenario implies the need for an intelligence able to control and orchestrate the optical network, in order to perform networking operations such as routing or circuit restoration, directly at the optical layer. All the application layers services we interface to, such as social networks or streaming services, are conveyed through the optical networks data transport facilities, whose requirements in terms of capacity, reliability and flexibility are becoming year by year more stringent. These trend will be confirmed by the ongoing deployment of 5G based services and the push towards an even more digital and connected world as a long-term consequence of the COVID-19 pandemic [155, 126]. Software-Defined-Networking (SDN) and Network-Function-Virtualization (NFV) technologies are driving this change by automating the networks' orchestration and management and removing the bottleneck of manual processes to deliver efficient and dynamic abstraction of network functions at higher levels.

This strong tendency to network automation is also paired to a continuous growth of the traffic demand [170]. As envisioned by the Cisco Visual Networking Index [36] the global IP traffic will reach 4.8 ZB per year, growing at a compound

annual growth rate (CAGR) of 26% from 2017 to 2022. Furthermore, in their Annual Internet Report [35] relative to the 2018-2023 time span, the global population penetration of the Internet access is projected to increase from 51% to 66%. By 2023, the 5G connections will represent the 10% of the total mobile connections, offering an average speed roughly 13x higher than current 4G connections. The machine-to-machine (M2M) connections will grow at 19% CAGR, empowered by the arising IoT technologies and representing one of the main drawing forces of the traffic growth [143]. In order to cope with this trend, previously, most of the effort was spent into the enhancement of the transmission technologies exploiting the large capacity offered by the optical fiber medium, especially in the core/backbone network segments where a large amount of tributaries are aggregated.

From the first 100G solutions, transceivers have been evolved supporting faster rates. Today to the 400G-ZR+ [34] modules delivering 400 Gbps per wavelength also in the long-haul are available, and 800G [171] is starting to be deployed on practical systems. However, such evolutions are nowadays mostly obtained by enlarging the spectral occupancy and not much more can be done from the spectral efficiency point of view as we have come to graze the Shannon limit [58]. On this side, the extension of the transmission bandwidth beyond the C-band has been proposed in order to increase the capacity per fiber, as we will see in chapter 7.

Together with the rise of increasingly bandwidth hungry services the management of the infrastructure has become a crucial point. Operators are in fact trapped in a crossfire: on one side they must be able to face the increasing traffic demand; on the other side they need to keep the business sustainable, since it has been predicted that the cost per bit will exceed the revenues [167].

In this context, emerging trends are the push towards the *opening* and *disaggregation* of the network elements to resolve *vendor lock-in* and be able to upgrade and expand the network seamlessly and efficiently, in a *vendor-agnostic* fashion, especially on the line terminal side, whose life-cycle is definitely shorter than the one of the line system. This vision is opposed to the traditional one of monolithic, single-vendor solutions, as it will be explained in chapter 2. Furthermore, operators want to exploit as much as possible the previous investments on the line system side, since fiber deployment is extremely expensive [166], so that the line system tends to be used as a transparent commodity.

To this aim, operators and vendors are stimulating the network softwarization by enhancing its flexibility in terms of management, reconfigurability and pushing the interoperability of different optical network's segments to a wider breathe. In this direction, in chapter 6, we propose the interoperability between different optical transmission techniques, such as legacy 10G IMDD transmission on DM networks and coherent channels delivering 100 Gbps and beyond. The availability of fast and reliable software and mathematical models for the estimation of lightpaths' QoT is then crucial for path computation and network orchestration.

In this thesis we show how a deep observation of the physical layer impairments arising from propagation of light signals through the network elements becomes fundamental, since it enables an easy abstraction of the signal quality metrics, which can be then used to perform efficient management and providing means for enhancing network flexibility towards the openness and disaggregation paradigm.

Chapter 2

Open and Disaggregated Optical Networks

In this chapter, the basic concepts of openness and disaggregation in optical networks are explained. We then present the main requirements of *spectral* and *spatial* disaggregation that, in our perspective, should be fullfilled when modeling the QoT. After, a review of the most significant phenomena arising in propagation of an optical channel along a piece of optical network is given. Finally, based on the suggested network paradigm, a method to abstract the network with respect to its QoT using the signal-to-noise ratio (SNR) metric is presented.

2.1 Open and Disaggregated Networks

As already mentioned in chapter 1, one of the greatest leaps in optical communications has been the availability of add-drop devices at the wavelength level enabling transparent optical transmission on complex topologies, basically allowing to establish a light circuit, at least within an optical domain [130]. However, even if transparent, optical networks are often monolithic systems where sub-parts of the network are sold by a unique vendor who also provides its proprietary management solutions which are tightly bound to the actual hardware and vertically integrated from the bare metal to the upper IP/Ethernet layers. The *vendor lock-in* prevents operators to carry out specific network upgrades which are needed to cope with the increasing capacity demand and save on capital expenditures (CAPEX) due to the increasing cost per bit. In this situation, operators push to open optical networking technologies and to interoperability between devices of different vendors has gained momentum [75, 92, 85], from the Data Center Interconnect (DCI) to the metro and core network scenario and in single- and multi-domain networks [79, 174, 151, 124]. Such trend acts synergistically, from the network management point of view, with the demand for flexibility and automation of optical networks.

Traditionally, in fact, optical networks have been managed mostly in a static way and often required manual intervention due to the traffic pattern characteristics or in case of software/hardware failures. However, the advent of 5G services [155, 126] and the NFV paradigm requires a fairly more elastic and dynamically reconfigurable network infrastructure, for example in the deployment of new lightpaths between two network nodes. This envisions an optical network evolution headed to the *automatiion* and *softwarization* of the existing functions with the aim, also, to provide a background for the deployment of further network services.

Hence, the implementation of SDN [40, 151, 67] goes through the development of a more-or-less centralized intelligence, having the large picture of the network and able to properly configure it to adapt dynamically to the traffic request or, for example, to automatically detect failures and take countermeasures [144, 154]. Such SDN architecture is briefly represented in Fig.2.1: the SDN controller is a software layer exposing standardized Application Programming Interface (API) which takes requests from the upper IP or application layers and possess the necessary knowledge and APIs to setup a service by configuring the network infrastructure.

In this context, *open* and *disaggregation* have become the two keywords for the next generation optical networks, together with SDN:

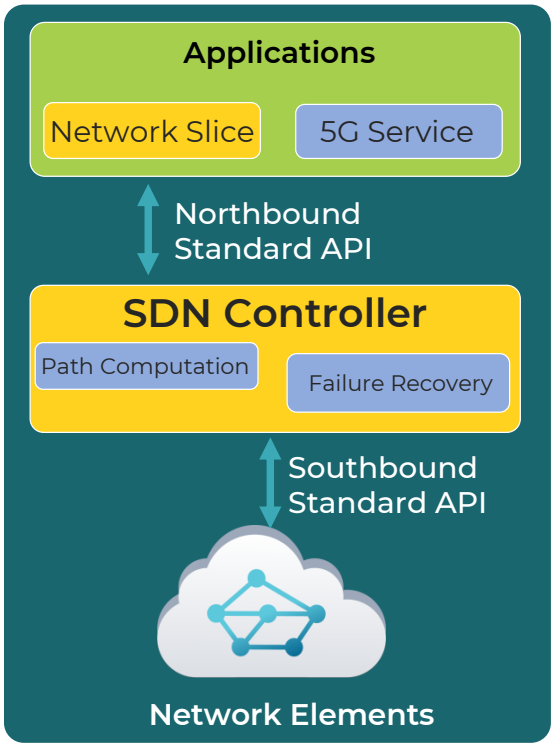

Figure 2.1: Schematic of SDN with some examples of the typical functions requested by the application layer and performed by the SDN controller

- **Open**: refers to the availability of open network devices, usually also called whiteboxes, exposing their configuration parameters which rely on open standards and managed with open source software solution which can be developed independently on the device vendor.
- **Disaggregation**: refers, to various extent, to the paradigm under which telco operators do not treat network elements or entire network segments as black boxes, but they are directly involved in the the design, testing and integration of them within their extended network infrastructures.

2.1.1 Network Disaggregation Models

In a traditional, fully-aggregated paradigm, the vendor provides an entire network segment to the operator, including the network elements and a network segment controller as a black-box. Northbound interface to upper layer services are defined by proprietary software and the the operator is boundend on them to deploy its service. From a system lifecycle perspective, the management is completely in charge of the vendor so that seamless, specific system upgrades to fulfill operator needs usually require invasive intervention.

In the network disaggregated paradigm, several network elements from different vendors can be interfaced, by breaking up the black box in its components more or less deeply. From the network orchestration point of view, this puts in charge of the operator to choose the interfacing standards and a controller layer tailored to its requirements. From the system lifecycle perspective, this allows seamless and more efficient upgrades to the single network entities. Two models have been emerged with respect to the way the optical system can be disaggregated [39]:

Partial Disaggregation

In the partial disaggregation model, exemplified in Fig.2.2, the WDM transport layer, composed by an *open* optical line system (OLS) made up of optical fibers, inline optical amplifiers (ILA) and, eventually, ROADMs, are still considered as a single entity but decoupled from the transceivers. The rationale behind this strategy is that the OLS lifespan is considerably longer than the transceiver's which are usually upgraded more frequently due to the increasing capacity demand. In this case, an SDN controller does not interact with single OLS elements but an OLS controller exposes some generic APIs and data structures to that and internally manages the OLS elements setup such as the ILAs working point. The advantage of such solution is that the analog part of the management, i.e. referring to the propagation of the signal through the OLS, is still in charge of the vendor but still enables more flexibility in the network configuration, and different solutions can be chosen for different domain segments.

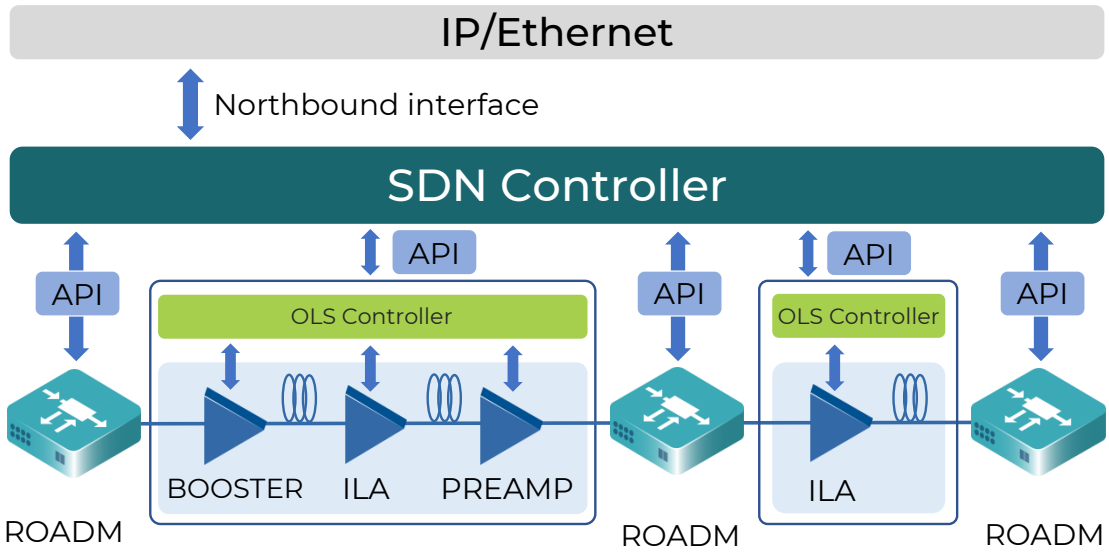

Figure 2.2: Block scheme of a section of a partially disaggregated network segment.

Full Disaggregation

In the full disaggregation model, instead, the OLS itself is further disaggregated in its network elements, as represented in Fig.2.3. In this case, every device, such as amplifiers and ROADMs, should be managed in a per-device fashion. Each device expose APIs to enable vendor-agnostic configuration of the line and implements standardized data structures to expose its parameters. Although this approach gives the operator the maximum flexibility, as the possibility to upgrade ILAs only for multi-band transmission, it surely requires substantial additional effort since the SDN controller must cope with all the analog transmission issues.

It is then clear that, moving from fully-aggregated locked-in solutions to the interoperability of diverse devices, in both a fully or partial disaggregation way, requires a huge effort in software development and standardization. In this direction, in the last years, several standardization consortia came out and a lot of research and trials have been carried out both from the industry players and academic side.

As for the standardization consortium is worth mentioning OpenROADM (led by AT&T) [101, 9], a multi-source agreement defining specifications and YANG models to describe compliant devices, OpenConfig (led by Google) [99] who has moved more in the partial disaggregated field and the Telecom Infra Project (TIP) (led by Facebook) [150], which is very active in diverse fields of open networking, by proposing a Transponder Abstraction Interface (TAI) and developing the GNPy [68] open source software solution for the estimation of QoT in optical networks. Furthermore, OpenDaylight [100] and ONOS [98] represents two options as open SDN controllers. Plenty of demonstrations of SDN controllers using open device models open and disaggregated networking technologies have been presented [31,

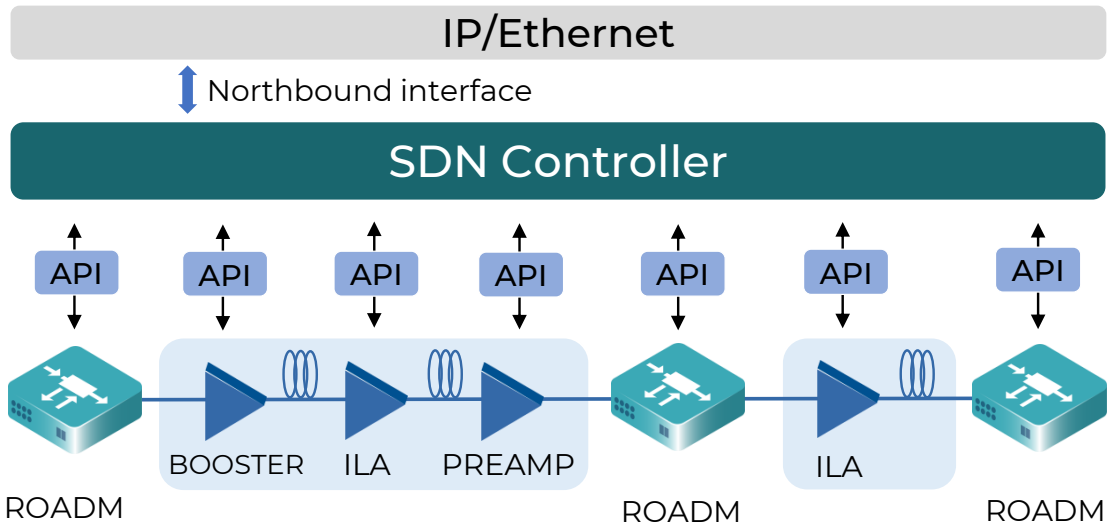

Figure 2.3: Block scheme of a section of a fully disaggregated network segment.

142, 33, 88, 83, 18] and the impact of various level of disaggregation has been studied [131, 39, 123, 124]. With respect to open technologies for QoT estimation, several works involving machine learning techniques for the refinement of the accuracy or for automatic failure localization have been reported, such as in [178, 48, 49, 144]. Within the TIP Open Optical Packet Transport - Physical Simulation Environment (OOPT-PSE) group activities, the GNPy tool has gained a lot of attention and has been experimentally tested providing excellent results [60, 59, 62, 63, 5] and has also been demonstrated to be integrated in other open solutions such as ONOS [82] employing open whitebox devices such as the Cassini [1] transponder for open pluggable coherent optics [161]. Cassini whitebox has raised a lot of interest among the operators thanks to the possibility of use of compact CFP2 coherent transceivers with rate up to 200 Gbps and the next iteration, the Phoenix whitebox [71] will come out soon supporting 400G-ZR+ pluggable coherent optics.

2.2 Propagation Impairments in Optical Fibers

In this section, with aim to introduce a network's physical layer abstraction later, we will first briefly review the main propagation impairments arising in propagation of modulated data signals in optical fibers.

2.2.1 Amplified Spontaneous Emission

Amplified Spontaneous Emission (ASE) is of the main impairment in optical transmission and it is originated by optical amplification with Erbium Doped Fiber

Amplifiers (EDFA) Indeed, together with the useful signal amplification, the EDFA introduces an amount of ASE noise which can be modeled as an additive white Gaussian noise (AWGN), whose bilateral power spectral density (PSD) G_{ASE}, i.e. including both the polarization states is given by:

$$G_{ASE} = hf_0F(G-1) \tag{2.1}$$

where h is the Planck constant, f_0 is the central frequency of the amplified channel, F is the amplifier noise figure and G is the amplifier gain in linear units. Note that, in principle, Eq.2.1 is valid only for EDFAs. However, in case of pure Raman or hybrid Raman-EDFA amplification it has been widely demonstrated [3, 76, 42] that, from a systemistic point of view, the same equation holds by considering an equivalent noise figure.

2.2.2 Chromatic Dispersion

In optical fibers light propagates over a dispersive medium, i.e. a medium whose phase velocity, or propagation constant, is a rather smooth function of the frequency of the propagating signal. The propagation constant $\beta(\omega)$ is conveniently expressed in terms of its Taylor expansion [3] when polarization effects can be neglected:

$$\beta(\omega) = \beta_0 + \beta_1(\omega-\omega_0) + \frac{1}{2}\beta_2(\omega-\omega_0)^2 + \frac{1}{6}\beta_3(\omega-\omega_0)^3 \tag{2.2}$$

In Eq.2.2, $\omega = 2\pi f$ is the angular frequency in rad/s, being f the frequency in Hz and $\omega_0 = 2\pi f_0$ is the central angular frequency of the Taylor expansion.

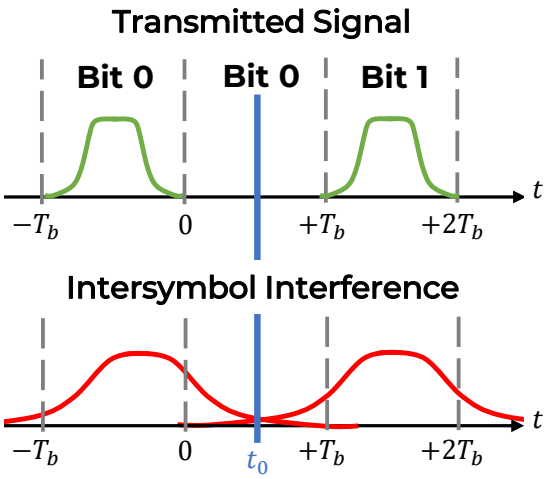

Figure 2.4: An example of the ISI introduced by chromatic dispersion on a sequence of NRZ pulses.

Hence different frequency components of an optical channel propagate at different speed. While β_0 and β_1 represents respectively a phase shift and a propagation delay, the second and third order terms introduce distortion of the propagating pulse due to the arising intersymbolic interference (ISI), depicted in Fig.2.4, impairing the QoT if not counteracted.

In particular, β_2 is the proper chromatic dispersion coefficient which has thus dimensions of s^2/m in fundamental units. β_2 is also commonly expressed in literature as ps^2/km or ps/THz/km, being the derivative of the phase with the optical frequency. However, the chromatic dispersion coefficient is also traditionally referred to in terms of the D parameter, which is basically the same thing except for being expressed in terms of wavelength rather than frequency, so it measures as ps/nm/km.

Stopping the Taylor expansion to the second order provides a good approximation of the propagation constant for WDM spectra occupying the 5 THz of the C-Band. However, for larger bandwidths, such as in multi-band C+L systems occupying $\approx$ 11 THz, the third order term β_3, usually called dispersion slope and expressed in ps^3/km (or $ps/THz^2/km$), must be taken into account, especially for the dispersion interplay with Kerr effect, as it can be understood as a non-negligible frequency dependence of the chromatic dispersion coefficient. As before, the dispersion slope is rather expressed in wavelength as S_0 parameters and it measures as $ps/nm^2/km$.

The chromatic dispersion can be compensated for either optically, by means of inline DCU placed at the end of each span (for 10G, IMDD systems), or electronically, in a proper DSP receiver stage that fully compensates for the accumulated dispersion at the receiver side (for systems carrying coherent channels).

2.2.3 Birefringence and PMD

Birefringence consists in the dependence of the refractive index on the polarization state of the light traveling in it. As a consequence, the expression of the propagation constant simply described in Eq.2.2 becomes matricial - $\mathbf{B}(\omega)$ - considering different values for the x and y polarization states of 0-th and 1-st order of the Taylor expansion of Eq.2.2. Considering only the polarization asymmetry for the β_0 term, the Jones vector of the electric field traveling in the fiber $\mathbf{E}(z,\omega)$ can be expressed in the frequency domain as:

$$\mathbf{A}(z,\omega) = e^{-j\beta_0 z} \cdot \begin{bmatrix} e^{-j\frac{\Delta\beta_0}{2}z} & 0 \\ 0 & e^{j\frac{\Delta\beta_0}{2}z} \end{bmatrix} \cdot \mathbf{A}(0,\omega) \tag{2.3}$$

where $\beta_0 = (\beta_{0,1} + \beta_{0,2})/2$, $\mathbf{A}(z,\omega) = \mathbf{P}_0^{-1} \cdot \mathbf{E}(z,\omega)$ and $\mathbf{P_0} = [\nu_{0,1}, \nu_{0,2}]$ is the direction of the birefringence principal axes. The terms $\beta_{0,1}$ and $\beta_{0,2}$ are the zeroth order propagation constant terms in the direction of the principal axes, hence

$\Delta\beta_0 = (\beta_{0,1} - \beta_{0,2})$ is the birefringence propagation constant difference and in Eq.2.3 induces a polarization rotation.

Considering instead the polarization asymmetry in the first order β_1 term, the simplified of Jones vector of the electric field traveling in the fiber $\mathbf{E}(z,\omega)$ can be expressed in the frequency domain as:

$$\mathbf{A}(z,\omega) = e^{-j\beta_1(\omega-\omega_0)z} \cdot \begin{bmatrix} e^{-j\frac{\Delta\beta_1}{2}(\omega-\omega_0)z} & 0 \\ 0 & e^{j\frac{\Delta\beta_1}{2}(\omega-\omega_0)z} \end{bmatrix} \cdot \mathbf{A}(0,\omega) \tag{2.4}$$

where $\beta_1 = (\beta_{1,1} + \beta_{1,2})/2$, $\mathbf{A}(z,\omega) = \mathbf{P}_1^{-1} \cdot \mathbf{E}(z,\omega)$ and $\mathbf{P_1} = [\nu_{1,1}, \nu_{1,2}]$ is the direction of the differential group delay (DGD) principal axes. The terms $\beta_{1,1}$ and $\beta_{1,2}$ are the first order propagation constant terms in the direction of the polarization axes, hence $\Delta\beta_1 = (\beta_{1,1} - \beta_{1,2})$ is a polarization dependent phase velocity difference inducing a DGD $\Delta\tau_g = \Delta\beta_1 z$ between the DGD polarization axes.

However, in typical optical fibers used in communication systems the birefringence evolves randomly in space and time, causing stochastic variations of the state of polarization (SOP) of the WDM signal during propagation. The concatenation of random birefringence-induced polarization rotations give rise to the polarization-mode-dispersion (PMD) due to the stochastic nature of the differential group delay, i.e. a propagation delay between the two main polarization components of the signal [66, 69].

Effects of PMD in optical communications have been studied extensively during the years, especially with respect to its interplay with non-linearities generated by Kerr effect and SRS [20, 164, 119, 140, 89], and before of the advent of DSP-based coherent receivers, which are able to compensate for PMD, it was considered one of the limiting impairments in communications. In this thesis, birefringence will be taken into account in chapter 6, when studying the mixed propagation between IMDD and coherent channels, since, also, they require extensive Monte-Carlo SSFM simulation campaigns to assess its effects.

2.2.4 Stimulated Raman Scattering

The stimulated Raman scattering SRS [121, 3] is a phenomenon related to the inelastic scattering of photons in optical fibers, causing an energy transfer from higher frequencies to lower frequencies. The efficiency of the energy transfer depends on the frequency distance between the spectral components. The typical efficiency profile for a standard single-mode fiber (SSMF) fiber is reported in Fig.2.5. It shows that it has its peak at a frequency distance of around 13 THz, so that SRS is one of the most important phenomena to consider in multi-band transmission, although the same phenomenon is also widely exploited for Raman amplification [76, 16, 19].

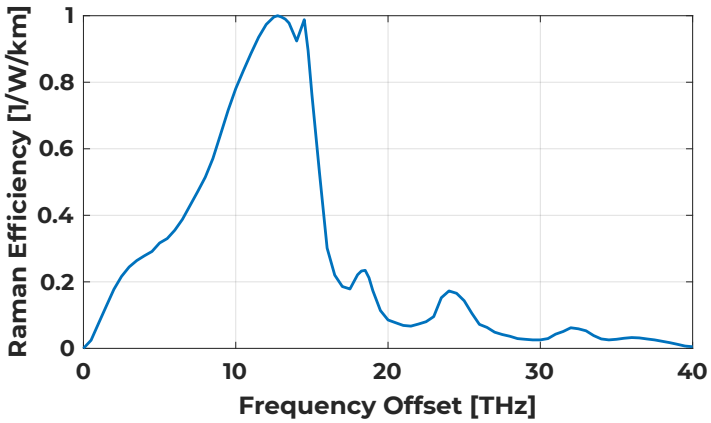

Figure 2.5: The normalized Raman efficiency vs the frequency distance for a typical optical fiber.

2.2.5 Kerr Effect

Thee Kerr effect [3, 86] consists in the refractive index of the optical fiber core slightly changing proportionally to the injected light intensity. In the WDM signal context, this leads to an instantaneous phase distortion on the observed optical channel which depends on its own power and on the other WDM channels power. The intensity of the Kerr effect, from a systemistic perspective, is commonly determined by the fiber non-linear coefficient γ, expressed in 1/W/km. Due to this dependence on the squared electric field, Kerr effect give rise to non-linear effects.

Due to the interplay with the chromatic dispersion, such phase modulation is partially converted into an amplitude disturbance, so that, in typical WDM systems, the Kerr effects can manifest as either an *amplitude* noise and as a non-linear *phase* noise (NLPN), becoming a main impairments in moderate to large length optical system, whose impact is commonly leveraged with adequate power setting strategies. In the transmission systems' power operating range, the Kerr effect can be treated as a *perturbation* of the optical signal propagation constant [3] so that the effect of non-linearities can be formalized on the received symbol sequence $r[t_s]$ as in Eq.2.5:

$$r[t_s] = x[t_s]e^{j\phi_{NL}[t_s]} + n_{NL}[t_s] \tag{2.5}$$

where $x[t_s]$ is the transmitted symbol sequence at the optimum sampling instant for the s-th symbol t_s, $\phi_{NL}[t_s]$ is the NLPN phase shift on each symbol, $n_{NL}[t_s]$ the interference part appearing as additive noise. Fig.2.6 shows an example of how amplitude noise and phase noise appears on the scattering diagram of a received QPSK constellation. NLPN (Fig.2.6a) appears as an elongation of the impaired clouds of the transmitted constellation points due to a correlation between their phase and and quadrature components. Since it is a disturbance on the phase, it can be modeled as a *multiplicative* noise to the electric field. Amplitude noise

(Fig.2.6b) shows up as a cloud of received points around the original transmitted constellation points, whose variance (i.e., the power) is the same for all symbols and quadratures, so that is also usually referred to as *circular* noise.

To get a general picture of the of the impairments generated by Kerr effect in a WDM transmission scenario, it is useful to look at the Manakov equation, governing the propagation of of the WDM signal in optical fibers when the propagation constant polarization dependence (birefringence) can be neglected:

$$\frac{\partial \mathbf{E}(z,t)}{\partial z} = -\alpha \mathbf{E}(z,t) - j\frac{\beta_2}{2}\frac{\partial^2 \mathbf{E}(z,t)}{\partial t^2} + j\gamma\frac{8}{9}\mathbf{E}^{\dagger}(z,t)\,\mathbf{E}(z,t)\,\mathbf{E}(z,t) \tag{2.6}$$

Here, the β_0 and β_1 coefficients relative to ω_0 of Eq.2.2 have been neglected since they carry a constant phase shift and a propagation delay. We also neglect the dispersion slope term β_3 for simplicity. The first term describe the field loss, the second term describes the chromatic dispersion, while the third is the Kerr effect term depending on the WDM field instantaneous power. $\mathbf{E}(z,t) = [E_x(z,t), E_y(z,t)]^T$ is the WDM field Jones vector of the WDM signal and $\mathbf{E}^{\dagger}(z,t)\,\mathbf{E}(z,t) = |\mathbf{E}(z,t)|^2$ its power, where † stands for the Jones vector conjugate transpose. The WDM signal $\mathbf{E}(z,t)$ can be thus conveniently expressed as the sum of the optical fields complex envelopes of its N_{ch} tributary channels $\mathbf{E}_k = [E_{k,x}(z,t), E_{k,y}(z,t)]^T$, each modulated at its central angular frequency $\omega_k = 2\pi f_k$.

$$\mathbf{E}(z,t) = \sum_{k=1}^{N_{ch}} \mathbf{E}_k(z,t)\, e^{j\omega_k t} \tag{2.7}$$

It is here useful to rewrite Eq.2.6 in a *spectrally separated* way, thus describing the propagation of the i-th channel of the WDM comb rather than it ensemble.

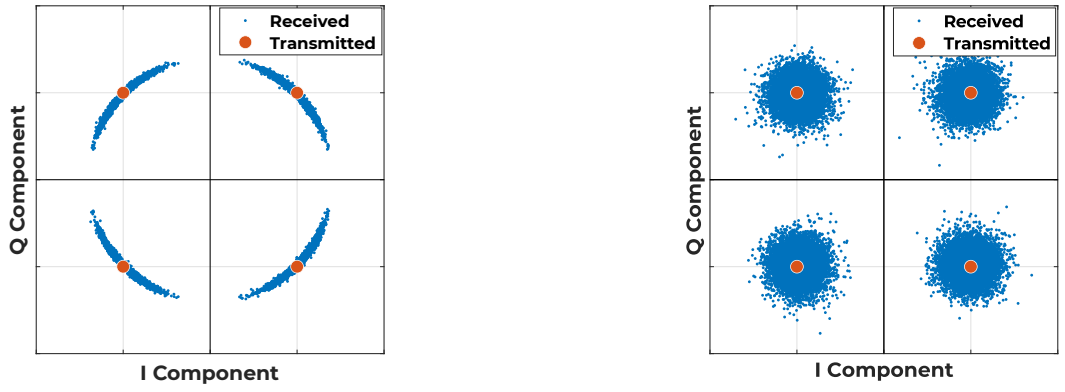

(a) (b)

Figure 2.6: Scattering Diagram of clean (orange) and noise-impaired (blue) QPSK constellations: (a) Multiplicative phase noise, (b) Additive circular noise only.

Substituting Eq.2.7 in Eq.2.6 is it possible to come up with a set of coupled differential equations describing the evolution of each channel, so that for the i-th channel we have:

$$\begin{aligned}\frac{\partial \mathbf{E}_i(z,t)}{\partial z} =& -\alpha \mathbf{E}_i(z,t) \\ &+ j\frac{\beta_2 \omega_i^2}{2}\mathbf{E}_i + \beta_2 \omega_i \frac{\partial \mathbf{E}_i(z,t)}{\partial t} - j\frac{\beta_2}{2}\frac{\partial^2 \mathbf{E}_i(z,t)}{\partial t^2} \\ &+ j\gamma\frac{8}{9}\sum_{(n,m,k)\in C_i} \mathbf{E}_n^{\dagger}(z,t)\,\mathbf{E}_m(z,t)\,\mathbf{E}_k(z,t)\,e^{j(\omega_m+\omega_k-\omega_n-\omega_i)t}\end{aligned} \tag{2.8}$$

In Eq.2.8, the second and third terms on the right-hand side come from the second order time derivative. They represent a *local* phase delay $\beta_{0,i} = \beta_2\omega_i^2/2$ and a *local* propagation delay $\beta_{1,i} = \beta_2\omega_i$ arising from the change of reference frequency from ω_0 to the i-th channel central frequency ω_i. The product in the Kerr term is a convolution in frequency, so that it has three-fold the bandwidth of the whole WDM field. Hence, for the i-th channel under test (CuT), the product encompasses only those terms falling in the i-th channel bandwidth, i.e. the channel index triplets (n,m,k) belonging to the generators set C_i:

$$C_i = \{(n,m,k) \mid \omega_m + \omega_k - \omega_n = \omega_i\} \tag{2.9}$$

This implies that the complex exponential in the Kerr term is always unitary and Eq.2.8 can be rewritten as:

$$\begin{aligned}\frac{\partial \mathbf{E}_i(z,t)}{\partial z} =& -\alpha \mathbf{E}_i(z,t) \\ &+ j\beta_{0,i}\mathbf{E}_i + \beta_{1,i}\frac{\partial \mathbf{E}_i(z,t)}{\partial t} - j\frac{\beta_2}{2}\frac{\partial^2 \mathbf{E}_i(z,t)}{\partial t^2} \\ &+ j\gamma\frac{8}{9}\sum_{(n,m,k)\in C_i} \mathbf{E}_n^{\dagger}(z,t)\,\mathbf{E}_m(z,t)\,\mathbf{E}_k(z,t)\end{aligned} \tag{2.10}$$

It is convenient, however, to change the reference system to the one tracking the i-th channel loss α, its phase $\beta_{0,i}$ and its propagation delay $\beta_{1,i}$. This is done by defining the retarted time frame $\tau = t - \beta_{1,i}z$ and operating the following signal substitution:

$$\mathbf{A}_i(z,t) = \mathbf{E}_i(z,\tau)e^{\alpha z - j\beta_{0,i}z} \tag{2.11}$$

so that it is possible to further rewrite Eq.2.10 as:

$$\frac{\partial \mathbf{A}_i}{\partial z} = -j\frac{\beta_2}{2}\frac{\partial^2 \mathbf{A}_i(z,t)}{\partial t^2} + j\gamma\frac{8}{9}e^{-2\alpha z}\sum_{(n,m,k)\in C_i} \mathbf{A}_n^{\dagger}(z,t)\,\mathbf{A}_m(z,t)\,\mathbf{A}_k(z,t)\,e^{-j\Delta\beta z} \tag{2.12}$$

where $\Delta\beta$ is the *phase matching coefficient* describing the phase mismatch between the channels interacting in the non-linear term:

$$\Delta\beta = (\beta_{0,i} + \beta_{0,n} - \beta_{0,m} - \beta_{0,k}) = \beta_2(\omega_i^2 + \omega_n^2 - \omega_m^2 - \omega_k^2) \tag{2.13}$$

Note that the phase matching coefficient is not always null because of the squared angular frequency values. By focusing on the non-linear term is possible to derive the common taxonomy for non-linearities, whose characteristics strongly depend on the indexes of the interfering channels in the Kerr term. Hence, in order to isolate the contribution falling into the i-th channel, we need to distinguish among the possible combinations of the indexes triplets (n, m, k) belonging to C_i.

Self Phase Modulation (SPM)

Self-Phase Modulation (SPM) occurs when $\omega_k = \omega_m = \omega_n$, thus all equal to ω_i. In this case $\Delta\beta = 0$, at least as far as the channels are approximated as Constant Waves (CW)s or have narrow bandwidth. In such case, the Kerr terms becomes:

$$j\gamma\frac{8}{9}|\mathbf{A}_i|^2\mathbf{A_i} = -j\gamma\frac{8}{9}\begin{bmatrix}(|A_{i,x}|^2 + |A_{i,y}|^2)\,A_{i,x}\\(|A_{i,x}|^2 + |A_{i,y}|^2)\,A_{i,y}\end{bmatrix} \tag{2.14}$$

Hence, SPM is essentially phase modulation originated by the channel under test on itself, proportional to its instantaneous power and it can be regarded also as self-channel interference (SCI). Hence, it is strongly correlated to the channel and compensation techniques at the DSP level have been proposed [177].

Cross Phase and Polarization Modulation (XPM and XPolM)

Cross-Phase Modulation (XPM) and Cross-Polarization Modulation (XPolM) occur when $\omega_m = \omega_n \Rightarrow \omega_k = \omega_i$ OR $\omega_k = \omega_n \Rightarrow \omega_m = \omega_i$; i.e. when one of the non-conjugated channels coincides with the conjugated. This still leads to $\Delta\beta = 0$. Both the phenomena can be regarded together as cross-channel interference (XCI). Therefore, considering the Jones vector notation, being n the interfering channel index and i the CuT, the two polarization components of the Kerr term can be expanded as:

$$j\gamma\frac{8}{9}\sum_{n\neq i}(\mathbf{A}_n^*\mathbf{A}_n\mathbf{A}_i + \mathbf{A}_n^*\mathbf{A}_i\mathbf{A}_n) = -j\gamma\frac{8}{9}\sum_{n\neq i}\begin{bmatrix}(2|A_{n,x}|^2 + |A_{n,y}|^2)\,A_{i,x} + A_{n,x}A_{n,y}^*A_{i,y}\\ \underbrace{\left(|A_{n,x}|^2 + 2|A_{n,y}|^2\right)A_{i,y}}_{\text{XPM}} + \underbrace{A_{n,x}^*A_{n,y}A_{i,x}}_{\text{XPolM}}\end{bmatrix} \tag{2.15}$$

Left-hand side of Eq.2.15 shows that the bulk of the XCI is additive over the set of interfering channels $n \neq i$, each one with a 2x multiplicity.

Furthermore, by expanding the Jones products as in the right-hand side of Eq.2.15, is possible to gain more insights on the nature of the phenomenon and distinguish between the XPM and XPolM contribution.In Eq.2.15 the first row of the matrix is relative to the impairment on the x polarization state of the CuT $A_{i,x}$, the second row on the y component. Hence, each XCI contribution on a polarization component is made up of two terms: the first one is the *pure XPM* term, acting similarly to the SPM, thus, in principle, a phase modulation on the CuT i operated by the interfering channel n. The second contribution is instead a crosstalk of one polarization component to the other mediated by the interfering channel cross product $A_{n,x/y}A^*_{n,y/x}$, commonly referred as XPolM [169, 80].

As in [169], it can be demonstrated that Eq.2.15 can be rewritten as:

$$j\gamma\frac{8}{9}\sum_{n\neq i}\left(\frac{3}{2}\mathbf{A}_n^*\mathbf{A}_n+\frac{1}{2}\mathbf{S}_n\cdot\vec{\sigma}\right)\mathbf{A}_i \tag{2.16}$$

where $\mathbf{S}_n$ is the Stokes vector of $\mathbf{A}_n$ and $\vec{\sigma}=(\sigma_1,\sigma_2,\sigma_3)^T$ is the Pauli vector with σ_i the (permuted) Pauli matrices [69]. In Eq.2.16 the second Stokes term rewrites the polarization crosstalk and shows that XPolM induces a depolarization, i.e. a change of the SOP of the CuT.

The joint effect of chromatic dispersion during propagation translates part of the NLPN due to XPM to signal intensity fluctuations [146, 51], i.e. amplitude noise. If also, non-linearities can be considered a small *perturbation* on the signal, which is the context of optical transmission systems, such intensity fluctuations can be regarded as additive disturbance to the CuT [112]. As a consequence, the entire XPM phenomenon can be effectively considered as *crosstalk* from an interfering channel to the CuT, other than the residual phase noise part.

Four Wave Mixing (FWM)

Four-Wave Mixing (FWM) occurs when $\omega_m,\omega_k\neq\omega_n$ (non-conjugate term different to the conjugate), so that $\omega_i\neq(\omega_m,\omega_n,\omega_k)$. In this case the Kerr term is as in Eq.2.10, unless $\omega_m=\omega_k$, indicated as *degenerate* FWM.

As opposed to the SCI and XCI terms which are proper phase modulation terms, FWM is the only case where three or two (degenerate FWM) channels interact to generate new frequencies falling in the i-th channel bandwidth. Furthermore, its intensity is weighted by the complex exponential of the phase mismatch $\Delta\beta$, which is here non-zero, so that it decays rapidly with the channel spacing, larger symbol rates and with larger dispersion fibers. For the latter reason especially, it is expected to have almost negligible impact in modern DU OLSs with highly dispersive fibers.

2.3 Physical Layer Abstraction

As already mentioned in chapter 1, the availability of DSP-based coherent transmission and the possibility of an all-optical network [130, 46], at least within the same network domains, thanks to the introduction of optical amplifiers and and ROADMs, has drastically changed the operative scenario enabling elastic and transparent optical networking [93, 130]. In this situation, optical channel can be dynamically established and reconfigured so that they can respond to the time-changing traffic pattern in a short time scale [46], also thanks to the availability of hybrid modulation format and flexible rate transceivers [70]. Since the WDM transport layer now operates almost completely in the optical domain, the awareness of the physical layer impairments has become a crucial point in the process of establishing a *lightpath* between two nodes of the network.

- **Lightpath**: a lightpath between two network nodes is defined as the pair made of the wavelength over which the optical channel is propagated in the WDM grid and the physical path crossed by the channel itself to link the desired nodes.

Hence, being able to estimate in advance the QoT of a lightpath becomes crucial in order to check the *path feasibility*, so that fast and efficient analytical model are required to perform this task. In the context of open and disaggregated optics, orchestrated by SDN controllers, with the aim to improve network flexibility and automation, the physical layer awareness gains even further significance. In order to obtain such QoT estimation tools, observation of the propagation phenomena properties becomes crucial to develop analytical models which can be expressed in closed formulas or semi-analytical forms capable of practical numerical integration.

Obviously, propagation impairment modeling has always been an hot topic starting from the earliest days of optics. However, what makes the difference in the modern networks is that the QoT estimation is fundamental not only in the network *design* phase but also in its *management* and *orchestration*:

- **Design**: in the design phase, an operator may want to use a QoT estimation tool to determine the system configuration able to support the required capacity or to address advantages and disadvantages of a certain system upgrade to maximize the ratio between CAPEX and performance.
- **Management**: in transparent networking, a QoT estimation tool may be integrated within the network or the OLS controller in order to find, among all the possible network paths, the one delivering the minimum required amount of QoT to support transmission to a certain rate. The same can apply, for example, in finding alternative backup paths in case of a link failure.

At the time of IMDD legacy systems, where the system configuration was specifically tailored to fixed spectral load characteristics, QoT estimation had the main role of aiding the optimization of the system in design phase, as systems were thought to operate statically, due to the interdependency of the transport infrastructure (fibers and ILAs) to the WDM content, as any deviation from the optimization define in the design phase may have potentially impaired existing deployed traffic.

Such constraint is lift in disaggregated networking enabled by optical transparency, so that propagation modeling used to manage an online network poses practical constraints on model properties. Path feasibility, for example, must be able to complete on a short time scale in order to be able to respond promptly to the change in traffic demand, requiring a QoT model comprehensive of the most significant impairments and simple enough to solve, for example, the routing problem, with low complexity and in a real-time scale level. In addition, it should provide slightly *conservative* QoT estimation in order to operate always on the safe side avoiding system out-of-service.

2.3.1 The SNR as Generalized QoT Metric

Hence, the first step to develop a QoT estimation framework is to determine a, possibly unique, metric for QoT. During the years, accordingly to the evolution of the optical technologies, several quality metrics have been proposed [65], such as the Q-factor, which was popular in the days of direct detection due to the QoT being evaluated on the electrical translation of the optical instantaneous power. However, whatever transmission technology one could consider, the ultimate merit figure of signal quality is still the bit error rate (BER). Fig.2.7 reports the main blocks of either a DSP-based coherent receiver and a direct-detection receiver used in legacy IMDD systems[133, 65]. In both cases in fact, whatever receiver ends with a FEC stage. A FEC stage ensures that at its output a virtually error free decoded

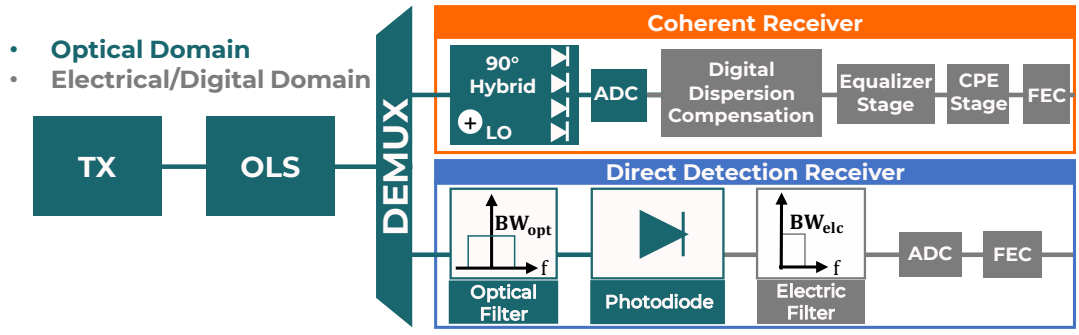

Figure 2.7: Principal system blocks of a coherent (orange) and legacy, direct detection (blue) receivers.

bit-stream is obtained if a target *pre-FEC BER threshold* is met. Therefore, the pre-FEC BER can be considered the ultimate quality metric. However, employing BER as target metric in both numerical simulation, modeling and real deployed equipment is not straightforward. In particular, SSFM based numerical simulations require very long data sequences to deliver reliable estimations, while real equipment needs to average over long time sequences and needs errors to actually occur, making impossible to measure it if the lightpath is not already established.

The introduction of coherent receivers, able to linearly map the polarization, phase and quadrature components of the optical field in the digital domain, has pushed towards a large use of the signal-to-noise ratio (SNR), which, in general, is defined as Eq.2.17:

$$\mathrm{SNR} = \frac{P_{ch}}{P_N} \tag{2.17}$$

where P_{ch} is the received channel power and P_N is the total noise power. Note that this expression is referred to the signal at the DSP stages, usually called *electrical SNR*, with the noise power measured on a bandwidth equal to symbol rate R_s of the CuT. However, thanks to linear mapping between the optical field and the signal in the digital domain, the same SNR can be translated linearly back to the optical domain, obtaining a metric directly related to observation of the powers of the *optical* signal and noise field.

In optical communications, the optical signal-to-noise ratio (OSNR) indicates the SNR measured in the optical field by means of an OSA, thus taking into account solely the degradation due to an ASE noise source with power P_{ASE} , which, we recall, can be modeled as an additive, locally white, Gaussian distributed noise:

$$\mathrm{OSNR} = \frac{P_{ch}}{P_{ASE}} \tag{2.18}$$

For historical reasons related to the typical resolution bandwidth of the OSAs, P_{ASE} is commonly measured on a noise integration bandwidth B_n of 0.1 nm, corresponding to about 12.5 GHz near the 1550 nm. The linear mapping to the electrical SNR of Eq.2.17 is thus obtained by simply rescaling the noise bandwidth:

$$\mathrm{SNR} = \mathrm{OSNR} \cdot \frac{B_n}{R_s} \tag{2.19}$$

Then, from the digital communications theory [120], when the channel is *additive* and *Gaussian*, the pre-FEC BER is uniquely determined by the signal-to-noise ratio (SNR) and the modulation format of the transmitted signal, as in Eq.2.20:

$$\mathrm{BER} = \alpha \cdot \mathrm{erfc}(\sqrt{\beta \cdot \mathrm{SNR}}) \tag{2.20}$$

where $\mathrm{erfc}(\cdot)$ is the complementary error function, α, β are constants depending on the modulation format cardinality. It follows that, if the optical transmission channel is AWGN by taking into account the relevant propagation impairments and at

least just before of the FEC stage, the SNR can be mapped directly to the pre-FEC BER and considered as the unique merit figure for QoT estimation of the optical system. This is a huge advantage since, from the point of view of the impairment observations by SSFM simulations, it allows to reduce the computational effort instead of simulating long signals for the BER counting. Furthermore, it allows in real system to assess the feasibility of an optical path just by SNR estimation, which is also more practical to derive in analytical modeling.

The BER to OSNR Characteristic Curves

It should be noted that Eq.2.20 is a lower bound for the pre-FEC BER at a fixed amount of additive Gaussian noise and modulation format, since it assumes an ideal transceiver. Fig.2.8 reports the BER vs OSNR curves measured by OSA of a real transceiver compared to the theoretical curves. Experimental curves present a penalty with respect to the theoretical bound due to implementation issues, which is considerably large especially at low BER. However, this does not change the general picture as a unique pre-FEC BER can be still determined from the SNR inverting the measured curve rather than the theoretical expression.

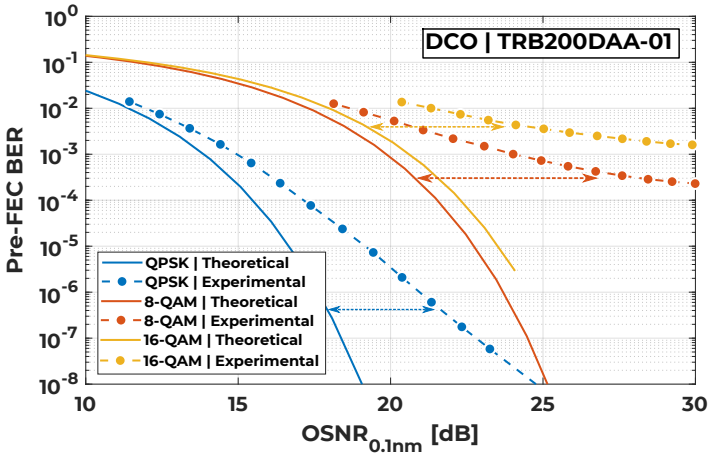

Figure 2.8: Experimental BER vs OSNR curves for a pluggable CFP2 transceivers compared to the theoretical curves. Dashed arrows indicate the penalty of the real transceiver performance with respect to the theoretical curves

Optical Transmission Channel Abstraction

The Eq.2.20 holds for coherent systems employing quadrature-amplitude modulation (QAM) formats, thanks to the already mentioned characteristics of coherent receivers which are able to compensate for chromatic dispersion and PMD in the digital domain [38, 17, 165, 133], converge to the matched filter in the adaptive

equalizer stage [133] and recover phase noise thanks to carrier phase estimation (CPE) algorithms [179, 162, 133]. It should be clear that all the magic holds *if and only if* all the impairments can be modeled as additive noise sources, Gaussian distributed. When considering ASE noise only, the validity of this assumption is straightforward. However, this is not necessarily true when non-linear effects come into play. Among these, SRS acts on the power profile of the WDM signal and becomes significant only at very large bandwidth, thus non-linearities induced by Kerr effects must not be overlooked.

As previously mentioned, Kerr effect is essentially a phase modulation (i.e. a multiplicative, imaginary noise) depending on the signal power itself. As such, in general, the optical transmission channel is not linear and cannot be modeled as an additive impairments. In the past decades, plenty of effort has been spent both on the observation and mathematical modeling of the coherent systems impairments.A remarkable results has been the discovery that signal propagation without any inline dispersion compensation, performed instead electronically at the receiver, mitigates the non-linearities due to Kerr effect. Also, thanks to the large accumulated dispersion, the signal itself appears as Gaussian distributed [43, 26]. In this uncompensated transmission scenario, in a low to moderate non-linear regime, it has been widely demonstrated that the net effect of Kerr non-linearities appears as an additive Gaussian distributed noise source, [152, 11, 136, 90, 139, 136, 112, 132, 78, 77], commonly indicated as non-linear interference (NLI).

On the modeling side, this led to the large family of the Gaussian noise (GN) models [112, 77, 139]. Gaussian noise models approximate the solution of the fiber propagation equation assuming the WDM signal composed by uncorrelated Gaussian spectral components. Such solutions allow to calculate easily the power of an equivalent additive noise source, whose value P_{NLI} comes out to be proportional to the third power of the channel power P_{ch} [112]:

$$P_{NLI} = \eta P_{ch}^3 \tag{2.21}$$

where η is the NLI efficiency depending on the spectral load and OLS physical parameters. This approach to non-linearities has been first proposed in 1993 [2] and later adopted for coherent, DU systems [26, 112, 117, 139]. More recently, an Enhanced GN model (EGN) has been proposed in order to account for the non-gaussianity of the channels in the first spans of propagation [29, 116]. In [21] the GN model approach is extended to take into account the interplay between non-linearities generation and SRS. Outside the GN-model family, some very interesting models approaching the non-linearity in the time-domain have been proposed [138, 90, 55, 53, 54], giving some more precise details on the NLI generation properties such as their dependence on the modulation format. In particular, the time-domain models predict actually that a significant fraction of the non-linear interference manifests as phase noise. However, the bandwidth of this phase noise component

has been shown to be narrow-band enough to be mostly compensated by CPE algorithms in DSP receivers [52, 54, 115]. This fact has been also further demonstrated by experimental field trial using Gaussian-noise model based QoT estimations [63, 62, 161], thus showing that for coherent transmission in DU OLSs, the non-linear channel can be *linearized*, assuming that phase noise is compensated by DSP and considered as an AWGN channel. This implies that, when phase noise is present, the transmission channel can be still considered AWGN, but only if extended to all the blocks of Fig.2.7 until the CPE stage included. In this scenario, a generalized SNR, accounting for both ASE noise and non-linearities, can be assumed as the unique figure for QoT. The *generalized signal-to-noise ratio* (GSNR) is thus defined as:

$$\mathrm{GSNR} = \frac{P_{ch}}{P_{ASE} + P_{NL}} \tag{2.22}$$

In Eq.2.22 P_{ch} is the average optical power of the channel, P_{ASE} is the optical ASE noise power arising from optical amplifiers, and P_{NL} is the optical noise power arising from the non-linear effects. Thanks to the additivity of the noise sources, the GSNR can be written as the inverse sum of its contributions:

$$\frac{1}{\mathrm{GSNR}} = \frac{1}{\mathrm{OSNR}} + \frac{1}{\mathrm{SNR_{NL}}} \tag{2.23}$$

In Eq.2.23, the OSNR, as in Eq.2.18 is the GSNR contribution due to the amplifier ASE noise only, while $\mathrm{SNR_{NL}}$ is the non-linear noise contribution:

$$\mathrm{SNR_{NL}} = \frac{P_{ch}}{P_{NL}} \tag{2.24}$$

Although these noise sources are not flat over the entire optical spectrum, we can safely assume they can be regarded as such within the channel bandwidth . The final pre-FEC BER performance of a lightpath can be thus obtained by the theoretical or experimental curves of Fig.2.8. This is possible since both the noise sources in the GSNR are Gaussian, thus they can be modeled as *equivalent* lumped noise sources at the beginning or end of the fiber span.

Hence, having the GSNR as a unique figure of QoT, enables us to build an *abstraction* of the physical layer needing the following information to provide a QoT estimation

- **Spectral Information**: the characteristics of the WDM spectra traveling in the fiber: channel power, symbol rate, modulation format, channels spectral allocation. These are needed for the evaluation of the NLI.
- **Network Description**: the description of the OLSs composing the network: fiber length, loss coefficient, chromatic dispersion, non-linearity coefficient which are needed for ASE and NLI evaluation.

2.3.2 The Network Weighted Graph Abstraction

The possibility to model the lightpath as an AWGN channel has crucial implications because it simplifies the network abstraction provided to the SDN controller to perform management operations. First, an OLS composed by N_s fiber spans can be abstracted with the cascade of equivalent blocks, as in Fig.2.9, each operating independently of the others. Then, the gain-loss profile determined by fiber attenuation and ILAs gain can be applied. Finally, ASE and non-linearities are modeled as equivalent lumped noise sources added at the beginning or end of each span, determining the GSNR of the lightpath after the propagation on that OLS.

Hence, a data structure effectively abstracting a WDM optical transport network is a *topology weighted graph*. As depicted in Fig.2.9, graph nodes are the ROADMs or optical switches and the edges are the OLSs connecting them, weighted by the introduced GSNR degradation.

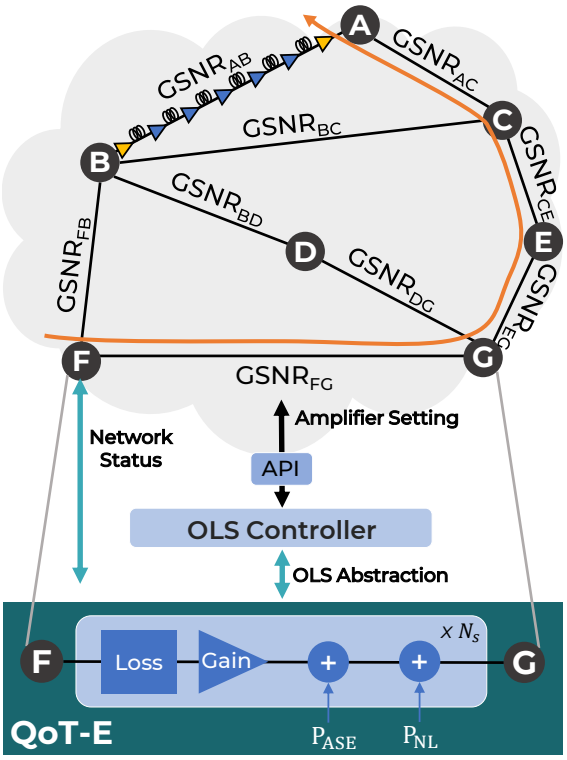

Figure 2.9: Weighted graph network abstraction: nodes are switching sites, edges are OLSs. OLSs are made of fiber spans with ILAs (blue in AB edge) and booster/pre-amp at the start/end of the OLS (yellow in AB edge). The OLS controller provides an AWGN OLS abstraction to the QoT-E module of the SDN controller to compute the GSNR for path computation and sets the working point of the amplifiers to optimize QoT.

The SDN controller builds the network abstraction by taking as input the network description from the OLS controller, together with information on the lightpath to analyze, the transceiver and the spectral information, returning the GSNR for each graph edge elaborated by the QoT-E module.

A QoT-E API can be used for different networking operation. For planning, the QoT-E is used assuming worst-case scenarios of full spectral load. For path computation, the QoT-E must be used with real-time network status as input, to enable minimum margin lightpath deployment, or also in automatic failure recovery. The QoT-E can also assist the OLS controller in order to set the line to operate at the optimal working point – maximum GSNR.

The proposed abstraction is very powerful and neat since it allows to *navigate* the graph to get the overall GSNR at the end of a specific path just by inverse summing the contributions:

$$\frac{1}{\mathrm{GSNR}_{\mathrm{FA}}} = \frac{1}{\mathrm{GSNR}_{\mathrm{FB}}} + \frac{1}{\mathrm{GSNR}_{\mathrm{BA}}} \tag{2.25}$$

Hence, the problem of finding the optimum path between a couple of nodes coincides with that of maximizing the GSNR of each of the crossed paths.

However, it is worth to underline some properties which may be convenient to satisfy in QoT modeling for the non-linearity, since they allow to speed up and ease the QoT computation over a large set of paths where the complexity burden is an issue:

Spectral Disaggregation

The $\mathrm{SNR}_{\mathrm{NL}}$ degradation on a coherent channel (the *probe*) caused by the effect of N_p channels (the *pumps*) is given by the inverse sum of the $\mathrm{SNR}_{\mathrm{NL},k}$ contribution

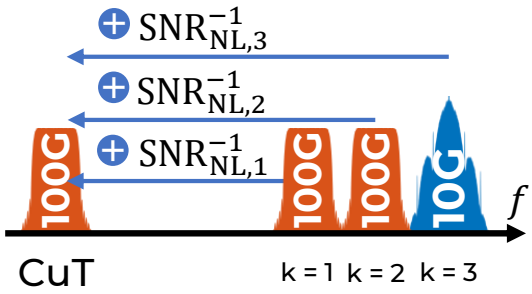

Figure 2.10: Graphical outline of the spectral disaggregation principle. Channels SNR contributions are inversely additive. The addition symbol stands for direct additivity in terms of noise power, while SNR contributions sum up in their inverse.

of each pump, as in Eq.2.26

$$\frac{1}{\mathrm{SNR}_{\mathrm{NL}}} = \sum_{k=1}^{N_p} \frac{1}{\mathrm{SNR}_{\mathrm{NL},k}} \tag{2.26}$$

where $\mathrm{SNR}_{\mathrm{NL},k}$ is the SNR degradation determined by the non-linear noise contribution P_{NL}, k of the k-th channel. The spectral disaggregation requirement basically stands for the possibility to evaluate independently the non-linear noise contribution generated by a single channel co-propagating with the CuT and then sum all the single contribution in a *pump-and-probe* fashion, as outlined in Fig.2.10. Note that we have represented also an IMDD channel in figure to underline that the idea, in principle, can be applied not only to coherent channels. This implies that the non-linearities originated by each pump do not show any correlation between them, which is a reasonable hypothesis since they carry independent data streams. This approach allows for a spectrally separated philosophy in the way non-linearity generation is seen, justified by the fact that cross-channel non-linear interaction is indeed the most significant contribution among the multichannel ones [53].

Spatial Disaggregation

The $\mathrm{SNR}_{\mathrm{NL},k,n}$ degradation of the k-th channel introduced by the n-th fiber span does not depend on the previous history traveled but on the current span and its spectral content only. Then, after N_s fiber spans Eq.2.27 holds:

$$\frac{1}{\mathrm{SNR}_{\mathrm{NL},k}} = \sum_{n=1}^{N_s} \frac{1}{\mathrm{SNR}_{\mathrm{NL},k,n}} \tag{2.27}$$

The spatial disaggregation (or *spatial incoherency*) property implies no spatial correlation among the NLI contributions introduced by the previous span, so that the $\mathrm{SNR}_{\mathrm{NL},k,n}$ - the SNR degradation introduced by n-th span - is a function of

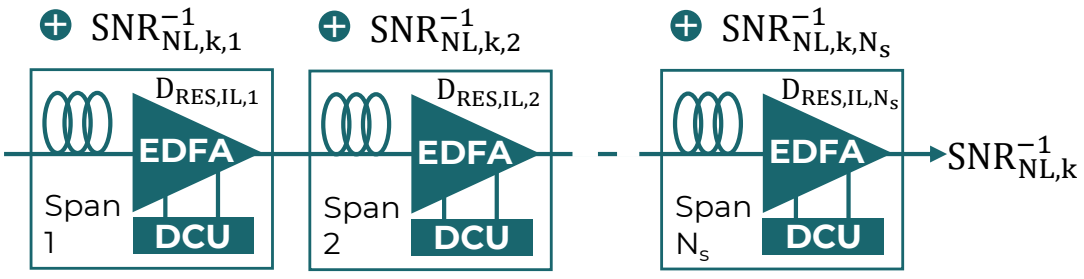

Figure 2.11: Graphical outline of the spatial disaggregation principles. Span SNR contributions are inversely additive. The addition symbol stands for direct additivity in terms of noise power, while SNR contributions sum up in their inverse.

only the n-th fiber span characteristics. In the context of the transparent, open network management this is a key assumption, since the channel to route may share the OLSs composing the path with different channels hop after hop. Some models, as the EGN [29] or the plain coherent GN model [113] take into account some amount of spatial coherency. However, if considered, it would imply that, in turn, the history of all the channels would be needed to compute the QoT, making basically unfeasible the QoT estimation in terms of complexity.

In addition to these two, as previously, mentioned, we expect a model to be also slightly **conservative** in $\mathrm{SNR_{NL}}$ prediction, so that one may be sure to operate in the safe side, i.e. below the out-of-service thresholds, without compromising too much, at the same time, the accuracy of the prediction. Hence, the disaggregation properties imply the additivity of the noise sources introduced by each span and each channel without any correlation among them, thus enabling to obtain the overall GSNR by inverse summing the single contributions as done in Eq.2.23.

Similar complexity constraints, such as in the case considered for the spatial coherency, holds for model's dependency on modulation format. It is actually well recognized that the NLI amount depends on the modulation format [53, 29]. However, introducing such dependency in modeling would couple the transceiver to the OLSs abstraction for GSNR computation as it would require multiple iteration since the modulation format itself is set accordingly to the available QoT.

In the direction of the properties listed is the Locally-Optimized-Globally-Optimized (LOGO) strategy for power optimization [107, 4, 108]. The LOGO approach exploits a spatially incoherent version of the GN model [113] in order to set the optimum power per channel P_{opt} at the input of the i-th span, which is given by:

$$P_{opt} = \sqrt[3]{\frac{P_{ASE}}{2\eta}} \tag{2.28}$$

where P_{ASE} is the ASE noise power injected in the i-th span and η is NLI efficiency obtained from the GN model such that $P_{NL} = \eta P_{ch}^3$ as in Eq.2.29,2.30:

$$\eta = \frac{8}{27}\frac{2\alpha\gamma^2 L_{eff}^2}{\pi|\beta_2|R_s^2}\mathrm{arcsinh}\left(\frac{\pi^2|\beta_2|B_{ch}^2 N_{ch}^{2\frac{B_{ch}}{\Delta f}}}{4\alpha}\right) \tag{2.29}$$

where L_{eff} is the fiber effective length and, with respect to the non-linearity generation, represent the length after which the NLI can be considered negligible thanks to fiber attenuation.

$$L_{eff} = \frac{1 - e^{-2\alpha L_s}}{2\alpha} \tag{2.30}$$

Note that the GN model as in Eq.2.29 does not include NLI dependency on the the modulation format. In addition, as previously, it relies on a spectral aggregated

approach since it models everything as a FWM-like disturbance. The LOGO strategy ensures that setting P_{opt} at each span maximizes the GSNR at the end of the OLS. As for ASE noise, the spatial disaggregation is always verified, since each ILA produces statistically independent noise contributions.

Chapter 3

Simulation of Light Propagation on Optical Line Systems

In chapter 2 we have introduced the open and disaggregated network paradigm and presented a powerful physical layer abstraction based on a topology graph whose edges are weighted with the GSNR of the network's OLSs. In order to obtain such GSNR is necessary to elaborate a convenient propagation model, especially for the non-linear interference deriving from Kerr effect or as for SRS, among the others, which are the main objects of the studies presented in this thesis.

We would like to underline that, because of the context where these models are going to be employed, there is actually no strict need for a detailed and complete description of the phenomena, comprehensive of all the subtle dependencies between the system parameters. On the contrary, a propagation model aimed at the design and management of an optical network, should, in our view, narrow down the view to focus on the significant characteristic of the phenomena. In our case this means to obtain a model able to decouple the transceiver from the transport infrastructure in a partially disaggregated fashion and providing a slightly conservative QoT predictions in order to operate always on the safe side, still being as much accurate as possible, provided that the physics of the phenomenon allow this.

In any case, the validation of a model must pass through an extensive experimental phase, first on a controlled laboratory environment, then on real commercial systems. However, especially in the development stage, in order to isolate the aforementioned most significant aspects of the propagation, one may need to decouple the propagation effects of interest in such a way an experiment does not allow to. For example, in the laboratory, isolate the non-linearities generation from ASE noise is impossible. To this aim, a *numerical simulation* phase of the propagation on an optical system, i.e. solving the equations governing the light propagation, assumes a noteworthy importance.

3.1 Introduction to the Split-Step Fourier Method

Propagation of light in optical fibers is governed, in the most general case, by the CNLSE, which is derived from the Maxwell equations. Starting from the derivation as in [91, 89] and writing it conveniently in the frequency domain we get:

$$\begin{aligned}\frac{\partial \mathbf{E}(z,\omega)}{\partial z} &= -\alpha(\omega)\mathbf{E}(z,\omega) - j\boldsymbol{B}(\omega)\mathbf{E}(z,\omega) \\ &+ j\frac{\gamma}{3}\mathcal{F}\left\{\begin{bmatrix} 3|E_x(z,t)|^2 + 2|E_y(z,t)|^2 & E_x^*(z,t)\,E_y(z,t) \\ E_x(z,t)\,E_y^*(z,t) & 2|E_x(z,t)|^2 + 3|E_y(z,t)|^2 \end{bmatrix}\mathbf{E}(z,t)\right\}\end{aligned} \tag{3.1}$$

In Eq.3.1 $\mathbf{E}(z,t) = [E_x(z,t), E_y(z,t)]^T$ is the time-domain WDM signal electric field (column) Jones vector. $\mathbf{E}(z,\omega)$ is the same field expressed in the frequency domain, being $\omega = 2\pi f$ the angular frequency and $\mathcal{F}\{\cdot\}$ the Fourier transform operator. The first two terms represents the linear effects in fiber propagation, attenuation and propagation constant, respectively. $\alpha(\omega)$ is the fiber optical field loss coefficient, expressed in neper/m and it can be frequency dependent, especially when considering ultra-wide bandwidth. In particular, $\mathbf{B}(\omega)$ represents the matricial propagation constants accounting for random birefringence inducing PMD and chromatic dispersion. The third term instead accounts for non-linear Kerr effect. Note that the Fourier transform of the Kerr terms remains implicit since a generalized closed form cannot be calculated. In order to simplify the discussion, we can consider the Manakov equation, which we have already seen in chapter 2.

The Manakov equation [89, 91] is obtained from the CNLSE by transforming the coordinate systems to the one rotating with birefringence and then averaging on its rapid variations, obtaining Eq.3.2:

$$\frac{\partial \mathbf{E}(z,t)}{\partial z} = -\alpha\mathbf{E}(z,t) - j\frac{\beta_2}{2}\frac{\partial^2\mathbf{E}(z,t)}{\partial t^2} - \frac{\beta_3}{6}\frac{\partial^3\mathbf{E}(z,t)}{\partial t^3} + j\gamma\frac{8}{9}\mathbf{E}^\dagger(z,t)\,\mathbf{E}(z,t)\,\mathbf{E}(z,t) \tag{3.2}$$

Here, $\mathbf{E}^\dagger(z,t)$ stands for the complex conjugate of $\mathbf{E}(z,t)$, so that $\mathbf{E}^\dagger(z,t)\,\mathbf{E}(z,t) = |\mathbf{E}(z,t)|^2$. The second and third term account for chromatic dispersion and dispersion frequency slope, becoming here explicit after birefringence is averaged and having neglected the β_0, β_1 terms inside the $\boldsymbol{B}(\omega)$ term of Eq.3.1. In the last non-linear term the $\frac{8}{9}$ coefficient comes out from birefringence averaging. Note that here the equation is fully expressed in the time domain.

The Manakov equation can be further simplified in the mostly ideal case in which all the optical channels are assumed in a single polarization state and no coupling happens between the polarization states. In this case, all along the propagation, the electric field becomes scalar $\mathbf{E}(z,t) = E(z,t)$ and the CNLSE degenerates in the scalar differential equation commonly called Non-Linear Schroedinger Equation (NLSE), where the $\frac{8}{9}$ factor in Kerr term is reasonably removed due to the absence

of birefringence [91]:

$$\frac{\partial E(z,t)}{\partial z} = -\alpha E(z,t) - j\frac{\beta_2}{2}\frac{\partial^2 E(z,t)}{\partial t^2} - \frac{\beta_3}{6}\frac{\partial^3 E(z,t)}{\partial t^3} + j\gamma|E(z,t)|^2 E(z,t) \quad (3.3)$$

The three equations presented can all be conveniently rewritten by defining two separate operators applied to complex field envelope: A linear operator $\mathcal{L}[\cdot]$ applying fiber loss, dispersion, birefringence and PMD in the frequency domain and a non-linear operator $\mathcal{N}[\cdot]$ applying Kerr effect in the time domain:

$$\frac{\partial \mathbf{E}(z,\omega)}{\partial z} = \mathcal{L}[\mathbf{E}(z,\omega)] + \mathcal{F}\{\mathcal{N}[\mathbf{E}(z,t)]\} \quad (3.4)$$

All the propagation impairments due to fiber propagation can be thus deduced from CNLSE or Manakov equation, when the random birefringence can be neglected. Theoretically, all the QoT prediction could be precisely obtained just by solving these equations. However, these equations do not admit closed form solution except in very specific and non realistic cases such as non-dispersive fibers or in absence of non-linearities. In practical cases they can be only numerically solved, thus requiring an enormous amount of CPU time which makes it unfeasible for fast QoT estimations. Propagation models are derived from the same equations by making simplifying assumptions to alleviate the burden. However, testing the correctness of these assumptions, such as those made in chapter 2, still pass from the numerical solution of the CNLSE/Manakov.

The Split-Step Fourier Method (SSFM) has been first applied for fiber propagation in 1973 [149] and since then has been the reference algorithm for simulation of optical propagation. The idea behind the SSFM is that, although the linear and non-linear operator act actually simultaneously, for a length step dz approaching zero they can be considered independent. Hence, as represented in Fig.3.1, the fiber length is subdivided in n_s steps of adequately small length dz. Then, within each step, first the linear step is a applied, i.e. on a virtually dispersive, lossy and birefringent only segment, then, on that output, the non-linear step is performed, thus

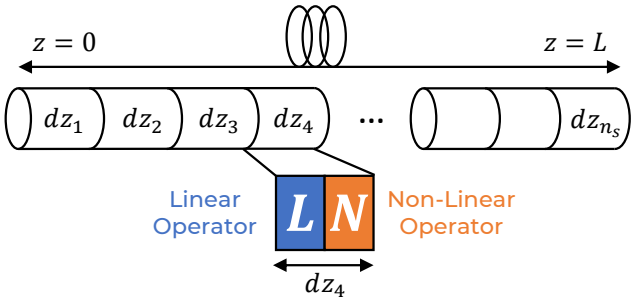

Figure 3.1: Scheme of the Split-Step Fourier Method. The linear $\mathcal{L}$ and non-linear $\mathcal{N}$ operators are applied separately in each dz step.

on a virtually non-dispersive, non-birefringent, lossless fiber. The linear step can be efficiently applied with a multiplication in the frequency domain, while the non-linear step is conveniently applied as a multiplication in the time domain to avoid the double convolution. Both of them are applied on a WDM signal of duration t_{sig} in the time domain which is substantially a discrete-time window of an ideally infinite transmitted signal, during which its statistical properties are stationary.

Hence, since no particular assumption are made in the derivation of the most general CNLSE, the SSFM can simulate the propagation of virtually any multiplex of co-propagating optical signals over an OLS setup. The only significant constraint of such method is the computational complexity which could translate in a excessive required simulation time. This complexity derives from the fact that, for each of the n length steps the fiber is subdivided in, the algorithm requires two runs of the Fast Fourier Transform (FFT) algorithm to switch back and forth between the linear and the non-linear operators, being the FFT the most computationally intensive task of the algorithm.

Hence, we can identify three simulation parameters impacting the complexity the most. Two of them, the simulation bandwidth and the data sequence length impact the computational cost of a single FFT run, while the third determines the multiplier of the number of the single FFT iterations:

- **Data sequence length**: this is the number of transmitted symbol N_{sym} in the CuT which we want to observe at the end of the receiver to calculate the QoT metrics. Hence, the larger N_{sym}, the longer the WDM signal duration t_{sig}, thus more computationally expensive will be the FFT applied to the WDM signal.

- **Simulation bandwidth**: the simulated signal bandwidth BW_s must be set large enough to accommodate all the WDM channels and the non-linear phenomena of interest, so that each transmitted symbol must be oversampled by N_{sps} samples per symbol (SpS). The larger BW_s, the more SpS are needed and the longer will be the WDM signal length in terms of samples $N_{samples} = N_{sym}N_{sps}$, thus enlarging FFT time.

- **Number of steps**: the SSFM method has been shown to converge to exact solution of the CNLSE-family equation when the dz step length converges to zero [8]. As the step length is shortened to increase the accuracy, the required time per fiber segment increases since $2n_s$ FFT iterations are required. Hence, adequate strategies must be implemented to properly set the step length accordingly to the required accuracy on the QoT metric evaluated.

3.2 The Simulator Framework Structure

The SSFM algorithm is the heart of the simulation of propagation on an optical fiber and its accuracy parameters must be tuned up carefully to ensure consistent results with a reasonable computational complexity. However, the simulation on a realistic multi-span transmission system is not only about the fiber segment, but it also involves a careful implementation of other blocks such as EDFAs, Raman effect (both for amplification and detrimental SRS) and especially the DSP-based transceiver when dealing with coherent channels, including the managing of several aspects of the simulated discretized time signal processing. In this section we will spend some words on the simulation software framework we employ, by describing the main process implemented to simulate an entire multi-span optical system and presenting the data structure used to define the network topology and the spectral information, coherently with the abstraction proposed in chapter 2.

3.2.1 Optical Transmission System Software Abstraction

The aim of our simulation framework is enabling the simulation of a wide range of transmission systems with the requirement to exploit the potentialities of Graphical Processing Units (GPU) computing. Many commercial solutions exist for optical transmission simulation, such as OptSim by Synopsis [102] or VPI Photonics [163]. However, having an open source solution was an unmissable requirement for our investigation since permits to have full control and simulate specific behaviors required in a research context. Furthermore, some commercial solutions do not support GPU computing based on on CUDA technology implemented by NVIDIA on its products. GPU computing has become a must have in simulation activity [103, 74, 110, 28] since it enables a substantial speed-up in the execution of parallelizable algorithms, such as the FFT, with respect to the execution on CPU. This

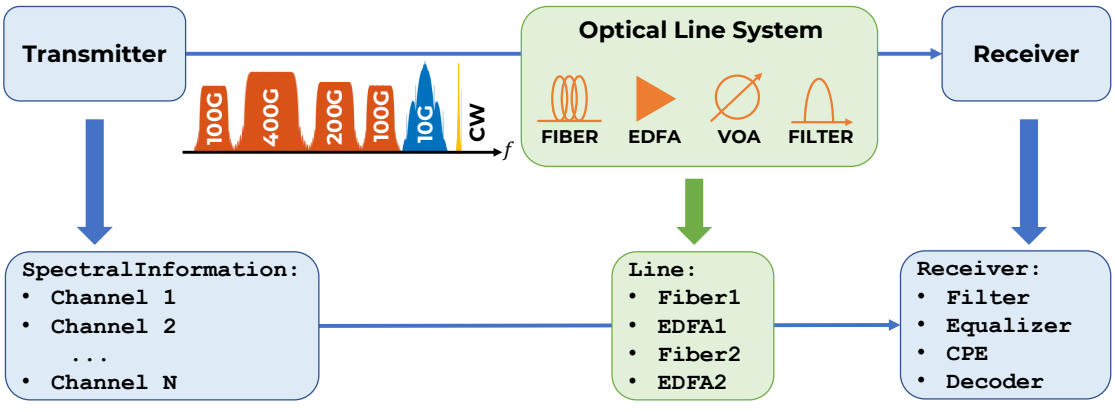

Figure 3.2: Scheme of a generic simulated optical transmission system and multi-service propagated spectrum (up) and its relative classes implementation (down).

requirement becomes more and more significant because of the increasing interest in multi-band transmission exploiting bandwidths far larger than the 5 THz of the C-band.

The simulation framework has been implemented in MATLAB. This platform has been chosen because it provides ready-to-go fast and efficient implementations of the FFTW, BLAS and LAPACK libraries for parallel numerical computation. As a second reason, the simulation framework has been rewritten by expanding the previous MATLAB implementation done by Pilori and Cantono [110] including fiber propagation and DSP techniques. The solution presented in [110] in fact has been expanded to support the propagation of mixed rate and mixed transceiver technologies spectral loads on non-periodic[1] and non-transparent[2] OLSs with and without optical dispersion compensation. A huge coding work has been carried out also to allow more flexibility to the configuration of the OLSs, so that other element such as inline filters (for investigations on filtering penalties, for example) or non-ideal amplifier gain frequency response can be seamlessly integrated - provided an adequate description - in order to speed-up the workflow in extensive simulation campaigns.

Such flexibility required a switch of coding paradigm from simple procedural scripting to object-oriented programming. To this aim, first the main blocks of a transmission system as more general as possible have been identified. The top of Fig.3.2 shows the block diagram of a typical optical transmission system. In a partially disaggregated manner, the OLSs is thought as an independent entity with respect to transmitter and receiver. The bottom of Fig.3.2 shows an outline of the classes implemented to model the transmission system.

Here, the transmitter is modeled with respect to the whole WDM comb as an object of the **SpectralInformation** class. It basically consists on a list of the **Channel** class instances. The Channel class models the content of each frequency slot in a fixed- or flexible- grid. As in Fig.3.2, the WDM tributaries can be either PM coherent channels at whatever symbol rate R_s and modulation format, or standard 10 Gbps IMDD NRZ-OOK channels. Also, non-data signals such as unmodulated Constant Waves (CW) can be included to simulate the impairments of/on time-frequency signals used for time distribution. An example of such mixed spectrum, directly obtaine from the time-domain signal, is depicted in Fig.3.3. Such flexibility in the spectral load definition thus enables the observation of the impairments for next generation open and multi-service optical networks [41].

In the same wake of openness and disaggregation, the OLSs is modeled as a

[1] A periodic OLS is intended as composed by the repetition of N_s identical fiber span, each of them composed by the sequence of an optical fiber, EDFA and, eventually, a DCU.

[2] An OLS is operated transparently when the EDFA recovers exactly for the signal loss introduced by the previous optical fiber.

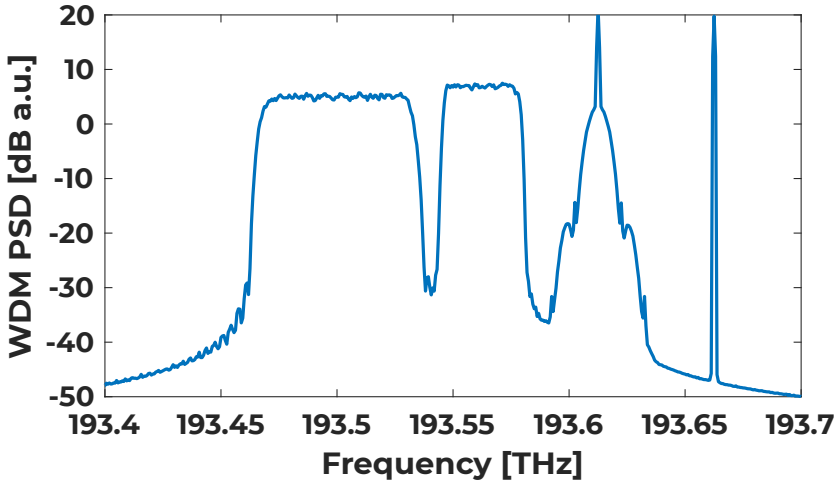

Figure 3.3: Estimated spectrogram of a multi-service WDM signal carrying a two coherent channels at 64 GBaud and 32 Gbaud, a 10G IMDD channel and a CW for Time-Frequency delivery.

generic **Line** class, simply consisting in a list of the network elements composing the OLS. As of the time of this writing, the allowed network elements are optical fibers, inline amplifiers, optical filters and VOAs. Both lumped and Raman distributed amplification are implemented. Amplifier tilting or frequency-dependent loss, noise figure and gain as well as dispersion slope effects can be included allowing to simulate the behavior of realistic in-field configurations. Also, including filters into the OLS description enables the study of filtering effects such as those induced by per-band amplification in multi-band systems or those caused by the crossed ROADMs of a deployed lightpath.

In a similar way, the **Receiver** class is implemented as a list objects representing each of the stages of the receiver chain. In this way, it is possible to elastically define the correct receiver chain for coherent or IMDD channels, as in Fig.2.7, or to build a custom chain, for example to filter out a CW and observe its amplitude and phase characteristics after propagation. Available stages in receivers are adaptive equalizers implementing the most common algorithms as Constant Modulus Algorithm (CMA) and Least Mean Squares (LMS) [133]. Viterbi-Viterbi [162] and Blind-Phase-Search [179] algorithms, data and non-data aided [32], are available for carrier phase estimation, together with the ideal phase recovery using the entire transmitted data sequence. Also optical filters with different shapes can be inserted for coarse or tight filtering of the received optical field. Finally a dedicated class for decoding of the processed signals is used, implementing the calculation of several quality metrics such as BER or SNR.

In particular, some words should be spent on the simulation of the DSP-based

receiver for coherent receivers. In chapter 2 we stated that the optical transmission channel for coherent transmission on DU OLSs can be substantially considered AWGN only if the channel includes also the DSP so that phase noise can be recovered. The rigid subdivision presented in Fig.2.7 reflects the way DSP-based receiver is implemented in our framework , while real devices are actually more complex [133], with some stages intertwined with feedbacks. Nevertheless, real DSP performance are implementation dependent and commercial solutions are closed source and may hide additional algorithms to improve performance such as single channel non-linear compensation [177] or diverse solutions for the chromatic dispersion compensation [17, 134, 38, 145]. Therefore, there is actually no way to exactly model each specific receiver so that one must consider a reasonably standard abstraction of it, taking into account the most significant stages employing standard algorithms, still being conscious that the simulated SNR may present some deviations when compared to the real system.

JSON Description of the Optical Transmission System

Keeping in mind the presented abstraction, it was then necessary to define a proper **data structure**. A data structure is intended as the comprehensive set of all the parameters necessary to describe the simulation setup and the rules to properly organized them in coherent structures.

To be consistent with the paradigm of open and disaggregated networking, we decided to extend the GNPy data structure. GNPy [68] is a Python-based software tool developed by the OOPT-PSE working group within the TIP whose aim is to provide a QoT estimation open source solution for optical network planning, path computation and benchmarking of disaggregated network solutions [5, 161, 82] which relies on the GN model for the estimation of $\mathrm{SNR}_{\mathrm{NL}}$. GNPy employs the JSON standard file format. The JSON syntax is used to store and transmit data objects consisting of attribute-value pairs. The optical system configuration to simulate is thus described by three JSON files:

- **`ssfm_parameters.json`**: contains the `ssfm_params` JSON object describing instead parameters not related to the system but needed to configure the simulation itself, as, for example, the SSFM method accuracy to determine the dz step length or the criterion to establish the simulation bandwidth. A sample of the `spectral_info` object is reported in Listing 3.1.

- **`spectral_information.json`**: contains the `spectral_info` JSON object which describes the WDM signal, i.e. the characteristics of each of the channels multiplexed. A sample of the `spectral_info` object is reported in Listing 3.2.

- **`line.json`**: contains the sequence of network elements describing the OLS. If the OLS is periodic and transparent only the elements composing a single

span can be given and they will be further expanded at runtime. Listing 3.3 reports an example of a 15 spans periodic and transparent OLS.

- **`receiver.json`**: contains the chain of stages composing the receiver for a given CuT, similarly to the line json.

Such syntax provides an easy and compact way to describe a wide range of optical systems. Also, it allows, for example, to describe the line once and simulate the propagation of several spectral load configurations on it. In addition, it is GNPy compliant, so that the same configuration files (although containing more parameters needed to run the SSFM simulation) can be easily passed to GNPy to obtain GSNR estimations based on its internally implemented models.

```
        "ssfm_params": {
          "equation": "cnlse",
          "pmd_seed": [1,100],
          "cut_indices": [1],
          "poldeg": 15,
          "nl_strategy": {
            "start_step": "fwm",
            "update_step": "cle",
            "max_nl_phase_shift": "Inf",
            "accuracy": 1
          },
          "propagation": "full",
          "npol": 2,
          "simulation_bandwidth": {
            "strategy": "inband",
            "bws": null
          },
          "filepath": "/path/to/simulation_file/",
          "optionals": {
            "verbose": false,
            "flag__force_bwa": false,
            "flag__overwrite_propagation": false,
            "flag__overwrite_receiver": false,
            "flag__save_csv": true,
          }
        }
```

Listing 3.1: Sample JSON code for SSFM parameters description.

```
        "spectral_info": {
          "frequency": [193.9e12, 194.4e12],
          "baud_rate": 32e9,
          "slot_width": 50e9,
          "channel_powers_dBm": [-20, 0.0],
          "modulation_format": 2,
          "psnm_predistortion": [800, 0],
          "laser_phase_noise": 0,
          "polrot": 0,
          "shaping_filter": {
            "rolloff": [0.15],
            "symbols": [18]
        }
```

Listing 3.2: Sample JSON code for spectral information description.

```
        "type_variety": "ols",
        "repetitions": 15,
        "elements": [
          {
            "uid": "SSMF",
            "type": "Fiber",
            "type_variety": "SSMF",
            "span_id": 1,
            "params": {
              "length": 80,
              "loss_coef": 0.18895,
              "length_units": "km",
              "con_in": 0,
              "con_out": 0,
              "dispersion": 16.7e-06,
              "gamma": 0.00127,
              "pmd_coef": 1.265e-15,
              "dispersion_ref_wavelength": 1.55e-06
            },
            "save": false,
            "dispersion_compensation": true
          },
          {
            "uid": "EDFA",
            "type": "Edfa",
            "type_variety": "EDFA17",
            "span_id": 1,
              "operational": {
              "gain_target": 15.116,
              "delta_p": null,
              "tilt_target": 0,
              "out_voa": 0,
              "nf_db": 5
            },
            "save": true,
            "dispersion_compensation": true
          }
        ]
```

Listing 3.3: Sample JSON code for OLS description.

3.2.2 The Simulator Procedure

Once the system description has been created as JSON files, the MATLAB software performs the simulation accordingly to the process described in Table 3.1.

	Simulation process
1	Parse `ssfm_parameters.json` to build SimulationParameters object
2	Parse `spectral_information.json` to build SpectralInformation object
3	Parse `line.json` to build the Line object
4	Parse `receiver.json` to build the Receiver object
5	Calculate the optimal simulation bandwidth
6	Set the signal duration t_{sig} by calculating the shaping filters, line, rx delays
7	Get the data sequences modulating the channels
8	Create each WDM channel and multiplex them
9	Apply predistortion if any
10	Propagate WDM signal over the Line network elements (OLS)
11	Perform chromatic dispersion compensation
12	Propagate each raw signal through the Receiver chain
13	Save the receiver output in a .mat file and/or .csv files

Table 3.1: Step taken to perform a simulation in our SSFM software framework.

Simulation Bandwidth Optimization

Taking a look at the procedure of Table 3.1 is a good opportunity to discuss some of the main aspects to take into account, relatively to the trade-off between accuracy and required computational time. At first, once parsed the system configuration, the simulation bandwidth BW_s is calculated. This means to define the largest sampling time $T_s = BW_s^{-1}$ assuring that all the significant phenomena are correctly represented avoiding aliasing effects. From the sampling theorem, this is accomplished by setting the simulation bandwidth equal to at least the bandwidth of the equivalent low pass signal to represent. The WDM signal bandwidth, with the simplifying assumption of N_{ch} channels with uniform rate R_s is $B_{WDM} = N_{ch}R_s$. However, in presence of the non-linear Kerr effect, the launched WDM signal subdues spectral broadening during the propagation because of the double convolution in the frequency-domain Manakov equation non-linear term, so that the actual signal bandwidth of interest is, in general, $3B_{WDM}$ and so should be BW_s to represent correctly all the non-linear terms. However, this translates in a factor three-fold $N_{samples}$ with respect to a linear-only simulation, thus in an larger simulation time. However, only the central portion has the interesting signal content, while the side portions of contain only the out-of-band FWM, which do not impact WDM signal,

other than being FWM itself negligible in most of the cases. Hence, unless the target of the simulation is the study of the out-band FWM, it is possible to narrow BW_s to at least $2B_{WDM}$ and accept some aliasing coming from the side replicas which overlap only within the out-of-band FWM (thus spuriously enhanced), with the advantage of saving substantial simulation time thanks to the reduced $N_{samples}$. As also reported in [95], one could theoretically further decrease BW_s if interested only in the center channel of WDM comb or in some of the inner channels, thus allowing some overlapping of side replicas with the rightmost and leftmost channels of the comb out of interest.

Time-Domain Signal Length Optimization

We then proceed to calculate the overall required length of the signal in terms of symbols. In our simulator we provide as input parameter the number of symbols N_{sym} for all the CuTs to average on at the receiver to calculate the QoT metrics. CuT are modulated with symbols sequences obtained using Pseudo Random Bit Sequences (PRBS) because of their known properties with respect to autocorrelation and 0/1 probability. Is it possible to use PRBS also for the purely interfering channels, however, since PRBS are finite in a number, there is the option to use uniformly distributed random sequences when the channel count is large. The simulator also allows to modulate channels with Gaussian distributed sequences when testing, for example, the limit assumptions of GN-like models for NLI [53].

The corresponding number of samples then depends on the symbol rate and the simulation bandwidth:

$$N_{samples} = N_{sym}\frac{BW_s}{R_s} \tag{3.5}$$

where the ratio $\frac{BW_s}{R_s}$ is the number of samples per symbol. It follows that in a mixed rate configuration, lower rate channel require larger $N_{samples}$ to represented the same N_{sym}. However, to multiplex all the channels into the same digitized WDM signal, they all must have the same $N_{samples}$. To solve the issue in such scenario, we decided to set the overall $N_{samples}$ of the WDM comb to the one of the CuTs having the lowest symbol rate, so that, within the propagated signal, all the CuTs contain at least one full repetition of the target PRBS symbol sequence. Higher rates will consequently have more than one repetitions of their unique N_{sym} PRBS symbol sequence in the same N_{sym}-long WDM signal. Note that the computation of the final $N_{samples}$ may also include the pure interfering signals rates. However, in cases as mixed Coherent/IMDD transmission with only coherent CuTs this may lead to definitely large $N_{samples}$ impacting simulation time. In such cases one may accept that the interfering channel writes non-linearities accordingly to less than one PRBS repetition, however, this aspect must be carefully considered to avoid too few symbols on the non-linearity interfering side and lacking of statistics.

However, a larger number of samples to actually transmit is required in order

to avoid numerical artifacts due to propagation delays. On one side, the chromatic dispersion introduces a group delay, proportional to the overall accumulated dispersion. Hence, if the walk-off length is larger than the signal length, a time-domain aliasing may occur due to the circular convolutions performed while applying the linear step with the FFT. In addition, optical filters, adaptive equalizers and CPE averaging introduce other transients that need to be trimmed out in order to obtain a clean signal. To cope with this issue, the approach is to calculate the total delay introduced by dispersion and filtering elements, and repeat the base symbol sequence a number of times which encompasses all the delays and, at the same time, makes the final $N_{samples}$ an exact power of 2, since the FFT is computationally more efficient with power of 2 lengths.

Once the WDM signals is characterized in the frequency and time domain, the set of independent PRBS sequences is generated, upsampled and shaped and predistorted to get single channels which are finally multiplexed. On each channel oen can also apply some amount of predistortion, in order to simulate a certain amount of dispersion accumulated from hypothetical previous propagation. Then, the simulation of the propagation on the OLS starts.

Non-Linear Step Length Optimization

As previously mentioned, the SSFM accuracy for the fiber propagation part in an optical system can be arbitrarily tuned by reducing the dz step length the fiber segment is split in. The error introduced by splitting the linear and non-linear operators independently is evaluated from the Baker-Hausdorff formula [3] and leads to an overestimation of the of the non-linear phase shift induced by the Kerr effect due to the fact that the dz segment is assumed lossless when applying the non-linear step, since fiber attenuation is a matter of the linear step in frequency domain. Hence, the $\mathrm{SNR_{NL}}$ would result underestimated, i.e. accounting for worse performance than what it should have. However, a step length not properly tuned may lead to (in some cases unnecessary) excessive simulation time for multi-span OLS with extended bandwidth signals, even on state-of-the-art GPU based computing

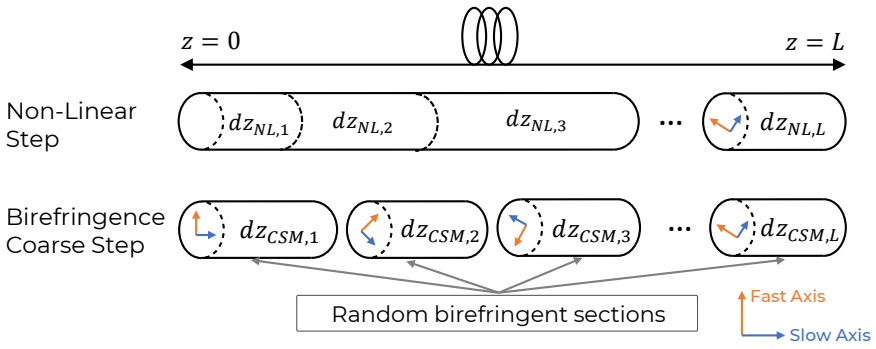

Figure 3.4: Outline of the joint CSM for birefringence and non-linear step method.

hardware.

Several strategies have been proposed in literature to efficiently tune up the step length [15, 95, 176, 175, 147] and reviewing all of them is out of the scope of this work. As proposed in [95], the problem can be reduced to the definition of of a rule to define the first step length dz_1 and a rule to update it iteratively along the remaining part of propagation. One of the most common strategies is tailored to the non-linear step and its philosophy is to set an upper bound the non-linear phase shift $\Delta\phi$ originated in each step:

$$\Delta\phi = \gamma P_{pk} dz \leq \Delta\phi_{max} \tag{3.6}$$

where P_{pk} is the peak power of the WDM signal at the input of the dz step due to chromatic dispersion induced power fluctuations. A second strategy, presented in [95] sets the first step length accounting for the dependence of the SSFM error on the phase matching coefficient $\Delta\beta$, thus on chromatic dispersion β_2 and the WDM bandwidth B_{WDM}:

$$dz_1 = \frac{\Phi_{FWM}}{|\beta_2| \left(2\pi B_{WDM}\right)^2} \tag{3.7}$$

where Φ_{FWM} is the maximum phase shift of the function $e^{j\Delta\beta dz}$.

All the strategies agree with the enlargement of the step size as the propagation progresses, due to the reduced intensity of the power-dependent non-linearities. In particular, in [95], together with the FWM first step rule of Eq.3.7, the use of the constant local error (CLE) step updating rule, first proposed by Zhang [176], is recommended. In our simulations we agreed to use mainly the FWM-CLE strategy, since the first step scales with fiber dispersion and the CLE updating rule ensures also a constant global error scaling the fiber parameters, which is an important aspect when comparing, for example, the generation of NLI in fibers with different dispersion. Also, in [95], these strategy has been also shown to scale the XCI intensity with the frequency distance between the pump and the probe.

The mentioned strategies are sufficient to set the SSFM step length when the solved propagation equation is the Manakov equation of Eq.3.2 or the single polarization SP NLSE of Eq.3.3, where the random birefringence effects are absent or averaged. SSFM simulations solving the more general CNLSE (Eq.3.1), instead, require a method to take into account the realization of the random birefringence during fiber propagation, which acts on the propagation constant matrix $\beta(\omega)$ inducing the a random DGD. Our SSFM framework uses the well-known coarse-step method (CSM) [119, 89, 164] to emulate the effect random birefringence and PMD, sketched in Fig.3.4. The CSM mimics the continuous birefringence by considering the fiber as the concatenation of birefringent segments of length dz_{CSM}, each characterized by a random orientation of the PSPs and by the fiber PMD coefficient. It is thus clear that this adds another constraint in the calculation of the SSFM step length when using CNLSE, so that at each iteration, the SSFM integration step is

chosen as the shortest between the CSM step and the above presented non-linear step, i.e. $dz_{CNLSE,n} = \min(dz_{NL,n}, dz_{CSM,n})$.

Transmission Metrics on SSFM Simulated Signals

After a receiver chain tailored to data modulated channels we obtain the discrete-time signals at 1 SpS. These correspond to the two recovered symbol sequences constellations on x and y polarization states for PM-M-QAM modulated coherent channels or to the single symbol sequence for 10G signals or M-QAM modulated coherent channels if the single polarization NLSE equation has been simulated, being M the modulation cardinality. The class **Decoder** is due to calculate the transmission metrics of interest. Here we review some metrics used in this thesis:

- **SNR**: the signal-to noise raio SNR here is calculated directly on the received constellation as electrical SNR for each polarization component:

$$\mathrm{SNR}_{x/y} = \frac{E[r^2_{x/y}[t_s]]}{\sigma^2_{r_{x/y}}} \tag{3.8}$$

  where $E[\cdot]$ and σ^2 are the statistical expectation operator and variance on the symbol sequence, respectively, as depicted in Fig.3.5 and t_s is the optimum sampling instant for the s-th symbol. As mentioned in chapter 2, this corresponds to the GSNR calculated in the R_s noise bandwidth for coherent channels. The average $\mathrm{SNR} = (\mathrm{SNR}_x + \mathrm{SNR}_y)/2$ can be taken as final metric.

- **NCI**: the non-circularity index (NCI) is used to quantify the presence of NLPN. As in [115], given a received noisy constellation $r[t_s]$ from a transmitted constellation $x[t_s]$ (being t_s the optimum sampling time for the s-th symbol), the noise *clouds* corresponding to each symbol are collapsed to a single cloud around the real axis as $\rho[t_s] = r[t_s]/x[t_s]$. In presence of NLPN, the variances of the in phase and quadrature components of the stochastic process $\rho[t_s]$ - $\sigma^2_{\rho_{I,x/y}}$, $\sigma^2_{\rho_{Q,x/y}}$ - are different, leading to non-circular constellation clouds. The NCI is thus defined as the ratio in dB between the variances on each polarization component.

$$\mathrm{NCI}_{x/y} = 10\log_{10}\left(\frac{\sigma^2_{\rho_{Q,x/y}}}{\sigma^2_{\rho_{I,x/y}}}\right) \tag{3.9}$$

  Hence, if NCI is ≈ 0 dB the I and Q variances are balanced with no phase noise. The average $\mathrm{NCI} = (\mathrm{NCI}_x + \mathrm{NCI}_y)/2$ can be taken as final metric.

- **NLPN**: this is another NLPN-related metric used to estimate the intensity of the NLPN. Assuming that the received signal is impaired by NLPN, such

that $r[t_s] = x[t_s]e^{j\phi[t_s]}$, being $x[t_s]$, $r[t_s]$, $\phi[t_s]$ the transmitted, received constellation and the phase noise process at the s-th symbol optimum sampling time, respectively, we evaluate the NLPN intensity as:

$$\mathrm{NLPN}_{x/y} = \mathrm{Var}\left[\angle\left(\frac{r_{x/y}[t_s]}{x_{x/y}[t_s]}\right)\right] \tag{3.10}$$

where Var[·] is the variance operator and $\angle(\cdot)$ is the phase of the argument. Still, the average $\mathrm{NLPN} = (\mathrm{NLPN}_x + \mathrm{NLPN}_y)/2$ can be considered as final metric. Note that there is a subtle similarity with the NCI. However, the NCI takes the ratio of the variances, here instead we consider the variance of the whole multiplicative noise, as depicted in Fig.3.5. We will employ this method for the evaluation of the NLPN intensity in chapter 6 about the study of mixed IMDD and coherent transmission.

- **BER**: the bit error rate (BER) is calculated by means of error counting over each polarization component received symbol sequences, so that a large N_{sym} per polarization is required to estimate it reliably with respect minimum target value.

$$BER_{x/y} = \frac{\text{number of counted errors on } x/y}{N_{sym}} \tag{3.11}$$

The average $\mathrm{BER} = (\mathrm{BER}_x + \mathrm{BER}_y)/2$ is taken as final metric.

- **AIR**: the achievable information rate (AIR) is calculated from the estimated SNR as the channel Shannon capacity. It thus offers an upper bound of the achievable capacity of the CuT with symbol rate R_s:

$$\mathrm{AIR} = 2R_s \log_2(1 + \mathrm{SNR}) \tag{3.12}$$

The factor 2 in Eq.3.12 takes into account PM. If the simulated system does not employ PM or is simulated in the SP abstraction, the 2 factor is removed.

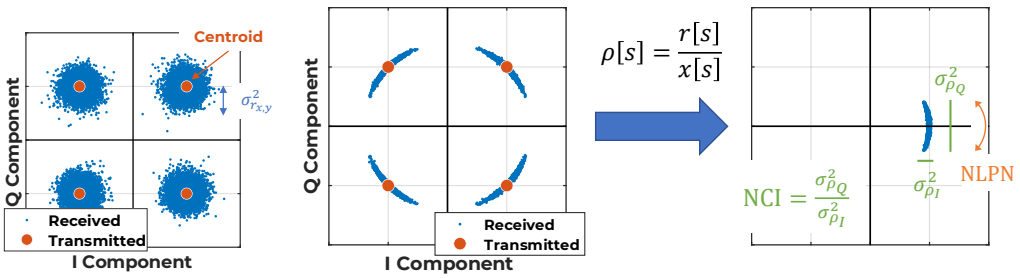

(a) (b)

Figure 3.5: Representation of the quantities involved in the metrics' calculations.

3.3 Simulation Methodology for Open and Disaggregated Optical Networks

In the previous sections we have reviewed the basic concepts of the SSFM and the strategies to control the tradeoff between accuracy and computational efforts. We now proceed presenting the methodologies employed in the next sections to perform extensive simulation campaigns aimed at verifying to what extent the non-linear impairment generation can be modeled according to the properties described in chapter 2 for open and disaggregated networking, i.e. in a *spectrally disaggregated* and *spatially incoherent* way. We will first review the pump and probe (P&P) approach and how to extract the metrics to the test the validity of those properties. Then, the Monte-Carlo simulation process, applying when the birefringence effects canot be averaged, will be reviewed.

3.3.1 The Pump and Probe Simulation Method

It has been widely demonstrated that the performance of a full coherent WDM comb on a DU OLS can be accurately described by means of the Manakov equation [22, 111], since PMD has a negligible impact and can be fully compensated by the DSP-based receiver [141], even filling the whole C-Band and beyond [57, 128, 105]. Such statement is extremely beneficial since it substantially removes the necessity for statistical treatment in the estimation of QoT metrics both in modeling and simulation, avoiding time consuming estimations of QoT probability density functions (PDFs) and outage probabilities. We have already stated, as in Eq.2.23, that ASE noise can be decoupled from NLI in the QoT estimation, since it is an independent source of noise. Hence, observation of NLI generation only is legit and can be accomplished by setting the noise figure of the amplifiers to zero in simulations, according to the ASE modeling of Eq.2.1. This way, the SNR metric evaluated by the SSFM simulator, as in Eq.3.8, coincides to the $\mathrm{SNR}_{\mathrm{NL}}$ and the additive noise found to P_{NL}.

The GN-model approach treats the NLI as a FWM-like noise [112] which suggests an aggregated approach with respect to the N_{ch} channels composing the WDM comb and generating the impairment on a given CuT. This comes from the hypothesis of considering the whole WDM spectrum as a continuum of statistically independent frequency components. Therefore, this vision implies that all the interfering channels must be jointly considered *as a whole* when estimating their impact on a CuT. In other words, this is a *spectrally aggregated* picture of the phenomenon, opposite to the disaggregation principle of modern optical networks, where each lightpath should be considered as an independent entity with respect to the other channels passing through some sections of the optical fiber highways.

At the same time, SCI and XCI are indeed the most significant non-linear

impairments in modern optical systems [80, 168, 54, 51, 172], since the phase matching condition between FWM involved spectral components, is less likely to hold thanks to the deployment of large dispersion fibers, i.e. $\Delta\beta \approx 0$. Furthermore, while FWM involves actually the generation of new frequency components at the expense of the pump frequencies, SPM and XPM are instead phase modulations of the CuT on itself and of a XPM pump on the CuT (the probe). Then, the interplay with the chromatic dispersion makes them to appear as disturbances on the field *amplitude*, i.e. something that could be modeled as an additive noise. Note that also the XPolM contributions to XCI, since it is essentially a crosstalk between independent polarization tributaries, can be in principle considered as an additive disturbance. From now on, we will use the term XPM to refer to the ensemble of XCI effects if not otherwise stated.

Therefore, the observation of what happens in a P&P configuration allows to better understand the characteristic of such impairments. In particular, it allows to check if the additivity of the NLI power generated by each pump hold in terms of the final P_{NL} seen after the DSP, for various system parameters' configurations. Hence, the additivity principle validity in terms of NLI power means that Eq.2.26 holds, so that the significant NLI generation is described as a spectrally disaggregated phenomenon.

Let us consider a target use case with a certain OLS configuration and a WDM comb made up of N_{ch} channels as in Fig.3.6a. In general, the same process can be applied also in case where Raman effects are significant. Usually, we target the central channel of the comb as CuT, so that N_{ch} is conveniently set odd. In general WDM channels can be unevenly spaced and have mixed symbol rates, modulation formats and nominal launched power P_{ch}. Here we consider, for simplicity, uniform channels evenly spaced of Δ_{WDM} GHz. Hence, the method to test the **spectral disaggregation** for each OLS configuration, involves, in a general picture, carrying out the simulation of three spectral load configurations:

- **Multi-Channel simulation**: in this case, as in Fig.3.6a, we perform a single simulation where all the N_{ch} channels are propagated and their power set to P_{ch} so that the bulk of the NLI due to both SPM and XPM is accounted in

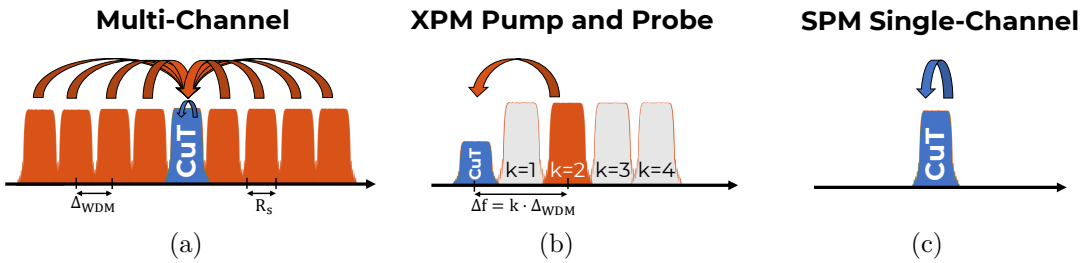

Figure 3.6: The spectral configurations simulated in the pump and probe approach. (a) Multi-channel. (b) Pump and probe with k-th interfering pump. (c) Single channel.

the SNR_{NL} of the CuT, including potential FWM in case low dispersion fiber. After the DSP, we obtain an SNR_{NL} estimation accounting for all the NLI power P_{NL}.

- **Dual-Channel Pump and Probe simulations**: in this case, as in Fig.3.6b, we perform a set of two-channels P&P simulations to isolate the XPM generated on the CuT (the probe) by the k-th interfering channel (the pump). The two channels are thus spaced $\Delta f = k\Delta_{WDM}$. The number of simulation runs can be reduced to $(N_{ch} - 1)/2$, i.e. taking into account only one side portion of the interfering channels of Fig.3.6a, since in absence of dispersion slope the XPM effect on a center CuT is reasonably considered symmetric. In order to isolate the XPM, the pump power is set to the nominal channel power P_{ch}, while the probe power is kept low to avoid SPM. We have usually set it to -20 dBm. After the DSP, we obtain an $\text{SNR}_{\text{XPM},k}$ estimation accounting for the NLI power contribution due to XPM noise power of the k-th pump $P_{XPM,k}$.

- **Single-Channel simulation**: in this case, as in Fig.3.6c, the single channel is propagated alone to the nominal power P_{ch} in order to isolate the degradation due to the SPM only. It can be thus considered as a P&P simulation where the pump and the probe coincide. After the DSP, we obtain an SNR_{SPM} estimation accounting for the NLI power contribution due to SPM P_{SPM}.

Therefore, if the additivity principle holds, the SPM and XPM must sum up in power to the NLI power obtained by the multi-channel simulation:

$$P_{NL} = P_{SPM} + \sum_{k \neq 0} P_{XPM,k} \tag{3.13}$$

which, in terms of SNR becomes the inverse sum:

$$\frac{1}{\text{SNR}_{\text{NL}}} = \frac{1}{\text{SNR}_{\text{SPM}}} + \sum_{k \neq 0} \frac{1}{\text{SNR}_{\text{XPM},k}} \tag{3.14}$$

Eq.3.14 clearly stands for a spectral disaggregated scenario. Consequently, whatever model will be able to guess SNR_{SPM} and $\text{SNR}_{\text{XPM},k}$ solely by the knowledge of the OLSs physical parameters and the channels involved.

We then describe the process to further test the **spatial disaggregation**. We rely on the same simulations performed for the spectral disaggregation, made on an OLS of N_s fiber spans, with each span made up of a piece of fiber followed by an EDFA. In general however, the OLS can be non-periodic and non-transparent and it could employ purely distributed or hybrid Raman amplification. As depicted in Fig.3.7, we look at the SNR_{NL} accumulation by ideally placing a coherent DSP receiver at the end of each fiber span, after the EDFA. We hence obtain a curve composed of the accumulated SNR at the end of each span, i.e. $\text{SNR}_{\text{NL},n}$. Then,

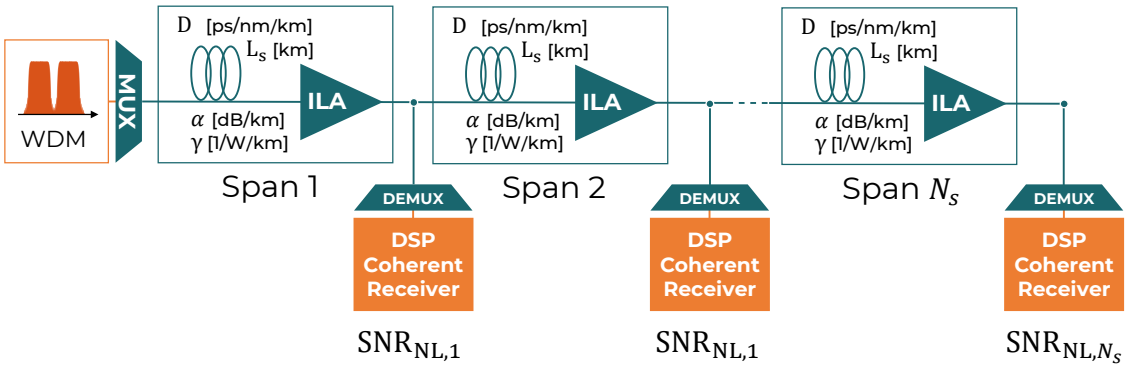

Figure 3.7: Outline of the simulation setup for spatial disaggregation. The CuT is received by the same DSP at the end of each fiber span.

from these curves, for both SPM and XPM P&P spectral configurations, we can calculate as a spatial incoherency metric the curve of $\mathrm{SNR_{NL}}$ degradation introduced by the n-th span $\Delta\mathrm{SNR_{NL},}_n$. This is basically the SNR one may calculate assuming as P_{NL} the one introduced by the n-th span alone, so that it is obtained easily as the inverse difference between the accumulated $\mathrm{SNR_{NL}}$ of two subsequent spans:

$$\Delta\mathrm{SNR}_{\mathrm{NL},n} = \left(\frac{1}{\mathrm{SNR}_{\mathrm{NL},n}} - \frac{1}{\mathrm{SNR}_{\mathrm{NL},n-1}} \right)^{-1} \tag{3.15}$$

In the spatially incoherent assumption, one would expect the $\Delta\mathrm{SNR_{NL}}$ curve to be substantially flat versus the span count, if the OLS is uniform. Differently, it would underline the presence of some sort of correlation between each span contribution. This would be detrimental for the path computation process since it implies a more or less strong dependency of the amount of noise found in a path dependent on the previous propagation history. On the contrary, the absence of such dependency would allow a far simpler path computation since, as in the LOGO approach [108, 107], the amount of NLI would exclusively depend on the characteristics of the considered span and of the spectral content traveling together with the CuT in it. Hence, referring to the network graph abstraction in chapter 2, the verification of the spectral and spatial hypothesis would allow to accumulate easily the QoT by simply *navigating* in space and spectrum the network topology, knowing the traffic or assuming the full spectral load for stable, worst case management.

Optimization of the DSP Parameters

It should be noted that all the described simulations require to pay attention to the configuration of the DSP. First of all, the adaptive equalizer parameters, especially its number of taps N_{taps}, must be set in order to ensure enough headroom to correctly encompass the accumulation of the SNR from the first to the last span.

In the simulations results presented in the next chapters, we have usually employed a LMS-based adaptive equalizer with $N_{taps} = 42$ with an adaptation coefficient $\mu = 10^{-4}$. The adaptive equalizer converges blindly to the optimal taps and they are later reapplied to the whole signal in static manner. Typical length values for equalizer in commercial equipment are around 16 taps, in order to leverage on power consumption and processing delay. Although unrealistic, our larger value has been chosen in order to maximize the SNR back-to-back performance of the simulated DSP receiver (i.e. the SNR obtained by receiving the signal before it gets launched in the OLS, as in Fig.3.7). Indeed, this sets an upper bound to the larger SNR detectable by the DSP. This choice is important when observing small phenomena as the NLI generation in the first fiber span to avoid clipping of the measured $\mathrm{SNR_{NL}}$ due to poor back-to-back performance.

It should be noted that the equalizer may have been also replaced with a simpler filtering stage matched to the transmission one. Some simulation tests have been done to compare the back-to-back SNR performance delivered by the LMS equalizer with the one of a simple matched filter stage. Those tests, here not reported, showed comparable results between the two strategies when the matched filter length was properly optimized and using Manakov equation. The choice for the adaptive equalizer has been then taken to standardize the receiver structure with respect to several simulation campaigns, including CNLSE-based investigations where equalizer was required to recover polarization.

Nevertheless, CPE stage represents another delicate question. It has been extensively demonstrated that total XPM effects accounts also for a significant contribution of NLPN [53, 54, 138, 148], especially in the first spans of propagation. Such NLPN has been shown also to be mostly compensated by CPE stages which also implement adaptive strategies to converge to the optimal correlation length [94, 52, 54, 115, 157]. Also, in practical cases, the optimum CPE length is traded off with the ASE noise rejection. Hence, in simulations isolating the non-linear impairments the CPE length must be thoroughly set in order to avoid unrealistic effects, especially in the first fiber spans, such as NLPN overcompensation.

3.3.2 Birefringence Aware Monte-Carlo Simulations

The previous analysis method based on P&P simulations is based on the solution of the Manakov equation which averages over the fast birefringence rotations and neglects PMD, which has demonstrated legit for uncompensated system operated with PM coherent channels [111]. However, as we will see in chapter 6, there are circumnstances in which averaging the random birefringence may be not valid because the evolution of the WDM channels SOP becomes significant in determining the $\mathrm{SNR_{NL}}$ of the polarization components of a PM coherent channel. In such cases the SSFM must be based on the solution of the more general CNLSE, which includes the statistical characterization of the random birefringence and PMD inside

the propagation constant term $\boldsymbol{B}(\omega)$ of Eq.3.1. In such situation, to a particular realization of the birefringence stochastic process will correspond a random QoT metric value determined by the stochasticity of the interplay between birefringence and non-linearities. It follows that the $\mathrm{SNR_{NL}}$ must be modeled as a random variable rather than considered as a deterministic value. Therefore, the $\mathrm{SNR_{NL}}$ must be characterized accordingly in order to estimate its PDF and its statistical moments of mean and variance. Knowledge of the $\mathrm{SNR_{NL}}$ PDF thus allows to estimate a worst-case value induced by the phenomenon, so that system designs and models can be tailored accordingly in order to operate always on the conservative side. The characterization of the $\mathrm{SNR_{NL}}$ stochastic process is done carrying out Monte-Carlo simulation campaigns. This means to extract N_{MC} different realizations of the random birefringence, perform the simulation with CNLSE for each of them, and collect the corresponding N_{MC} SNR outcomes to estimate its PDF with an histogram.

As already represented in Fig.3.4, the implementation of the random birefringence in the CNLSE is done using the CSM, i.e. by subdividing the fiber in birefringent sections with the PMD coefficient of the fiber and PSPs orientation determined by a random rotation θ_n with respect to the previous section output. Therefore, on the implementation side, one must generate the sequence of rotations θ_n to characterize a realization of the random birefringence process. At the input of the n-th SSFM dz step, the rotation of the PSPs is applied in the non-linear step by multiplying the Jones vector of the WDM signal by the rotation matrix $\mathbf{M}_n$ [119]:

$$\mathbf{M}_n = \begin{bmatrix} \cos\theta_n & \sin\theta_n \\ -\sin\theta_n & \cos\theta_n \end{bmatrix} \begin{bmatrix} e^{j\frac{\Delta\tau_{g,n}}{2}} & 0 \\ 0 & e^{-j\frac{\Delta\tau_{g,n}}{2}} \end{bmatrix} \begin{bmatrix} \cos\theta_n & -\sin\theta_n \\ \sin\theta_n & \cos\theta_n \end{bmatrix} \tag{3.16}$$

$$\Delta\tau_{g,n} = \frac{3}{8}\pi\delta_{PMD}\sqrt{dz_n}f \tag{3.17}$$

where $\Delta\tau_{g,n}$ is the DGD of the birefringent section n, δ_{PMD} is the fiber PMD coefficient in $\mathrm{ps}/\sqrt{(\mathrm{km})}$. It can be easily shown this $\mathbf{M}_n$ is a unitary matrix ($\mathbf{M}_n \cdot \mathbf{M}_n^{\dagger} = \mathbf{M}_n^{\dagger} \cdot \mathbf{M}_n = \mathbf{I}$), thus representing a polarization rotation.

3.3.3 SSFM Accuracy Parameters Optimization

As a summary to the previously discussed issues regarding the accuracy of a SSFM-based simulation, we present here a brief set of results investigating the effects of the non-linear step strategy and length of the PRBS (i.e., the PRBS polynomial degree) on the SNR estimated after the simulation of the propagation over a 15 spans OLS. The PRBS polynomial degree practically defines the number of symbols N_{sym} which are averaged at the DSP to calculate the SNR, after have removed the excess repetitions accounting for propagation delays.

Regarding the spectral load, we have considered a single-channel propagation and two P&P cases. We have considered $\Delta f = 50$ GHz and $\Delta f = 500$ GHz of frequency spacing between pump and probe. Channel are coherent, PM-QPSK modulated at $R_s = 32$ GBaud. Channel Power P_{ch} is set to 0 dBm.

On the OLS side, the effect of two fibers chromatic dispersion coefficients have been taken into account: $D = 2$ ps/nm/km and $D = 16.7$ ps/nm/km to deal with typical low and high dispersion values. Fig.3.8 shows the $\mathrm{SNR_{NL}}$ at the end of the 15-th span, after CPE stage, vs the PRBS polynomial degree for the considered Φ_{FWM} values in the three spectral configurations.

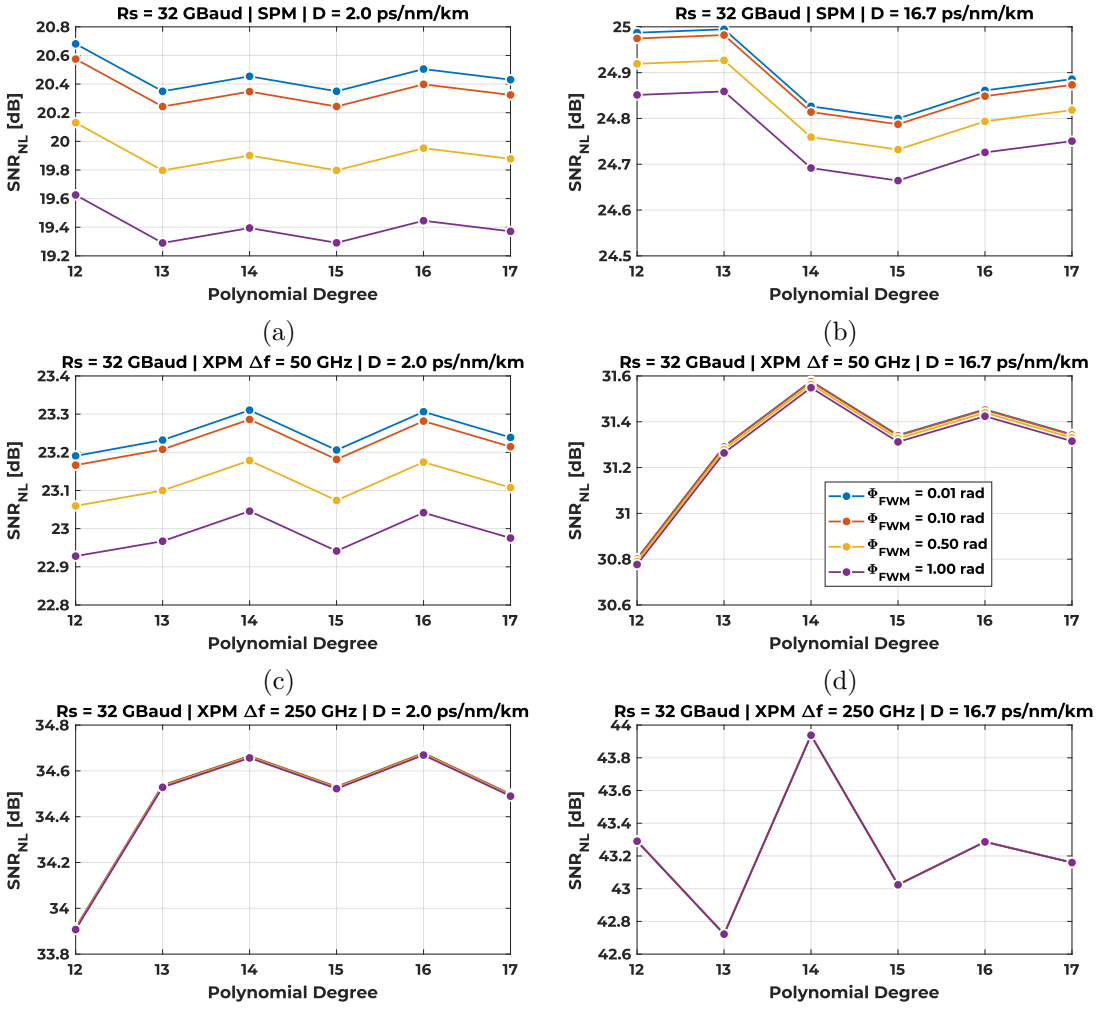

(a) (b) (c) (d) (e) (f)

Figure 3.8: SNR obtained by SSFM simulation varying the PRBS polynomial degree and non-linear step accuracy Φ_{FWM}. Left column: $D = 2.0$ ps/nm/km. Right Column: $D = 16.7$ ps/nm/km. 1st Row: Single channel simulation. 2nd row: P&P with $\Delta f = 50$ GHz. 3rd row: P&P with $\Delta f = 250$ GHz.

With respect to the polynomial degree, the XPM cases show a larger variability to the single channel SPM cases simulations. On SPM, The $\mathrm{SNR_{NL}}$ with $D = 2.0$ ps/nm/km is substantially stable for degrees larger than 13 with a max gap of nearly 0.05 dB which is negligible. The gap is around 0.2 dB between polynomial degree 13 and 15 for the $D = 16.7$ ps/nm/km case, instead, then $\mathrm{SNR_{NL}}$ goes slightly larger at degrees 16 and 17. Hence, to be conservative, we decided to set the polynomial degree for single channel simulations to 17. Regarding the P&P simulations, the considered configurations converge starting from degree 15. The largest gap is found at $D = 16.7$ ps/nm/km and $\Delta f = 250$ GHz of 1.2 dB between degree 13 and 14. Hence, to save on P&P simulation time, which increases drastically with Δf, we decided to set the polynomial degree to 15.

Regarding the Φ_{FWM} setup instead we found some differences with respect to suggested values in [95]. P&P seem substantially independent on the chosen accuracy values when the dispersion and/or the frequency spacing Δf is large, accordingly to the recommendation of $\Phi_{FWM} = 4$ radians in [95]. SPM shows a gap of 1 dB passing from $\Phi_{FWM} = 1$ to 0.01 radians in the $D = 2.0$ ps/nm/km and gets reduced to 0.1-0.2 dB in the other cases where the gap is appreciable. This may be explained with the fact that at low β_2 and B_{WDM}, the first step as in Eq.3.7 implies a large non-linear phase shift which may be limited implementing a further constraint on the maximum non-linear phase shift allowable on the first step. Hence, with respect to the accuracy, we decided to set $\Phi_{FWM} = 0.01$ radians for single channel simulations and $\Phi_{FWM} = 1$ for P&P simulations.

It should be underlined that the SNR convergence with the step length seems to not only depend on whether the spectral content is single channel or in a P&P configuration, since a 0.3 dB gap between the smaller and largest step length is still present for the P&P configuration with $\Delta f = 50$ GHz and $D = 2.0$ ps/nm/km. In addition, within the single channel cases, this gap is already reduced increasing the dispersion coefficient. This fact suggests that this behaviour is more related to the interaction among the non-linearities generation and the simulatenous signal spreading induced by chromatic dispersion. A possible strategy to investigate on such hypothesis may be an observation of the convergence applying some predistortion to the signal launched into the fiber and it will be considered for future investigations.

Chapter 4

Observation of Non-Linear Impairments in Full Coherent, Uncompensated Networks

In this chapter we will present the results of an extensive simulation campaign based on the P&P method described in chapter 3 applied on a DU OLS operated with a WDM comb made up of only coherent channels in order to the test the disaggregation hypotheses on these configurations.

We will first describe the spectral and OLSs configurations taken into account, we will then look at the SNR_{NL} gradient characteristic in a subset of peculiar cases together with their behavior with increasing pump-to-probe frequency spacing. After, the spectral disaggregation hypothesis will be discussed by means of superposition of the P&P simulations' results and compared to the NLI amount given by aggregated simulations and the analytical model described in [159]. We then take a step further and test the spatial disaggregation incoherency assumption and re-evaluate the error metric with respect to the full multi-channel simulations, showing that the XPM reaches a spatially incoherent asymptotic value, opposed to the SPM which shows spatial correlation.

4.1 Description of the Simulation Scenario

The observation of the non-linear phenomena generation is based on the comparison of the simulated propagation outcomes between a full multi-channel scenario, also indicated as *full-spectrum*, and the P&P configured simulations, i.e. the simulation of the non-CuT WDM constituents channels considered alone with the CuT. Sample spectra taken from simulations of the two configurations are reported in Fig.4.1a and Fig.4.1b, respectively. Hence, the description of the simulation scenario starts from that of the full-spectrum WDM comb, which are shown in Table

4.1. A variety of system configurations were tested by varying pairs of symbol rates, R_s, and WDM grid spacings Δ_{WDM}, in order envision the industry tendency to the symbol rate enlargement [87]. With the exception of the presently extensively deployed $R_s = 32$ GBaud, $\Delta_{WDM} = 50$ GHz spacing scenario, all configuration retains an identical R_s/Δ_{WDM} ratio of 0.85 in order to observe the effect of varying the symbol rate.

In every case, the total WDM number of channels N_{ch} is set to occupy approximately 1 THz of the optical spectrum. N_{ch} is accordingly set odd so that the CuT is always the center channel of the WDM comb, which is known to be the most impaired in uniform WDM multiplex [112]. Although the presented results can be considered valid independently on it, the channel launch power P_{ch} is set according to the LOGO strategy [107, 4, 106, 108] to the optimum channel power P_{opt} as in Eq.2.28 from the optimum NLI PSD for each symbol rate. The LOGO strategy ensures the global optimization by locally optimizing the propagation on each fiber span depending on its physical parameters. Since we vary only the fiber dispersion, the corresponding optimum power for each symbol rate, frequency grid, dispersion is reported also in Table 4.1. The choice of number of channels and launch powers ensures a fair comparison of the QoT performance between different symbol rates and frequency spacing schemes. The CuT is always PM-QPSK modulated. Exploration of others modulation format, which are known to deliver slightly different performance [55], is demanded to future investigations. Each quadrature of the two polarization components is generated using an independent PRBS with a 15-th degree polynomial for either full-spectruma and P&P simulations and 17-th degree for single-channel simulations, as from the results of chapter 3. From the same preliminary outcomes, we decided to set the Φ_{FWM} SSFM accuracy to 1 and 0.01 for multi-channel and single-channel simulations, respectively. Concerning the interfering channels - the XPM pumps - we investigate two distinct scenarios: first they are simulated as PM-QPSK modulated without any pre-distortion in order to

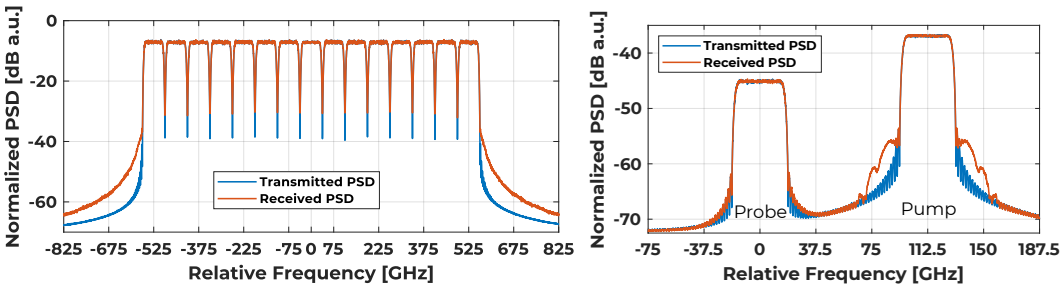

(a) (b)

Figure 4.1: The normalized PSD observed before (blue) and after (red) propagation through 20 fiber spans for: (a) full-spectrum simulation with $N_{ch} = 15$, $R_s = 64$ GBaud, $\Delta_{WDM} = 75$ GHz, $D = 2.0$ ps/nm/km (b) P&P simulation with $R_s = 32$ GBaud, $\Delta f = 112.5$ GHz, $D = 5.0$ ps/nm/km.

represent the transmission over an OLS considered as a standalone system. This case is later referred in figures as *modulated pump*. Secondly, the interfering channels are generated as Gaussian modulated signals, i.e. modulated with a sequence of Gaussian distributed random symbols, in order to consider a more general case where the line is a subsystem of a larger network with interfering channels that have each traveled various distances. WDM channels within an OLS can be considered as Gaussian modulated if a sufficient amount of dispersion has been accumulated during propagation over these distances [27, 137]. Each channel is shaped with a raised cosine-filter with a roll-off of 0.15. Although commercial devices can afford sharper roll-off, within this campaign we preliminarily observed no significant difference in the total amount of NLI generated when varying this parameter.

As mentioned in chapter 3, in order to isolate the XPM contribution in the P&P scenario, the probe power is set to -20 dBm for non-adjacent pumps, i.e. with pump index $k > 1$. For the pump adjacent to the probe, i.e. $k = 1$, the probe power is set to the LOGO P_{opt} attenuated by 4 dB, in order to mitigate the linear crosstalk of the pump on the probe, as illustrated in Fig.4.1b, also because of pump spectral broadening. In the latter case, a small amount of SPM can be still present on the probe due to the enlarged power, but it is removed by evaluating the residual SPM

R_s [GBaud]	Grid [GHz]	$\frac{R_s}{\Delta_{WDM}}$	N_{ch}	B_{WDM} [GHz]	D [ps/nm/km]	LOGO [dBm]
32	50	0.64	21	1050	2.0	-1.6
					5.0	-3.1
					16.7	-4.1
32	37.5	0.85	29	1087.5	2.0	-2.0
					5.0	-3.6
					16.7	-4.7
42.5	50	0.85	21	1050	2.0	-0.8
					5.0	-2.3
					16.7	-3.4
64	75	0.85	15	1125	2.0	-0.9
					5.0	-0.6
					16.7	-1.7
85	100	0.85	11	935	2.0	-2.2
					5.0	0.7
					16.7	-0.5

Table 4.1: The spectral load configurations considered in the simulation campaign. For each symbol rate and spacing the number of channel is set to occupy roughly 1 THz in all the cases. Launched channel power is set by the LOGO strategy, thus depending on the varying fiber dispersion coefficient.

power by means of single channel simulation at $P_{ch} = P_{opt} - 4$ dBm and removed with the inverse SNR rule as from Eq.3.14.

On the OLS side, as recapped in Fig.4.2, we considered one composed of $N_s = 20$ fiber spans, each $L_s = 80$ km long, for a total 1600 km reach, thus encompassing the typical length of terrestrial core network, which are more likely to be elastically reconfigured with respect to longer, ad-hoc links of the submarine class. However, since the accumulation of non-linear noise along the OLS is observed, the present discussion does not preclude discussion of shorter length at span length granularity. Each fiber has a fiber loss coefficient, $\alpha_{\text{dB}} = 0.18895$ dB/km and a non-linearity coefficient, $\gamma = 1.27$ 1/W/km. We did not explore all the physical parameters space, whilst focusing on the fiber dispersion, which strongly affects the entity of the overall XPM. For the dispersion coefficient we have tested three values; $D = 2.0$, 5.0 and 16.7 ps/nm/km. These dispersion values show a general picture of the dispersion effect upon the NLI generation for different symbol rates, encompassing some of the most relevant commercial fiber types which can be still found deployed in optical networks: the Non-Zero Dispersion Fiber (NZDF), the Non-Zero Dispersion Shifted Fiber (NZDSF) and the Standard Single-Mode Fiber (SSMF), respectively. Furthermore, we considered uniform, periodic OLSs where all the fiber spans have the same fiber parameters. Given the principle of spatial disaggregation, each fiber span can be considered separately. Therefore, restricting the simulations to uniform OLSs does not undermine the generality of the presented methodology. The subsequent approach can be thus extended to non-uniform OLS scenarios, with different dispersion coefficients, as will be done in future investigations.

Propagation loss is recovered transparently at the end of each span by ideal, flat, noiseless EDFAs. For the LOGO power calculation, the EDFA noise figure is assumed to be 5 dB. The propagated signal is then processed by a DSP-based receiver. The optical hybrid is considered ideal so that the four quadratures are recovered with no additional impairment. Noise arising from quantization errors within the ADC and electrical noise are not considered, in order to focus on the NLI measurements. The receiver chain as is thus so composed: the CuT is filtered by resampling at 2 SpS and passed through the adaptive equalizer stage which converges to the matched filter. The equalizer, unless explicitly mentioned, is based on the LMS algorithm, with $N_{taps} = 42$ taps and one adaptation coefficient value

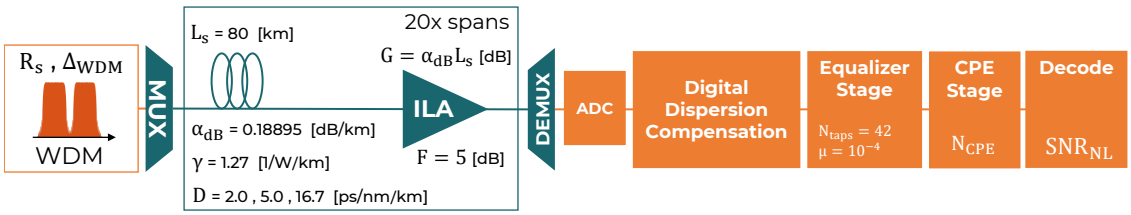

Figure 4.2: OLS setup considered in the simulation campaign.

$\mu = 10^{-4}$, over the entire observed signal [133]. Although typical receivers implements much shorter equalizers, in the order of 16 taps, we increased the number of taps of our equalizer software implementation to increase the back-to-back performance and be able to appreciate small non-linearities even in the first fiber spans of pump and probe simulations with farther XPM pumps. The signal at 1 SpS is subsequently processed by a CPE stage that utilizes the Viterbi-Viterbi algorithm [162], allowing recovery of the NLPN, with a length of L_{CPE} symbols set to number of symbols trading off between best performance and ASE rejection in full-spectrum, noise-loaded simulations. Note that the chosen CPE strategy is legit since the CuT (the probe) is always PM-QPSK modulated, while is the pump only considered also as Gaussian modulated. The output constellation (and, when needed, also the pre-CPE constellation with average phase compensation only) at 1 SpS is finally fed to the Decoder stage for the calculation of the SNR and NCI as described in chapter 3.

4.2 Analysis of the Single Channel and Pump and Probe Simulations

As already mentioned in chapter 2, the bulk of the non-linearities manifests both as amplitude disturbance and NLPN on the signal constellation points. The mechanisms behind the generation of the NLPN component, which is indeed stronger on modulation formats with larger cardinality than the considered QPSK [54], has been tackled in detail in many notable works throughout the years [53, 54, 127, 94, 172] and it is outside of the scope of this work. NLPN component understanding and its relative weight with respect to amplitude disturbance is of outmost importance, however, since we focus here on the QoT estimation in a networking scenario, the long correlated component can be considered well compensated by CPE stage. Some residual NLPN can be still present [56] but it is usually more significant in the first fiber spans and short reach links [53] or minimal with respect to the degradation induced by the part modeled as AWGN [127].

In our simulations, it is thus important to set the memory of the CPE stage compensating the NLPN. Here, we assume the abstraction of ideal noiseless EDFA, however it is common knowledge that, in presence of ASE noise the CPE memory must be traded off between the overall phase noise compensation (due to Kerr effect and laser linewidth) and the rejection of the ASE noise. In commercial DSPs this is usually accomplished with adaptive length algorithms. In our investigations we instead fixed every time the CPE length. It follows that an optimal choice of the CPE length in presence of ASE would not be that when observing only NLI accumulation. For each of the scenarios of Table 4.1, we then performed SSFM simulations with ASE noise loading at the end of propagation and tested several CPE lengths to find the one maximizing the performance. The GSNR accumulation

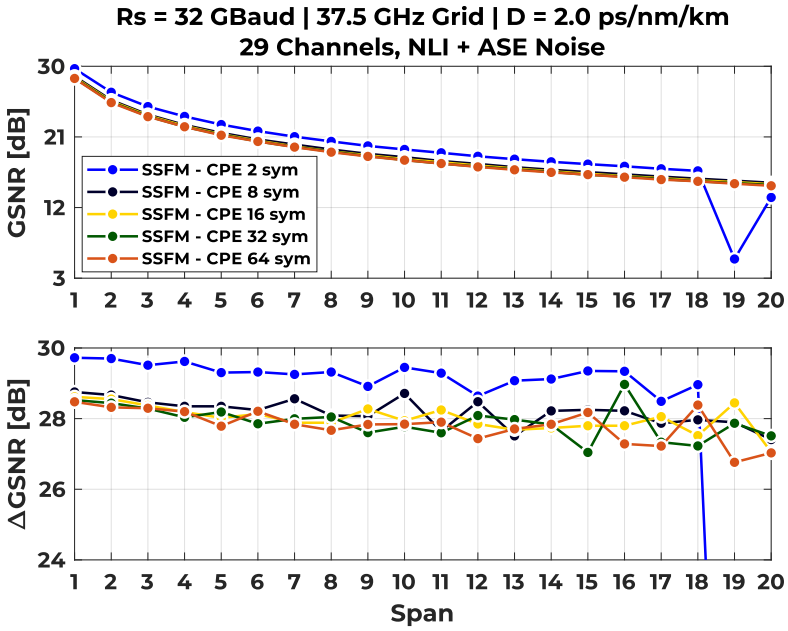

Figure 4.3: Accumulated GSNR and gradient out of a SSFM simulation with noise loading at the end of the OLS. Too short CPEs break the correct GSNR estimation in presence of ASE noise.

and its gradient ΔGSNR vs CPE lengths for the 32 GBaud on 50 GHz grid is reported as example in Fig.4.3. As can be seen, the 2 symbols CPE seems to deliver slightly better overall performance. However, it fails at the 19th span because the phase averaging is too fast and mistakingly tracks also ASE noise. The optimal CPE length is thus set to 8 symbols, although all the other values deliver similar performance. Consequently, except when explicitly mentioned, in the following observation of P&P single channel and full-spectrum simulations isolating NLI we set the CPE to the length optimizing the overall full-spectrum simulation with ASE.

4.2.1 XPM Noise Space and Frequency Accumulation

Before looking at those results addressing the additivity of the XPM pumps effects, it is worth to spend some words on the accumulation of the XPM noise originated by a single pump, i.e. in a P&P configuration, by looking also at the first spans transient, which are related to the figure of the CPE phase noise compensation. It is well known that the XPM entity is strongly dependent on the **walk-off effect**, between the symbols belonging to the pump and the probe. By taking a look in the time domain, as proposed by Dar et al. in [51, 90, 55], the entity of the XPM effect as phase or amplitude disturbance depends mostly on whether a probe symbol subdues a complete or incomplete collision with a pump symbol. A probe symbol may see one or more pump symbols walking off because of the different group velocity and symbol spreading in time due to chromatic dispersion. The *walk-off* length L_{wo} is thus the spatial length in fiber needed for a pump symbol to completely walk-off a probe symbol:

$$L_{wo} = \frac{1}{|\beta_2| 2\pi \Delta f R_s} \tag{4.1}$$

where Δf is the pump-to-probe central frequencies distance and R_s is their symbol rate assuming uniform rate spectral loads. We have thus considered four P&P configurations with different pump-to-probe spacing Δf propagating on high and low chromatic dispersion OLSs previously described. Those configurations are reported in Table 4.2 together with their corresponding walk-off length. For each of them we have also considered the pump being both PM-QPSK modulated and Gaussian modulated. In all of the cases, we have also progressively applied predistortion to the transmitted signal from 0 to 8 times the amount of chromatic dispersion introduced by a single 80 km span of the OLS the signal is propagating through. The consideration of both predistortion and Gaussian modulated pumps allows to look at the effect of the probe and pump *Gaussianization* separately, since it has been widely observed that the accumulation of large chromatic dispersion make the channel appear as a stationary Gaussian process. This mimicks the networking scenario in which a lightpath is established and copropagated with channels which have already accumulated a more or less large amount of dispersion [127].

R_s [GBaud]	Δf [GHz]	D [ps/nm/km]	L_{wo} [km]
32	100	2.0	19.50
32	100	16.7	2.34
32	250	16.7	0.93

Table 4.2: The walk-off lengths calculated by means of Eq.4.1 for the considered pump and probe scenarios. The fiber is 80 km long with $\alpha_{\text{dB}} = 0.18895$ dB/km so that $L_{eff} \approx 22$ km.

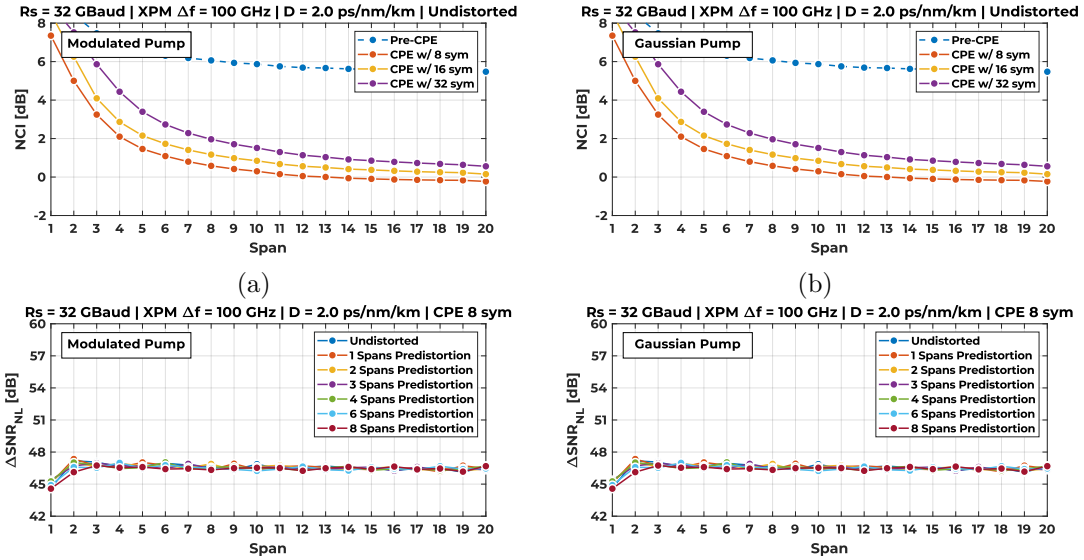

Figure 4.4: SSFM P&P at $R_s = 32$ GBaud, $\Delta f = 100$ GHz on OLS with $D = 2.0$ ps/nm/km. 1st row: NCI at each OLS span output with no CPE and CPE length of 8, 16, 32 symbols, no predistortion. 2nd row: $\Delta\text{SNR}_{\text{NL}}$ of each OLS span output vs predistortion from 0 to 8 spans. Left column: PM-QPSK modulated pump. Right column: Gaussian modulated pump.

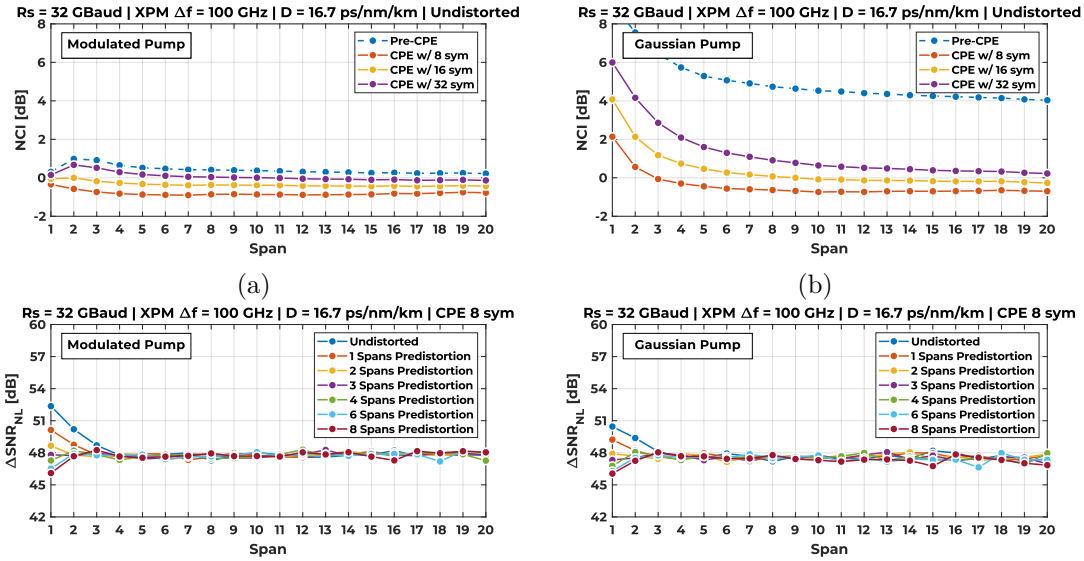

Figure 4.5: SSFM P&P at $R_s = 32$ GBaud, $\Delta f = 100$ GHz on OLS with $D = 16.7$ ps/nm/km. 1st row: NCI at each OLS span output with no CPE and CPE length of 8, 16, 32 symbols, no predistortion. 2nd row: $\Delta\text{SNR}_{\text{NL}}$ of each OLS span output vs predistortion from 0 to 8 spans. Left column: PM-QPSK modulated pump. Right column: Gaussian modulated pump.

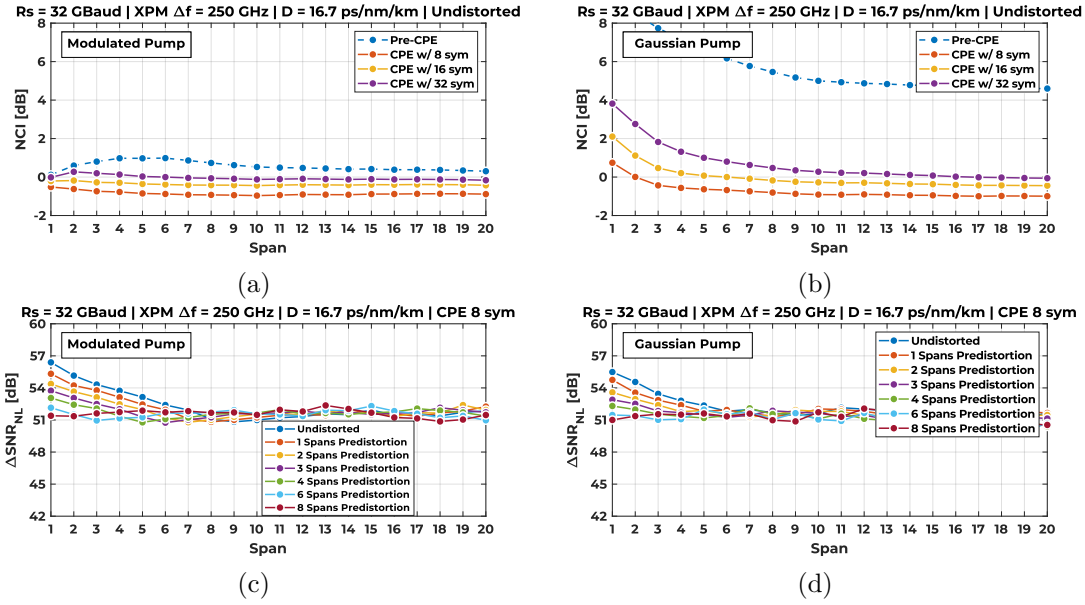

Figure 4.6: SSFM P&P at $R_s = 32$ GBaud, $\Delta f = 250$ GHz on OLS with $D = 16.7$ ps/nm/km. 1st row: NCI at each OLS span output with no CPE and CPE length of 8, 16, 32 symbols, no predistortion. 2nd row: $\Delta\text{SNR}_{\text{NL}}$ of each OLS span output vs predistortion from 0 to 8 spans. Left column: PM-QPSK modulated pump. Right column: Gaussian modulated pump.

The simulations results, showing both the NCI vs the CPE length at each span and the $\Delta\text{SNR}_{\text{NL}}$, that is, the amount of SNR degradation introduced by each span (Eq.3.15), are shown in Fig.4.4, 4.5, 4.6. In this order, figures refer to cases with increasing L_{wo}. SNR_{NL} and $\Delta\text{SNR}_{\text{NL}}$ are quantities referring blindly at the generic non-linear noise found in simulation. Since we are observing pumps and probe, we here refer to them specifically as SNR_{XPM} and $\Delta\text{SNR}_{\text{XPM}}$

Let us first focus of the plot (a) and (b) of the three figures reporting the NCI curves for different CPE. It can be noted that in the first case with low dispersion both the modulated and Gaussian pump propagation generate NLPN prior to the CPE (blue curve), while in the other high dispersion cases NLPN prior to the CPE is predominant only with Gaussian pump. This can be explained with the fact that the first low dispersion case is the only one whose walk-off length is comparable to the fiber effective length, (19.5 km and 22 km, respectively), after which NLI generation is negligible. Since the walk off process is so slow, there is not enough space in fiber to average on many collisions showing more NLPN. In the second and third case, with short walk-off length and large dispersion instead the modulated case quickly tackles gaussianity and NLPN component is fundamentally suppressed, while, surprisingly, the Gaussian case still shows a large NLPN component. However, in all the cases, the CPE is able to compensate the NLPN, i.e. when NCI reaches nearly 0 dB, even at low dispersion and without predistortion. In addition, all the cases converge to an *asymptotic* value of $\Delta\text{SNR}_{\text{XPM}}$

which is the same for all the predistortion values. Also, as it is known [127, 26, 27, 25], the increasing predistortion makes the $\Delta\text{SNR}_{\text{XPM}}$ to converge quickier to the asymptotic value with a similar figure for both the modulated and Gaussian pump, suggesting that the first span propagation characteristics after CPE do not depend only on the gaussianization of the pump but strongly on the spreading of the probe signal as well. This allows to consider, yet in a elementary P&P configuration, a dispersed interfering channel as a Gaussian pump whose net effect after CPE are mostly indistinguishable from those of a modulated pump and, more importantly, to state that the asymptotic $\Delta\text{SNR}_{\text{XPM}}$ is independent on the previous propagation history of the pump.

Starting from the $\Delta\text{SNR}_{\text{XPM},n}$ curves obtained from simulation (with n the span index), we can then define a rule to evaluate the *asymptotic SNR degradation* from them, which we indicate as $\Delta\text{SNR}_{\text{XPM},\infty}$. We define a number of span N_∞ starting from which the transient is exhausted and the SNR degradation reaches the steady state. Hence, simulatively, we can assess $\Delta\text{SNR}_{\text{XPM},\infty}$ as the average on all the measured $\Delta\text{SNR}_{\text{XPM},n}$ at the steady state:

$$\Delta\text{SNR}_{\text{XPM},\infty} = \langle \Delta\text{SNR}_{\text{XPM},n} \rangle_{n \geq N_\infty} \tag{4.2}$$

where $\langle \cdot \rangle$ stands for the average. Averaging on all the steady state values is done to smooth out negligible variations as shown in Fig.4.5, 4.6, 4.4. Showing here all the curves for every considered scenario is unpractical, however we have seen that a N_∞ value valid for all the considered scenario is of 10 spans.

XPM Pump and Probe vs Frequency Distance

The previous curves do not give the scaling picture of the XPM effect of a pump with the frequency distance Δf from the probe. In Fig.4.7 we report the asymptotic $\Delta\text{SNR}_{\text{XPM},\infty}$ introduced by a single span and originated by each pump of the right side of the populated WDM spectrum with respect to the CuT, for each spectral load/OLS configuration of Table 4.1. Together with the $\Delta\text{SNR}_{\text{XPM},\infty}$ for both modulated and Gaussian pumps, we also give the same value as predicted by the analytical model presented in [159]. The mentioned model is derived from a spectrally disaggregated approach and gives an asymptotic estimation of the XPM noise power of a single pump based on the Gaussian assumption, thus neglecting modulation format dependence. As expected, the $\Delta\text{SNR}_{\text{XPM},\infty}$ improves logarithmically with frequency distance. Furthermore, the modulate and Gaussian cases both converge to the same value since the both pump and probe are sufficiently dispersed. Also, the analytical model prediction are always conservative, thus allowing to operate on the safe side in a networking scenario.

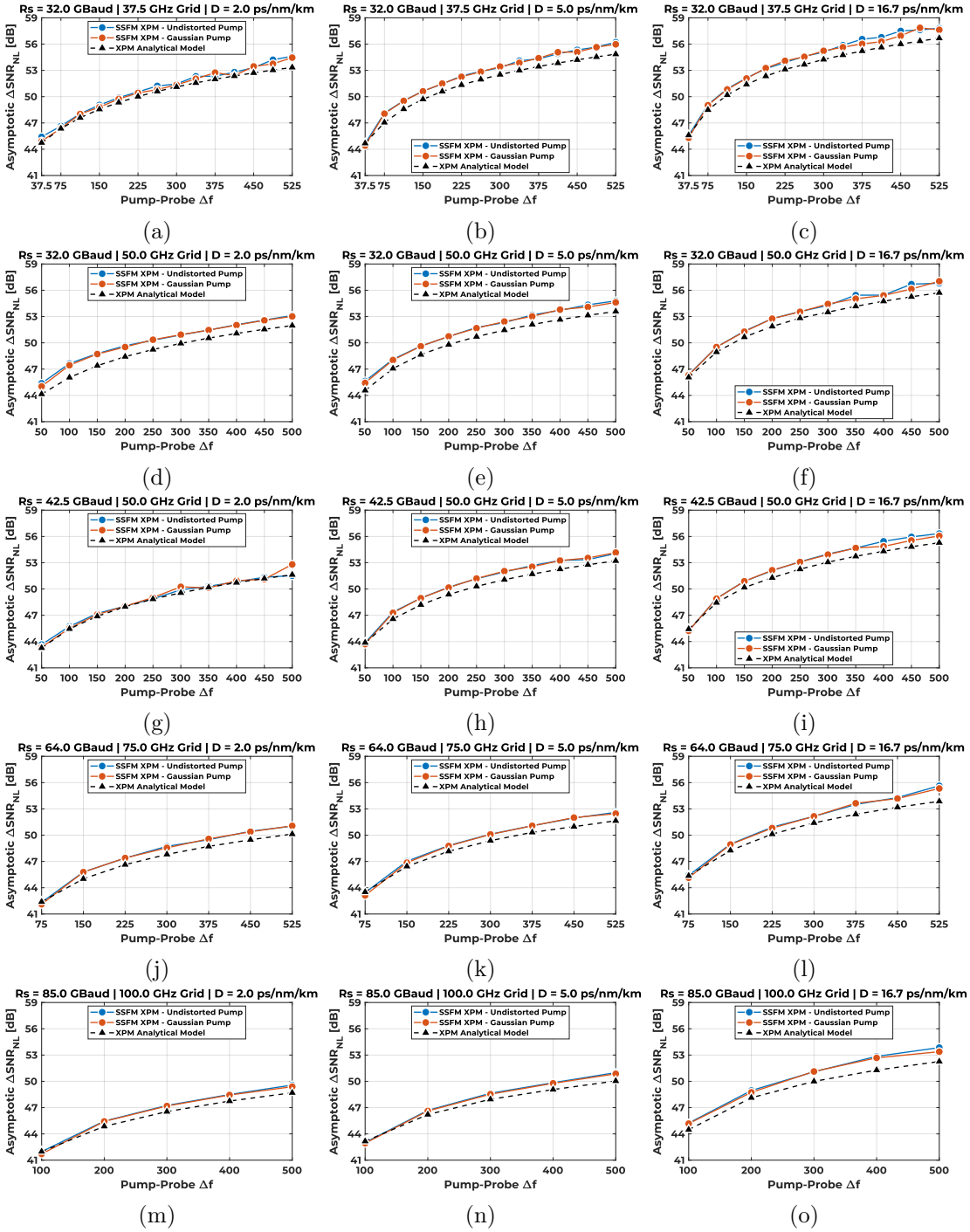

Figure 4.7: The asymptotic $\Delta\text{SNR}_{\text{XPM,k},\infty}$ vs k-th pump-to-probe frequency spacing. 1st column: $D = 2.0$ ps/nm/km OLS. 2nd column: $D = 5.0$ ps/nm/km OLS, 3rd column: $D = 16.7$ ps/nm/km OLS. 1st row: $R_s = 32$ GBaud, $\Delta_{WDM} = 37.5$ GHz. 2nd row: $R_s = 32$ GBaud, $\Delta_{WDM} = 50.0$ GHz. 3rd row: $R_s = 42.5$ GBaud, $\Delta_{WDM} = 50.0$ GHz. 4th row: $R_s = 64$ GBaud, $\Delta_{WDM} = 75.0$ GHz. 5th row: $R_s = 85$ GBaud, $\Delta_{WDM} = 100$ GHz.

4.2.2 SPM Noise Spatial Accumulation

A similar study has been carried out also for single-channel SPM simulations, whose results for NCI and $\Delta\text{SNR}_{\text{NL}}$ for dispersions $D = 2.0$ ps/nm/km and $D = 16.7$ ps/nm/km are shown in Fig.4.8. We thus indicate here the SNR_{NL} and $\Delta\text{SNR}_{\text{NL}}$ as SNR_{SPM} and $\Delta\text{SNR}_{\text{SPM}}$. The upper row of Fig.4.8 shows that SPM generates some amount of NLPN which is still compensated by CPE using, in this case, a larger length of roughly 32 or 16 symbols, making the NCI to converge to nearly 0 dB after a few spans. The convergence is faster at larger dispersion because of the quickier symbol spreading. SPM can be seen as a P&P scenario where the pump is the probe itself, hence the non-linear phase writing is completely correlated. This translates, on a $\Delta\text{SNR}_{\text{SPM},n}$ not converging to an asymptotic value but rather showing a *correlation* of the amount of NLI introduced in each span with the contributions of the previous spans, regardless of the predistortion. This phenomenon is in accordance with the correlation observed in spectrally aggregated approaches to NLI as in [115]. With this regard the single channel NLI cannot be considered spatially incoherent and must be treated in a networking scenario with a worst-case accumulation approach, as done in [50].

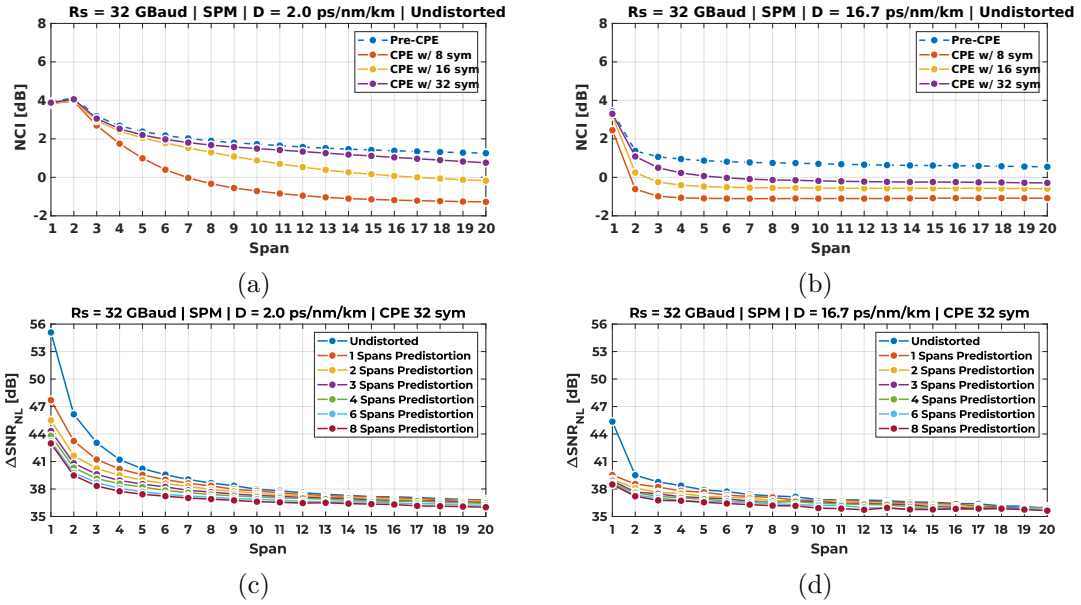

Figure 4.8: SSFM single-channel at $R_s = 32$ GBaud on OLS with $D = 2.0$ ps/nm/km (left column) and $D = 16.7$ ps/nm/km (right column). 1st row: NCI at each OLS span output with no CPE and CPE length of 8, 16, 32 symbols, no predistortion. 2nd row: $\Delta\text{SNR}_{\text{NL}}$ of each OLS span output vs predistortion from 0 to 8 spans.

4.2.3 NLI Probability Distribution Estimation

For the P&P and single-channel configurations just studied, we have also observed the statistical distribution of the amount of NLI introduced by each span. Without intending to be exhaustive, we report here a subset of the results. Each span contribution has been isolated by assuming that, after the NLPN compensation, the sequence of symbols $r_n[t_s]$ at a generic span $n = 1 \dots N_s$ can be expresses as Eq.4.3 (being t_s the optimum sampling instant for the s-th symbol), regardless of the SPM coherency:

$$r_n[t_s] = r[t_s] + \sum_{i=1}^{n} q_{NL,i}[t_s] \tag{4.3}$$

where $x[t_s]$ is the transmitted symbol sequence, $q_{NL,i}[t_s]$ is the non-linear noise field amplitude sample sequences introduced by the i-th span. q_{NL} corresponds to the SPM in single channel simulations and to XPM in P&P simulations. We have omitted the XPM pump index k for simplicity. Consequently, the $r_n[t_s]$ are obtained by receiving the propagated signal at each EDFA span output, so that the discretized NLI field introduced by the i-th span can be obtained as in Eq.4.4 after proper time alignement:

$$q_{NL,i}[s] = r_i[t_s] - r_{i-1}[t_s] \tag{4.4}$$

The distribution of each span contribution is estimated by the histogram of the isolated field. Estimated PDF of the NLI field of the 1st and 20th span are reported in Fig.4.9 together with their Gaussian fit, showing that after CPE compensation the NLI distribution is well approximated by Gaussian distribution, already at the first span and for both the SPM and XPM cases. The PDFs in Fig.4.9 are actually estimated from a single realization of the symbol sequences for both the pump and probe. A thorough evaluation would have required a Monte-Carlo approach by varying the polynomial number of the 15-th degree PRBS used to generate the symbol sequences and average on the symbol statistics. We performed some preliminary simulation varying the PRBS polynomial number on a subset of the presented cases without finding any qualitative difference in the shape of the distribution, which may derive from a first averaging over the probe symbols of a single realization. Consequently, we decided to show only the single realization results. It is worth noting, especially for the first span contribution of the SPM with low dispersion (Fig.4.9a), both the phase and quadrature component after CPE with 32 symbols, already appear substantially Gaussian distributed with indistiguishable variances, although Fig.4.8a shows a NCI far from 0 dB. This imbalance in fact is less visible when the overall intensity of the noise is small, as it is in the first spans.

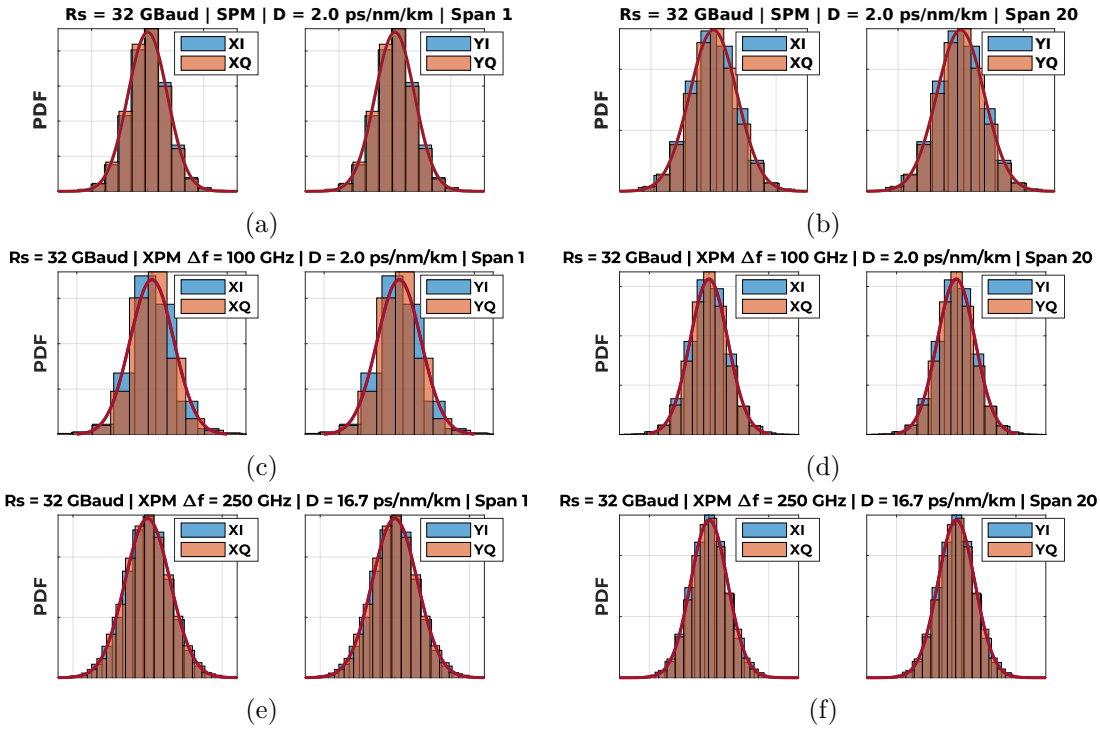

Figure 4.9: Estimated PDF of the x and y NLI noise field contribution (phase I and quadrature Q components) introduced by the n-th span obtained on the constellation after CPE with 8 symbols length, no predistortion, at 1 SpS. All channel $R_s = 32$ GBaud modulated. Left column: span $n = 1$. Right column: span $n = 20$. 1st row: SPM on OLS with $D = 2.0$ ps/nm/km. 2nd row: XPM $\Delta f = 100$ GHz on OLS with $D = 2.0$ ps/nm/km. 3rd row: XPM $\Delta f = 250$ GHz and $D =$ ps/nm/km. Continuous lines are Gaussian fit of the estimated PDFs. X axis are normalized to underline the PDF shapes.

4.3 Spectral Disaggregation

In the previous section we have observed some characteristics of the single channel propagation and the P&P propagation. Here, we are going to take a step ahead by testing the *spectral disaggregation* of the overall NLI with respect to the SPM of the center CuT and the XPM by each of the other channel, first by do not considering the spatial incoherency. This means that each XPM pump will be considered with its first spans transient and its accumulation $\Delta\text{SNR}_{\text{XPM},n}$. We will indicate here as SNR_{NL} the overall non-linear effect, measured or estimated by superposition. Testing the spectral disaggregation means to compare the SNR_{NL} of the full-spectrum scenario with the one obtained by inverse summing the SPM $\Delta\text{SNR}_{\text{SPM},n}$ and the single XPM pump $\Delta\text{SNR}_{\text{XPM},n}$ degradations as in Eq.3.14.

It is thus necessary to determine an **error metric** to measure the goodness of the SNR_{NL} superposition. We define it as the difference ϵ_n between the accumulated SNR_{NL} at the end of n-th span of the full-spectrum simulation and the superposition of SPM and XPM P&P simulations:

$$\epsilon_n = \text{SNR}_{\text{NL,Full},n} - \text{SNR}_{\text{NL,Sup},n} \tag{4.5}$$

where $\text{SNR}_{\text{NL,Full},n}$ is the SNR_{NL} in dB observed at the end of n-th span in the full spectrum simulation and $\text{SNR}_{\text{NL,Sup},n}$ is the SNR_{NL} estimation, in dB, obtained by inverse summing the $\text{SNR}_{\text{SPM},n}$ observed at the end of the n-th span (single channel simulations) and the $\text{SNR}_{\text{XPM},k,n}$ obtained from P&P simulations, i.e.:

$$\text{SNR}_{\text{NL,Sup},n} = \left(\frac{1}{\text{SNR}_{\text{SPM},n}} + \sum_{k \neq 0} \frac{1}{\text{SNR}_{\text{XPM},k,n}} \right)^{-1} \tag{4.6}$$

where k is the pump index. Consequently, a positive value of ϵ_n means that the superposition delivers a conservative QoT with respect to the full-spectrum result. In this case, we set $n = N_s$ and evaluate the superposition error after the propagation over $N_s = 20$ spans. In Fig. 4.10 we show the results of this analysis, for both Gaussian pumps and PM-QPSK modulated pumps, plotting ϵ_{20} against the parameter θ that fully encloses the characteristics of all the spectral loads in Table 4.1 [50]:

$$\theta = \pi |\beta_2| L_s R_s^2 \tag{4.7}$$

where β_2 is the dispersion of the OLS, L_s the span length (80 km), R_s the symbol rate of the considered spectral configuration. For all cases analyzed, it is visible that ϵ_{20} lies within a 0.5 dB range (area highlighted in green), for both the undistorted and Gaussian modulated transmission scenarios. Furthermore, there exists one extreme case ($R_s = 32$ GBaud, $\Delta_{WDM} = 37.5$ GHz, $D = 2.0$ ps/nm/km) without which the maximum error would be halved. Moreover, for the case where the dispersion and symbol rate remain identical but the WDM grid spacing is increased ($R_s = 32$ GBaud, $\Delta_{WDM} = 37.5$ GHz and $\Delta_{WDM} = 50$ GHz) there is an

improvement in the accuracy of the superposition. This is a consequence of simulations with smaller WDM grid spacings generating noisier results, especially in the lowest dispersion case. Furthermore, Fig. 4.10 shows how an increase of chromatic dispersion for a constant symbol rate and WDM grid spacing improves the accuracy of the superposition with respect to the full-spectrum scenario. These findings are valid for all simulations performed within this work, for both the undistorted and Gaussian modulated pump cases. Remarkably, even for the worst case configuration scenario, Eq. 4.6 provides an accurate estimation for the total $\mathrm{SNR}_{\mathrm{NL}}$, confirming the spectral disaggregation hypothesis.

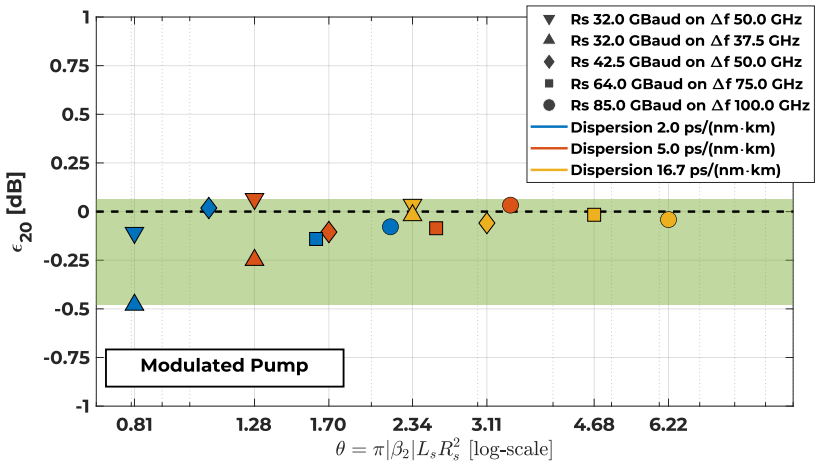

(a)

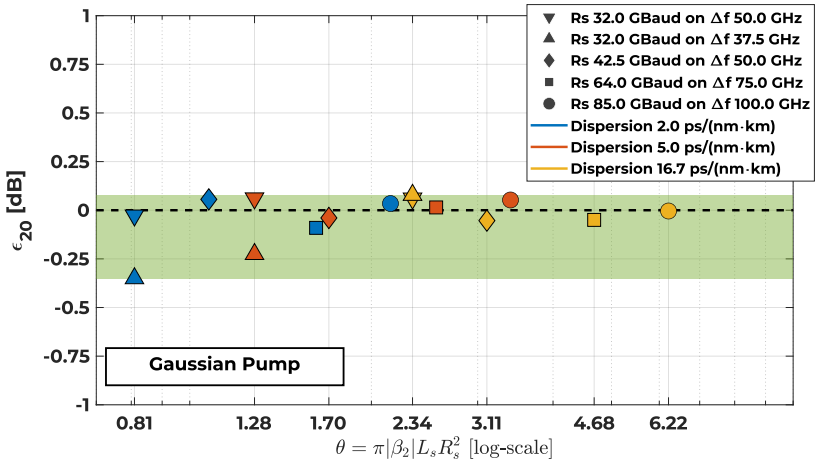

(b)

Figure 4.10: The error at the last span ϵ_{20} between the superimposed and full-spectrum simulations assuming spectral disaggregation for all simulation campaign configurations for: (a) PM-QPSK modulated pumps and (b) Gaussian modulated pumps.

4.4 Spatial Disaggregation

We now tackle the prospect of *spatial disaggregation* by considering the SNR span-by-span degradation $\Delta\text{SNR}_{\text{NL},n}$. In the previous section we have already observed the spatial accumulation of the single P&P and SPM contributions. For a subset of the P&P configurations it has been observed that an asymptotic amount of SNR_{NL} degradation $\Delta\text{SNR}_{\text{NL},\infty}$ can be defined.

We now exploit the spectral disaggregation in order to observe the overall amount of XPM originated by $N_p = N_{ch} - 1$ pumps in its accumulation along the OLS. The overall XPM contribution is thus obtained by inverse summing the amount of XPM degradation of each pump introduced at the end of the n-th span.

$$\Delta\text{SNR}_{\text{XPM},n} = \left(\sum_{k \neq 0} \frac{1}{\Delta\text{SNR}_{\text{XPM},k,n}} \right)^{-1} \tag{4.8}$$

where $\Delta\text{SNR}_{\text{XPM},k,n}$ is the SNR degradation introduced by k-th pump at the n-th span directly obtained from the corresponding P&P simulation. In simple terms, we basically add up the degradation curves presented earlier by each pump and probe in order to assess also the relative balance of the XPM to the amount of SPM.

In Fig. 4.11, 4.12, 4.13, 4.14, 4.15 we present these curves for all the configurations tested of Table 4.1, including the SPM degradation and both PM-QPSK and Gaussian modulated XPM pumps variants. As an additional reference, we include the corresponding estimations obtained aggregating the analytical prediction of each XPM pump contribution presented in [159], which produces a conservative SNR degradation in all analyzed scenarios.

Within these figures, which hence mixes up all the initial transient by each P&P, it is visible that the spectrally superimposed $\Delta\text{SNR}_{\text{XPM},n}$ still reaches an asymptotic steady value $\Delta\text{SNR}_{\text{XPM},\infty}$ after a number of fiber spans N_∞ which can be still set around 10 spans, representing a fully spatially incoherent accumulation regime, for all analyzed configuration scenarios. Furthermore, such asymptotic overall XPM SNR degradation is substantially **conservative** with respect the first span transient and can be thus expressed as the superposition of the asymptotic figures of each pump and probe, updating Eq.4.8 for incoherent accumulation:

$$\Delta\text{SNR}_{\text{XPM},\infty} = \left(\sum_{k \neq 0} \frac{1}{\Delta\text{SNR}_{\text{XPM,k},\infty}} \right)^{-1} \tag{4.9}$$

Therefore, we can conclude that, at least for the XPM, spatial disaggregation is achieved, meaning that the corresponding final SNR of an OLS depends only upon the single-span contribution. On the other hand, as already mentioned, the $\Delta\text{SNR}_{\text{SPM},n}$ keeps decreasing in all cases, showing the coherent accumulation of

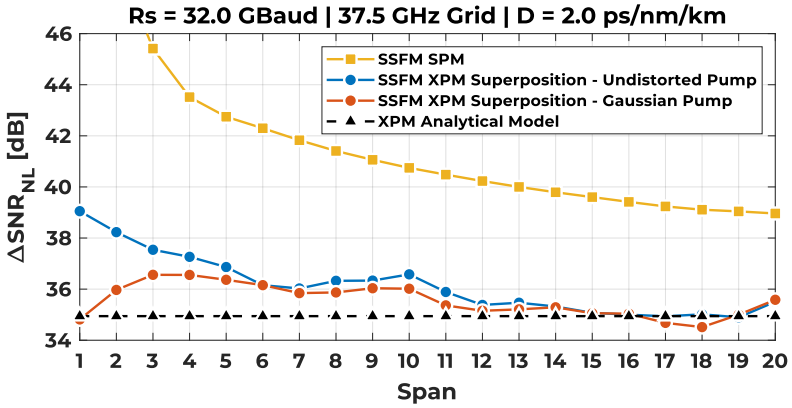

(a)

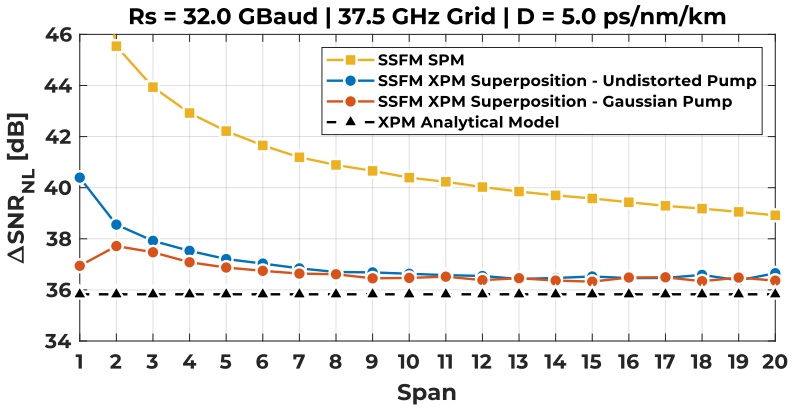

(b)

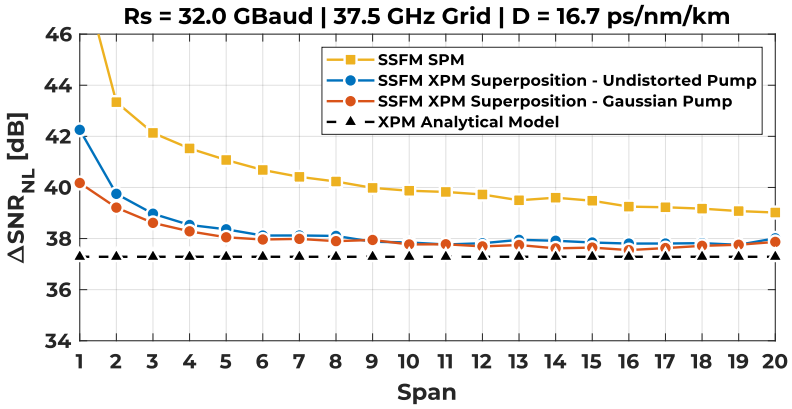

(c)

Figure 4.11: SNR degradation introduced by each OLS span $\Delta\text{SNR}_{\text{NL}}$ due to SPM (yellow curve) and due to superposition of XPM pumps (blue: Modulated Pumps, red: Gaussian pumps) in spectral configuration $R_s = 32$ GBaud, $\Delta_{WDM} = 37.5$ GHz on OLS (a): $D = 2.0$, (b): $D = 5.0$, (c): $D = 16.7$ ps/nm/km. Black curve is the incoherent XPM analytical model in [159].

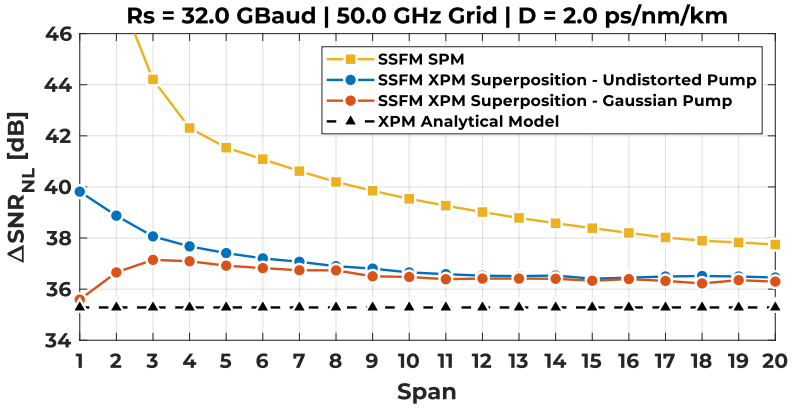

(a)

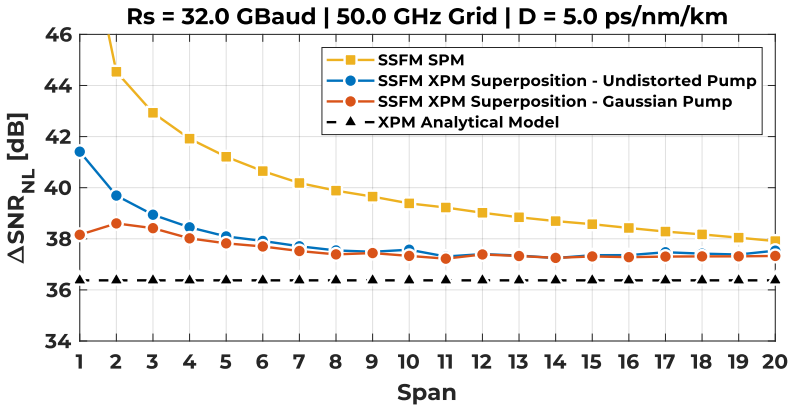

(b)

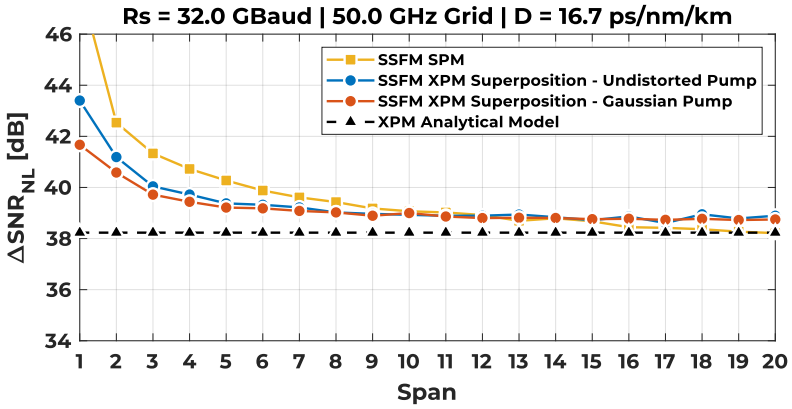

(c)

Figure 4.12: SNR degradation introduced by each OLS span $\Delta\text{SNR}_{\text{NL}}$ due to SPM (yellow curve) and due to superposition of XPM pumps (blue: Modulated Pumps, red: Gaussian pumps) in spectral configuration $R_s = 32$ GBaud, $\Delta_{WDM} = 50$ GHz on OLS with (a): $D = 2.0$, (b): $D = 5.0$, (c): $D = 16.7$ ps/nm/km. Black curve is the incoherent XPM analytical model in [159].

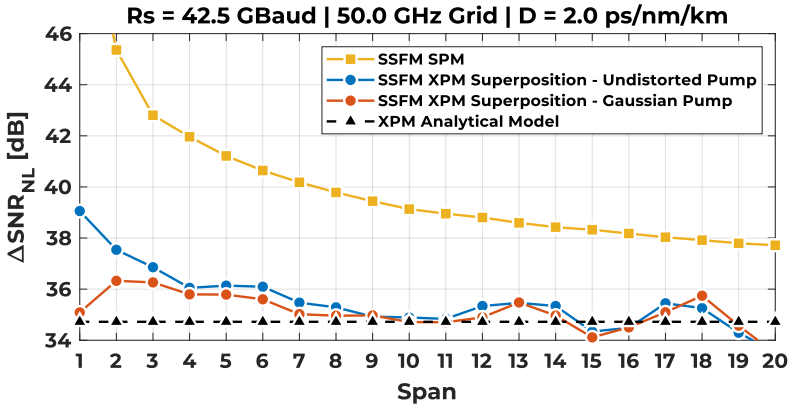

(a)

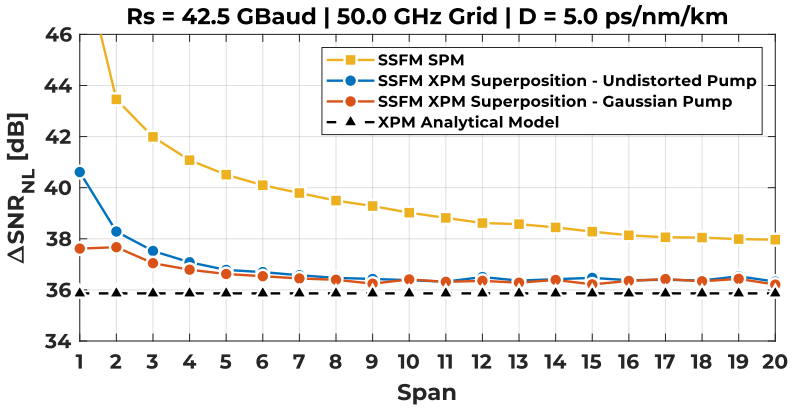

(b)

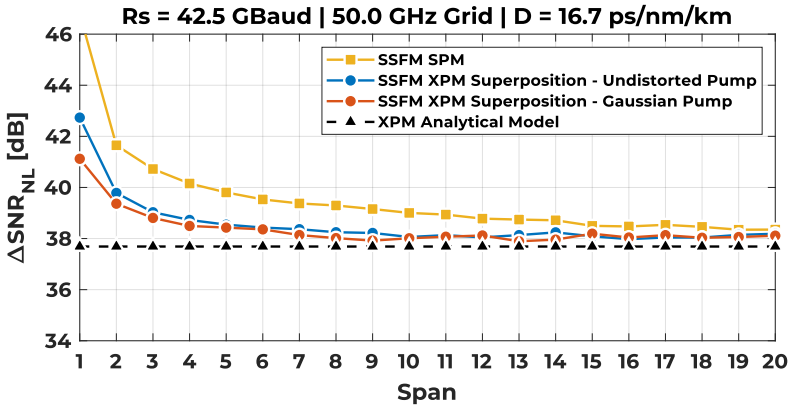

(c)

Figure 4.13: SNR degradation introduced by each OLS span $\Delta\text{SNR}_{\text{NL}}$ due to SPM (yellow curve) and due to superposition of XPM pumps (blue: Modulated Pumps, red: Gaussian pumps) in spectral configuration $R_s = 42.5$ GBaud, $\Delta_{WDM} = 50$ GHz on OLS with (a) $D = 2.0$, (b) $D = 5.0$, (c) $D = 16.7$ ps/nm/km. Black curve is the incoherent XPM analytical model in [159].

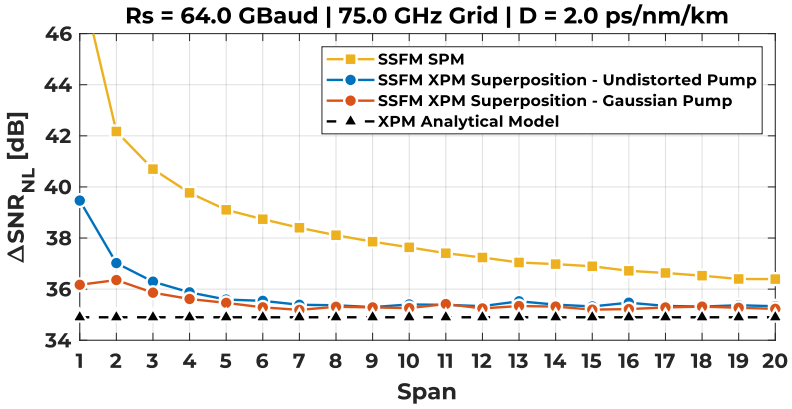

(a)

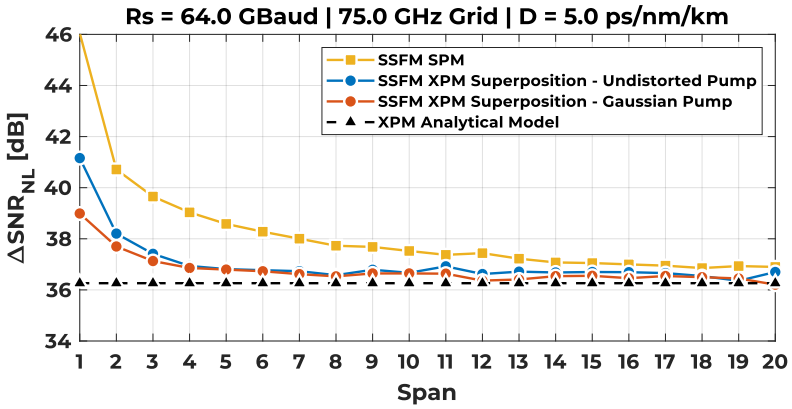

(b)

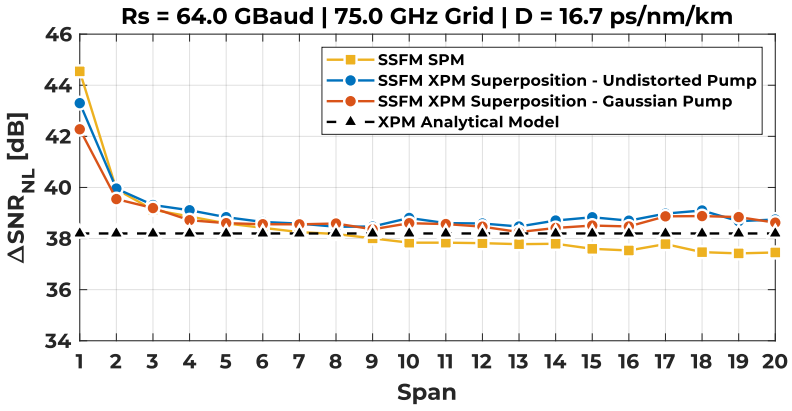

(c)

Figure 4.14: SNR degradation introduced by each OLS span $\Delta\text{SNR}_{\text{NL}}$ due to SPM (yellow curve) and due to superposition of XPM pumps (blue: Modulated Pumps, red: Gaussian pumps) in spectral configuration $R_s = 64$ GBaud, $\Delta_{WDM} = 75$ GHz on OLS with (a): $D = 2.0$, (b): $D = 5.0$, (c): $D = 16.7$ ps/nm/km. Black curve is the incoherent XPM analytical model in [159].

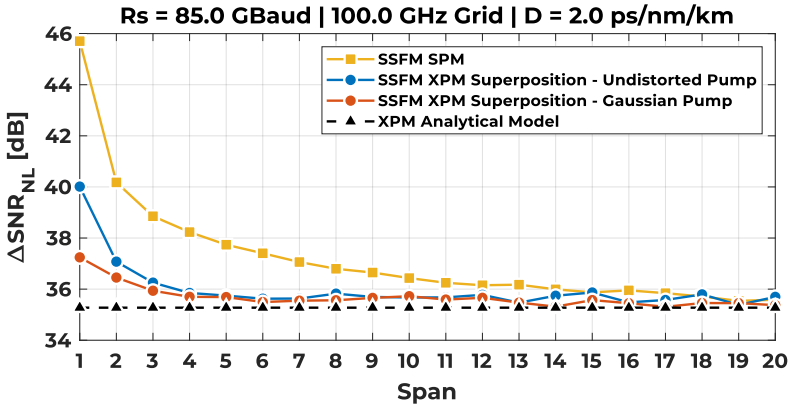

(a)

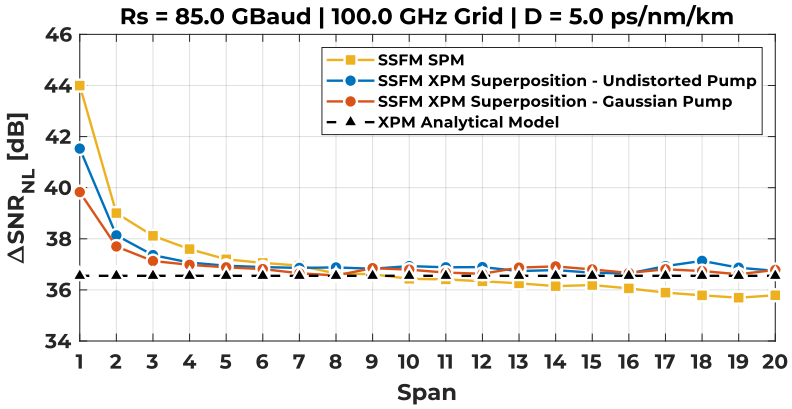

(b)

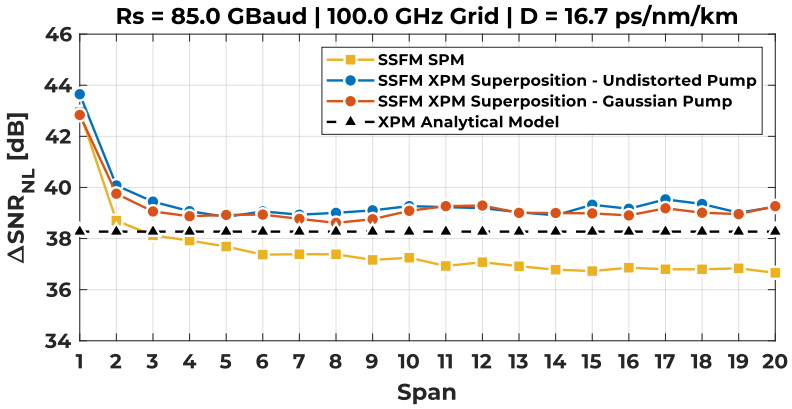

(c)

Figure 4.15: SNR degradation introduced by each OLS span $\Delta\text{SNR}_{\text{NL}}$ due to SPM (yellow curve) and due to superposition of XPM pumps (blue: Modulated Pumps, red: Gaussian pumps) in spectral configuration $R_s = 85$ GBaud, $\Delta_{WDM} = 100$ GHz on OLS with (a): $D = 2.0$, (b): $D = 5.0$, (c): $D = 16.7$ ps/nm/km. Black curve is the incoherent XPM analytical model in [159].

the SPM through the previously crossed fiber spans. Following this, the obstacle to a completely spatially disaggregated approach is solely the SPM contribution to the NLI. Nevertheless, as shown in [50], it is possible to estimate a correction coefficient which maximizes the coherency effect to enable the SPM management in a spatially disaggregated approach.

Among these set of results there is still space to make some comments on the relative weight of the self-channel and inter-channel effect. At $R_s = 32$ GBaud, $\Delta_{WDM} = 37.5$ GHz the XPM is predominant since more interfering channels are densely packed and their reduced frequency distance to the probe makes their effect stronger due to the logarithmically XPM frequency behavior shown in Fig.4.7. Also, the reduced walk-off effect may explain the more pronounced swinging of the effect around the average asymptotic value. As the symbol rate increases the SPM gets more intense until the $R_s = 64$ GBaud, $\Delta_{WDM} = 75$ GHz and $R_s = 85$ GBaud, $\Delta_{WDM} = 100$ GHz cases where, in the considered OLS, SPM and XPM intensities are balanced or show opposite hierarchies. However, rather than to the symbol rate increase itself, this can be attributed to the larger frequency grid slots needed to accomodate the channels, which decrease the XPM crosstalk efficiency due to the larger distance of the CuT to the first XPM pump. Furthermore, it is shown also that larger dispersion play a role by further pushing the SPM intensity towards the XPM level. At the same time, the XPM analytical predictions improve with larger dispersion, decreasing a conservative gap to even less than 1 dB.

Such considerations are based on the XPM relative weight obtained with a bandwidth occupancy up to nearly 1 THz, as showed in Table 4.1. One may then argue that such comparison should be done at least considering the full C-Band occupancy (roughly 4.8 THz). However, with the available data there is still space for some approximate estimation for the full C-Band scenario. First, for the $R_s = 32$ GBaud, $\Delta_{WDM} = 37.5$ GHz case, the addition of further XPM pump enhances the XPM prevalence over SPM. On the opposite side, the $R_s = 85$ GBaud, $\Delta_{WDM} = 100$ GHz on an OLS with $D = 16.7$ ps/nm/km shows an asymptotic $\Delta\text{SNR}_{\text{XPM},\infty}$ due to 11 pumps of around 39 dB (Fig.4.15c) which is nearly 3 dB less intense than the SPM. In this case, 4.8 THz are filled by 48 channel on the 100 GHz grid. Hence, we need to estimate the degradation of further 38 *far-field* channels. From Fig.4.7o we can do the strongly conservative assumption that each of the remaining channels introduces an asymptotic $\Delta\text{SNR}_{\text{XPM,k},\infty}$ degradation of 53 dB (which is the $\Delta\text{SNR}_{\text{XPM,k},\infty}$ of the farthest simulated pump). Hence, a worst-case SNR degradation estimation due to the *far-field* channels would be of $53 - 10\log_{10} 38 = 37.3$ dB. Summing up such additional degradation to the simulated 39 dB for 11 channels with the inverse SNR rule delivers around 35 dB of full C-Band XPM, which is comparable to the SPM ($\approx$ 1 dB worse) but still strongly conservative.

These considerations assume significant importance relatively to the market

tendency in increasing the symbol rate, meaning that the SCI will become more and more significant in QoT estimations, together with the complications arising to the modeling loss of accuracy due to its coherency.

4.5 SNR Estimation in Disaggregated Paradigm

As just showed, the overall XPM impairment given by the pump superposition converges to an asymptotic value, spatially incoherent, which is a worst case along the measured XPM from simulation, thus enabling spatial disaggregation. Hence, the incoherent XPM total $\mathrm{SNR}_{\mathrm{XPM},n}$ accumulation can be evaluated inversely summing up the asymptotic XPM degradations of Eq.4.9 up to the n-th span. Hence, due to span independence of the asymptotic $\Delta\mathrm{SNR}_{\mathrm{XPM},\infty}$, it simply becomes:

$$\mathrm{SNR}_{\mathrm{XPM},n} = \frac{\Delta\mathrm{SNR}_{\mathrm{XPM},\infty}}{n} \tag{4.10}$$

The whole $\Delta\mathrm{SNR}_{\mathrm{NL},n}$ and $\mathrm{SNR}_{\mathrm{NL},n}$ with incoherent XPM accumulation can be estimated just by inverse summing up the SPM contribution, which is instead coherent:

$$\begin{aligned} \Delta\mathrm{SNR}_{\mathrm{NL},n} &= \left(\frac{1}{\Delta\mathrm{SNR}_{\mathrm{SPM},n}} + \frac{1}{\Delta\mathrm{SNR}_{\mathrm{XPM},\infty}} \right)^{-1} \\ \mathrm{SNR}_{\mathrm{NL},n} &= \left(\sum_{i=1}^{n} \frac{1}{\Delta\mathrm{SNR}_{\mathrm{SPM},i}} + \frac{n}{\Delta\mathrm{SNR}_{\mathrm{XPM},\infty}} \right)^{-1} \end{aligned} \tag{4.11}$$

Fig.4.16 reports these quantities compared to the ones directly obtained from the full spectrum simulations in a subset of the spectral/OLS configurations. It can be seen that the spatially incoherent-XPM accumulations loses some accuracy in the very first span with respect to the full-spectrum scenarios, where it is still conservative, except for the Fig.4.16a where the first span of the Gaussian pump full-spectrum goes below the superposition curve.

As stated within section 4.3, the metric of accuracy of the spectral superposition is expressed using Eq. 4.5 evaluated at the final span N_s. These results may be refined by incorporating a compensation for the transient contribution and isolate the error of only the asymptotic part. To do this, we re-scale the accumulations of both the full-spectrum and superposition cases to their respective $N_\infty = 10$ spans values, where, for all scenarios, a steady value for the $\Delta\mathrm{SNR}_{\mathrm{NL}}$ XPM part is reached. The re-scaled span-by-span SNRs for the full-spectrum and superposition cases, $\overline{\mathrm{SNR}}_{\mathrm{NL,Full},n}$, and $\overline{\mathrm{SNR}}_{\mathrm{NL,Sup},\infty,n}$, respectively, can hence be expressed as:

$$\begin{aligned} \overline{\mathrm{SNR}}_{\mathrm{NL,Full},n} &= \left(\mathrm{SNR}^{-1}_{\mathrm{NL,Full},n} - \mathrm{SNR}^{-1}_{\mathrm{NL,Full},n=N_\infty} \right)^{-1} \\ \overline{\mathrm{SNR}}_{\mathrm{NL,Sup},n} &= \left(\mathrm{SNR}^{-1}_{\mathrm{NL,Sup},n} - \mathrm{SNR}^{-1}_{\mathrm{NL,Sup},n=N_\infty} \right)^{-1} \end{aligned} \tag{4.12}$$

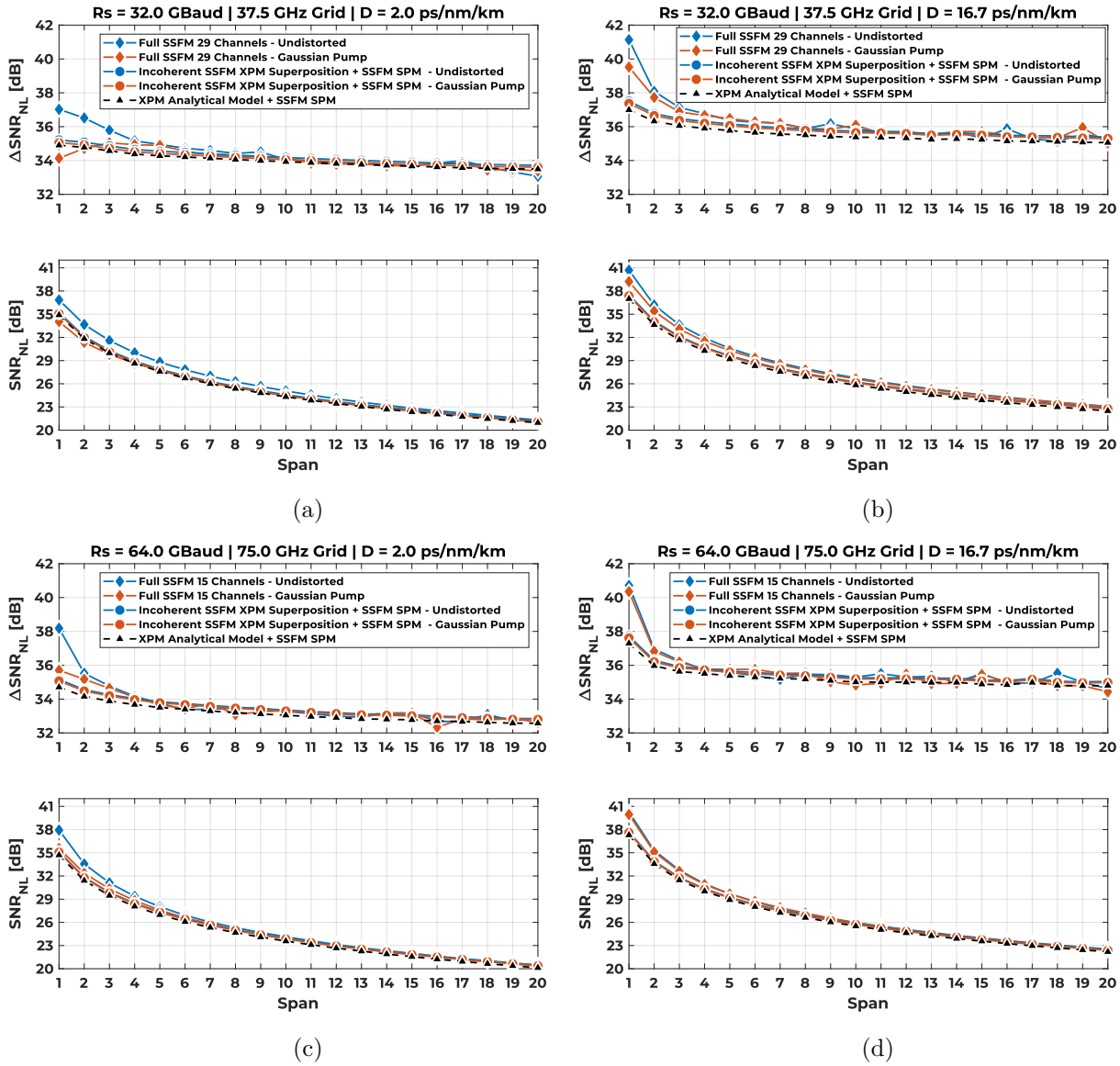

Figure 4.16: $\Delta\text{SNR}_{\text{NL}}$ gradient and accumulated SNR_{NL} estimated assuming incoherent accumulation with $\Delta\text{SNR}_{\text{XPM},\infty}$ value compared to the $\Delta\text{SNR}_{\text{NL}}$ and SNR_{NL} obtained from full-spectrum simulations. 1st row: $R_s = 32$ GBaud, $\Delta_{WDM} = 37.5$ GHz, 2nd row: $R_s = 64$ GBaud, $\Delta_{WDM} = 75$ GHz. OLS with $D = 2.0$ (left column) and $D = 16.7$ (right column) ps/nm/km.

$\overline{\text{SNR}}_{\text{NL,Sup},n}$ is here calculated in the incoherent XPM and spectrally disaggregated way as in Eq.4.11. Hence, its rescaling is simply equivalent to calculate Eq.4.11 setting $n = N_s - N_\infty$. The superposition error at the 20th span $\bar{\epsilon}_{20}$ is still given by Eq.4.5 using the quantities of Eq.4.12 and reported in Fig.4.17. Here, the error is not always conservative and swings around the zero, demonstrating that the recovery of the full-spectrum results using the superposition method reaches an even higher level of accuracy with respect to Fig. 4.18, with a maximum non-conservative error of -0.2 dB for $R_s = 32$ GBaud, $\Delta_{WDM} = 37.5$ GHz, $D = 2$ ps/nm/km. We want to underline that such small non-conservativity of the superposition error is expectable

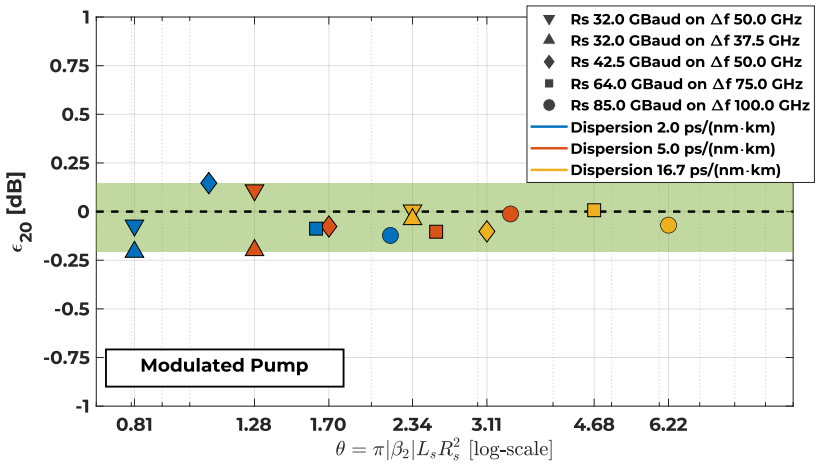

(a)

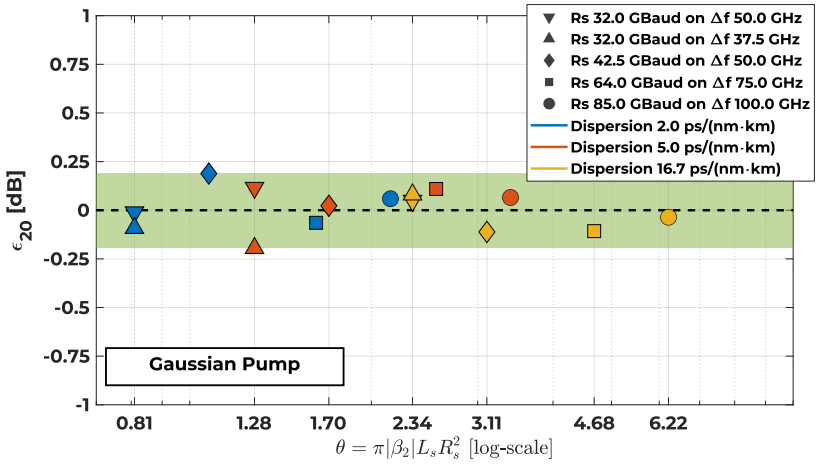

(b)

Figure 4.17: The error at the last span ϵ_{20} between the full-spectrum simulations superposition assuming and spectrally disaggregated and incoherent accumulation rescaled at the 10-th span, for all simulation campaign configurations for: (a) PM-QPSK modulated pumps and (b) Gaussian modulated pumps.

precisely because of the removal of the transient effects. Fig.4.18 report the error at the last span between the full spectrum and the superposition without rescaling to the 10-th span.

Taking into account the transients, where the spatially incoherent approach is conservative, makes the overall error to the reference full-spectrum scenario substantially always conservative, within less than 0.5 dB. The non-conservativity brings an error of less than 0.1 dB in the $R_s = 32$ GBaud, $\Delta_{WDM} = 37.5$ GHz with Gaussian pumps, which however improves at large dispersion.

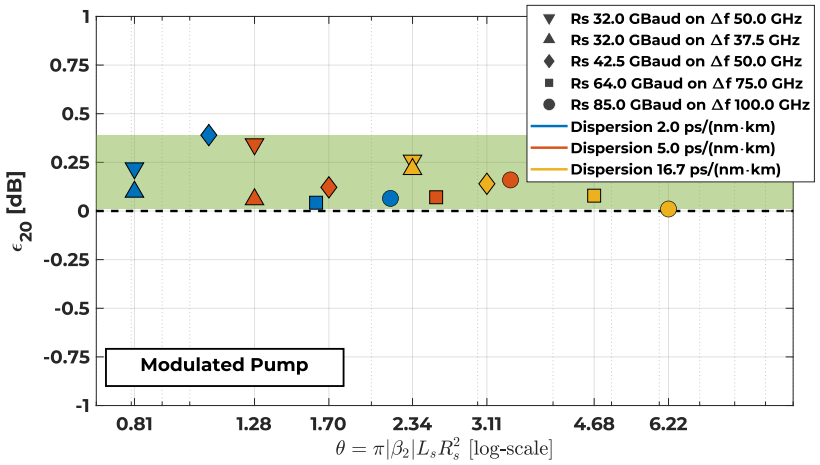

(a)

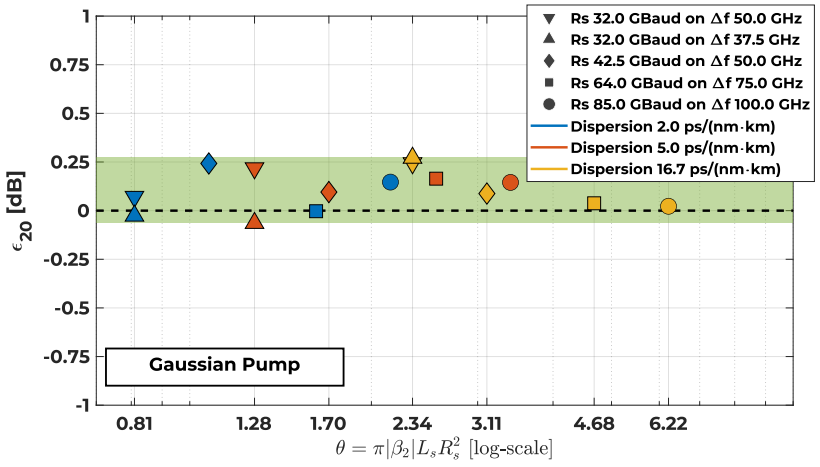

(b)

Figure 4.18: The overall error at the last span ϵ_{20}, including first spans effects (no N_∞ rescaling) between the full-spectrum simulations superposition assuming and spectrally disaggregated and incoherent accumulation, for all simulation campaign configurations for: (a) PM-QPSK modulated pumps and (b) Gaussian modulated pumps.

Such conservativity feature comes actually very useful when employing the spatial and spectral disaggregation strategies in the networking scenario for path computation. In addition, this conclusion allows analytical models, such as the one in [159], effectively estimating the XPM impairment, which is a spectrally disaggregated phenomenon itself, instead of treating all the NLI generation as an aggregated FWM-like process.

In this context, one could separate two *worst-case* conditions which allow to simplify the process of path feasibility and setting of the allocated rate or in the launch power optimization:

- **Spectral worst-case**: the estimation of the GSNR is done assuming that the amount of NLI is the one obtained by fully populating the available spectrum. This assumption slightly overestimates NLI thus underestimating the maximum allowable lightpath capacity [12, 114, 108] but greatly simplifies the control plane complexity, avoiding the retuning of the existing lightpaths channel powers when a new lightpath is deployed.

- **Spatial worst-case**: the estimation of the GSNR is done assuming the asymptotic $\mathrm{SNR}_{\mathrm{NL}}$ degradation for XPM and a worst case correlation for the SPM degradation. Even in this case, the overall NLI gets overestimated, but it still allows for a LOGO-like optimization approach, where the optimal working point does not depend on the previous propagation history of each channel, thus enabling a huge simplification of the routing process.

Chapter 5

QoT Estimation of 10G IMDD Lightpaths on Dispersion Managed Networks

In this chapter, the propagation of IMDD channels delivering 10Gbps per lightpath on DM OLS will be addressed. Core and metro network segments were mainly operated with such transmission technologies until the rise of the coherent transmission market in the first decade of 2000s. The generation of non-linearities in such system has been widely investigated in the 90s, mostly from a phenomenological point of view, in order to *statically* optimize their performance. 10G transmission is however still diffused and, thanks to the advancements in the FEC technologies allowing larger ASE noise to be tolerated, deserves a more systemistic approach to the QoT estimation, with the aim to enable some elasticity in the network control, at least to extent allowed to the architecture of these systems. In the following sections, we will first review more deeply the context of use and QoT modeling for IMDD on DM OLS systems to the present day dominated by coherent and transparent networks. We then show that the GSNR in the optical domain cannot be directly translated to the final BER performance as described in chapter 2. We provide a method to consider the effect of ISI in the BER estimation and employ a well-assessed model for the XPM noise impact on BER. The software tool for QoT estimation is then validated with SSFM-based simulation campaign and experimentally. Finally, an application of the tool in the perspective of network planning and management is proposed.

5.1 The 10G Transmission in the Transparent Optics Era

Differently from coherent transmission, legacy 10G systems exploit simpler intensity modulation (i.e. on-off keying (OOK) of a laser diode. At the receiver side, as depicted in Fig.5.1, after a coarse optical filtering stage in order to select the channel of interest, the signal is directly detected with a simple photodiode, basically getting the instantaneous power of the optical field, thus throwing away any information on the phase. The decision sequence of samples is just brought to the FEC stage after ADC sampling. Since the photodiode is a non-linear device computing the optical field square module (the instantaneous power), the optical field cannot be linearly mapped from the analog to the digital domain, as in coherent receivers, thus excluding DSP operation on the optical field components and consequently any autonomous channel equalization capability. For the same reason, practical PM implementation has not been commercially available in IMDD systems and PMD is a limiting phenomenon since it cannot be compensated electronically. Nevertheless, a pre-FEC BER threshold is still the metric that must not be exceeded to get error-free decoding after FEC.

For these reasons, system designers were forced to implement in-line chromatic dispersion compensation by using fixed-value DCUs between the two typical EDFAs' stages at the end of each span in order to set the so-called *dispersion map*, as depicted in Fig.5.1,5.2. Typically, the dispersion map is set by leaving a certain amount of accumulated inline residual chromatic dispersion $D_{RES,IL}$ [ps/nm] at the end of each span and a final D_{POST} [ps/nm] to meet a certain amount of accumulated chromatic dispersion D_{TOT} [ps/nm]. In fact, full compensation of chromatic dispersion has been shown to be strongly detrimental because it enhances the generation of non-linear interference. Sometimes the inline DCUs may also perform some dispersion overcompensation due to their compensation value granularity. All of this strongly prevented the capability of lightpath transparent routing, because of the DCUs needed by the IMDD to operate at the optimal dispersion map. So, line

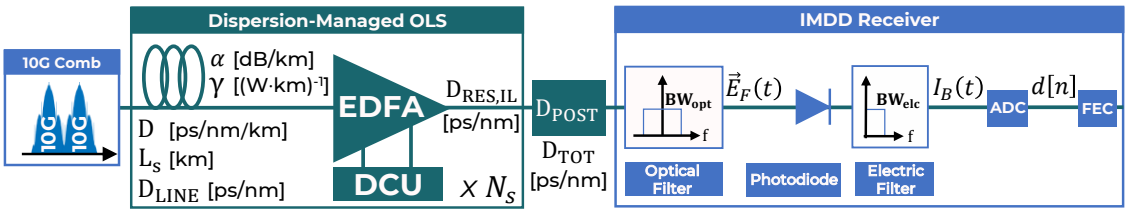

(a)

Figure 5.1: Layout of a DM OLS showing the apparatus for 10G-only transmission. The main system blocks for direct-detection receiver are shown.

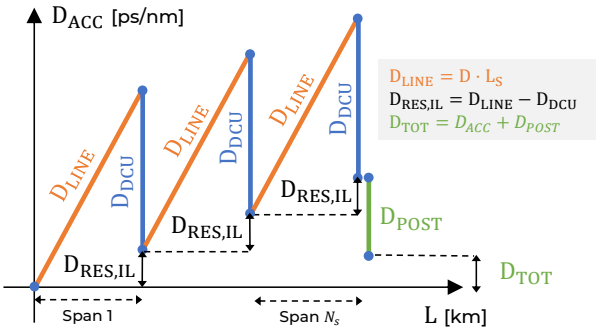

(a)

Figure 5.2: Schematic of chromatic dispersion accumulation on a DM OLS. DCUs have opposite sign dispersion coefficient to compensate the D_{LINE} to the $\mathrm{D_{RES,IL}}$ of the desired dispersion map. Additional $\mathrm{D_{POST}}$ can be applied to set a final $\mathrm{D_{TOT}}$ accumulated dispersion.

systems supporting WDM optical data transport were closed systems with very-limited re-configurability over their lifetime. That implied the exploitation of data transport by networking management as a closed commodity, practically impeding physical layer aware networking, for planning, signaling, control and restoration.

However, the metro and access network segments, covering distances between tenth and hundreds of kilometers, are still largely operated with 10G IMDD transceivers on DM OLSs, which, nevertheless of their limitations still represents an attractive, low cost solution where spectral efficiency is not the main requirement. Here, networks are usually arranged in meshed or ring topologies and it would be really handy to be able to interface and manage transparent lightpath routing on non-homogeneous network section with multi-vendor devices, different fiber types and transmission technologies. In this market segment, in fact, the upgrade to coherent technology is certainly foreseen but still not convenient due to large required CAPEX. Silicon photonics technology integration will surely decrease the price, footprint and the operational costs of the coherent transceivers but it still requires improvements to represent a convenient upgrade in a relatively smaller capacity network segment. In addition, some systems are still operated with ancient time-division-multiplexed protocols such as PDH, SDH or SONET. For these systems, 10G WDM architectures would be effective from a cost/advantage point of view.

From the perspective of the traditional IMDD systems only, despite to the previously mentioned rigidity, it is necessary to allow some flexibility in their configuration with DM OLS to enable real-time 10G lightpath and network management. Nevertheless, the peculiar properties of signal propagation in optical fibers cannot be overlooked. The simple availability of a fiber path between two nodes does not imply channel compliance with the required QoT. In the next sections we propose a framework to fill this gap, thanks to the advancement in FEC algorithms allowing

larger pre-FEC BER threshold, thus enabling simpler and more reliable QoT estimations for network design and management. Both the SPM and XPM interplay, due to the signal to noise beating, were taken into account, neglecting only FWM.

5.2 Quality of Transmission Estimator for Full 10G Optical System

We proceed here by illustrating the 10G transmission setup in order to derive an expression of the received signal which underlines the characteristics of QoT estimation in this context. The typical system layout is here replicated in Fig.5.1. On the transmitter side, the optical channel is generated by modulating a CW out of a laser at the channel central wavelength with Mach-Zender or Electro-Absorption modulators and NRZ-OOK so that 0 and 1 levels are hold for the whole bit duration $T_b = {R_b}^{-1}$. Gross bit-rate will be the standard $R_b = 11.3$ Gbps rate hereafter, delivering 10 Gbps with about 15% FEC overhead. Although widely investigated in literature, PM in IMDD transceivers has never seen popular commercial deployment because of the huge complexity issues in absence of DSP for direct-detection transceivers. This implies that IMDD tranceivers output is *polarized* with a random, fixed polarization state. We do not consider here random birefringence impairments, since it is assumed that the amount of PMD is tolerated by the system. The 10G comb of N_{ch} channels is then propagated through a DM OLS. The dispersion map is practically determined by the amount of inline residual $\mathrm{D_{RES,IL}}$ left by the DCU and by the accumulated dispersion at the end of the OLS $\mathrm{D_{TOT}}$. Traditionally, the tuning of these parameters, together with the power setting, was performed in the system planning phase in order to keep under control the non-linearity generation with the perspective of keeping almost static the system configuration for its whole expected life, because of the absence of adaptive techniques at the receiver enabled by DSP and of simple modeling for QoT estimation. The first stage of a typical receiver is a coarse optical filter, with optical bandwidth BW_{opt}, selecting the CuT, whose optical field complex envelope is indicated with $\boldsymbol{E}_F(t)$. Then, a photodiode performs the conversion to the electrical domain and a post-detection electric Bessel filter of bandwidth BW_{elc} refines the coarse optical filtering. The output is an electrical signal $I_F(t)$ proportional to the optical field power, including both useful signal and additive optical noise sources:

$$I_B(t) \propto |\vec{E}_F(t)|^2 \tag{5.1}$$

The electric signal is then sampled at the optimum sampling time $t_{opt} = t_{j,opt}$ of the j-th bit, obtaining the decision sample sequence $d[t_{j,opt}]$. The bit decision is done accordingly to soft-decision (SD-FEC) or hard-decision (HD-FEC) algorithms. Simpler HD-FEC stage performs a first threshold-based decision obtaining the data sequence to perform error recovery.

In chapter 2 we clarified that coherent DSP-based receivers simplify the OLS abstraction since they decode the signal acting on the optical field components, so that the GSNR before the DSP is substantially identical to the SNR on the electrical signal. This is not true in full 10G systems with direct detection transceivers, where the photodiode performs the square modulus on the optical field, introducing a further term of *signal-to-noise beating*. As a consequence, assuming that noise sources are additive and Gaussian distributed on the optical field, the decoding is done on the electrical signal $I_B(t = t_{opt})$ which, by Eq.5.1, can be expressed as:

$$I_B(t = t_{opt}) = \mu + 2\sqrt{\mu} n_I(t) + \left[n_I^2(t) + n_Q^2(t) \right] \Big|_{t=t_{opt}} \tag{5.2}$$

In Eq.5.2, $n_I(t)$ and $n_Q(t)$ are respectively the *in phase* and *quadrature* components of the total optical noise field, including both ASE and non-linear noise. $\mu 0 \mu(t = t_{opt})$, instead, is the modulated signal power level and is considered *deterministic* on each considered bit, so that μ_0 and μ_1 indicate the amplitude electrical levels of the bit 0 and 1, respectively. One of the main issues is that those levels on the received signal can not coincide with the transmitted levels since they carry the ISI distortion due to the joint interaction between chromatic dispersion and SPM.

By analyzing Eq.5.2, the first term is the useful signal, the others are additive noise. The second term is the beating between the amplitude level of the current bit and the in-phase amplitude component of the noise. The third term is instead the power of the optical noise field alone. The former is Gaussian distributed, with σ_n^2 variance of $n_I(t)$ and $n_Q(t)$: the latter, being the sum of two squared Gaussian processes, is Chi-squared distributed with $k = 2$ degrees of freedom, with variance $4\sigma_n^4$ from the Chi-squared distribution properties.

A comment is worth to be done on the squared noise term. As noted in [64], the post-detection electrical filter does not leave its statistic unchanged whilst leaving more degrees of freedom.

We kept the $k = 2$ since, as it will be shown in section 5.3, such approximation still delivered accurate estimations of the BER performance. An explanation of why such approximation still holds may be related to the larger amount of noise tolerated by modern FEC, that shifts the working point on the noise PDF towards a region where the tails of the noise PDF have less weight on the performance estimation. In addition, the choice of the optimum decision threshold plays a role. We have also investigated the validity of our framework setting the decision threshold to a fixed one, which led to a far less accurate estimation. Such results have not been here reported since they are out of the scope of this work.

Due to the signal-to-noise beating term, the intensity of the noise depends on the transmitted bit, since the bit 1 power level pumps the $n_I(t)$ noise, so that the noise on bit 1 is always more intense than 0. However, noise on bit 0 is never null because of ISI and finite extinction ratio of the transmitter, which has been set to 9 dB in our simulations. It is then clear that such signal-to-noise beating

does not allow even the spectral disaggregation of the non-linearities, since the estimation of the additive noise part on the decision signal, which is determined by the XPM pumps in the non-linear contribution, depends also on the single channel propagation impairment.

5.2.1 Accounting for ISI in BER Estimation

The noise intensity imbalance between 0 and 1 levels can also be seen in Fig.5.3, where the eye diagram of a 10G NRZ electrical signal after the photodiode impaired by additive noise and ISI is shown. The eye diagram can be regarded as the way to represent qualitatively an IMDD signal, similarly to the scattering diagram for QAM coherent modulations. Signals traces of the duration of n bits are superimposed. The two bit electrical levels form an eye-like shape: the more the eye is open, the better is the QoT. On the eye diagram right side we also show an example of the PDF of the overall noise on the 0 (blue) and 1 (orange) levels. The PDF are centered on the average signal power levels μ_0, μ_1 and they have variance σ_0, σ_1. They include both the Gaussian and Chi-squared contributions, which are obtained as mean and variance of the $I_B(t = t_{opt})$ signal:

$$\begin{aligned} \mu_{0,1} &= \mathbf{E}\left[I_B(t = t_{opt})\right] \\ \sigma^2_{0,1} &= \mathbf{E}\left[\left|I_B(t = t_{opt})\right|^2\right] - \mathbf{E}^2\left[\left|I_B(t = t_{opt})\right|\right] \end{aligned} \tag{5.3}$$

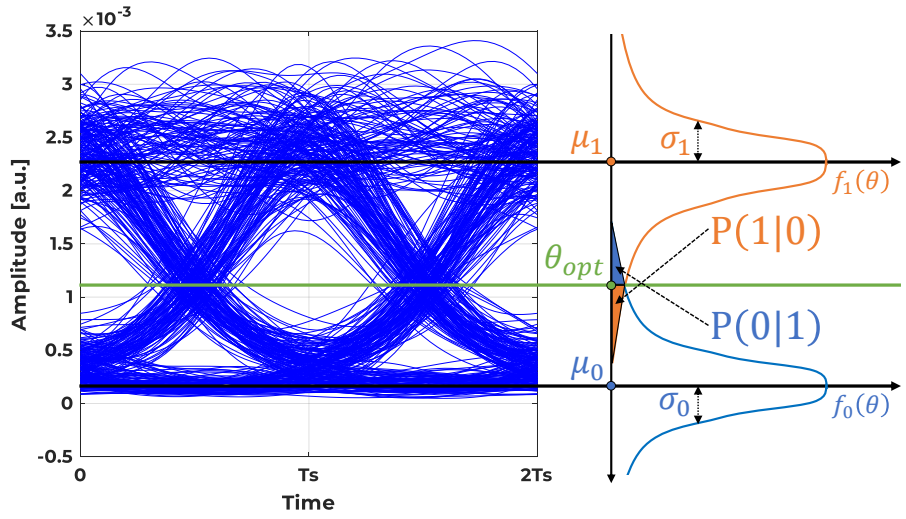

Figure 5.3: Sample eye diagram for 16x SSMF spans OLS with $D_{RES,IL} = 50$ ps/nm, $D_{TOT} = 800$ ps/nm impaired by ISI and ASE noise only. Left side shows the Gaussian PDF approximation of noise centered on μ_0 and μ_1 levels with standard deviaton σ_0 and σ_1. Colored areas identify the error probability mass on zeros $P(0|1)$ and ones $P(1|0)$.

where 0 or 1 depends on the bit transmitted at $t = t_{opt}$. In Fig.5.3, the optimum electrical signal level threshold θ_{opt} for hard-decision is also shown. The PDF area portions overlapping around θ_{opt} are the mass probability of error (i.e. the BER).

On the 0-bits the μ_0 is very small, so that the Gaussian signal-to-noise beating component is small and comparable in variance to the Chi-squared contribution. The PDF shape is thus more similar to the Chi-squared with longer tails than the Gaussian, especially at large SNR. On the 1-bits instead, the μ_1 pumps the signal-to-noise contributions and the overall noise is predominantly Gaussian. At the heyday of 10G the required SNR was so high that the optimal working region was between the tails of the error distributions, where the Gaussian approximation of noise could lead to significant errors in BER estimation. Nowadays instead, much more noise can be tolerated (i.e. a lower SNR) thanks to the modern high-gain FECs, which can support a pre-FEC BER of the order of 10^{-2} or 10^{-3}. In this situation, even the 0-bit Chi-squared PDF can be approximated to Gaussian since a substantially larger portion than its tails concurs to error probability. Hence, the Gaussian noise assumption on the photo-detected signal is a reliable approximation, with benefits for error probability prediction that is calculated by integrating the Gaussian PDF, hence using the erfc function, as:

$$\mathrm{BER} = \frac{1}{2}\,\mathrm{erfc}\left(\frac{\mu_1 - \theta_{opt}}{\sqrt{2}\sigma_1}\right) + \frac{1}{2}\,\mathrm{erfc}\left(\frac{\theta_{opt} - \mu_0}{\sqrt{2}\sigma_0}\right) \tag{5.4}$$

Eq.5.4 assumes that the μ values are constant and unique for each bit level. However, this is not true in our case, where the ISI significantly alters the bit signal shape, as displayed in the eye diagram of Fig.5.4, which is the result of a single-channel propagation over an OLS with $\mathrm{D_{RES,IL}}$ = 40 ps/nm and $\mathrm{D_{TOT}}$ = 1400 ps/nm. Here, the eye diagram distortion is the result of the joint interaction between the chromatic dispersion and the SPM, excluding any cross-channel non-linear effects and ASE noise. The resulting ISI in fact, basically introduces a memory of M symbols, meaning that the signal level on a certain bit depends on M bits, including the bit itself and the preceding/following in time. With a simulative campaign based on the SSFM, we have determined that a memory of M = 3 bit is enough to take into account the whole ISI effects. It should be clear however that the M value able to intercept the ISI depends on the overall chromatic dispersion accumulated during the propagation over the OLS. Hence, rather than on the particular fiber chromatic dispersion coefficient, M should depend on the dispersion map ($\mathrm{D_{RES,IL}}$) (i.e. the accumulated dispersion at the end of each fiber span) and on the number of fiber spans N_s composing the OLS, i.e. the compensated network extension. It would be then easy to generalize the approach and estimate the number of M interfering bits for different compensation schemes and reach. However, M = 3 has been found out as a sufficient value encompassing the configurations of interest of our investigation. Fig.5.4 shows a 3x bit-duration T_s signal window eye diagram using different color for each of the $2^M = 8$ *symbols*

of 3 bit, being the central the bit we want to evaluate the μ level distortion. The central bit level assumes almost the same value every time the same 3-bit pattern is encountered. In order to encompass the ISI effect, we then calculate the error probability on symbols of 3-bits rather than bit-by-bit, thus on 8 Gaussian PDFs, one for each symbol. Hence, similarly to Eq.5.4, the BER estimation is corrected as:

$$\mathrm{BER} = \frac{1}{8}\left[\sum_{s\in S_1} P\left(0_{Rx} \mid 1_{Tx}\right)\Big|_s + \sum_{s\in S_0} P\left(1_{Rx} \mid 0_{Tx}\right)\Big|_s\right] \tag{5.5}$$

where the two terms indicate the error probability on the 0 and 1 center bits of the 3-bit symbol c, respectively, with $S_0 = \{000, 001, 100, 101\}$, $S_1 = \{010, 011, 110, 111\}$ the sets of 3-bit symbols having 0 or 1 as the center bit. Each of these contributions can be thus expressed as a simple erfc Gaussian integration:

$$\begin{aligned} P\left(0_{Rx} \mid 1_{Tx}\right)|_{s\in S_1} &= \frac{1}{2}\,\mathrm{erfc}\left(\frac{\mu_{1|s} - \theta_{opt}}{\sqrt{2}\sigma_{1|s}}\right) \\ P\left(1_{Rx} \mid 0_{Tx}\right)|_{s\in S_0} &= \frac{1}{2}\,\mathrm{erfc}\left(\frac{\theta_{opt} - \mu_{0|s}}{\sqrt{2}\sigma_{0|s}}\right) \end{aligned} \tag{5.6}$$

Wrapping up: unlike DSP-based coherent transmission, QoT of IMDD channels cannot be determined exclusively by knowing the GSNR on the optical field. On

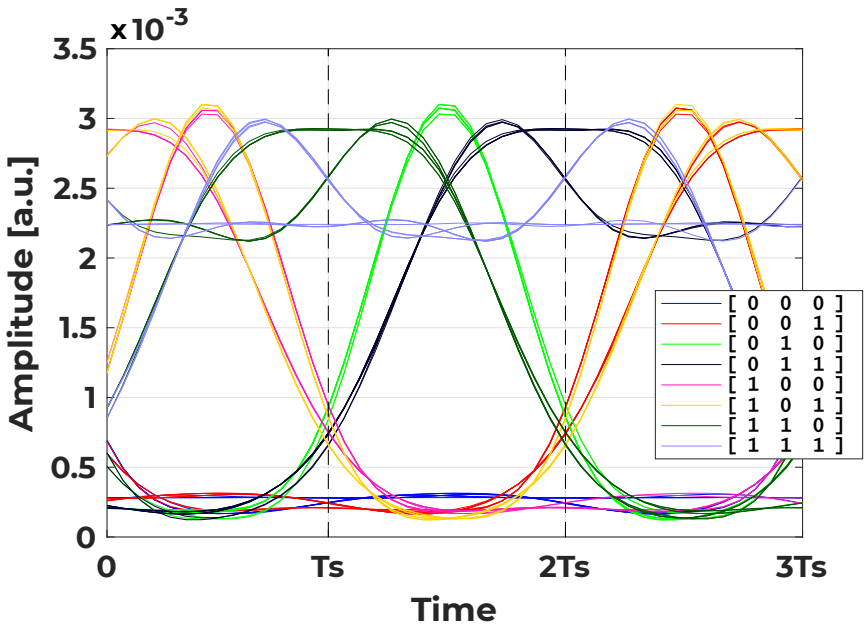

Figure 5.4: M = 3 bit eye diagram for 16x SSMF spans with $D_{RES,IL}$ = 40 ps/nm and D_{TOT} = 1200 ps/nm using different colors for each 8 possible symbols of 3 bit. On the center bit, the bit under test, each symbol has different μ_0 and μ_1 levels.

the contrary, the photodiode breaks the direct relationship between GSNR and electrical SNR and complicates the impairment evaluation by adding a signal-to-noise beating. However, the pre-FEC BER, assuming optimal decision threshold, can be still estimated by keeping as quality metrics the variance of the overall additive noise due to ASE and XCI effects and the μ levels determined by the joint chromatic dispersion-SPM ISI introducing M-bit memory.

The developed QoT-E software faces the estimations of the two quality metrics with a semi-analytical approach:

- **ISI-induced $\mu_{0,1|s}$ levels distortion**: they are evaluated with a specialized SSFM-based simulation module tailored to consider only chromatic dispersion and SPM and running in the seconds time-scale to keep real-time operation. Simulation is performed by propagating a single 10G channel on the OLS of interest with noiseless amplifiers. As already shown in Fig.5.4, the received electrical signal is sampled at t_{opt} and each received sequence transmitting a symbol s in S_0 and S_1 is isolated. Then, the sample of the sequence corresponding to center bit is taken as the reference $\mu_{0,1|s}$ for that M-bit symbol.

- **Overall noise variances $\sigma_{0,1|s}$**: the overall amount of noise variance is determined by the ASE noise and the XCI non-linear effects (XPM and FWM), which are statistically independent random noise processes. Among the latter, the FWM is considered negligible so that only XPM is left. Hence, from Eq.5.2,5.3 we get:

$$\sigma^2_{0,1|s} = 4\mu_{0,1|s}\left(\sigma^2_{XPM} + \sigma^2_{ASE}\right) + 4\left(\sigma^4_{XPM} + \sigma^4_{ASE}\right) \tag{5.7}$$

  where σ^2_{ASE} and σ^2_{XPM} are the variances of the optical ASE noise field and the XPM noise-like power, respectively. The σ^2_{ASE} component is given by the well-known formula of Eq.2.1: Note that $\mu_{0,1|s}$ is also needed for the evaluation of the overall electric noise, so there is an inter-dependence between single channel and cross channel non-linearities. Our investigations have been instead focused on the estimation of the XPM-induced non-linear part.

5.2.2 Review of XPM Model for 10G QoT Estimation

Once the SPM interplay with dispersion has been managed, the goal is to find a method to estimate the overall $\sigma^2_{XPM,i}$ noise power on the i-th channel of the 10G comb made up of N_{ch} channels. In the past years several models have been developed for assessment of the XPM in IMDD systems. The well-know GN family of NLI models, introduced in chapter 2, has been developed for the transmission of coherent channels over OLSs whose main characteristics is the free accumulation of chromatic dispersion which is compensated all at once, in the digital domain at the receiver. Such fundamental hypothesis is surely not satisfied on DM links, at least

with the common dispersion maps leaving around $\mathrm{D}_{\mathrm{RES,IL}} = 50$ ps/nm per span on average.

Here we have chosen to implement the model developed by Pachnicke et al. in [104] and based on the previous work by Cartaxo [30] and Bellotti [6]. The model allows the estimation of XPM variance in the optical field. Although the net effect in the electric decision signal interacts with CuT single channel effect, the considered model is spectrally disaggregated in the optical domain, i.e. the $\sigma^2_{XPM,i}$ of $N_{ch} - 1$ IMDD pumps is given by the sum of the $\sigma^2_{XPM,ik}$ noise powers of the k-th pump on the i-th channel:

$$\sigma^2_{XPM,i} = \sum_{\substack{k=1 \\ k \neq i}}^{N_{ch}} \sigma^2_{XPM,ik} \tag{5.8}$$

The model also considers arbitrary dispersion compensation schemes and on a span-by-span basis, so that is suited for the utilization in control of 10G networks. The amount of noise powers $\sigma^2_{XPM,ik}$ caused by a single 10G pump is calculated with the *XPM filter transfer function* approach: the XPM phenomenon is modeled as a filter causing the non-linear crosstalk from channel k to channel i [104], whose transfer function is $H_{XPM,ik}(\omega)$ given by Eq.5.9:

$$\begin{aligned} H_{XPM,ik}(\omega) = 2g_{net} \cdot \sum_{l=1}^{N_s} \gamma^{(l)} \exp\left\{\left(j\omega\Delta\lambda_{ik}\mathrm{D}^{(l-1)}_{\mathrm{RES,IL}}\right)\right\} \cdot \prod_{n=1}^{l-1} \left[\exp\{(-\alpha_l L_l)\, g_l\}\right] \cdot \\ \cdot \left(\frac{a^{(l)}_{ik}\left(C_i - 2D^{(l)}_i\right) - 2b_i}{\left(a^{(l)}_{ik} + 2b_i\right)^2} + \frac{\sin C_i}{a^{(l)}_{ik}} \right) \end{aligned} \tag{5.9}$$

where, $\omega = 2\pi f$ is the angular frequency, g_{net} the net gain profile of the OLS, g_l the gain of the l-th fiber span ILA, $\Delta\lambda_{ik}$ the wavelength distance between the channels i and k, $\gamma^{(l)}$ the non-linear coefficient of the l-th fiber span, $\mathrm{D}_{\mathrm{RES,IL}}$ the inline residual dispersion at the end of the l-th span. C_i, $D^{(l)}_i$, $a^{(l)}_{ik}$, b_i parameters defined as in Eq.5.10:

$$\begin{aligned} C_i &= \frac{\omega^2\lambda_i^2}{4\pi c}\mathrm{D}_{\mathrm{TOT}} & a^{(l)}_{ik} &= \alpha - j\omega D^{(l)} \cdot \Delta\lambda_{ik} \\ D^{(l)}_i &= \frac{\omega^2\lambda_i^2}{4\pi c}\mathrm{D}^{(l-1)}_{\mathrm{RES,IL}} & b_i &= \frac{\omega^2\lambda_i^2}{4\pi c} D^{(l)} \end{aligned} \tag{5.10}$$

being $D^{(l)}$ the chromatic dispersion coefficient of the l-th span, λ_i the wavelength of the i-th channel, c the speed of light. More details can be found in [104]. The final XPM variance is found by integrating Eq.5.9 in the signal chain and summing the channel contributions as in Eq.5.11:

$$\sigma^2_{XPM,i} = P^2_{ch,k} \sum_{\substack{k=1 \\ k \neq i}}^{N_{ch}} \frac{1}{2\pi} \int_{-\infty}^{\infty} \mathrm{PSD}_k(\omega) \cdot \left|H_{XPM,ik}(\omega)\right|^2 \cdot \left|H_{FILT}(\omega)\right|^2 d\omega \tag{5.11}$$

where $P_{ch,k}$ is the k-th channel launched power, $\mathrm{PSD}_k(\omega)$ the (normalized) power spectral density (PSD) of the k-th channel, $H_{FILT}(\omega)$ an equivalent cascade transfer function of the optical filter and electrical Bessel filter in the signal chain as in Fig.5.1.

It should be noted that, although the XPM model seems to be compatible with an also *spatially incoherent* form, the final evaluation of $\sigma_{0,1|s}$ is spatially aggregated because of the dependency on $\mu_{0,1|s}$ due to SPM and dispersion, which would surely show coherency with respect to the previous span crossed.

5.3 Simulative and Experimental Validation

The presented semi-analytical framework has been implemented as a software module. Such framework can be implemented as the QoT-E of the OLS controller, similarly as depicted in Fig.2.9 in chapter 2, with the substantial difference that here the GSNR cannot be used as QoT metric, but more complex BER estimation must be done and compared to the required target pre-FEC BER. The QoT-E, as mentioned generally in chapter 2, takes as input the *network description* and the *spectral information*. The network description includes the fiber types together with their loss, chromatic dispersion and non-linearity coefficients, the $\mathrm{D_{RES,IL}}$ and $\mathrm{D_{TOT}}$ defining the dispersion map and the amplifier noise figures. The spectral information includes the number of IMDD channels, together with their rate R_b and arrangement in the spectral grid. Power evolution of the k-th channel, defined also by the amplifiers working point, can be either an input parameter or the optimization target whether if the QoT-E is used for current QoT estimation on a given channel or for power optimization of deployed channels. Then, the QoT-E evaluates the $\mu_{0,1}$ due to chromatic dispersion and SPM effects by means of a specialized SSFM simulation and considering a memory of M = 3 bit. Simulations is run in a simulation bandwidth $BW_s = 170$ GHz to take into account the non-linear propagation effects while keeping computational time in the order of the seconds on a common workstation for an OLS made of 1 to 30 spans. The σ^2_{XPM} is then obtained by multiple numerical integration of Eq.5.11 per each IMDD pump. Here, the computational time depends on the frequency distance between the IMDD pump and the CuT and it is still of the order of the seconds until about 20 pumps. Further numerical integration speed-up could be however done by clipping the integral calculation for the farthest pumps whose contribution to the XPM can be considered negligible and/or further optimization of the specialized split-step module for SPM, for example, with respect to the simulation bandwidth. The ASE noise contribution σ^2_{ASE} is analytically obtained by Eq.2.1. Those contributions define the pre-FEC BER as QoT-E output, which is obtained combining them as in Eq.5.5,5.6,5.3.

The QoT-E has been extensively validated with respect to full SSFM simulations

Fiber commercial name	SSMF	TrueWave-RS	
Attenuation Coefficient α [dB/km]	0.23	0.23	0.23
Dispersion Coefficient D [ps/nm/km]	16.7	5.0	2.58
Non-Linear Coefficient γ [1/W/km)]	1.27	1.41	1.96

Table 5.1: Physical parameters of the optical fiber considered in the simulative validations and in the application example.

and experiments performed at the Links Foundation laboratories, by comparing the respective BER vs OSNR curves. In both experiments and simulations, the OSNR has been varied in the range between 10 and 18 dB performing ASE noise loading at the end of the OLS considered, i.e. varying the σ^2_{ASE} contribution, while the non-linear part is determined by the physical and spectral parameters. Reference SSFM simulations have been performed on a OLS layout as in Fig.5.1. We considered $N_s = 16$ fiber spans of $L_s = 50$ km of average length since real installed OLS are not strictly periodical. This makes the residual dispersion at the end of each span $D_{RES,IL}$ slightly different from the target value, providing a more reliable estimation of the non-linear impairments, but keeping the target residual in average. This becomes important when assessing optical performances in the context of network flexibility and reconfigurability rather than a simple system planning and leans towards the prediction of optimal/sub-optimal power levels for network optimization in 10G networks. We have tested two different types of fiber in this validation section, whose physical parameters are reported in Table 5.1, a typical high-dispersion fiber (SSMF) and a low-dispersion fiber of the NZDSF type (TrueWave). Simulations have been carried out with ideal, noiseless and transparent optical amplification, i.e. ILAs with null noise figure and recovering exactly the fiber propagation loss, thus accumulating only non-linear noise along propagation. Hence, the OSNR is set solely by the lumped ASE noise added at the end of the OLS, whose amount is determined by inverting the OSNR formula as $\sigma^2_{ASE} = P_{ch}/\text{OSNR}$, where P_{ch} is set to 1 dBm in these simulations. The BER is then evaluated by counting the errors on the received signal, ensuring enough signal length to provide a reliable estimation. Fig.5.5 displays the validation done with respect to SSFM simulations for SMF and TrueWave fiber types using different dispersion maps. $N_{ch} = 16$ channels at $R_b = 11.3$ Gbps filled the spectrum on the $\Delta_{WDM} = 50$ GHz WDM grid. The center channel (the 8-th) was probed while neighboring channels were pumping cross-channel phenomena. Fig.5.5a,5.5b show the QoT-E outcome with respect to an OLS made up of SSMF fibers with $D_{RES,IL} = 0$ ps/nm and 50 ps/nm maps, while Fig.5.5c,5.5d compares the QoT-E to simulations for TrueWave fibers with $D_{RES,IL} = 20$ ps/nm and 50 ps/nm maps. Blue curves refer to the single channel case, i.e where ASE, dispersion and SPM effects are considered. These curves alone confirm that the M = 3 bit value well exhausts

the ISI memory. Orange curves instead refer to the multi-channel case, so that the OSNR penalty at a target BER with respect to the single channel case accounts for the multi-channel non-linearities. Results confirm a good agreement of the QoT-E evaluation. In particular, the $D_{RES,IL}$ = 50 ps/nm without any additional post compensation (since 50 × 16 spans gives 800 ps/nm) configuration is confirmed as the most favorable configuration with SSMF fiber which minimizes the XPM effect. Such dispersion maps leaving roughly half of a bit period of walk-off seems in fact to break down the coherent accumulation of XPM [104]. On lower dispersion values, instead, we find, as expcted, a larger penalty due to the multi-channel effects, still smaller for $D_{RES,IL}$ = 50 ps/nm.

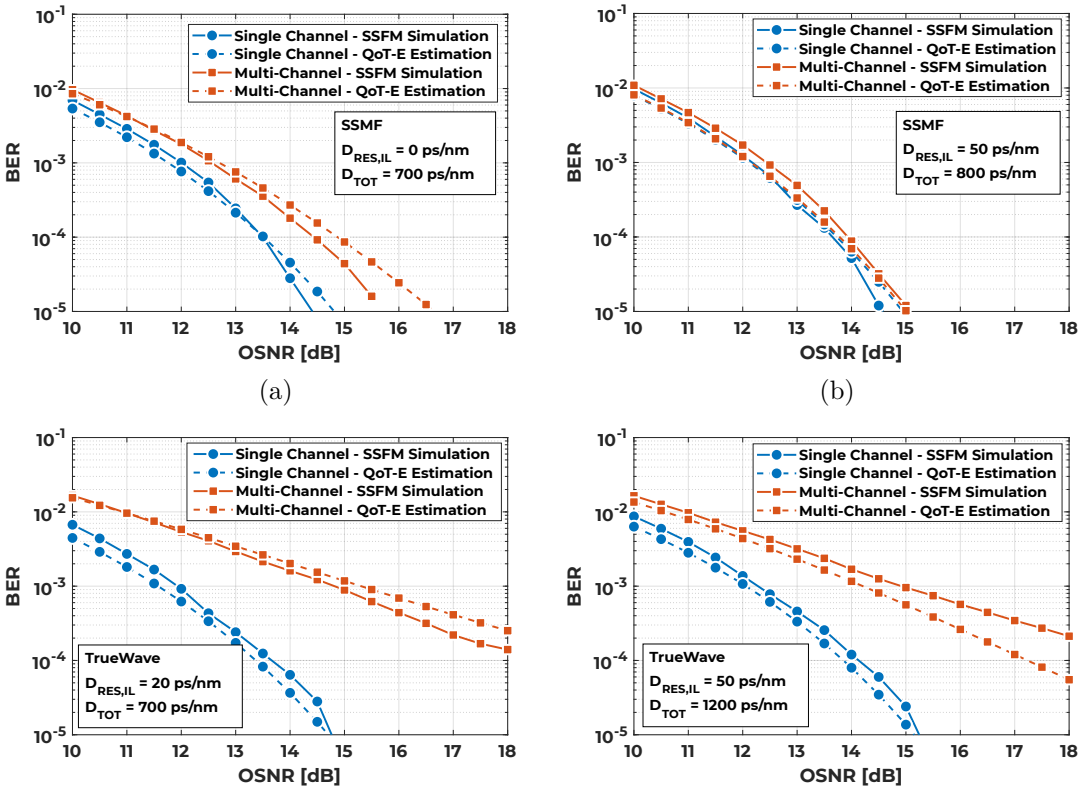

Figure 5.5: Model Validation vs SSFM Simulations showing BER vs OSNR curves for different dispersion maps and fibers - SSMF with D = 16.7 ps/nm/km and TrueWave with D = 2.58 ps/nm/km. Blue curves are single channel case considering only ASE, chromatic dispersion and SPM. Orange curves include the XPM noise of 16 10G pumps in the Δ_{WDM} = 50 GHz grid, being the 8-th channel the CuT.

Experimental Validation

Fig.5.7 shows instead the comparison between the QoT-E result and experiments. The laboratory setup is briefly depicted in Fig.5.6. On the transmitter side, we have here $N_{ch} = 11$ IMDD channels, at $P_{ch} = 1$ dBm, being the center channel the CuT. Channels are independently modulated with Mach-Zender modulators, multiplexed and fed into a recirculating loop of 4 fiber spans enabling emulation of 4,8,12,16x spans OLS. Figures consider the performance of the $N_s = 16$ spans case. The signal at the output of the loop is sampled at the optimum sampling time t_{opt} and recorded for offline processing. Further ASE noise loading to vary the OSNR is done in the digital domain, then the corresponding BER is obtained by error counting with the same software routines used for SSFM comparison. Fig.5.7a,5.7b,5.7c show the comparison for a loop made of SMF fibers with residuals $D_{RES,IL} = 0$ ps/nm with two post-compensation values setting $D_{TOT} = 700$ ps/nm and $D_{TOT} = 1000$ ps/nm and $D_{RES,IL} = 50$ ps/nm with $D_{TOT} = 800$ ps/nm, being the latter the most practical case in real systems. Another configuration made of TrueWave fibers with an average $D_{RES,IL} = 154$ ps/nm and $D_{TOT} = 864$ ps/nm is also shown in Fig.5.7d. This last case is practically obtained by removing some of the DCUs because of their too coarse granularity. In any case the model curves show a very good agreement with the experimental curves. Only the TrueWave case shows a small gap in the multichannel case, where the additional penalty of the experimental curve can be explained with a residual FWM contributions due to lower dispersion, not accounted for in our model.

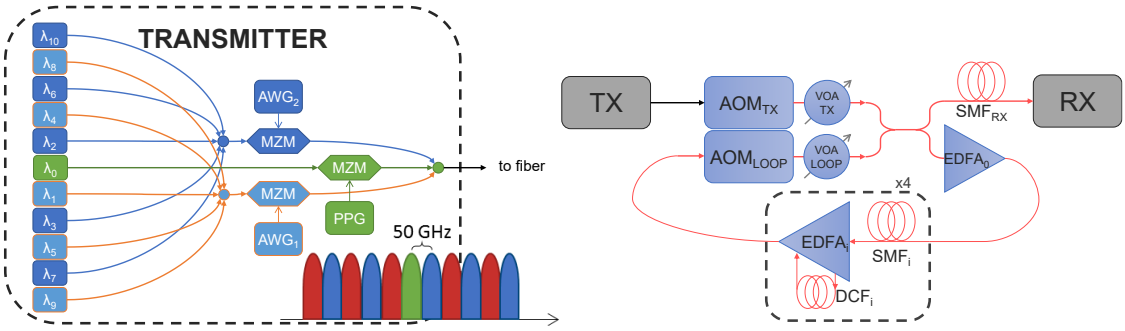

(a) (b)

Figure 5.6: Block Diagram of the laboratory setup. (a) The transmitter multiplexes 11 independent data channels modulated with Mach-Zender modulators. CuT data stream is made of PRBS sequence (b) Recirculating loop made up of 4 fiber spans

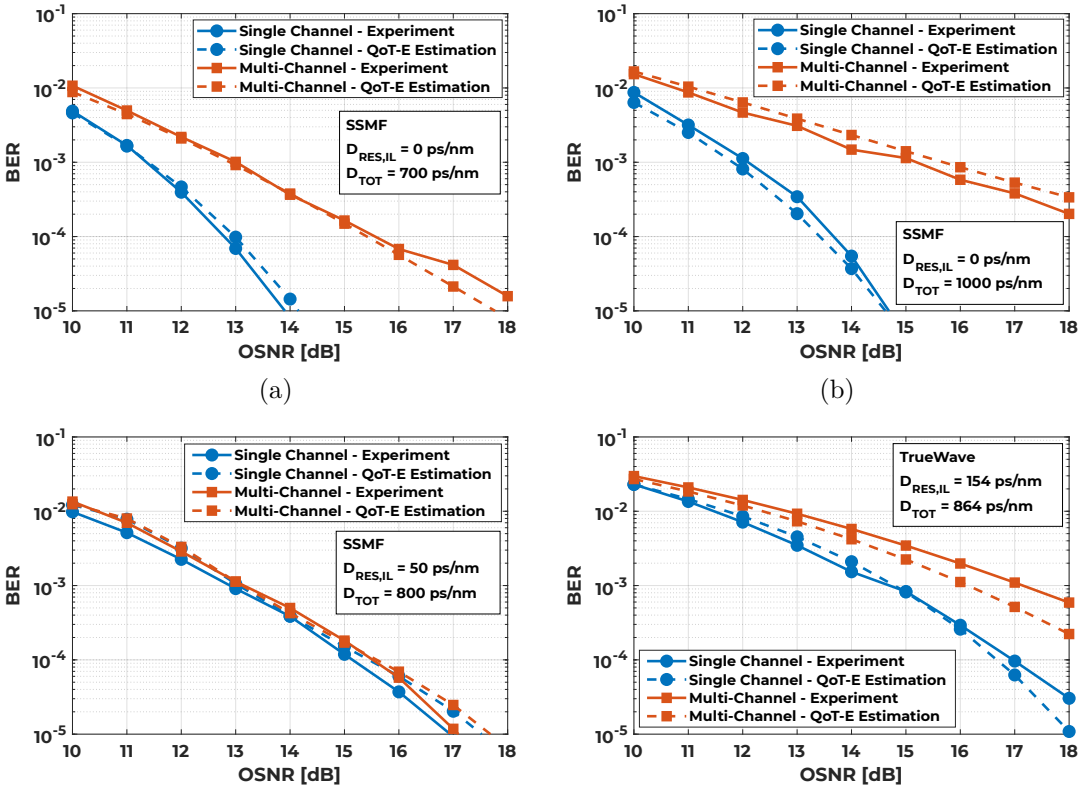

Figure 5.7: Model Validation vs Experiment with recirculation loop showing BER vs OSNR curves for different dispersion maps and fibers (SSMF and TrueWave). Blue curves are single channel case considering only ASE, chromatic dispersion and SPM. Orange curves include the XPM noise of $N_p = 11$ 10G pumps in the $\Delta_{WDM} = 50$ GHz grid, being the 6-th channel the CuT.

5.4 Application of QoT-E in Network Planning and Management

Previous section showed that QoT-E delivers a fast yet accurate estimation of the required OSNR at the Rx, enabling a quick test of the lightpath feasibility. In this section instead we present an application of the developed QoT-E in a 10G network context. In particular, we focus here on the estimation of the available OSNR margin, i.e. the margin related to the ASE generation only, but still considering the non-linearities in the BER estimation. Following the taxonomy proposed by Pointurier in [118], we take into account the *Unallocated OSNR Margin* (UM) as a metric intended to perform network design, orchestration and margin optimization with physical layer awareness. In this application example, we consider a DM meshed network deployed using SSMF and LEAF fibers whose parameters are described in Table 5.1. $L_s = 50$ km of average span length is assumed with typical

$D_{RES,IL}$ = 50 ps/nm. We do not set the number of span N_s since they depend on the number of hops required to route the lightpath. We first consider the available OSNR at the Rx - $OSNR_{RX}$, determined *solely* by the accumulation of the ASE noise on the N_s spans route. $OSNR_{RX}$ is thus calculated assuming standard ILA noise figure of 5.5 dB, 8 dB of additional system and design margin [118] and, for each span, 6 dB of lumped loss due to patch panels, as likely in brown field metro network segments. Such scenarios in fact usually have many connection points and could present several losses due to fiber cuts and joints which are very common in terrestrial systems. The $OSNR_{RX}$ is thus the offered QoT by the N_s spans link, without considering the non-linear effects.

We then consider the requested OSNR at the receiver $OSNR_{req}$, which is the minimum value required to support error-free transmission (target pre-FEC BER = 10^{-3}) considering all the propagation effects, including CD and non-linearities. Hence, the UM is computed as the difference between $OSNR_{RX}$ by ASE accumulation and the OSNR at Rx $OSNR_{req}$ provided by the QoT-E.

$$UM = OSNR_{RX} - OSNR_{req} \tag{5.12}$$

Since the $OSNR_{req}$ involves non-linearities, the UM is channel power dependent and represents the headroom left for power/spectral optimization in the OLS considered. The UM has been calculated for P_{ch} between -6 and 6 dBm, varying the span count N_s from 1 to 30 and on both the Δ_{WDM} = 37.5 GHz and Δ_{WDM} = 50 GHz WDM grid, populating the C-Band with 107 and 81 10G channels, respectively. The span count defines the extension of the longest allowed path in the meshed network.

Fig.5.8 shows how the UM varies with channel power P_{ch} and increasing the path length of both the SSMF and LEAF networks at the 37.5 GHz and 50 spacing. When the optical path is short, the UM increases almost linearly with P_{ch}, so that performance is limited only by ILAs ASE noise. As the span count increases, the non-linear impairments become predominant at moderate to large powers, so that is possible to obtain an optimal power delivering the largest margin. This is more evident on LEAF network with narrow spacing due to the stronger non-linear effects, limiting the maximum reach to less than 30 spans. Finally, at lower powers and longer paths, the optical feasibility is limited by the accumulation of CD, and the corresponding tolerance of the transceiver.

Fig.5.9 shows the extended set of results arranged on a *margin mask*, which is a set of iso-UM curves vs channel power and number of spans. Here, the network dimension is set as the maximum span count an optical path may include. The maximum $P_{ch,max}$ is set by the EDFA total output power. By jointly satisfying these two constraints, we can identify the region where the system may operate. For both SSMF and LEAF (Fig.5.9), the $P_{ch,max}$ of 2 dBm guarantees nearly 3 dB of UM for the entire routing space. Also, lower power levels are feasible at the cost of decreased margin, for example, targeting energy saving management criterion.

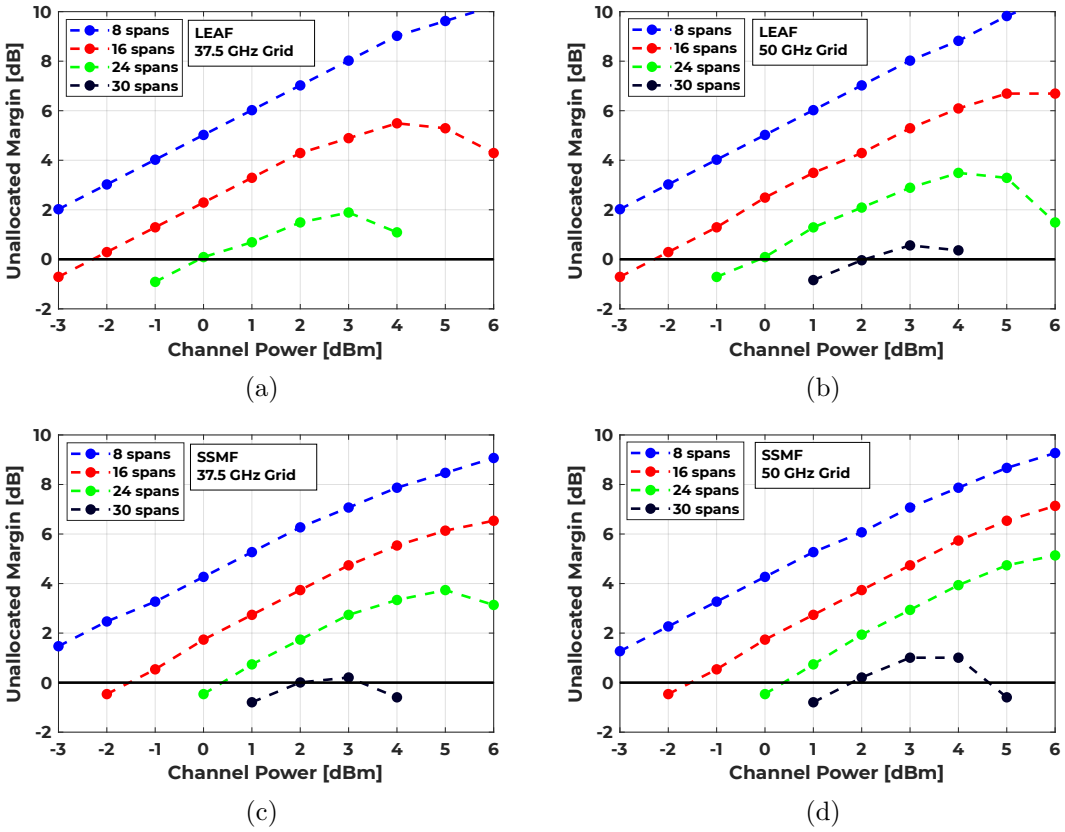

Figure 5.8: Unallocated Margin vs Channel power vs Number of spans for (upper row): LEAF network, (lower row): SSMF fiber network at (left column): $\Delta_{WDM} = 37.5$ GHz and (right column): $\Delta_{WDM} = 50$ GHz. The black continuous line sets the zero-margin threshold below which the lightpath is out of service.

In Fig.5.10, we then provide the cut of the power mask by setting a constraint of the total EDFA output power. We have considered a typical maximum output power of 22 dBm and thus calculated accordingly the maximum allowed power per channel $P_{ch,max}$. We observed the UM vs the number of spans at both the considered WDM spacings, leading to $P_{ch,max} = 2$ dBm at $\Delta_{WDM} = 37.5$ GHz and $P_{ch,max} = 3$ dBm at $\Delta f = 50$ GHz. This allows us to make some interesting considerations, for example in a path recovery scenario. Assuming a path length of 700 km (14 spans) both spacings deliver nearly the same 5 dB margin. In case of link failure, this permits to recover the same lightpath by routing it along a much longer path still providing enough margin.

Hence, although because of the propagation characteristics of the 10G systems, is not possible to reach the same flexibility in QoT management as for transparent coherent networks, it is still possible to allow some degree of flexibility in 10G network management.

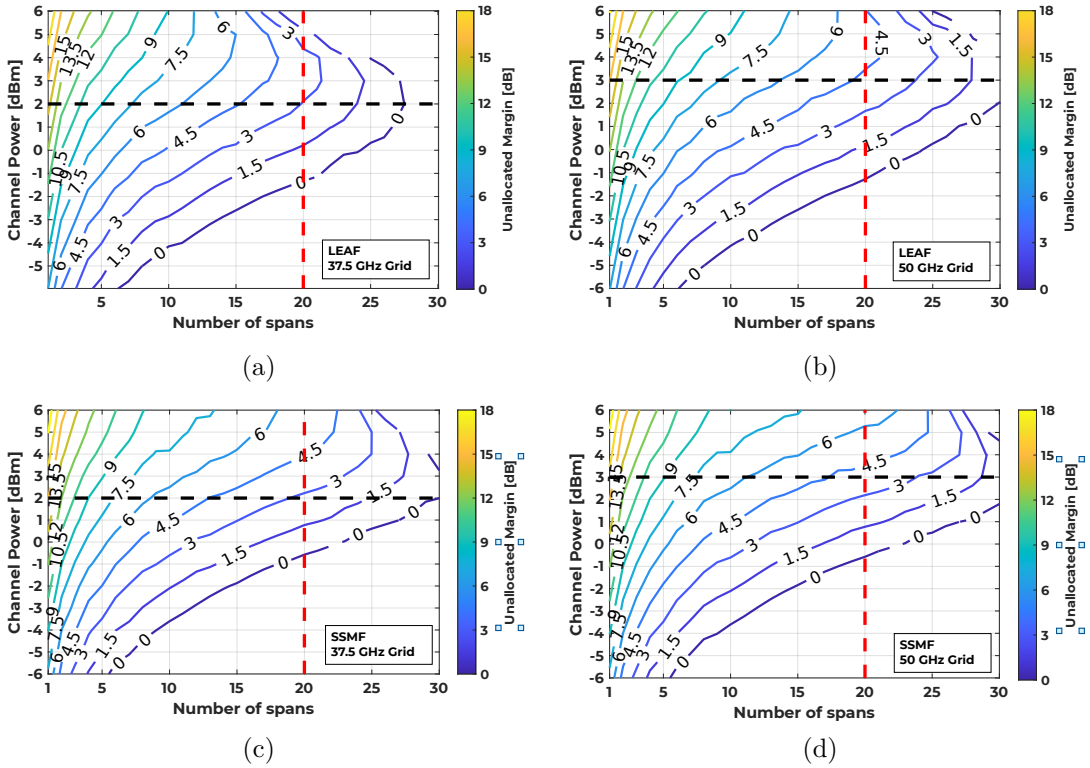

Figure 5.9: Unallocated Margin mask for (upper row): LEAF network, (lower row): SSMF fiber network at (left column): $\Delta_{WDM} = 37.5$ GHz and (right column): $\Delta_{WDM} = 50$ GHz. Black dashed line is the $P_{ch,max}$ constrained to total EDFA output power of 22 dBm and 107 or 81 WDM channels. Red dashed line sets the maximum number of spans a path in the network.

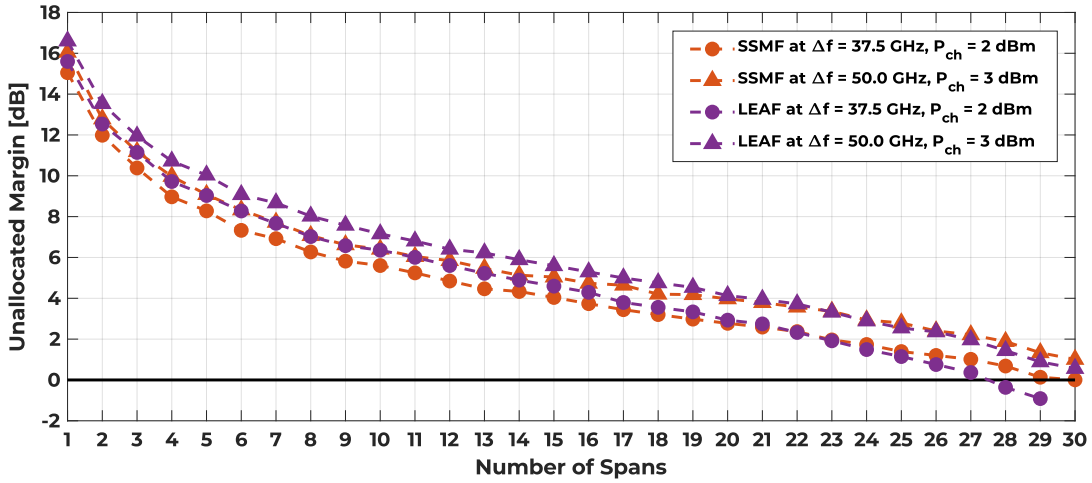

Figure 5.10: Unallocated Margin vs Number of spans with channel power constrained to WDM spacing and total EDFA output power of 22 dBm with OLS made of SSMF (orange) and LEAF (purple). Circles and triangles refer to a spectral allocation of 107 channels on 37.5 GHz grid with $P_{ch} = 2$ dBm and 81 channels on 50 GHz grid with $P_{ch} = 3$ dBm, respectively. Black continuous line sets the zero-margin threshold below which the lightpath is out of service.

Chapter 6

Mixed 10G-100G Transmission on Dispersion Managed Networks

In this chapter we will address the problem of QoT estimation for coherent channels in the scenario of copropagation with 10G IMDD channels in a section of DM OLS. The investigation here presented are an extension of the results previously published in [157, 156].

Focusing on the non-linear interaction of the 10G channels on 100G channel, we will first give the context of the investigation and identify the main phenomena. In particular, we will focus on the inter-channel effects generated by 10G channels on coherent channels. We then proceed by presenting a semi-analytical model developed for an estimation of the joint XPM-polarization noise, which is both *spectrally* and *spatially* disaggregated and reporting a summary of the preliminary simulations results analyzing the XPM NLPN generation. This simple-yet-effective model, serving as a QoT-E software module, is then validated by comparing its result with SSFM-based Monte-Carlo simulations including random birefringence campaign, showing that it provides QoT predictions which are always conservative. Finally, an experimental validation of the QoT estimator, carried out on a laboratory setup is presented.

6.1 The Context of Mixed 10G-100G Transmission

As previosly mentioned in chapter 5, the IMDD transmission is still widespread and florid thanks to its contained costs in those contexts who do not require aggregation of large capacities. At the same time, these systems are extremely rigid in terms of reconfigurability, with the spectral load tightly bound to the dispersion map of the OLS. This is in contrast to the transparency paradigm of coherent optics, where the decoupling of the transceiver side from the line system hardware is

pursued in an open and disaggregated networking scenario. Consequently, usually, these two technologies are definitely kept separated. Nevertheless, filling this gap would lie exactly in the same open and disaggregation ground. From the perspective of different network segment interfacing and transparent routing, being able to route coherent optical channels through a section of 10G-loaded metro network, made up of DM OLS becomes a convenient opportunity to save on CAPEX and improve either the network flexibility and the utilization of the optical spectrum, of which just a relatively small portion is usually occupied in the 10G systems. It should be clear that the opposite, i.e. propagating 10G signals over multi-span dispersion-uncompensated core network paths, is not possible since 10G channels require in-line DCU to keep under control QoT degradation, at least when the dispersion tolerance of the 10G transceiver is exceeded. A scenario of interest is pictorially represented in Fig.6.1. In orange we have a section of core/backbone network which is operated with coherent channels on DU links due to the larger bit-rate requests. We will usually indicate in this chapter coherent channels as 100G lighpaths, since we focus on 32 GBaud channels PM-QPSK modulated, delivering around 100 Gbps of net rate. Besides that, a section a of *metro* network, with smaller rate requirements, operated with legacy 10G channels and optical links with in-line dispersion compensation is represented in blue.

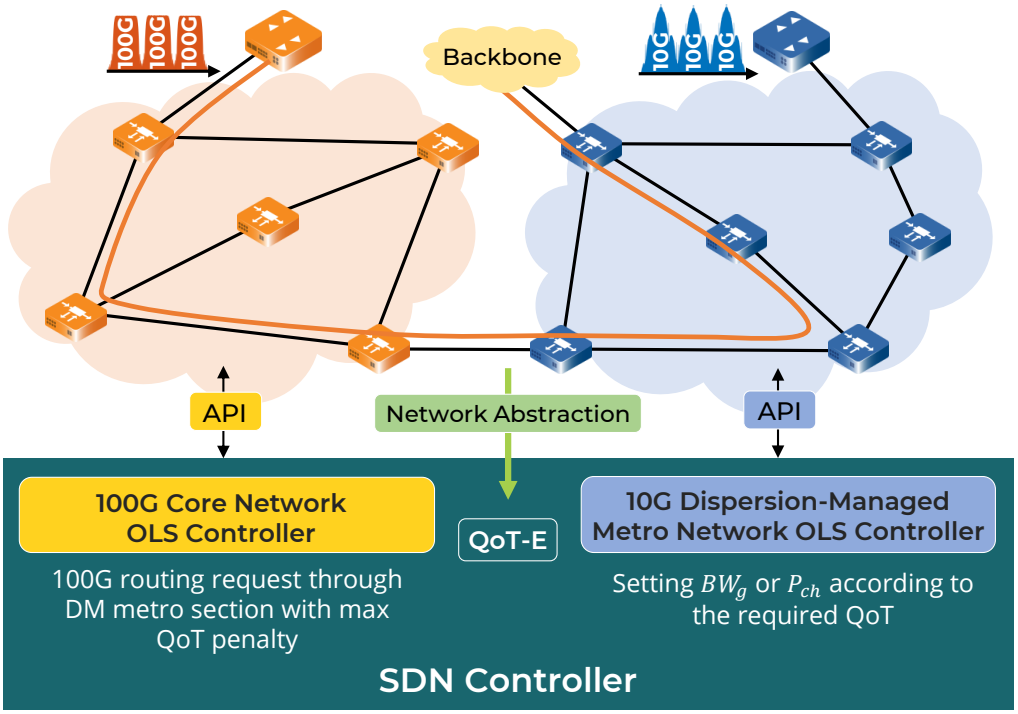

Figure 6.1: Use case for the interaction of DU coherent networks with 10G-loaded DM metro segments and the network control plan structure.

In this case, some 100G coherent channels coming from a section of DU core network are routed through a section of a DM network already populated with 10G IMDD channels. This enlarges the routing space of the possible 100G lightpaths and increases the spectral utilization of the 10G operated segment. Fig.6.1(a) also outlines our proof-of-concept of the 100G (orange) and 10G DM (blue) network segments interaction. The represented nodes are ROADMs, i.e. bridges from/to the optical infrastructure to/from the Ethernet/IP layers, linked by OLSs (black lines) composed of fiber spans and optical amplifiers. A 100G lightpath allocation request is handled on the SDN controller, performing path discovery according to a QoT metric and/or a maximum acceptable QoT penalty of 100G channels. From another point of view, the problem could also be seen as the wavelength assignment of a 100G lightpath in a DM OLS to support previous 10G traffic. In both cases, the availability of a QoT estimator, used together with network abstraction and real-time status as input, comprehesive of all the peculiar non-linear interaction in such joint propagation, is crucial. The OLS controller sets the working point of each amplifier and, consequently, the input power of each fiber span, possibly to the optimal working point maximizing the QoT metric, determined synergistically with the QoT-E.

6.2 Overview of the Physical Layer Impairments

As stated in chapter 2, in order to perform path computation, it is necessary to elaborate an abstraction of the physical layer and get an estimation of the QoT degradation experienced by the coherent channels while travelling through the core segment and the metro segment. This has been shown possible in chapter 4 for uniform coherent transmission on DU OLSs allowing for a simpler QoT estimation based on the GSNR, given that the transmission channel can be modeled as AWGN, with ASE noise sources and equivalently lumped NLI sources.

In mixed 100G-10G transmission, due to the different nature of signals interacting, it instead convenient to classify the significant non-linear interactions as in Fig.6.2. In a spectrally disaggregated way, non-linearities involving the 10G or

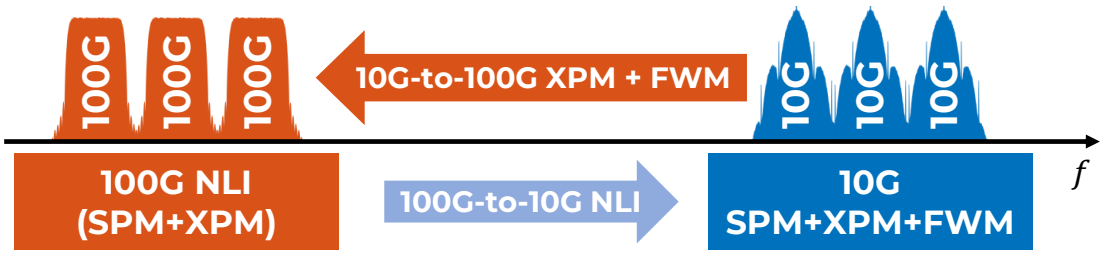

Figure 6.2: Brief classification of mixed 10G-100G transmission on DU OLSs non-linear effects.

100G comb alone are represented in rectangles. Arrows instead, summarize the potential sources of non-linear interaction between the combs using different transmission technologies. The 10G SPM, XPM and FWM on the 10G comb, have been discussed in chapter 5, when considering the propagation of 10G channels alone. As for the 100G-to-10G NLI, it is made of the XPM and FWM originated by the 100G and impairing the 10G performance but it is out of the scope of this study.

Let us instead focus on the non-linearities impairing the 100G comb. Regarding the 100G NLI we refer to the NLI generated by the 100G comb alone on the DM OLS. From the spectral content point of view, the situation is the same as in chapter 4. However, the inline dispersion compensation changes the figure of XPM and SPM accumulation because of the reduced accumulated walk-off. Consequently the Gaussian noise-like modeling hypothesis may not be met, so that this impairment source will be addressed in further studies. The remaining impairment are thus the XPM and FWM generated by the 10G comb on the 100G channels. As for the FWM, it can be neglected since it is weak in typically used high-dispersion optical fiber types [157, 169, 80, 148, 10].

In this chapter we then focus on the 10G-to-100G XPM. The joint propagation of 10G and 100G signals on DM OLS has been widely observed in previous literature and coherent channels have been demonstrated to suffer strong non-linearities from copropagating 10G IMDD channels on DM OLS [43, 24, 122, 7, 135]. Such effects are traditionally mitigated by setting a *guard-band* between 100G and 10G channels WDM combs [7, 45], which are placed in separated portion of the spectrum, and/or with appropriate power setting strategies. Also, several mathematical derivations modeling the phase noise component on coherent channels have been developed in the past [81, 10, 148, 173]. However, some of them mostly focused on the performance degradation due to dispersion compensation, some other did not considered the dual polarization propagation effects due to birefringence, or they did not considered modern raised-cosine shaping and state-of-the-art DSP-based capabilities, especially in the recovering of the NLPN, in a more phenomenological perspective rather than systemistic. In the open and disaggregated network context, in fact, it would be useful to derive an approach for the evaluation of the 10G-to-100G XPM impairment compliant to the spectrally and spatially disaggregated principles described in chapter 2.

6.2.1 Polarization Issues in Mixed 10G-100G Transmission

As outlined in chapter 2, the XPM noise manifests as a multiplicative non-linear phase noise (NLPN) and as an additive noise-like contribution. From Eq.2.15, one contribution is a pure XPM phase modulation interacting with dispersion, the other is the XPolM contribution which causes a polarization crosstalk. In addition, by expressing the Kerr term by means of Stokes vector, as in Eq.2.16, we saw that the XPolM causes a change of the SOP, in this case, of the coherent signal caused

by the 10G interfering pump. We can then argue that, the NLPN component can be still recovered by CPE algorithms [157]. An additive noise-like part instead originates mainly by the interplay between the XPM effect and the polarization effects as birefringence and PMD [89, 156], other than XPolM.

While polarization effects have been demonstrated to not give rise to any significant implications on the measured GSNR in full coherent transmission systems [111], their contribution is peculiar of the interaction between 100G and 10G channels, because of the polarization characteristics of the two technologies. 100G coherent channels exploit polarization multiplexing on the two orthogonal polarization components to carry independent PM-QPSK-modulated signals. As a consequence, they are *depolarized* signals, meaning that they do not maintain a fixed polarization state. Oppositely, 10G channels are instead *polarized*. These differences are better understood by looking at the IMDD and the coherent signal in the Stokes space on the Poincare sphere as in Fig.6.3, obtained by means of SSFM. Fig.6.3 plots the SOP evolution of a 10G and a 100G signals at 1 SpS in single channel propagation before the launch in a DM OLS (blue) and after 20 span (orange). Results using both the polarization-averaged Manakov equation and CNLSE with $\delta_{\mathrm{PMD}} = 0.1\,\mathrm{ps}/\sqrt{\mathrm{km}}$ are reported. It can be seen that the SOP of the 10G channel is fixed in the Poincare sphere, with a minor depolarization induced by birefringence in CNLSE case, due to the nature of the OOK signal and its independence on the orthogonal polarization states. The 100G PM-QPSK modulated signal, launched at $P_{ch} = -20$ dBm to avoid SPM, is instead depolarized already at the launch in the OLS since it has no fixed SOP due to the independent phase modulated data streams on the orthogonal polarization states. Note that a negligible amount of further depolarization on the received signal is present in CNLSE case due to random birefringence.

In Fig.6.4, instead, we represent the same SOP evolution scenarios but in a P&P configuration, thus accounting for the interaction between the polarization effects and the XPM. The coherent probe here is still set to $P_{ch} = -20$ dBm to avoid SPM effects. The 10G probe is shown further depolarized due to the non-linear interaction with PMD. The 100G probe is here tested with both a 100G pump and a 10G pump. In both cases, with the Manakov equation averaging the stochastic birefringence, some spreading of the SOP is present due to the XPolM SOP-diffusion [80]. However the difference with the CNLSE case in presence of PMD is almost negligible [22]. The effects seems instead enhanced when considering a 10G pump with CNLSE, due to the interaction of XPM/XPolM with birefringence.

This thus suggests that in the mixed 100G-10G transmission context, the interaction of non-linearities generations cannot be overlooked. In the full-coherent case, the validity of the Manakov equation is a consequence of the interaction of signals which are in their nature depolarized, so that, in average, their effect on - and due to - their independent polarization components gets averaged. In the

mixed 100G-10G case instead, the polarized nature of the interfering 10G channels breaks this simmetry and the entity of the XPM/XPolM impairments on the coherent channel depends on their relative polarization state and its evolution with the randomly varying polarization rotations induced by birefringence. Hence, more than the DGD induced by the PMD on a coherent channel, which can be recovered by DSP-based receivers, is the evolution of the 10G polarization alignment with respect to the 100G to be significant.

As depicted in Fig.6.5, one could consider the polarization frame x,y corresponding to the orthogonal polarization components of the 100G probe. Then, the fixed polarization state of the 10G pump will form, at launch, a relative polarization

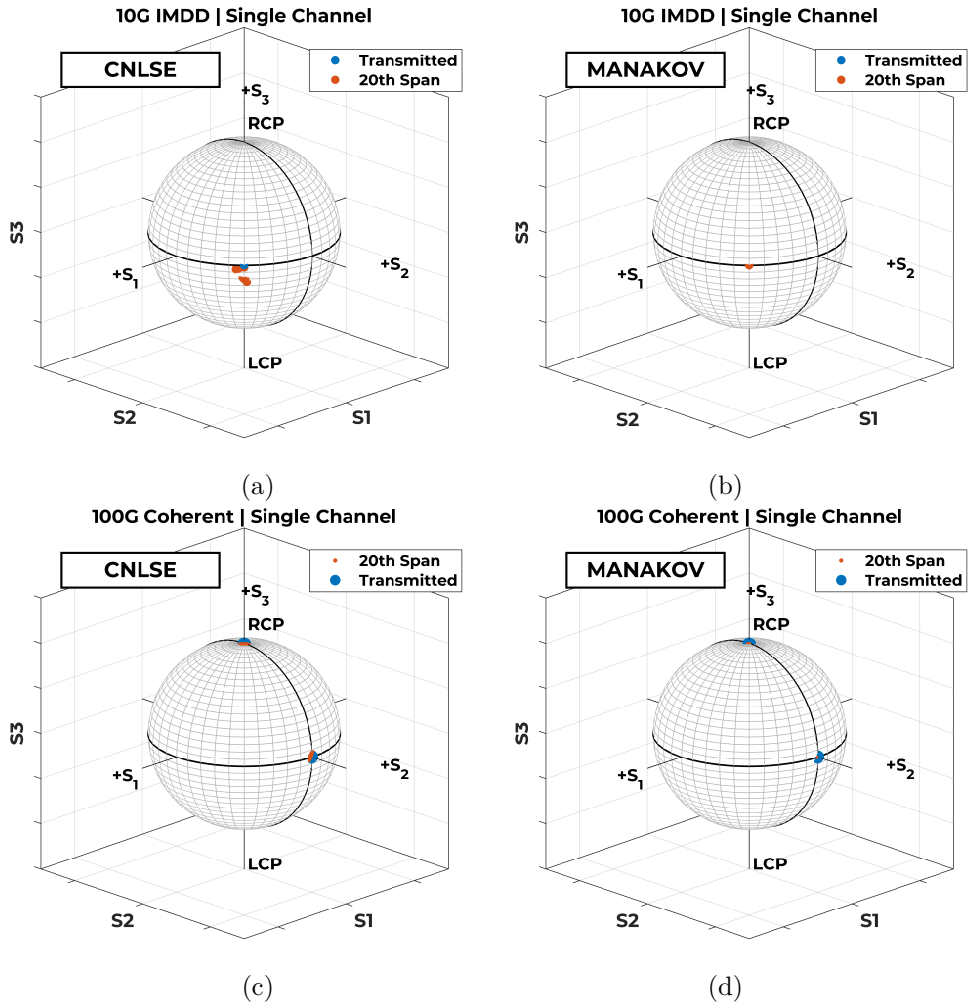

Figure 6.3: Probe SOP on the Poincare sphere in single channel configuration. Left column: CNLSE-SSFM with $\delta_{\mathrm{PMD}} = 0.1\,\mathrm{ps}/\sqrt{\mathrm{km}}$. Right column: Manakov-SSFM on a 20x OLS with $D = 16.7$ ps/nm/km and $\mathrm{D}_{\mathrm{RES,IL}} = 50$ ps/nm. Blue dots: Transmitted signal. Orange dots: after 20th span. 1st row: single 10G IMDD. 2nd row: single 100G coherent.

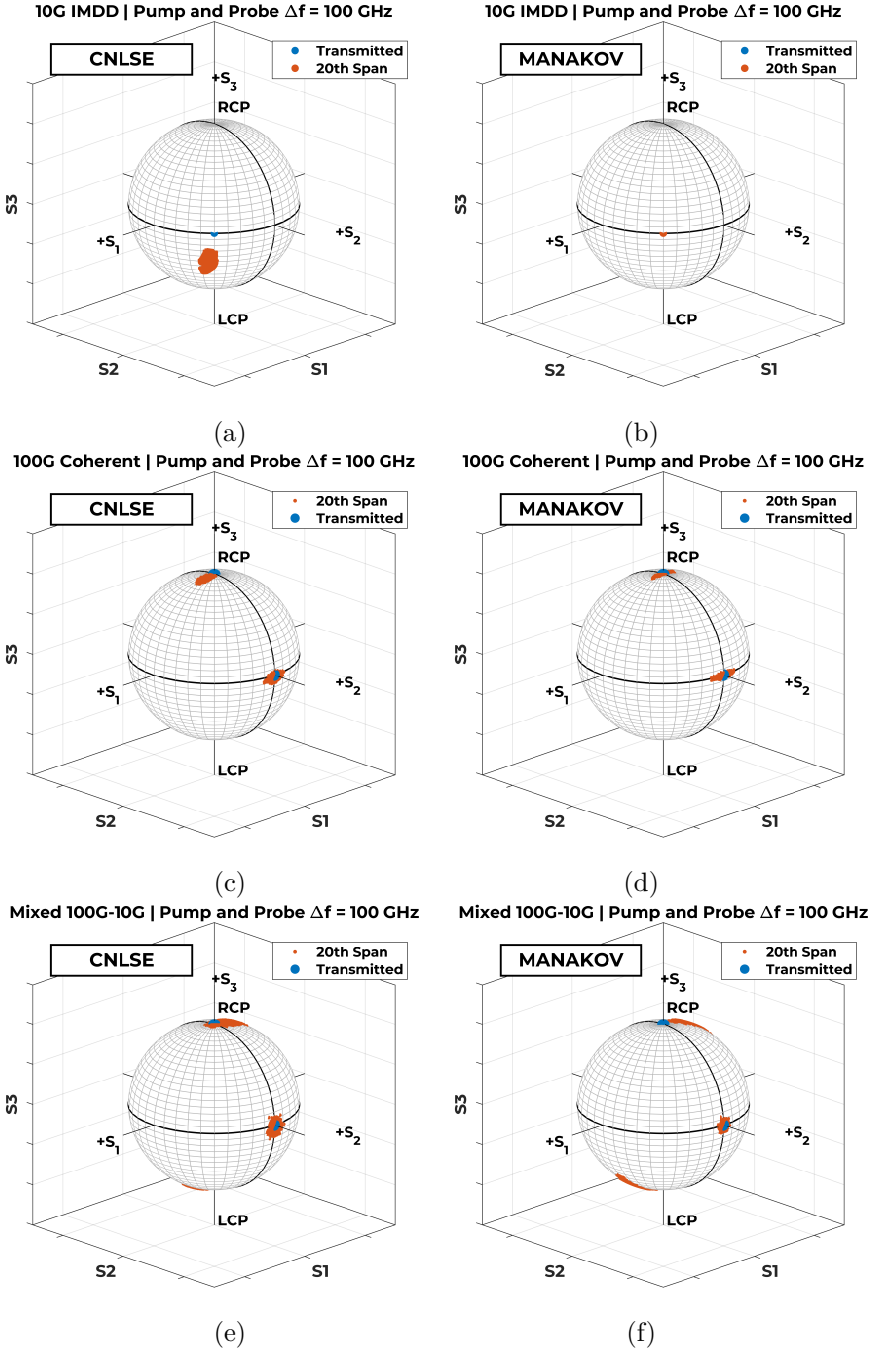

Figure 6.4: Probe SOP on poincare sphere in P&P configuration with $\Delta f = 100$ GHz. Left column: CNLSE-SSFM with $\delta_{\mathrm{PMD}} = 0.1\,\mathrm{ps}/\sqrt{\mathrm{km}}$. Right column: Manakov-SSFM on a 20x OLS with $D = 16.7$ ps/nm/km and $\mathrm{D}_{\mathrm{RES,IL}} = 50$ ps/nm. Blue dots: Transmitted signal. Orange dots: after 20th span. 1st row: 2x 10G channels. 2nd row: 2x 100G channels. 3rd row: 100G probe, 10G pump.

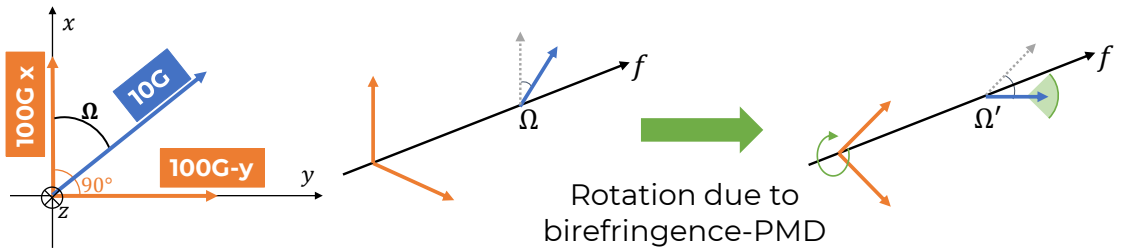

(a) (b)

Figure 6.5: (a) Representation of the relative polarization angle Ω between the 10G polarized channel and the two 100G PM components. (b) Polarization frame rotation due to birefringence. Also, 10G progressively depolarize due to random birefringence.

angle Ω with the x component of the 100G. By tracking in propagation the 100G polarization frame, the 100G will see the 10G SOP varying due to birefringence, thus writing XPM with different intensities on the x or y components according to the evolution of the local relative polarization state. When the 10G is aligned with the x component, the non-linear interaction is maximized, as opposed to when aligned with the y component.

It is then necessary to take into account the realizations of the SOP evolution when assessing the impairment in mixed 100G-10G propagation, thus needing Monte-Carlo simulations campaigns accounting for the random birefringence realizations as described in chapter 3. From these simulations we estimate the PDF of the net $\mathrm{SNR_{NL}}$ on the 100G probe, determined by the aggregated impairment arising from a comb of N_p 10G channels pumps. The PDF estimation allows to observe the worst case result which must be considered for design and control of an optical network segment with mixed propagation.

6.2.2 Definition of the Simulation Scenarios

We then proceed by defining the SSFM simulation scenario where to observe the QoT degradation on a coherent probe due to a 10G signals comb. On the OLS side, the layout is depicted in Fig.6.6. We have considered $N_s = 20$ span

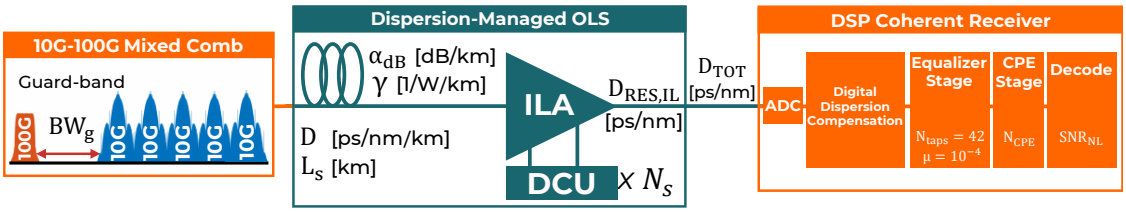

Figure 6.6: Layout of a DM OLS showing the configuration for mixed 10G-100G transmission simulations. The main system blocks for coherent receiver are shown.

of length $L_s = 50$ km. All the fibers have a loss coefficient $\alpha_{\text{dB}} = 0.2$ dB/km and non-linearity coeffiecient $\gamma = 1.27$ 1/W/km. Two fiber dispersion values are now considered, $D = 8.0$ and $D = 16.7$ ps/nm/km. The dispersion map is here uniquely defined by the inline residual dispersion $\text{D}_{\text{RES,IL}}$ so that the accumulated dispersion at the end of the OLS D_{TOT} is just the sum of the inline residuals as the post-compensation value D_{POST} degree of freedom is removed, differently to the use-case of chapter 5. DCU lengths L_{DCU} have been set, accordingly to the fiber dispersion coefficient, to explore three values of $\text{D}_{\text{RES,IL}} = 30, 50, 90$ ps/nm. DCU non-linearities have been neglected by simulating them as purely linear and lossless pieces of fibers.

With respect to the spectral loading, we first perform the simulation campaign on a multi-channel scenario, considering the effect of a $N_p = 5$ 10G pumps, as in Fig.6.6 on a single 100G probe whose power is kept at -20 dBm to avoid self channel effects and isolate the inter-channel XPM crosstalk. 10G pumps are spaced 50 GHz with $P_{ch} = -1$ dBm and a guard-band BW_{g} is set between the 100G probe and the 10G pumps. Such guard-band is set, on the $\Delta_{WDM} = 50$ GHz granularity and accordingly to the $\text{D}_{\text{RES,IL}}$ value, so that the walk-off between a 100G and a 10G exceeds the 10G bit duration $T_b = R_b^{-1}$:

$$\text{BW}_{\text{g}} \geq \frac{1}{2\pi R_b \left(\beta_2 L_s + \beta_{2,DCU} L_{DCU}\right)} \tag{6.1}$$

where the term $\beta_2 L_s + \beta_{2,DCU} L_{DCU}$ is the $\text{D}_{\text{RES,IL}}$ expressed with respect to frequency rather than wavelength. This choice of the guard-band has the rationale to consider one pump symbol collision, at least on the first compensated span. We remark that such guard-band value is here calculated on a single span basis, so that, in principle, the following span will see the walk-off of another, independent pump symbol. Clearly, in a *spatially aggregated* perspective the symbol's sliding extends along the whole optical point-to-point, together with the non-linearity generation which enhances after each amplifier site. As described in chapter 2, our target to disaggregated networking push towards the development of *local* networking rules, thus focusing on a span-per-span basis without any necessary knowledge of the past/future propagation. Table 6.1 reports each of the considered configurations, together with its guard-band BW_{g}.

The 100G probe after the 20 span propagation is then received by means of a DSP-based receiver, similarly to the one employed in chapter 4. The adaptive equalizer has $N_{taps} = 42$ and adaptation coefficient $\mu = 10^{-4}$, followed by a CPE of length $N_{CPE} = 8$ symbols recovering for NLPN. The final receiver stage calculates the SNR_{NL} that coincides with only the XPM effect in considered configuration. Each of the configurations has been simulated using both the CNLSE and the single polarization Manakov equation, i.e. the NLSE in Eq.3.3. CNLSE simulation campaign has been done averaging on $N_{MC} = 100$ realizations of the random birefringence, setting a fairly large worst-case PMD value of 0.5 ps/$\sqrt{\text{km}}$. The relative

$D_{RES,IL}$ [ps/nm]	BW_g [GHz]	D [ps/nm/km]	DP-CNLSE SNR_{NL}[dB] Mean	DP-CNLSE SNR_{NL}[dB] Std.Dev.	DP-CNLSE SNR_{NL}[dB] Worst-Case	SP-NLSE SNR_{NL}[dB]
30	450	16.7	33.51	1.58	28.02	39.64
30	450	8.0	30.96	1.42	27.68	36.90
50	300	16.7	32.30	1.40	28.22	37.69
50	300	8.0	30.34	1.15	27.39	35.51
90	150	16.7	30.09	0.73	28.03	33.90
90	150	8.0	28.40	0.51	27.17	30.91

Table 6.1: The guard-band values BW_g set between the 100G probe and the $N_p = 5$ 10G pumps for each considered inline residual $D_{RES,IL}$. Average, standard deviation and minimum value of the SNR_{NL} obtained by dual polarization DP-CNLSE-based SSFM simulation and the SNR_{NL} for single polarization SP-NLSE-based simulatons are reported.

polarization angle Ω at launch between the 10G pumps and the x component of the 100G probe has been set to 45°. The NLSE instead assumes the simplified single polarization propagation on the OLS. Hence, in this case, the coherent probe is not polarization multiplexed but made of a unique polarization state, which is aligned with the 10G pumps. No polarization rotation and/or coupling thus exist since the channel are one-dimensional with respect to polarization and there is no stochasticity in the final SNR_{NL} metric. The estimated PDF of the average SNR_{NL} between the polarization components, together with the value obtained with NLSE are plotted in Fig.6.7. The latter is reported also in Table 6.1, together with the statistical average, standard deviation and worst-case SNR_{NL} values extrapolated by the CNLSE PDF.

It can be seen that PDF encompassing polarization effects always show a substantial penalty with respect to the single polarization NLSE values, which is indeed a mathematical abstraction but allows to directly check for the relative weight in the QoT of the phenomena involved. From Eq.2.15, in fact, it can bee seen that in the single polarization NLSE only the *pure XPM* component is present which is essentially a phase modulation interacting with dispersion, thus very likely to show up mainly as NLPN, especially in DM OLS with small walk-off. Going to dual polarziation propagation, the polarization related effects, i.e. birefringence and XPolM, inflict large penalties of several dB on the final QoT. In Table 6.1 we can measure 11.6 dB penalty from NLSE propagation to CNLSE worst-case for $D_{RES,IL} = 30$ ps/nm and $D = 16.7$ ps/nm/km. The penalty then reduces as we increase the inline residual.

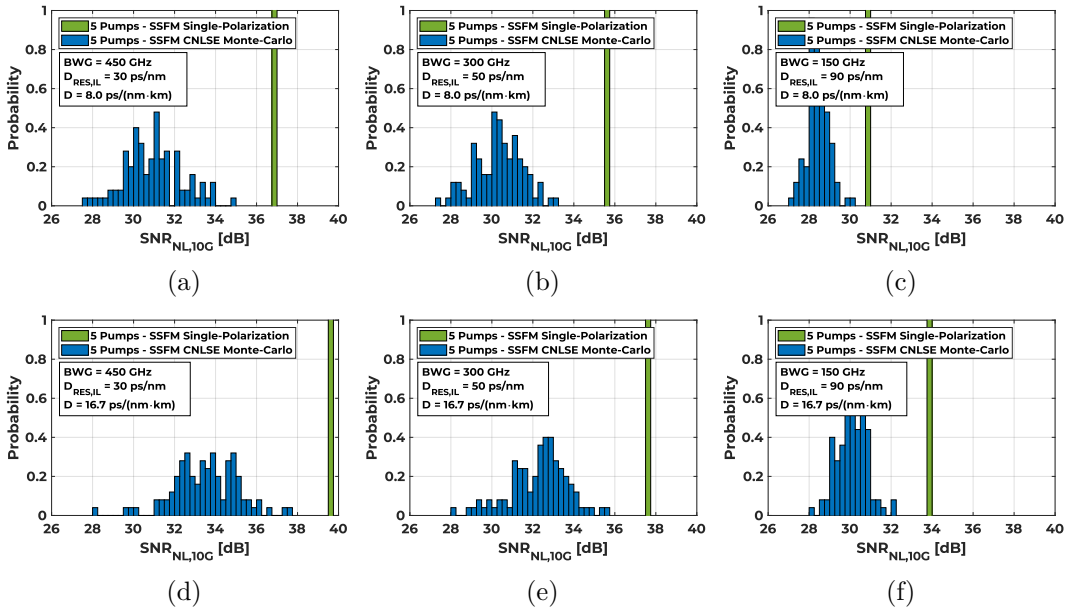

Figure 6.7: $N_p = 5$ pumps SP-NLSE vs Monte-Carlo DP-CNLSE SSFM simulations PDF for an OLS with $D_{RES,IL} = 30$ ps/nm, $\Delta f = 450$ GHz (a,d), $D_{RES,IL} = 50$ ps/nm, $\Delta f = 300$ GHz (b,e), $D_{RES,IL} = 90$ ps/nm, $\Delta f = 150$ GHz (c,f) made up of 20x fiber spans with $D = 8$ ps/nm/km (upper row), $D = 16.7$ ps/nm/km (lower row).

6.3 Single Polarization NLPN Analysis

The results in Fig.6.7 thus remind to a coupling of the XPM effect through the polarization evolution. A rigorous mathematical modeling of the non-linear interaction phenomena with birefringence and PMD would require a complex stochastic solution of CNLSE, which is out of the scope of this study. Here instead the goal is to provide a simple QoT-E tool suitable to plan and provision lightpaths along both the 10G and 100G network. For this purpose, our goal is to develop a simple model which is possibly both *spectrally* and *spatially* disaggregated, providing a conservative estimation of the net 10G-to-100G noise. In order to develop this abstraction we started to observe the XPM phenomenon through single polarization NLSE-based SSFM simulations where the coherent probe and the 10G signal are aligned in polarization. We then performed an extensive simulation campaign using the P&P approach for the NLPN due to XPM of each 10G pump. We have considered the setup of Fig.6.6, varying $D_{RES,IL}$ from 10 to 90 ps/nm, with dispersion coefficients D set to 4.0, 8.0, 12.0 and 16.7 ps/nm/km. After propagation, the coherent channel is received by applying only the adaptive equalizer and recovering the average phase rotation. The CPE algorithm has been thus disabled to observe the NLPN generation.

In mixed 100G-10G propagation, due to the large difference in symbol durations between the coherent probe and the pump, we may argue that in single polarization

scenario the XPM manifests essentially as a NLPN on the coherent channel phase, so that it can be modeled as a multiplicative noise:

$$E_R(t) = E_T(t)e^{j\phi_{XPM}(t)} \tag{6.2}$$

where $\phi_{XPM}(t)$ is the NLPN random process arising by the XPM of 10G channels on the 100G channel, whose received and transmitted complex field envelopes are $E_R(t)$ and $E_T(t)$. Assuming that each of the N_p 10G pumps generates a NLPN $\phi_{XPM,k}$, $k = 1 \dots N_p$, we can assume the additivity of the NLPN processes generated by each 10G pump, so that the overall NLPN can be considered spectrally disaggregated and the $\phi_{XPM}(t)$ of Eq.6.2 can be written as:

$$\phi_{XPM}(t) = \sum_{k=1}^{N_p} \phi_{XPM,k}(t) \tag{6.3}$$

In Fig.6.8 and Fig.6.9, sample histograms of the extrapolated NLPN noise process at 1 SpS after matched filter and without CPE, thus encompassing the full NLPN are reported. They are obtained with a single interfering 10G pump on a 100G probe, at two different Δf and combination of $\mathrm{D_{RES,IL}}$ and dispersion. They show that the accumulated NLPN is Gaussian distributed, even in the limit case of lower $\mathrm{D_{RES,IL}} = 30$ ps/nm and $D = 4.0$ ps/nm/km. Also the PSD of the NLPN processes is reported, showing that even in case of mixed 100G-10G propagation, the NLPN

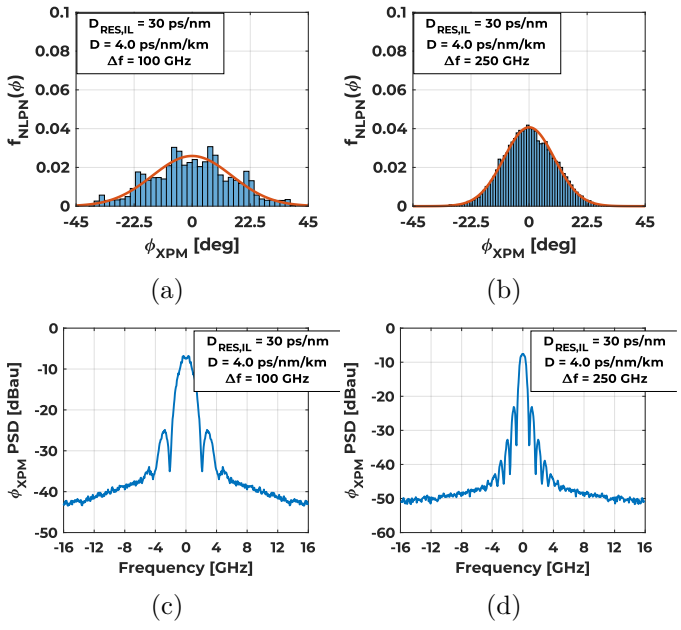

Figure 6.8: NLPN PDF with Gaussian fit (1st row) and PSD estimation (2nd row) extrapolated by SSFM simulations for a 20x span OLS with $\mathrm{D_{RES,IL}} = 30$ ps/nm, $D = 4.0$ ps/nm/km, originated by a single 10G pump at two sample frequency spacings of (a) 100 GHz and (b) 250 GHz.

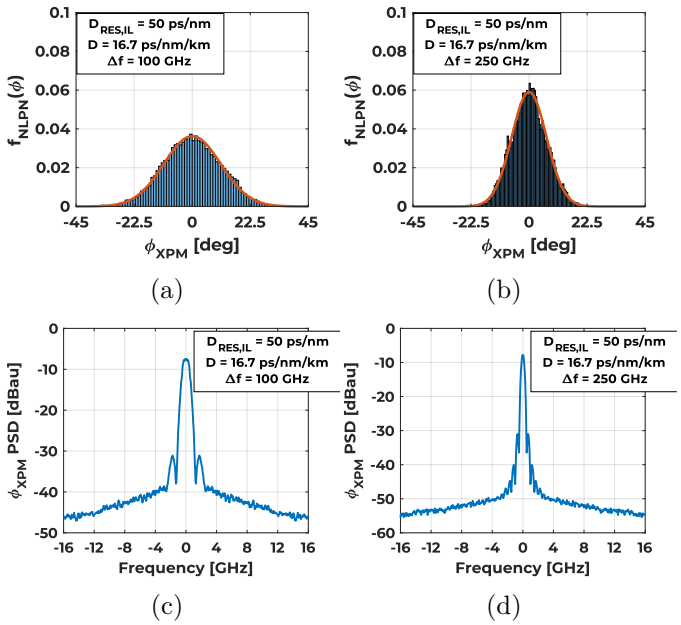

Figure 6.9: NLPN PDF with Gaussian fit (1st row) and PSD estimation (2nd row) extrapolated by SSFM simulations for a 20x span OLS with $D_{RES,IL}$ = 50 ps/nm, D = 16.7 ps/nm/km, originated by a single 10G pump at two sample frequency spacings of (a) 100 GHz and (b) 250 GHz.

is a narrowband process, with respect to the coherent symbol rate, so that it can be tracked by common CPE stages. It should be noted however that tracking may fail if the NLPN is so intense that cycle-slips happen and the CPE algorithm loses the lock to the phase. In such cases, differential decoding is known to help [72], and can be applied in this mixed transmission context.

Regarding the intensity of the accumulated NLPN, its amount can be obtained by single polarization SSFM simulations on the considered setup made up of $N_s = 20$ fiber spans by turning off the CPE stage. The NLPN process $\phi_{XPM}(t)$ can be extrapolated from the $E_R(t)$ and $E_T(t)$ obtained by SSFM simulation, so that its intensity is evaluated as described in Eq.3.10. The NLPN process is extracted as the ratio between the received and the transmitted 100G signals, under the XPM generated by a single 10G pump placed at increasing frequency spacing in the 50 GHz grid, then its variance is calculated. We indicate here the so calculated intensity of the NLPN process $\phi_{XPM}(t)$ as $\sigma^2_{\phi XPM}$ for simplicity. The aforemention NLSE-based SSFM simulation campaign lets us to study the spatial accumulation of the NLPN, with an approach similar to the one pursued in chapter 4. In a spatial incoherent approach, by receiving the signal at the end of each span, we evaluated the intensity (i.e. the variance) of accumulated NLPN until the n-th span and generated by the k-th 10G pump $\sigma^2_{\phi XPM,n,k}$, thus placed at $\Delta f = k\Delta_{WDM}$ GHz from the coherent probe on the $\Delta_{WDM} = 50$ GHz grid. Then, we calculate

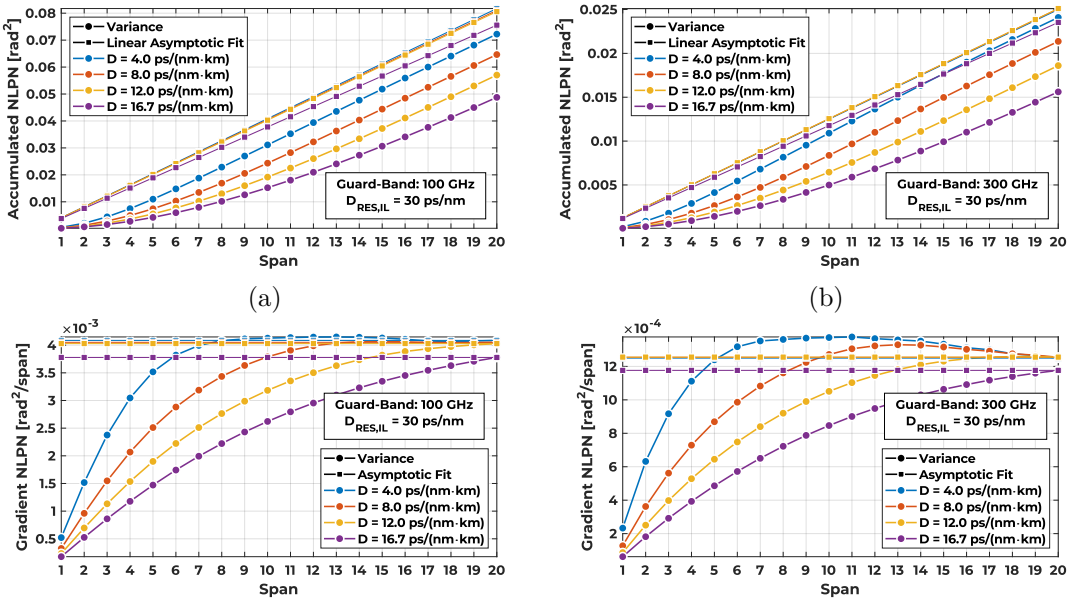

Figure 6.10: NLPN accumulation (1st row) and gradient (2nd row) on a OLS with $D_{RES,IL} = 30$ ps/nm for pump and probe spaced 100 GHz (Left column) and 300 GHz (Right column)

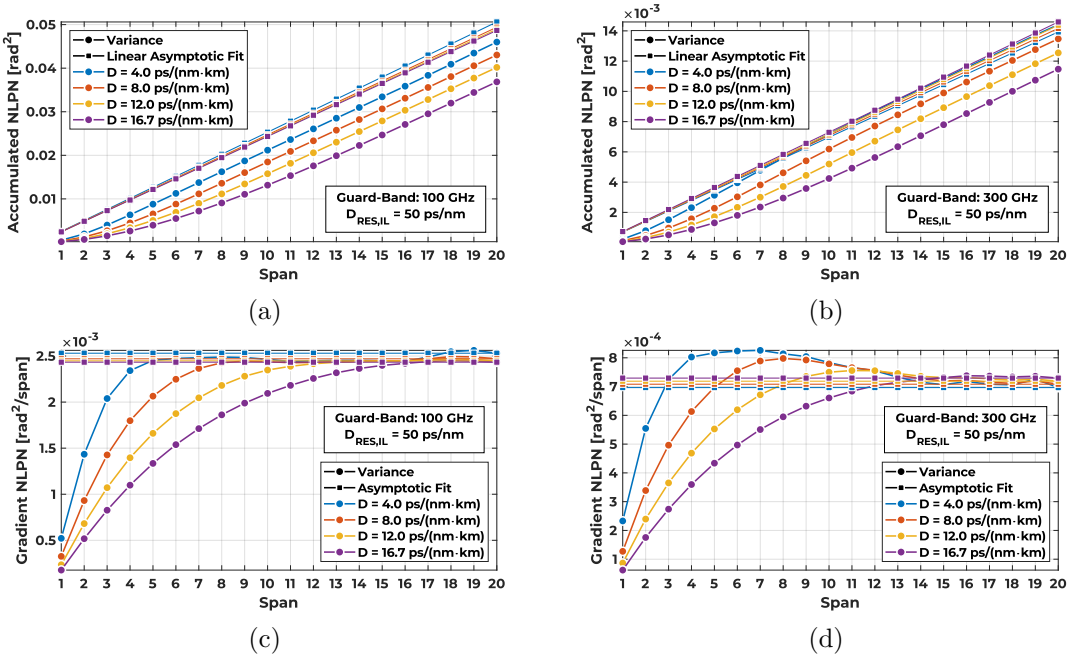

Figure 6.11: NLPN accumulation (1st row) and gradient (2nd row) on a OLS with $D_{RES,IL} = 50$ ps/nm for pump and probe spaced 100 GHz (Left column) and 300 GHz (Right column)

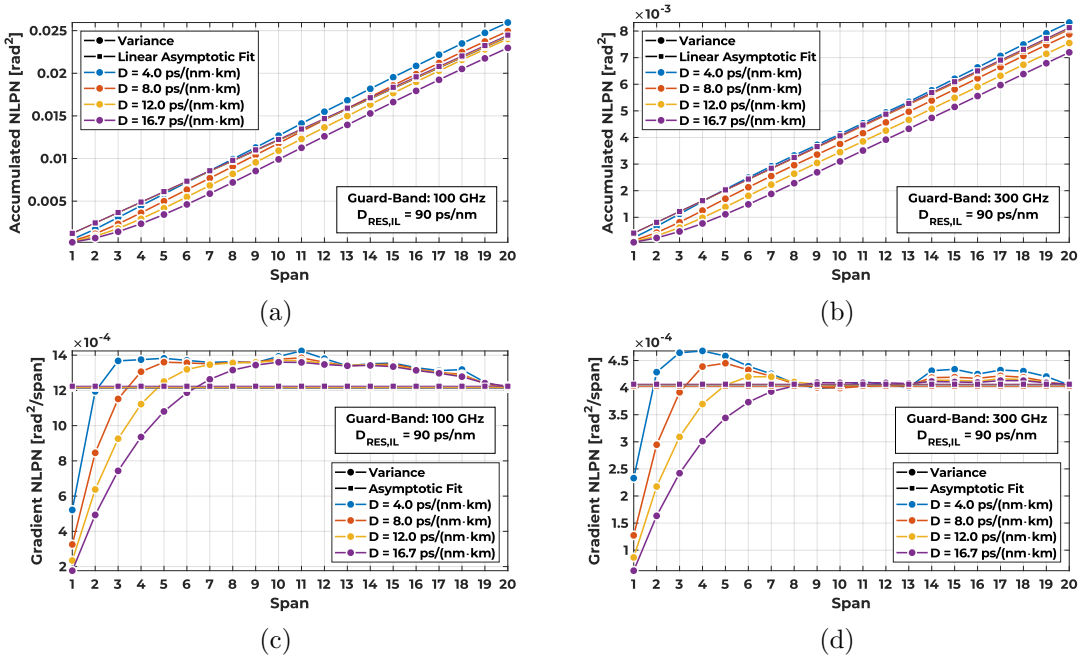

Figure 6.12: NLPN accumulation (1st row) and gradient (2nd row) on a OLS with $D_{RES,IL} = 90$ ps/nm for pump and probe spaced 100 GHz (Left column) and 300 GHz (Right column)

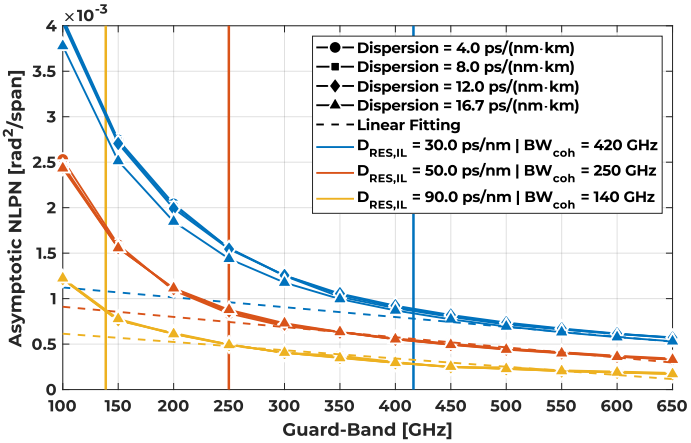

Figure 6.13: Pump and probe asymptotic NLPN per span vs guard-band, dispersion coefficient and inline residual dispersion

the NLPN gradient $\Delta\phi^2_{XPM,n,k}$, i.e. the amount of NLPN introduced by the n-th span and k-th pump, as:

$$\Delta\phi^2_{XPM,n,k} = \sigma^2_{\phi XPM,n,k} - \sigma^2_{\phi XPM,n-1,k} \tag{6.4}$$

In Fig.6.10,6.11,6.12 (c,d) we have plotted a subset NLPN gradient for $D_{RES,IL}$ of 30, 50, 90 ps/nm, respectively. The main finding is that, after a transient

depending on the fiber chromatic dispersion coefficient, the NLPN gradient converges substantially to the same asymptotic value. The transient length elongates at smaller residual, presumably due to the longer walk-off, encompassing even almost the whole considered OLS at $D_{RES,IL} = 30$ ps/nm. The transient is instead strongly dependent on the fiber chromatic dispersion, which also determine in some cases whether the NLPN gradient becomes larger than the asymptotic value before reaching it, so that the asymptotic value is not always conservative.

Fig.6.10,6.11,6.12 (a,b) report the corresponding accumulated NLPN, together with the linear fit obtained using the asymptotic amount of NLPN per span. In all the cases, after a transient, the NLPN growing is substantially linear. This enables a spatially incoherent estimation for NLPN: the amount of accumulated NLPN can be approximated span by span, without apriori knowledge of the whole OLS, by the asymptotic fit. Although is not always conservative with respect to the transient spans, the non conservative sections are somewhat balanced by the first spans where the asymptotic NLPN is quite conservative with respect to them. These peculiarities can be also seen by plotting the asymptotic NLPN behavior vs the frequency distance between the 100G probe and a 10G pump, as in Fig.6.13. The NLPN intensity does not depend on the absolute value of the fiber span chromatic dispersion but only on the amount of residual inline dispersion $D_{RES,IL}$. In addition, we can notice that, for each value of $D_{RES,IL}$, the decay with the frequency spacing Δf becomes linear when exceeding the guard-band BW_g after which the walk-off exceeds a 10G bit duration, as calculated by Eq.6.1.

6.4 Modeling the Mixed 10G-100G XPM

As showed in section 6.2 however, the NLPN analysis in single polarization do not encompass the total XPM impairment originated by 10G, since is the polarization effects interplay with non-linearities which determine the main QoT noise degradation. We then want to develop an analytical model estimating conservatively the amount of this degradation. We first start adapting the OLS abstraction for the 100G channel introduced in chapter 2 with Eq.2.23. As depicted in Fig.6.14, Eq.2.23 can be specialized for a 100G in mixed transmission expanding the non-linear contributions in SNR_{NL} with: an SNR_{NLI} contribution due to the NLI of the 100G comb alone in DM OLS and a $SNR_{NL,10G}$ contribution due to the 10G-to-100G XPM which is the target of our study. The OSNR is still determined by the optical amplifiers' ASE noise as usual:

$$\frac{1}{GSNR} = \frac{1}{OSNR} + \frac{1}{SNR_{NLI}} + \frac{1}{SNR_{NL,10G}} \tag{6.5}$$

SNR_{NLI} includes the non-linear noise generated by the propagation of the 100G channels comb on itself, thus encompassing the 100G SPM and the XPM of the

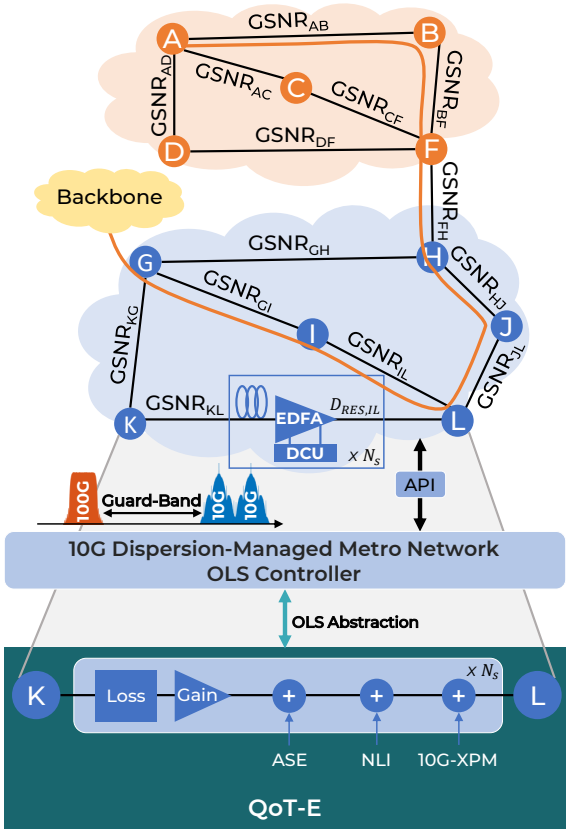

Figure 6.14: Physical layer abstraction for QoT estimation and path computation on mixed 10G-100G transmission. With respect to the general Fig.2.9 model also the 10G noise source is present.

100G channels on the 100G CuT. As previously mentioned, this contribution is well-known and addressed [44, 47] for propagation on an uncompensated network, instead should be more deeply investigated in DM OLS and it will be the object of further studies. Approximating the solution of the CNLSE thoroughly taking into account the random birefringence and the consequent evolution of the SOP determining the non-linear crosstalk intensity between pump and probes, would require a complex derivation [20]. From a networking perspective, it might be more useful to develop a simpler, worst-case abstraction aimed at planning and control of 100G lightpaths in mixed scenarios which allows a spectrally disaggregated and spatially incoherent approach to the phenomenon.

As already mentioned, the XPM manifests as a multiplicative NLPN component and an additive noise component due to the polarization coupling effects [156]. However, we have shown in previous section that practical DSP-based receivers are able to compensate the XPM NLPN [157] since it is a narrowband effect, so that the whole *residual* XPM effect is included in the $\mathrm{SNR}_{\mathrm{NL,10G}}$ within the GSNR. As a consequence, the OLS abstraction provided to the SDN controller can be updated

for the 10G-100G mixed transmission (Fig.6.14) and can be used to to set a proper guard-band between 10G and 100G to keep under control the QoT degradation or to set the optimum amplifier working point.

The $\mathrm{SNR}_{\mathrm{NL,10G}}$ is due to the additive noise contribution arising from the XPM and birefringence interaction, together with the XPolM SOP-diffusion. Its entity thus depends on the relative polarization angle Ω between the polarized 10G channels and the 100G channel independently-modulated polarization components, as depicted in Fig.6.5a. Also, it depends on the evolution of the polarization rotations induced by *stochastic* birefringence, which randomly couples the two 100G polarization states. Fig.6.5b briefly describes this concept: fiber can be thought as a sequence of random birefringent sections each introducing a random polarization rotation, i.e. the birefringence axes and magnitude change randomly with the z propagation direction. To fulfill the spectral and spatial disaggregation requirements, we propose a simple modeling approach assuming that the stochastic birefringence-induced polarization rotations couples the NLPN written by the 10G on the 100G x and y components in an additive noise crosstalk.

In order to do this, we generalize the multiplicative NLPN for single-polarization of Eq.6.2 to the dual polarization case as in Eq.6.6:

$$\mathbf{E}_R(t) = \mathbf{\Phi}(t) \cdot \mathbf{R} \cdot \mathbf{E}_T(t) \tag{6.6}$$

$$\mathbf{\Phi}(t) = \begin{bmatrix} e^{j\phi_{XPM,x}(t)} & 0 \\ 0 & e^{-j\phi_{XPM,y}(t)} \end{bmatrix} \tag{6.7}$$

$$\mathbf{R} = \begin{bmatrix} \cos\theta e^{j\psi} & -\sin\theta e^{-j\psi} \\ \sin\theta e^{j\psi} & \cos\theta e^{j\psi} \end{bmatrix} \tag{6.8}$$

where $\mathbf{E}_R(t) = [E_{Rx}(t), E_{Ry}(t)]'$, $\mathbf{E}_T(t) = [E_{Tx}(t), E_{Ty}(t)]'$ are the Jones column vectors of the optical field at the output and input of a fiber span, respectively. $\mathbf{\Phi}(t)$ is the 2x2 unitary matrix of the NLPN process on the two polarization components written by a single 10G pump. We omit here for clarity the index of span n and of the 10G channel k. $\mathbf{R}$ is a unitary equivalent polarization rotation matrix with rotation θ accounting for random birefringence axes evolution [69, 119]. The product $\mathbf{\Phi}(t) \cdot \mathbf{R}$ can be seen as the fiber transmission matrix $T(t)$ responsible for NLPN and NLPN-polarization effects mixing. By reworking $\mathbf{\Phi}(t)$, $\mathbf{T}(t)$ can be rewritten as Eq.6.9:

$$\mathbf{T}(t) = \mathbf{\Phi}(t) \cdot \mathbf{R} = e^{j\bar{\phi}(t)} \cdot \begin{bmatrix} e^{j\Delta\phi(t)} & 0 \\ 0 & e^{-j\Delta\phi(t)} \end{bmatrix} \cdot \begin{bmatrix} \cos\theta e^{j\psi} & -\sin\theta e^{-j\psi} \\ \sin\theta e^{j\psi} & \cos\theta e^{j\psi} \end{bmatrix} \tag{6.9}$$

$$\begin{cases} \phi_{XPM,x}(t) = \phi_{XPM}(t) \cdot \cos\Omega \\ \phi_{XPM,y}(t) = \phi_{XPM}(t) \cdot \sin\Omega \end{cases} \tag{6.10}$$

$$\begin{cases} \bar{\phi}(t) = \dfrac{\phi_{XPM,x}(t) + \phi_{XPM,y}(t)}{2} \\ \Delta\phi(t) = \dfrac{\phi_{XPM,x}(t) - \phi_{XPM,y}(t)}{2} \end{cases} \tag{6.11}$$

As in [157, 156], $\Delta\phi(t)$ is a *differential* NLPN term depending on the initial relative polarization angle Ω between the k-th 10G pump and 100G channel, while $\bar{\phi}(t)$ is a *common mode* NLPN term which is the same for both signal polarization component. Regarding the $\phi_{XPM,x}(t)$ and $\phi_{XPM,y}(t)$ NLPN processes they are supposed to be Gaussian distributed, as shown in section 6.3, and obtained by distributing the amount of polarization-aligned NLPN observed in section 6.3 $\phi_{XPM}(t)$ accordingly to the relative polarization angle Ω. As depicted in Fig.6.15, at the end of each fiber span, we ideally receive the 100G probe with a DSP-based coherent receiver to look at the residual impairment until that point of the OLS.

The DSP processing on the coherent probe will basically estimate the time average $\langle \mathbf{T}(t) \rangle$ of the transmission matrix in Eq.6.9 and multiply $\mathbf{E}_R(t)$ by its inverse in order to compensate for polarization rotation and NLPN by means of adaptive equalizer and CPE algorithm. We then obtain the residual impairment on the received signal $\mathbf{T}_{res}(t)$ as the product of $\mathbf{T}(t)$ by its inverse time average,

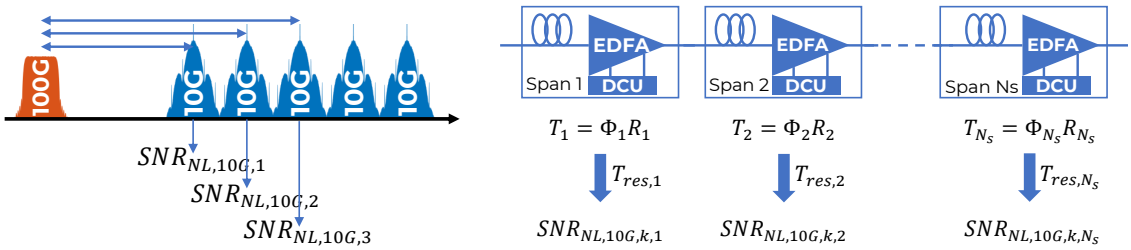

Figure 6.15: Model $\mathrm{SNR}_{\mathrm{NL,10G}}$ estimation assumptions for (left): Spectral disaggregation, (right): Spatial disaggregation.

which lets us have a look at the residual impairment after DSP:

$$\mathbf{T}_{res}(t) = \langle \mathbf{T}(t) \rangle^{-1} \cdot \mathbf{T}(t) = \tag{6.12}$$

$$e^{j\bar{\phi}_e(t)} \begin{bmatrix} \sin^2\theta e^{-j\Delta\phi_e(t)} + \cos^2\theta e^{-j\Delta\phi_e(t)} & -j\sin 2\theta \sin\Delta\phi_e(t) \\ j\sin 2\theta \sin\Delta\phi_e(t) & \sin^2\theta e^{-j\Delta\phi_e(t)} + \cos^2\theta e^{-j\Delta\phi_e(t)} \end{bmatrix}$$

In Eq.6.12, $\bar{\phi}_e(t) = \bar{\phi}(t) - \bar{\phi}_a(t)$ and $\Delta\phi_e(t) = \Delta\phi(t) - \Delta\phi_a(t)$. $\bar{\phi}_a(t)$ and $\Delta\phi_a(t)$ are the expectations of the *common mode* and *differential* NLPN terms random processes, respectively. The signal after the DSP processing $\mathbf{E}_{\text{DSP}}$ is thus given by the product of $\mathbf{T}_{res}(t)$ and $\mathbf{E}_R(t)$:

$$\vec{E}_{\text{DSP}} = \begin{cases} E_{\text{DSP},x} = T_{res,11} \cdot E_{Rx} + T_{res,12} \cdot E_{Ry} \\ E_{\text{DSP},y} = T_{res,22} \cdot E_{Ry} + T_{res,21} \cdot E_{Rx} \end{cases} \tag{6.13}$$

The first terms on Eq.6.13 are thus the useful signal on the considered polarization state, while the second are noise crosstalk terms originated by the opposite polarization components and depending on the antidiagonal element of $\mathbf{T}_{res}(t)$. Hence, they define the $\text{SNR}_{\text{NL,10G}}$ which can be easily obtained by calculating their power. Hence the $\text{SNR}_{\text{NL,10G},k,n}$ originated by the k-th 10G pump until the n-th span is given by:

$$\text{SNR}_{\text{NL,10G},k,n} = \frac{1}{\sin^2 2\theta_n E[|\sin\Delta\phi_{e,k,n}(t)|^2]} \tag{6.14}$$

Note that in Eq.6.14 we have reinserted the index relative to the 10G pump and the span. The angle θ_n is an equivalent polarization rotation due to birefringence relative to the n-th span which can be set to the worst-case value of 45° to stay conservative. $\Delta\phi_{e,k,n}(t)$ the differential NLPN of the k-th pump accumulated until the n-th span.

As already proposed in [156], we use the worst-case polarization-aligned simulations to obtain the $\phi_{XPM}(t)$ variance, from which we calculate the $\Delta\phi(t)$ with Eq.6.9. In particular, the asymptotic NLPN variance can be used to estimate the accumulated differential NLPN term and the crosstalk noise, so that the estimation is also spatially disaggregated. The $\text{SNR}_{\text{NL,10G}}$ at the end of the OLS is calculated as in Eq.2.27 with inverse SNRs. This enables the estimation of the $\text{SNR}_{\text{NL,10G},k,n}$ independently on the previous spans crossed, that is, neglecting the transients shown in section 6.3. From Eq.6.14, when the 10G pump is aligned with the X or Y polarizations of the 100G probe, the NLPN differential term is maximum, otherwise, the initial polarization-aligned NLPN is split between the two X and Y 100G polarization components accordingly to simple sine/cosine relationships. Using Eq.6.14 together with Eq.2.26,2.27 gives a very simple and fast estimation of the $\text{SNR}_{\text{NL,10G}}$ degradation of a single fiber span, which sums up with the inverse SNR relationship over a complete multi-span OLS and N_p 10G channels.

6.5 10G-100G Transmission Model Validation

In this section we compare the $\mathrm{SNR}_{\mathrm{NL,10G}}$ estimation of Eq.6.14 with the results obtained by SSFM Monte-Carlo simulation campaign on the setup of Fig.6.6 to validate the model predictions. This is similar to the setup used to obtain the $\mathrm{SNR}_{\mathrm{NL}}$ estimations presented in Fig.6.7 accordingly to Table 6.1. We remind that the OLS is a 20x 50 km long fiber spans with loss $\alpha_{dB} = 0.18$ dB/km, non-linear coefficient $\gamma = 1.27$ 1/W/km. Here however, we have tested chromatic dispersion coefficients of $D = 4.0$ ps/nm/km and $D = 16.7$ ps/nm/km. Optical amplifiers are also noiseless, so that the GSNR estimated by the DSP corresponds to the $\mathrm{SNR}_{\mathrm{NL,10G}}$ alone in Eq.6.5. 100G probe channel is PM-QPSK modulated at $R_s = 32$ GBaud. At the DSP is received by an LMS equalizer with $N_{taps} = 42$ taps followed by a Viterbi-Viterbi [162] CPE stage recovering NLPN.

The dispersion maps under test are still $\mathrm{D}_{\mathrm{RES,IL}} = 30, 50, 90$ ps/nm for both the fiber dispersion considered. The interfering 10G comb is still made of $N_p = 5$ channels placed with a guard-band BW_{g} from the probe. For each value of dispersion and inline residual, we have however tested all the guard-band values reported in Table 6.1. Among the dispersion maps, the one leaving nearly $\mathrm{D}_{\mathrm{RES,IL}} = 50$ ps/nm is the most common value in deployed DM systems, the others at $\mathrm{D}_{\mathrm{RES,IL}} = 30$, 90 ps/nm take into account realistic deviation from the nominal residual and potential overcompensation due to DCU granularity or additional dispersive elements such as filters.

For each case the model estimation has been evaluated in two ways: one is the fully spatially and spectrally disaggregated approach, using the asymptotic NLPN variance for the $\mathrm{SNR}_{\mathrm{NL,10G}}$ estimation, the other is the spectrally disaggregated only approach, which employs the span-by-span NLPN gradient to accumulate the $\mathrm{SNR}_{\mathrm{NL,10G}}$, thus accounting for the NLPN transients seen in section 6.3 for the calculation of Eq.6.14. We have set $\Omega = 22.5°$ as the 100G-10G relative polarization angle for the distribution on x and y components of the single polarization NLPN (Eq.6.9), which heuristically delivered more accurate estimations with respect to Monte-Carlo simulations.

The results are reported in Fig.6.16 Fig.6.17 and Fig.6.18 for $\mathrm{D}_{\mathrm{RES,IL}} = 30$ ps/nm, $\mathrm{D}_{\mathrm{RES,IL}} = 50$ ps/nm and $\mathrm{D}_{\mathrm{RES,IL}} = 90$ ps/nm, respectively, together with the gap between the modeling tool result and the simulated PDF worst-case $\mathrm{SNR}_{\mathrm{NL,10G}}$.

The estimation scales correctly with the guard-band between the 100G probe and the 10G comb and the inline residual dispersion, although the gap increases at larger guard-bands and dispersion coefficients. However, the model is always conservative, thus letting operation of the lightpath always in the safe side and avoiding out of service when employed in network context. The conservativity gap gets also larger when considering the fully-disaggregated approach, simply because it ignores the NLPN transients. The independence of the results on dispersion coefficient of

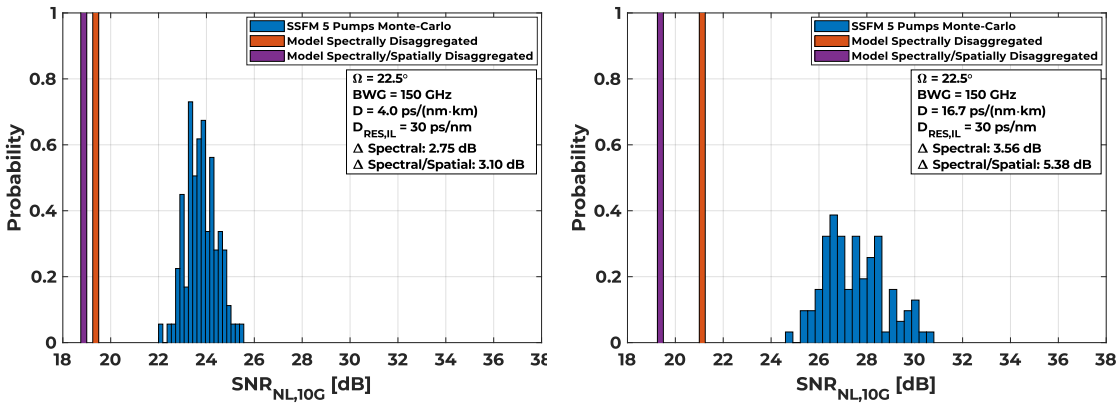

(a)

(b)

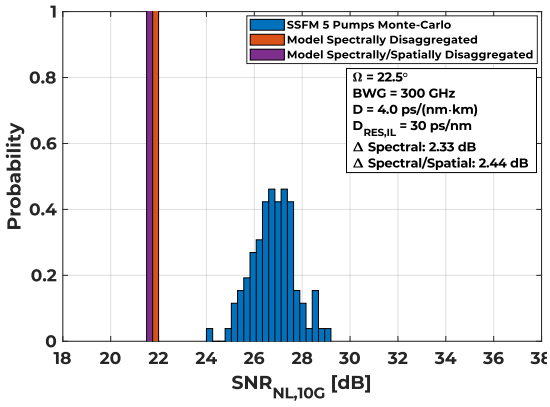

(c)

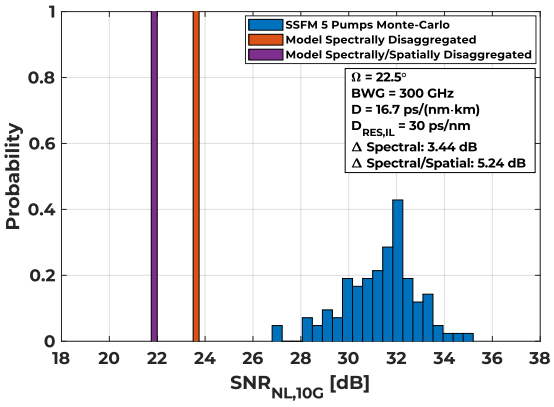

(d)

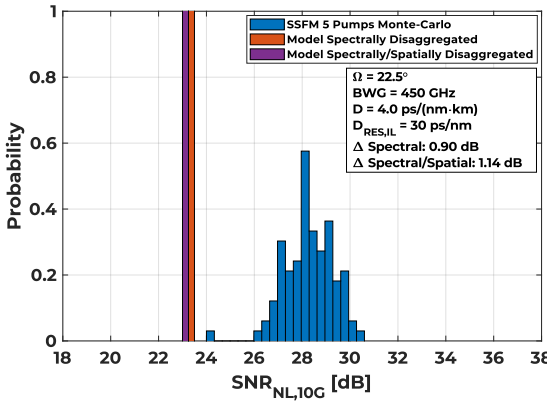

(e)

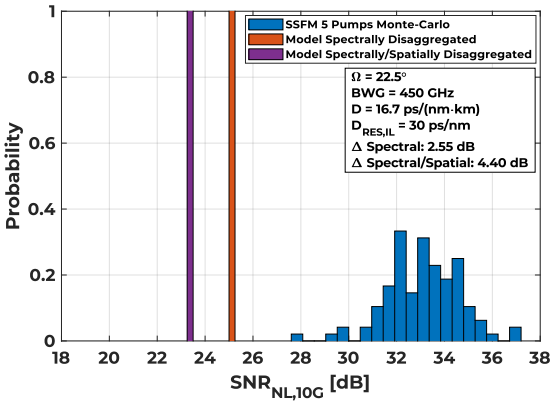

(f)

Figure 6.16: Model vs CNLSE-based SSFM Monte-Carlo simulations with N_p = 5x 10G pumps for an OLS with $D_{RES,IL}$ = 30 ps/nm: D = 4 ps/nm/km (left column), D = 16.7 ps/nm/km (right column). Guard-Band 150 GHz (1st row), 300 GHz (2nd row), 450 GHz (3rd row).

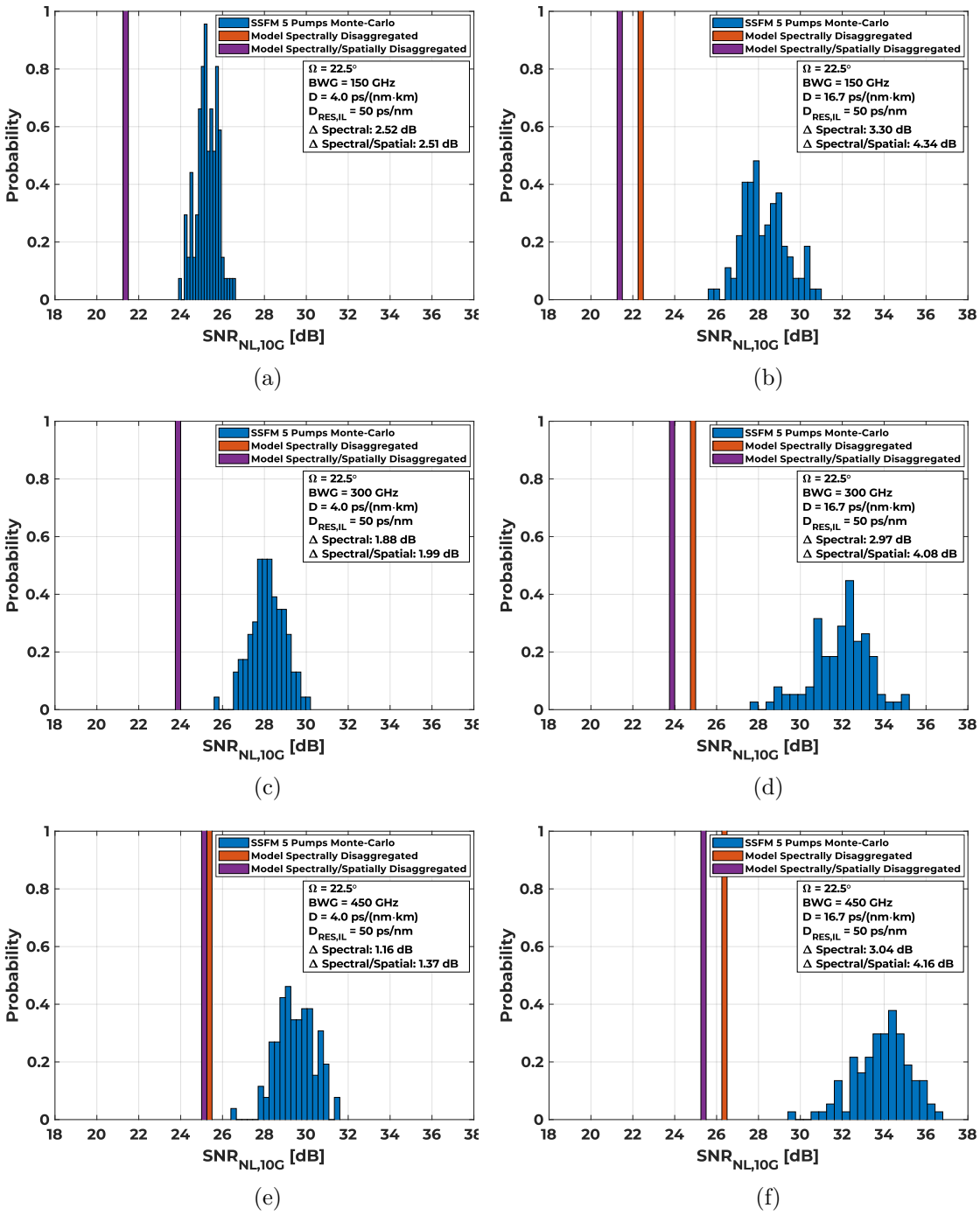

Figure 6.17: Model vs CNLSE-based SSFM Monte-Carlo simulations with N_p = 5x 10G pumps for an OLS with $D_{RES,IL}$ = 50 ps/nm: D = 4 ps/nm/km (left column), D = 16.7 ps/nm/km (right column). Guard-Band 150 GHz (1st row), 300 GHz (2nd row), 450 GHz (3rd row).

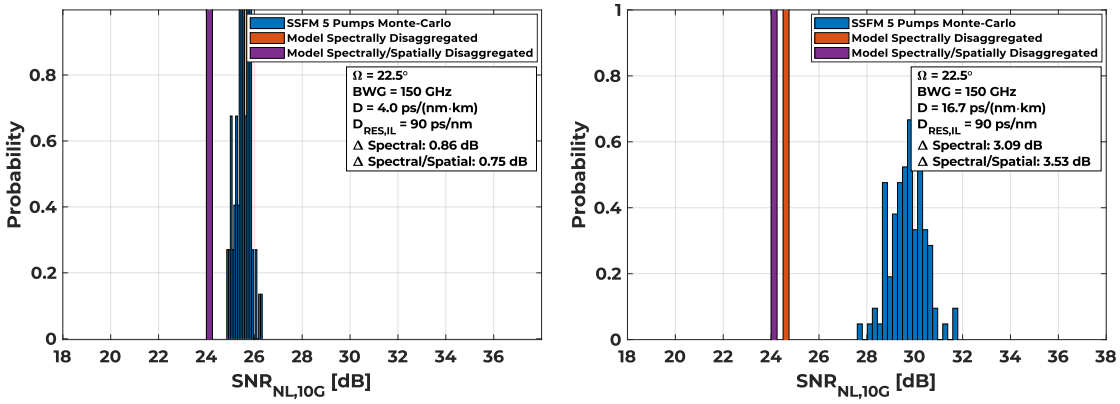

(a)

(b)

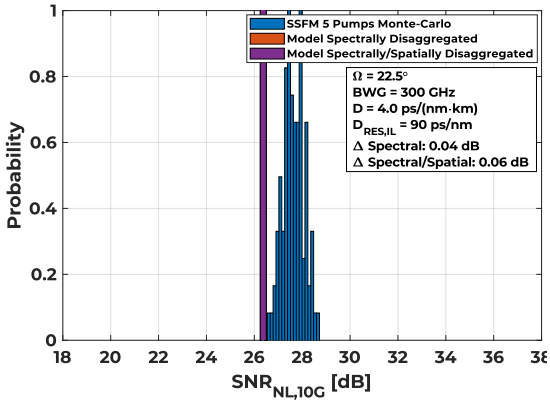

(c)

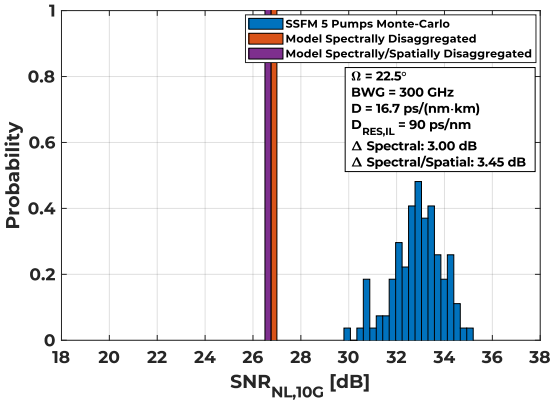

(d)

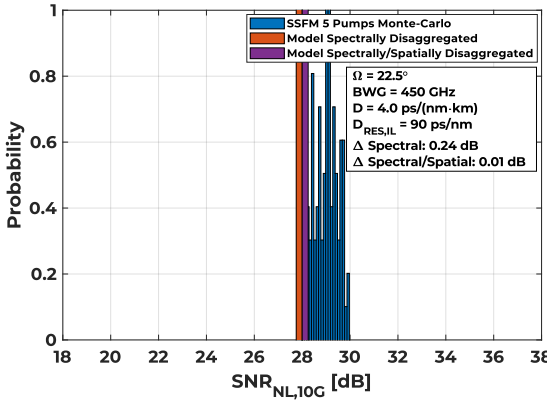

(e)

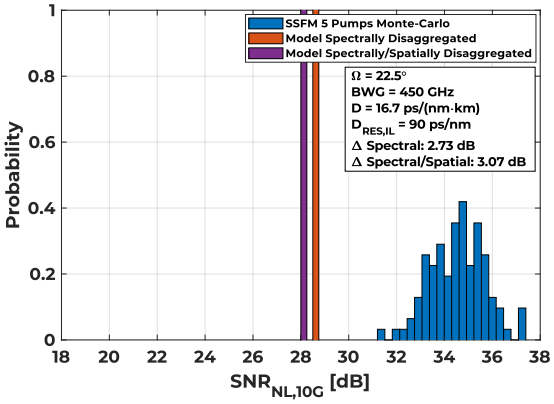

(f)

Figure 6.18: Model vs CNLSE-based SSFM Monte-Carlo simulations with N_p = 5x 10G pumps for an OLS with $D_{RES,IL}$ = 90 ps/nm: D = 4 ps/nm/km (left column), D = 16.7 ps/nm/km (right column). Guard-Band 150 GHz (1st row), 300 GHz (2nd row), 450 GHz (3rd row).

the fully-disaggregated model is a direct consequence of the same independence of asymptotic NLPN per span of Fig.6.13. In fact, using the asymptotic NLPN value, on one side ignores the different transient dispersion coefficient dependent, on the other side, however, enables spatial disaggregation and thus a fast and simple QoT estimation and path computation.

As for the estimation accuracy with respect to SSFM simulations worst case, we get a maximum gap of 5.38 dB, 4.34 dB and 3.53 dB for $D_{RES,IL} = 30, 50, 90$ ps/nm, respectively. In particular, the largest gap of 5.38 dB holds in the $D_{RES,IL} = 30$ ps/nm with $D = 16.7$ ps/nm/km and with the both spatially and spectrally disaggregated version of the model. The asymptotic NLPN gradient is used, in this case, for the calculation of the model (Eq.6.14). From Fig.6.10c is clearly visible that low $D_{RES,IL}$ and large D give the slowest convergence along the OLS towards the asymptotic NLPN. Hence, the inaccuracy is exaggerated by the overestimation of the actual NLPN transient using the asymptotic value. The spatially aggregated version of the model - using the actual NLPN increments instead of the asymptotic - in fact, improves the accuracy by nearly 2 dB.

It should be noted that, although it can seem quite large, this margin is not the overall GSNR margin but only with respect to the inter-channel component between the 100G and 10G non-linearities on the DM OLS. Hence, the overall conservativity gap should be also seen by including the SNR_{NLI} component of Eq.6.5, which will be presumably stronger or comparable, since it involves the self channel effects and the XPM of adjacent 100G channels to the probe, thus decreasing the weight of the lack of accuracy of this 10G-to-100G XPM components in the overall GSNR estimation.

6.5.1 Experimental Validation

A final validation of the analytical model has been also carried out experimentally in collaboration with the laboratories of SM-Optics in Vimercate. The goal was to estimate, in a real experimental setup, the 10G-to-100G XPM noise and compare the experimental values with the SNR PDF estimated by DP-CNLSE-based Monte-Carlo simulation and with the model estimation in the both spatially and spectrally disaggregated approach. The OLS was a 16x span with average span length of $L_s = 50$ km. The DCU were placed at every span leaving an average $D_{RES,IL} = 50$ ps/nm. Optical fibers were SSMF with $\alpha_{dB} = 0.2$ dB/km, $\gamma = 1.27$ 1/W/km and dispersion coefficient $D = 16.7$ ps/nm/km.

With respect to the spectral load, a single 100G probe PM-QPSK modulated at $R_s = 32$ GBaud was launched. The 10G comb was made up of $N_p = 12$ channels, placed after a guard-band of $BW_g = 100$ GHz from the probe. In the experimental setup all the channels were launched in fiber with $P_{ch} = -1$ dBm. The SSFM DP-CNLSE Monte-Carlo simulation, averaging the birefringence over $N_{MC} = 100$ realizations with $\delta_{PMD} = 0.1\text{ps}/\sqrt{\text{km}}$, has been done setting $P_{ch} = -20$ dBm in

the probe to isolate the XPM effects and avoid self-channel effect and $P_{ch} = -1$ dBm for the pumps. The relative polarization angle Ω between each of the 10G pumps and the 100G probe has been set randomly in order to emulate the random 10G transceiver polarization state when launched in fiber. SSFM results have been obtained using the DSP-based receiver employed in the previous section, with optimized CPE to recover residual NLPN. On the experimental side, the 100G channel has been deployed using both *differential* and *non-differential* encoding, in order to check also their tolerance to NLPN. The estimated PDF obtained by Monte-Carlo SSFM campaign, the experimental values and the worst-case model predictions have been reported in Fig.6.19.

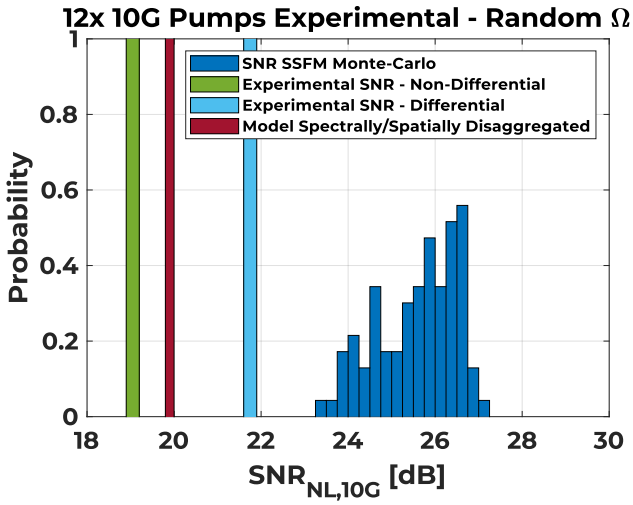

(a)

Figure 6.19: $\mathrm{SNR}_{\mathrm{NL,10G}}$ at the end of the experimental 16x span OLS setup for a 12x 10G pumps configuration, placed at $\mathrm{BW_g} = 100$ GHz from the probe. Spectrally and spatially disaggregated model estimation are reported, together with the $\mathrm{SNR}_{\mathrm{NL,10G}}$ PDF estimation by means of CNLSE-based SSFM campaign with random relative polarization Ω and $\delta_{\mathrm{PMD}} = 0.1\,\mathrm{ps}/\sqrt{\mathrm{km}}$

The experimental $\mathrm{SNR}_{\mathrm{NL,10G}}$ values reported are 19.16 dB and 21.74 dB for the non-differential and differential encoding, respectively.

The model prediction stood on 19.82 dB, thus reporting a gap of 0.66 dB and -1.92 dB to the experimental values. The model prediction stays in the middle between the two encoding techniques results, being conservative only with respect to the differential encoding. Such different behavior can be explained with the fact that the differential encoding is far more robust with respect to cycle-slips [73, 72], since with a guard-band as small as of 100 GHz the NLPN component is presumably so intense to trigger them. Consequently, the non-differential QoT measured could be so decreased because of error bursts that are due to the CPE losing the track on the phase. In this case the NLPN cannot be correctly recovered and the fundamental hypothesis of our abstraction - the GSNR being the unique

QoT figure - does not hold anymore. However, we have not been able to check the experimental scattering diagram to prove this, although the roughly 3 dB large difference between the two encoding schemes seems to go towards this direction.

It should be also mentioned that the experimental $\mathrm{SNR}_{\mathrm{NL,10G}}$ estimation are also prone to inaccuracies. They are in fact obtained indirectly as differential measures, using the inverse SNR relationship, from OSNR observations in single/multi channel and in linear and non-linear regime. This also may explain the penalty of the differential value with respect to the 23.9 dB obtained as the worst case of the SSFM campaign. With respect to it, the disaggregated model prediction shows a 4.08 dB gap, which is consistent with the previously reported validation with extensive SSFM campaigns. Although it would be interesting to experimentally test the model in cases where it is less conservative, such as with lower dispersion fibers; the presented experimental result showing about 2 dB overestimation would be acceptable in the overall GSNR computation ensuring margin to operate lightpaths robustly in a networking scenario.

Chapter 7

Optimized Power Control in Multi-Band C+L Line Systems

In this chapter we present the results of SSFM-based simulations performed on a multi-band transmission setup exploiting the extended spectrum of the C+L bands, populated with coherent channels only and propagated on a DU OLSs. The motivation of this analysis is associated to the establishment of a simplified power optimization strategy in the context of seamless upgrades from a single C-band solution to C+L multi-band transmission.

In the following sections, We will first briefly report the motivations supporting the deployment of C+L systems. In order to keep under control the intense SRS arising in this situation, we propose our band-wise approach power optimization strategy. We then report the results of time consuming SSFM simulations over 10+ THz, showing that it is possible to decouple the L-band power optimization from the C-band with limited penalty, thus allowing a easier planning and deployment of multi-band upgrades of existing single-band systems.

7.1 C+L Systems Motivations and Criticalities

As previously discussed in chapter 1, the development of transparent coherent optical systems has provided an answer to the growing capacity demand [36], spurred by innovations in cutting-edge end-user services such as 5G-enabled networking [155, 126] and cloud computing solutions [153], along with traffic challenges arising from the COVID-19 era. Such capacity increase, over the last years, has been obtained by pushing towards advanced modulation techniques and improved DSP solutions enhancing the spectral efficiency on the 4.8 THz of the C-band, which has been traditionally employed because of its minimum of attenuation in the optical spectrum. State-of-the-art coherent transceivers allow up to $N_{ch} = 64$x 400G-ZR+ WDM channels in the $\Delta_{WDM} = 75$ GHz WDM grid covering distances

of hundreds of km, thanks to PM-16-QAM modulation at $R_s = 64$ GBaud. However, the capacity growth enabled by further improvements of the transponder side [170] will not be enough to cope with capacity request growth rate, so that other solutions must be explored.

To tackle this capacity problem, spatial division multiplexing (SDM) and band division multiplexing (BDM) have been proposed as capacity scaling strategies. In its simplest form, SDM stands for the deployment of new fibers or lighting up of existing dark fibers establishing new spatial channels. On the other side, BDM extends the transmission bandwidth on operating fibers from the traditional C-band to, at least, the L-band. While C+L band commercial solutions are already available [97, 96, 23], further extension to S-Band and beyond is under investigation [37].

From a networking perspective, both SDM by fiber doubling and BDM with C+L transmission deliver twice the traffic offered by current single-band systems, with a limited penalty of the C+L systems due to extended bandwidth QoT degradation and routing constraints [158, 129, 61]. At the same time, BDM represents a more convenient solution since it avoid the costly deployment of new fibers, thus maximizing the return of investment on the deployed infrastructure because of the more efficient exploitation of available and already used fibers [23]. This becomes even more attractive in case of shortage of dark fibers to light up.

We will here focus on the BDM upgrade of deployed single-band systems to C+L multi-band scenario. For this upgrade, the addition of transceivers and ILAs tailored to L-band represent the largest CAPEX requirement. The availability of L-band amplifiers has enabled C+L systems with bandwidths up to 10 THz, at least for terrestrial long-haul segments [23]. However, this expanded capacity comes with a cost in terms of propagation impairments. On one side, the frequency dependence of the fiber attenuation and chromatic dispersion (the dispersion slope β_3) may become significant. However, limiting the upgrade to the L-band still keeps these aspects on the back burner. Their significance becomes indeed stronger when considering the lower wavelength region around S and O band, due to the absorption waterpeak and the zero-dispersion wavelength.

As already mentioned in chapter 2, the extension to such large bandwidths makes instead SRS significant due to the power transfer from higher- to lower-frequency channels (from C- to L-band) and its interaction with NLI noise generation must be considered. In fact, due to the SRS power transfer, the accumulation figure of the NLI changes with propagation, ending up with a spectral tilting of the $\mathrm{SNR}_{\mathrm{NL}}$ contribution. Furthermore, on the linear ASE noise part, the OSNR presents also spectral tilt due to the different noise figures in C and L bands and also due to the frequency dependence of the accumulated loss to recover when the OLS is operated in transparency. Consequently, in a multi-band scenario, more complex power control strategies are required to maintain the desired QoT. In absence of SRS indeed, one can reasonably assume a spectrally flat optimum channel power,

accordingly to the classic LOGO strategy based on GN model [4, 108, 114]. When considering instead the mentioned frequency variations of the QoT figures, an absolute optimal configuration of the launched power thus exists for each spectral configuration. However, from a networking perspective, this raises a huge complexity issue, since every channel should be reconfigured every time a new lightpath gets deployed. It is then crucial to overcome this problem by developing strategies on both the sides of the QoT computation and of the optical system's practical operation. The optical system could be kept on a steady state by filling the portion of the spectrum which are not occupied by deployed channels with shaped ASE noise. Accordingly, on the QoT estimation side for control and path computation, the QoT is evaluated in the spectral worst-case scenario, i.e. assuming full spectral load.

Within this work we assume a partially disaggregated networking scenario, where reconfigurable optical add-drop multiplexer (ROADM)-to-ROADM amplified optical lines may be independent OLSs. As showed in Fig.7.1, from the network management perspective, a power control unit (PCU) within the OLS controller separately sets the working points for the C- and L-band ILAs. The optimum working point is determined with the aid of a QoT-E implementing models taking into account the interplay between SRS and NLI generation.

On the modeling side, the GN-like models have been updated to consider this issue, such as with the generalized GN (GGN) model [21, 137]. The QoT-E evaluates the GSNR, encompassing contributions from both the ASE noise and the NLI [45]. We focus upon the problem of power optimization when upgrading from state of the art C-band only systems to C+L. As mentioned, since the lighting up of a new bandwidth may induce further QoT degradations of the existing one, we put the requirement that the previously deployed C-band must stay in-service with zero-touch on the existing power configurations. Due to the interplay between the bandwidths, in fact, a joint power optimization between the channels in L-band and the existing one in C-band should be done. We show that separately optimizing

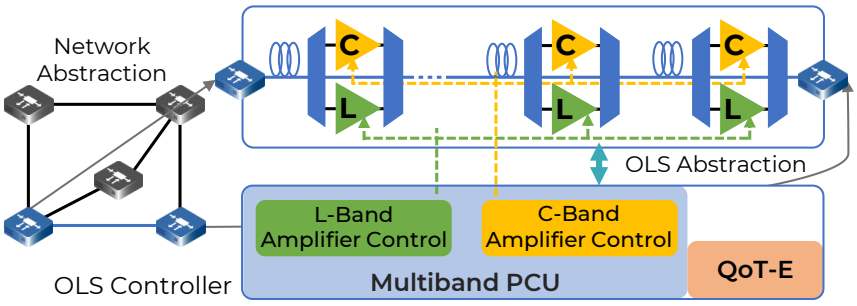

Figure 7.1: (a) Network and OLS representation of C+L transmission. The C- and L-bands are amplified by separate ILAs. The OLS controller implements a QoT-E module that calculates a (sub-)optimum power profile set by the PCU.

the C- and L-bands on a per-band basis enables extension to larger bands with a limited QoT penalty with respect to the optimal joint C+L multi-band power control.

7.2 OLS Setup and Power Optimization

As shown in chapter 4, the GSNR, given by Eq.2.22, is commonly employed as a unique figure for lightpath QoT [63], allowing contributions that arise from both linear and non-linear losses to be separately quantified. Even in presence of SRS, the GSNR can be separately expressed by means of its linear part, the OSNR and its non-linear part, the $\mathrm{SNR_{NL}}$, as in Eq.2.23, since SRS has effect on the frequency dependence of the constituent degradation sources. Note that assuming the full spectral load for the $\mathrm{SNR_{NL}}$ estimation, makes the spectral disaggregation property still holds.

In order to test the C+L upgrade delivered performance, we have carried out SSFM simulations on a DU OLS consisting of $N_s = 10$ identical spans of $L_s = 75$ km. Fibers are SSMF, with chromatic dispersions of $D = 16.7$ ps/nm/km and non-linearity coefficient $\gamma = 1.27$ 1/W/km. A more realistic fiber characterization has been accomplished implementing a frequency dependent loss coefficient obtained with a polynomial expansion in the 10 THz of the C+L bands, whose profile is is reported in Fig.7.2. The considered loss has a minimum of 0.188 dB/km at 192.6 THz and increases going towards the L-band lower frequencies. As shown in Fig.7.1, the C- and L-band are amplified by independent EDFAs using frequency-dependent noise figures on a per-channel basis. The noise figure values used within this work are obtained via characterization of real devices, with average values of 4.68 dB and 4.24 dB for the L- and C-bands, respectively. Each band is spectrally loaded with 64 channels, which are PM-16-QAM modulated with a symbol rate of $R_s = 64$ GBaud on the $\Delta_{WDM} = 75$ GHz grid, yielding a total of $N_{ch} = 128$ channels in the

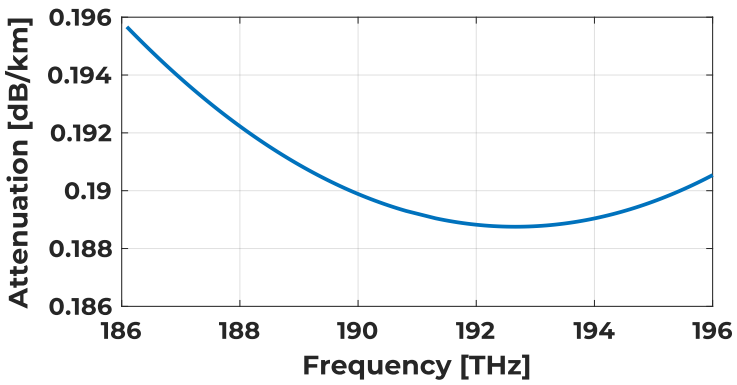

Figure 7.2: The frequency dependent loss coefficient α_{dB} [dB/km] used in SSFM simulations.

C+L scenario, each one delivering 400 Gbps. The C- and L-band channel combs are separated by a 500 GHz guard-band to avoid penalties due to band demultiplexing and separate amplification strategies.

To keep the impact of the SRS upon the GSNR under control, an optimization of the channel input power profile has been performed. As previously mentioned, the optimization has been done assuming full spectral load. It should be noted that it would be possible to derive a per-channel optimal power with accurate modeling of the SRS accumulation, as already proposed in literature [84, 125]. However, a precise per-channel optimization has some implications in the power management of existing traffic increasing complexity for QoT optimization. In addition, ILAs need to have both output power (or gain) and tilt set to correctly operate. Such tilt must be determined consistently with the frequency power profile evolution due to SRS and frequency dependent loss [160, 13]. Also, the amplifier gain response is dependent on the power profile at its input [48, 49, 14] and this needs to be taken into account for accurate management of ILAs.

As depicted in Fig.7.3, rather than determine the optimum launch power channel by channel, in this work we present a sub-optimum but simplified approach for power optimization. We apply a band-wise *power offset* and frequency *tilt* to each of the two band WDM combs to compensate for the tilt induced by propagation. Such tilt can be indeed practically set by most of the common commercial EDFA operating on the gain profile.

The criterion to obtain such offset and tilt is targeted to the QoT metric, i.e. the GSNR. The optimal power profile is thus the one both maximizing and flattening the GSNR of each band. Such profile optimization is performed following a brute force approach [158], iterating over a predefined space of offsets and tilts in C- and L- bands. Since the launch power profile is recovered by ILAs at the end of each of the N_s spans, the problem of finding the optimal offset and tilt values is reduced to the single span case.

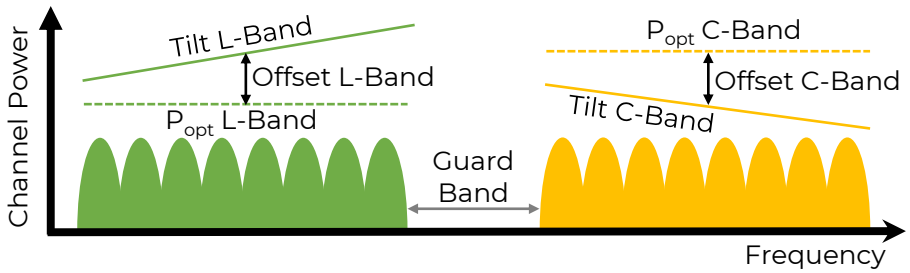

Figure 7.3: Representation of spectral load in C+L systems, with launch power offset and tilt used to compensate for SRS.

The Power Optimization Algorithm

The optimization procedure begins by finding a starting, spectrally flat, channel power. Such value is found using the classic LOGO strategy [107] and it is computed separately for each spectral band. Hence, it means basically to calculate the optimum power derived from GN model assuming no SRS and flat loss and noise figure in each band.

In our configuration, the classic LOGO approach yields $P_{opt} = -0.46\,\text{dBm}$ and $P_{opt} = -0.62\,\text{dBm}$ per channel for L- and C-bands, respectively. Next, each combination of power offset and tilt in the considered space are applied on each band using the LOGO value as an initial guess. The GSNR delivered by this power configuration is evaluated by means of the GGN model [21]. For each configuration, the average GSNR among all the CuTs is evaluated and all profiles within the top 1% are chosen and from these the profile with the optimal flatness value is selected.

In this study, we investigated tilt values varying from -0.4 to $0.4\,\text{dB/THz}$ with a granularity of $0.1\,\text{dB/THz}$ for both bands. The power offset values were varied from -1.0 to $2.0\,\text{dB}$ for the C-band and from -2.0 to $1.0\,\text{dB}$ for the L-band, both with a granularity of $0.5\,\text{dB}$. The optimization algorithm has been run on four different scenarios: First, the C- and L-bands were optimized independently, i.e., considering them as a single-band systems, with the former representing the typical state of an already deployed system which may be upgraded to a C+L-band scenario. We then considered C+L transmission in two cases: in the first, C- and L-bands are jointly optimized by assuming that there are no restrictions upon the tilt and offset values for either band. In the second (fourth overall) scenario, the C+L transmission is optimized with constrained tilt and offset values for the C-band: we retain the optimum single-band C-only power profile as previously set and we investigate the

Optimization	Offset [dB]		Tilt [dB/THz]		Avg. GSNR [dB]		Max. Δ from avg GSNR [dB]	
	L	C	L	C	L	C	L	C
C-only		0.0		0.3		20.75		0.09
L-only	0.0		0.3		20.40		0.12	
Joint C+L	-0.5	0.5	0.4	0.4	20.65	20.46	0.07	0.02
C+L, Fixed C	-0.5	0.0	0.4	0.3	20.59	20.21	0.09	0.05

Table 7.1: Table reporting the offset (dB difference from the LOGO power) and tilt (dB/THz) values obtained from the input power profile optimization algorithm for single-band (C-only, L-only) and multi-band cases (Joint C+L and the C+L case where the C-band profile is fixed). For each optimization profile the average GSNR per band and the maximum deviation from this value is reported.

optimum tilt and offset for L-band. This final scenario refers to a practical use case where the deployed C-band configuration must not be changed, meaning that the L-band upgrade must be performed seamlessly in order to avoid out-of-service on the deployed C-band lightpaths. The resulting optimum profiles are reported in table of Table 7.1. We note that L-band offset and tilt for both multi-band profiles are equal only incidentally. A finer granularity in the explored parameters could have potentially led to different values.

SSFM Simulation Details

As already mentioned, the optimization procedure relies on the GSNR estimated by the GGN model. The GGN model is able to deliver good estimation of QoT due to the NLI interplay with SRS. This is accomplished by giving it as input the gain loss profile $\rho(z, f)$, i.e. the surface describing the power evolution of the WDM signal in frequency and along the fiber length. The gain loss profile has been obtained by means of the *Raman solver* implemented within the GNPy tool [68, 59], which solves the differential equations governing the Raman effect power transfer [16] and include also the frequency dependent loss. Among the tested combinations, the $\rho(z, f)$ surfaces corresponding to the four optimum profiles are fed as input to perform SSFM simulations on these configurations with the results plotted in Fig.7.4.

SSFM simulations have been carried out using the Manakov equation, with $\Phi_{FWM} = 1$ radians. The gain-loss profile $\rho(z, f)$ is applied in the linear step together with dispersion. No dispersion slope β_3 has been taken into account. For each band, 7 out of 64 channels have been considered as CuTs and their QoT estimated. The remaining channels were Gaussian modulated. These CuTs are modulated by PRBS to the 16^{th} degree and are received by an LMS-based adaptive equalizer with $N_{taps} = 42$ taps and adaptation coefficient $\mu = 10^{-4}$, followed by a CPE stage based on the blind-phase-search strategy with an optimized length of $N_{CPE} = 16$ symbols.

7.3 SSFM Simulation Results

In Fig.7.4a we present the OSNR caused by the ASE noise: for all cases, its behavior depends mostly upon the fiber loss and less upon variations within the noise figure. In particular, the C+L scenario with fixed C-band optimization provides smaller OSNR due to a larger power transfer to the L-band, thus generating more ASE noise as a consequence of the larger needed gain for transparency. The penalty with respect to single C-band case is instead much smaller with the joint C+L optimization because it minimizes the SRS power transfer thanks to the flexibility in the C-band power offset and tilt setting.

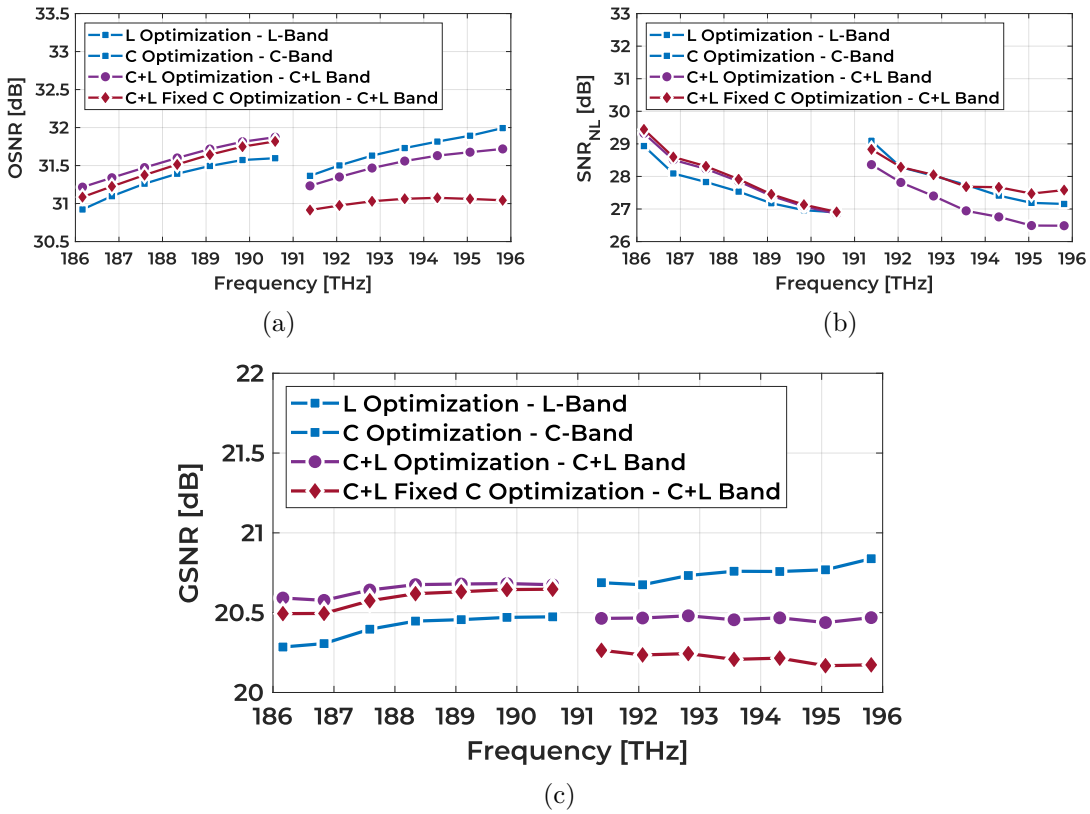

Figure 7.4: The QoT metrics for 10 spans of $L_s = 75$ km of SSMF OLS, with 7 CUTs per band: (a) OSNR (b) SNR_{NL} (c) GSNR vs channel frequencies.

The SNR_{NL} contribution due to NLI is shown in Fig.7.4b: The single C-band and single L-band cases are substantially identical, since their spectral load is the same and the dispersion slope is neglected. Some negligible differences in the GSNR of the extremes channels are due to the slightly different attenuation value experienced by the CuTs in the two bands, which impacts the NLI through the fiber effective length.

Going to the multi-band scenarios, the L-band performance are slightly improved because of the negative power offset of -0.5 dB, which leverages NLI generation with respect to the single-band case, and to the distributed pumping effect of the C-band due to SRS. Note that both the joint and fixed C-band profiles deliver practically the same NLI performance on the C-band, suggesting that the inter-band non-linear crosstalk is not that significant. The C+L, fixed C case, instead, shares the same profile in C-band with the single C-band case: the difference of SNR_{NL} in the farthest channels is in fact due to the power transfer to the L-band. On the NLI side, the joint C+L optimization profile shows instead a larger penalty due to SRS with respect to the fixed C-band profile, which is however balanced by the improvement in the OSNR.

Considering these results from a network management perspective, we highlight some interesting considerations that arise from the final QoT metric of the GSNR, shown in Fig.7.4c. Table 7.1 shows that for the system under test the average GSNR after 10 spans is always $\approx 20.5\,\mathrm{dB}$. Furthermore, for every scenario, the maximum difference with respect to the average GSNR is reported, with a value practically always smaller than 0.1 dB. For the single-band cases, the best QoT is found for the C-band, whereas the L-band benefits from C-band pumping due to SRS, causing a larger QoT in both multi-band scenarios. We remark that a joint C+L optimization enables capacity doubling at the cost of only $\approx 0.25\,\mathrm{dB}$ of penalty per 10 spans in the C-band, but requiring a change in the working points of the C-band ILAs, which an operator may be not allowed to do immediately, for example, in order to comply with the quality of service agreement made with a customer. However, if an additional 0.25 dB of QoT penalty can be tolerated by the deployed C-band system margins, the upgrade to C+L multi-band OLS can be performed seamlessly without impairing the traffic already deployed on the C-band. It should be noted that, although the simulations performed were specific to the considered scenarios, the results here presented should hold in the general picture and different full-spectrum system configurations exploiting more in-depth optimization strategies may be chosen.

Chapter 8

Conclusions

We started this thesis with a brief overview of the evolution of optical communications from single point-to-point connections to complex meshed networks performing all-optical, transparent networking. We have also reported the current trends in traffic growth demanding for larger capacity. To fulfill these requests, operators are pushing towards the openness and disaggregation of optical networks, allowing for interoperability between different vendor devices and decoupling of the line systems from the line terminal equipment, with the latter evolving at a higher pace.

In this context, in chapter 2, we have proposed a simple network abstraction as a topology graph whose edges, representing the OLSs, are weighted with the GSNR as a unique metric for QoT. Such abstraction allows an easy assessment of the QoT experienced by a lightpath traveling along a sequence of OLSs, which is crucial for design and control of the network. To this aim, we have proposed simple guidelines for QoT modeling in the networking context: a QoT estimator should be, in our view, spectrally disaggregated, spatially incoherent and provide slightly conservative evaluations independently on the modulation format of the lightpath to simplify the bit-rate assignment process.

In chapter 3, we have presented our simulation framework, able to simulate a wide range of spectral and line configuration which can be easily described by means of JSON syntax, compliant with the GNPy open source QoT estimation tool.

In chapter 4, we have observed the accumulation of NLI in full coherent transmission systems operated on DU OLSs for several symbol rate and frequency grid configurations and fiber dispersion values, showing that SPM and XPM are the main non-linear phenomena. While SPM shows a coherent spatial accumulation, which must be treated with a spatial worst-case approach, the XPM SNR degradation is spectrally disaggregated and converges in all the considered cases to an asymptotic, spatially incoherent value, thus enabling a worst-case QoT estimation independent on the previous history of the interfering channels crossed by the CuT.

Such observation from the SNR accumulation point of view has been shown for the first time to our knowledge. In this sense, the analysis will be expanded in future studies to higher cardinality modulation formats to test if a worst-case, modulation format-agnostic assessment of the QoT degradation introduced by each span can be derived. Also, the same accumulation figures should be observed in OLSs made up of mixed fiber types in order to validate the spatial incoherency of the XPM contribution introduced in each span with respect to the fiber dispersion values.

Then, in chapter 5 we addressed the problem of the QoT estimation for the legacy IMDD channels delivering 10 Gbps in DM links. These systems are in fact still widespread in (extended) metro and regional network segments with less stringent capacity requirements, where the cost of coherent technology is still prohibitive. In this scenario, we haved presented a QoT estimator allowing for fast and accurate pre-FEC BER evaluation accounting for SPM-dispersion ISI interaction with XPM and ASE on the final BER. Although a homogeneous GSNR-based approach for QoT is here not possible as in full coherent systems, further capabilities in the 10G management with respect to the traditional fixed configurations are enabled.

In chapter 6 we then passed to face the problem of the mixed propagation of coherent and IMDD channels on DM optical networks. In this case, the GSNR-based QoT approach can be kept by integrating the QoT degradation originated by the 10G comb on the 100G channels. Also, being able to do this adds further network routing flexibility, enabling routing of 100G channels through sections of metro DM networks already loaded with 10G channels. We proposed an original QoT-E tailored to the implementation in the network control plane and able to quickly (seconds timescale) and efficiently estimate the GSNR penalty due to the inter-channel non-linear interaction of the 10G channels on the 100G channels. The tool has shown to provide conservative QoT estimation, with respect to the worst-case GSNR obtained by accurate SSFM Monte-Carlo simulation campaigns and also with respect to experimental observations. In addition, the model is spectrally and spatially disaggregated: this allows the network control plan to perform lightpath provisioning in a traffic-agnostic fashion, i.e. without knowing the propagation history of the coherent channels. Further studies could focus on the completion of the QoT estimation encompassing all the relevant the estimation of the 100G NLI part arising on DM OLSs.

Finally, in chapter 7, we have considered the upgrade of an existing C-band optical system to multi-band transmission, enlarging the transmission bandwidth to both C+L band, for a total of around 10 THz of occupied bandwidth. BDM has been proposed as a solution to enlarge the network capacity. However, they require careful power profile optimization to leverage the effects of SRS. We have shown that L-band can be lit up without modifying the power work point of existing C-band portion with a minimal penalty with respect to joint C- and L-band power profile optimization.

Acronyms

ADC Analog-to-Digital Converter. 3, 60, 86

AIR Achievable Information Rate. 47

API Application Programming Interface. 8, 27

ASE Amplified Spontaneous Emission. 2, 11, 31, 61, 93, 107, 134

AWGN Additive White Gaussian Noise. 12, 26, 38, 61, 107

BDM Band Division Multiplexing. 134, 144

BER Bit Error Rate. 21, 47

CAGR Compound Annual Growth Rate. 4

CAPEX Capital Expenditures. 7, 106

CLE Constant Local Error. 45

CMA Constant Modulus Algorithm. 37

CNLSE Coupled Non-Linear Schrodinger Equation. 32, 109, 115

CPE Carrier Phase Estimation. 24, 25

CSM Coarse-Step Method. xi, 44, 45, 53

CuT Channel Under Test. 17, 34, 43, 47, 48, 57, 88, 121, 138

CW Constant Wave. 18, 36, 88

DCI Data Center Interconnect. 7

DCU Dispersion Compensating Units. 2, 36, 86

DGD Differential Group Delay. 14, 45, 53

DM Dispersion-Managed. xv, 1, 4, 105, 106, 107, 144

DP Dual-Polarization. ix, 114

DSP Digital Signal Processing. 3, 13, 35, 60, 86, 108, 133

DU Dispersion-Uncompensated. iii, xv, 1, 24, 38, 57, 106, 133

EDFA Erbium-Doped Fiber Amplifier. 2, 12, 35, 60, 86, 136

EGN Enhanced Gaussian-Noise. 24

FEC Forward Error Correction. iv, 21, 85

FFT Fast Fourier Transform. 34

FWM Four-Wave Mixing. iv, 19, 88, 108

GGN Generalized GN-Model. 135

GN Gaussian-Noise. 24

GPU Graphical Processing Unit. 35

GSNR Generalized Signal-to-Noise Ratio. iii, x, 25, 26, 31, 61, 85, 107, 135

HD-FEC Hard Decision Forward Error Correction. 88

ILA Inline Amplifier. x, 9, 26, 96, 134

IMDD Intensity-Modulated, Direct-Detected. iv, 1, 2, 13

ISI Intersymbolic Interference. 13

LMS Least Mean Square. 37, 60, 125

LOGO Local-Optimization-Global-Optimization. 29, 51, 58, 135

NCI Non-Circularity Index. 46

NFV Network-Function-Virtualization. 3, 8

NLI Non-Linear Interference. iv, 24

NLPN Non-Linear Phase Noise. 15, 19, 46, 52, 61, 105, 108

NRZ Non Return to Zero. 36, 88

NZDF Non-Zero Dispersion Fiber. 60

NZDSF Non-Zero Dispersion Shifted Fiber. 60

OLS Optical Line System. x, 9, 26

OOK On-Off Keying. 2, 36, 86, 88

OSA Optical Spectrum Analyzer. 22

OSNR Optical Signal-to-Noise Ratio. 22, 96, 120

P&P Pump and Probe. xi, xii, xv, 48, 49, 50, 51, 52, 54, 55, 57, 58, 59, 62, 63, 64, 65, 66, 68, 69, 71, 73, 109, 111, 115

PCU Power Control Unit. 135

PDF Probability Density Function. xiv, 48, 53, 69, 89, 90, 112

PM Polarization-Multiplexed. iii, xv, 3, 36, 47, 52, 54, 58, 86, 88, 112

PMD Polarization Mode Dispersion. 3, 14

PRBS Pseudo Random Bit Sequence. 43, 58

PSD Power Spectral Density. xi, 12, 58, 95, 116

QAM Quadrature Amplitude Modulation. 3, 23

QoT Quality of Transmission. x, 1, 3, 4, 7, 26, 87

QoT-E Quality of Transmission Estimator. x, 1, 26, 135

QPSK Quadrature Phase Shift Keying. 15, 58

ROADM Reconfigurable Optical Add-Drop Multiplexer. 3, 9, 37, 107

SCI Self-Channel Interference. iv, 18, 19, 48, 80

SD-FEC Soft Decision Forward Error Correction. 88

SDM Spatial Division Multiplexing. 134

SDN Software-Defined-Networking. 3, 8

SNR Signal-to-Noise Ratio. 7, 22, 46

SOP State of Polarization. 14, 19, 52, 108

SP Single-Polarization. ix, 45, 47, 114

SPM Self-Phase Modulation. 18, 49, 57, 88, 108, 143

SpS Samples per Symbol. xii, 34, 46, 60, 61, 70, 109, 116

SRS Stimulated Raman Scattering. iv, 14, 133

SSFM Split-Step Fourier Method. 1, 14, 33, 58, 85, 93, 105, 133, 144

SSMF Standard Sigle Mode Fiber. xiv, 14, 60, 90, 97, 129, 136

TIP Telecom Infra Project. 10

UM Unallocated OSNR Margin. 99

WDM Wavelength Division Multiplexing. 2

XCI Cross-Channel Interference. iv, 18, 19, 45, 48, 49

XPM Cross-Phase Modulation. 18, 49, 50, 57, 85, 105, 108, 143

XPolM Cross-Polarization Modulation. 18, 19, 49, 108

Bibliography

[1] *'EdgeCore Cassini Whitebox Transponder'*. https://www.edge-core.com/productsList.php?cls=291&cls2=347.

[2] C. Kurtzke A. Splett and K. Petermann. "Ultimate Transmission Capacity of Amplified Optical Fiber Communication Systems taking into Account Fiber Nonlinearities". In: *1993 European Conference and Exhibition on Optical Communications*. Vol. 2. 1993, pp. 41–44.

[3] G.P. Agrawal. *Nonlinear Fiber Optics*. Optics and Photonics. Elsevier Science, 2010. ISBN: 9780080555423. URL: https://books.google.it/books?id=UaY1MLmC780C.

[4] "Analytical extension of LOGO approach for commercial optical networks and experimental validation". English. In: *IET Conference Proceedings* (Jan. 2015), 4 .–4 .(1). URL: https://digital-library.theiet.org/content/conferences/10.1049/cp.2015.0105.

[5] Jean-Luc Auge et al. "Open optical network planning demonstration". In: *Optical Fiber Communication Conference (OFC) 2019*. Optical Society of America, 2019, M3Z.9. DOI: 10.1364/OFC.2019.M3Z.9. URL: http://www.osapublishing.org/abstract.cfm?URI=OFC-2019-M3Z.9.

[6] G. Bellotti et al. "Intensity distortion induced by cross-phase modulation and chromatic dispersion in optical-fiber transmissions with dispersion compensation". In: *IEEE Photonics Technology Letters* 10.12 (1998), pp. 1745–1747. DOI: 10.1109/68.730489.

[7] Oriol Bertran-Pardo et al. "Overlaying 10 Gb/s Legacy Optical Networks With 40 and 100 Gb/s Coherent Terminals". In: *Journal of Lightwave Technology* 30.14 (2012), pp. 2367–2375. DOI: 10.1109/JLT.2012.2198432.

[8] Christophe Besse, Brigitte Bidégaray, and Stéphane Descombes. "Order Estimates in Time of Splitting Methods for the Nonlinear Schrödinger Equation". In: *SIAM Journal on Numerical Analysis* 40.1 (2003), pp. 26–40. ISSN: 00361429. URL: http://www.jstor.org/stable/4100942.

[9] Martin Birk et al. "The OpenROADM initiative". In: *IEEE/OSA Journal of Optical Communications and Networking* 12.6 (2020), pp. C58–C67.

[10] A. Bononi et al. “Cross-Phase Modulation Induced by OOK Channels on Higher-Rate DQPSK and Coherent QPSK Channels”. In: *Journal of Lightwave Technology* 27.18 (2009), pp. 3974–3983. DOI: 10.1109/JLT.2009.2021537.

[11] A. Bononi et al. “Modeling nonlinearity in coherent transmissions with dominant intrachannel-four-wave-mixing”. In: *Opt. Express* 20.7 (Mar. 2012), pp. 7777–7791. DOI: 10.1364/OE.20.007777. URL: http://www.opticsexpress.org/abstract.cfm?URI=oe-20-7-7777.

[12] Alberto Bononi et al. “Load-aware transparent reach maximization in flexible optical networks”. In: *2014 19th European Conference on Networks and Optical Communications - (NOC)*. 2014, pp. 165–172. DOI: 10.1109/NOC.2014.6996847.

[13] Giacomo Borraccini et al. “Autonomous Raman amplifiers in multi-band software-defined optical transport networks”. In: *J. Opt. Commun. Netw.* 13.10 (Oct. 2021), E53–E62. DOI: 10.1364/JOCN.424025. URL: http://jocn.osa.org/abstract.cfm?URI=jocn-13-10-E53.

[14] Giacomo Borraccini et al. “Cognitive and autonomous QoT-driven optical line controller”. In: *J. Opt. Commun. Netw.* 13.10 (Oct. 2021), E23–E31. DOI: 10.1364/JOCN.424021. URL: http://jocn.osa.org/abstract.cfm?URI=jocn-13-10-E23.

[15] G. Bosco et al. “Suppression of spurious tones induced by the split-step method in fiber systems simulation”. In: *Photonics Technology Letters, IEEE* 12 (June 2000), pp. 489–491. DOI: 10.1109/68.841262.

[16] Jake Bromage. “Raman Amplification for Fiber Communications Systems”. In: *J. Lightwave Technol.* 22.1 (Jan. 2004), p. 79. URL: http://jlt.osa.org/abstract.cfm?URI=jlt-22-1-79.

[17] H. Bulow, F. Buchali, and A. Klekamp. “Electronic Dispersion Compensation”. In: *Journal of Lightwave Technology* 26.1 (2008), pp. 158–167. DOI: 10.1109/JLT.2007.913066.

[18] A. Campanella et al. “ODTN: Open Disaggregated Transport Network. Discovery and Control of a Disaggregated Optical Network through Open Source Software and Open APIs”. In: *2019 Optical Fiber Communications Conference and Exhibition (OFC)*. 2019, pp. 1–3.

[19] M. Cantono et al. “Physical Layer Performance of Multi-Band Optical Line Systems Using Raman Amplification”. In: *J. Opt. Commun. Netw.* 11.1 (Jan. 2019), A103–A110. DOI: 10.1364/JOCN.11.00A103. URL: http://jocn.osa.org/abstract.cfm?URI=jocn-11-1-A103.

[20] M. Cantono et al. “Polarization-Related Statistics of Raman Crosstalk in Single-Mode Optical Fibers”. In: *Journal of Lightwave Technology* 34.4 (2016), pp. 1191–1205. DOI: 10.1109/JLT.2015.2506481.

[21] Mattia Cantono et al. “On the interplay of nonlinear interference generation with stimulated Raman scattering for QoT estimation”. In: *IEEE / OSA Journal Lightwave Technology* 36.15 (2018), pp. 3131–3141.

[22] Mattia Cantono et al. “Observing the Interaction of PMD with Generation of NLI in Uncompensated Amplified Optical Links”. In: *OFC Conference*. OSA, 2018, W1G.4. DOI: 10.1364/OFC.2018.W1G.4.

[23] Mattia Cantono et al. “Opportunities and Challenges of C+L Transmission Systems”. In: *Journal of Lightwave Technology* 38.5 (2020), pp. 1050–1060. DOI: 10.1109/JLT.2019.2959272.

[24] A. Carena et al. “Guard-Band for 111 Gbit/s coherent PM-QPSK channels on legacy fiber links carrying 10 Gbit/s IMDD channels”. In: *Optical Fiber Communication Conference and National Fiber Optic Engineers Conference*. Optical Society of America, 2009, OThR7. DOI: 10.1364/OFC.2009.OThR7. URL: http://www.osapublishing.org/abstract.cfm?URI=OFC-2009-OThR7.

[25] A. Carena et al. “Impact of the transmitted signal initial dispersion transient on the accuracy of the GN-model of non-linear propagation”. In: *39th European Conference and Exhibition on Optical Communication (ECOC 2013)*. 2013, pp. 1–3. DOI: 10.1049/cp.2013.1515.

[26] A. Carena et al. “Modeling of the Impact of Nonlinear Propagation Effects in Uncompensated Optical Coherent Transmission Links”. In: *J. of Lightwave Tech.* 30.10 (May 2012), pp. 1524–1539. DOI: 10.1109/jlt.2012.2189198.

[27] A. Carena et al. “Statistical characterization of PM-QPSK signals after propagation in uncompensated fiber links”. In: *36th European Conference and Exhibition on Optical Communication*. 2010, pp. 1–3. DOI: 10.1109/ECOC.2010.5621509.

[28] Andrea Carena et al. “A Time-Domain Optical Transmission System Simulation Package Accounting for Nonlinear and Polarization-Related Effects in Fiber.” In: *Selected Areas in Communications, IEEE Journal on* 15 (June 1997), pp. 751–765. DOI: 10.1109/49.585785.

[29] Andrea Carena et al. “EGN model of non-linear fiber propagation”. In: *Optics express* 22.13 (2014), pp. 16335–16362.

[30] A. V. T. Cartaxo. “Cross-phase modulation in intensity modulation-direct detection WDM systems with multiple optical amplifiers and dispersion compensators”. In: *Journal of Lightwave Technology* 17.2 (1999), pp. 178–190. DOI: 10.1109/50.744218.

[31] R. Casellas et al. "Abstraction and Control of Multi-Domain Disaggregated Optical Networks With OpenROADM Device Models". In: *Journal of Lightwave Technology* 38.9 (2020), pp. 2606–2615. DOI: 10.1109/JLT.2020.2969248.

[32] Haiquan Cheng et al. "Experimental Demonstration of Pilot-Symbols-Aided Cycle Slip Mitigation for QPSK Modulation Format". In: *Optical Fiber Communication Conference*. Optical Society of America, 2014, Th4D.1. DOI: 10.1364/OFC.2014.Th4D.1. URL: http://www.osapublishing.org/abstract.cfm?URI=OFC-2014-Th4D.1.

[33] K Christodoulopoulos et al. "Toward efficient, reliable, and autonomous optical networks: the ORCHESTRA solution". In: *IEEE/OSA Journal of Optical Communications and Networking* 11.9 (2019), pp. C10–C24.

[34] Ciena. *What is ZR+?* https://www.ciena.com/insights/articles/What-is-ZR-plus.html. [Online]. 2019.

[35] Cisco. *Cisco Annual Internet Report (2018-2023)*. https://www.cisco.com/c/en/us/solutions/service-provider/visual-networking-index-vni/index.html. [Online]. 2018.

[36] Cisco. *Cisco Visual Networking Index: Forecast and Trends (2017-2022)*. https://davidellis.ca/wp-content/uploads/2019/05/cisco-vni-feb2019.pdf. [Online]. 2017.

[37] Bruno Correia et al. "Networking Performance of Power Optimized C+L+S Multiband Transmission". In: *GLOBECOM 2020 - 2020 IEEE Global Communications Conference*. 2020, pp. 1–6. DOI: 10.1109/GLOBECOM42002.2020.9322068.

[38] R. Corsini et al. "Blind Adaptive Chromatic Dispersion Compensation and Estimation for DSP-Based Coherent Optical Systems". In: *Journal of Lightwave Technology* 31.13 (2013), pp. 2131–2139. DOI: 10.1109/JLT.2013.2262211.

[39] F. Cugini et al. "Designing Disaggregated Optical Networks". In: *2020 International Conference on Optical Network Design and Modeling (ONDM)*. May 2020, pp. 1–3. DOI: 10.23919/ONDM48393.2020.9133039.

[40] Filippo Cugini et al. "Toward Plug-and-Play Software-Defined Elastic Optical Networks". In: *J. Lightwave Technol.* 34.6 (Mar. 2016), pp. 1494–1500. URL: http://jlt.osa.org/abstract.cfm?URI=jlt-34-6-1494.

[41] V. Curri and D. Calonico. "Multi-Band and Multi-Service Open Optical Networks: Applications and Perspectives". In: *2020 22nd International Conference on Transparent Optical Networks (ICTON)*. 2020, pp. 1–4. DOI: 10.1109/ICTON51198.2020.9203143.

[42] V. Curri and A. Carena. "Merit of Raman Pumping in Uniform and Uncompensated Links Supporting NyWDM Transmission". In: *Journal of Lightwave Technology* 34.2 (2016), pp. 554–565. DOI: 10.1109/JLT.2015.2477599.

[43] V. Curri et al. "Dispersion Compensation and Mitigation of Nonlinear Effects in 111-Gb/s WDM Coherent PM-QPSK Systems". In: *IEEE Photonics Technology Letters* 20.17 (2008), pp. 1473–1475. DOI: 10.1109/LPT.2008.927906.

[44] V. Curri et al. "Dispersion Compensation and Mitigation of Nonlinear Effects in 111-Gb/s WDM Coherent PM-QPSK Systems". In: *IEEE Photonics Technology Letters* 20.17 (2008), pp. 1473–1475.

[45] Vittorio Curri. "Software-defined WDM optical transport in disaggregated open optical networks". In: *2020 22nd International Conference on Transparent Optical Networks (ICTON)*. IEEE. 2020, pp. 1–4.

[46] Vittorio Curri, Mattia Cantono, and Roberto Gaudino. "Elastic All-Optical Networks: A New Paradigm Enabled by the Physical Layer. How to Optimize Network Performances?" In: *Journal of Lightwave Technology* 35.6 (Mar. 2017), pp. 1211–1221. DOI: 10.1109/jlt.2017.2657231.

[47] Vittorio Curri et al. "Extension and validation of the GN model for nonlinear interference to uncompensated links using Raman amplification". In: *Optics express* 21.3 (2013), pp. 3308–3317.

[48] Andrea D'Amico et al. "Using machine learning in an open optical line system controller". In: *J. Opt. Commun. Netw.* 12.6 (June 2020), pp. C1–C11. DOI: 10.1364/JOCN.382557. URL: http://jocn.osa.org/abstract.cfm?URI=jocn-12-6-C1.

[49] A. D'Amico et al. "Enhancing Lightpath QoT Computation With Machine Learning in Partially Disaggregated Optical Networks". In: *IEEE Open Journal of the Communications Society* 2 (2021), pp. 564–574. DOI: 10.1109/OJCOMS.2021.3066913.

[50] A. D'Amico et al. "Quality of Transmission Estimation for Planning of Disaggregated Optical Networks". In: *2020 International Conference on Optical Network Design and Modeling (ONDM)*. 2020, pp. 1–3. DOI: 10.23919/ONDM48393.2020.9133012.

[51] R. Dar et al. "Inter-Channel Nonlinear Interference Noise in WDM Systems: Modeling and Mitigation". In: *Journal of Lightwave Technology* 33.5 (Mar. 2015), pp. 1044–1053. ISSN: 1558-2213. DOI: 10.1109/JLT.2014.2384998.

[52] Ronen Dar, Mark Shtaif, and Meir Feder. "New bounds on the capacity of the nonlinear fiber-optic channel". In: *Opt. Lett.* 39.2 (Jan. 2014), pp. 398–401. DOI: 10.1364/OL.39.000398. URL: http://ol.osa.org/abstract.cfm?URI=ol-39-2-398.

[53] Ronen Dar et al. "Accumulation of nonlinear interference noise in fiber-optic systems". In: *Opt. Express* 22.12 (June 2014), pp. 14199–14211. DOI: 10.1364/OE.22.014199. URL: http://www.opticsexpress.org/abstract.cfm?URI=oe-22-12-14199.

[54] Ronen Dar et al. "Properties of nonlinear noise in long, dispersion-uncompensated fiber links". In: *Optics Express* 21.22 (Oct. 2013), p. 25685. DOI: 10.1364/oe.21.025685.

[55] Ronen Dar et al. "Pulse collision picture of inter-channel nonlinear interference in fiber-optic communications". In: *J. of Lightwave Tech.* 34.2 (2016), pp. 593–607.

[56] Gabriella Bosco Dario Pilori F. Forghieri. "Residual Non-Linear Phase Noise in Probabilistically Shaped 64-QAM Optical Links". In: *Optical Fiber Communication Conference/National Fiber Optic Engineers Conference 2018*. 2018.

[57] Daniel J. Elson et al. "Investigation of bandwidth loading in optical fibre transmission using amplified spontaneous emission noise". In: *Opt. Express* 25.16 (Aug. 2017), pp. 19529–19537. DOI: 10.1364/OE.25.019529. URL: http://www.opticsexpress.org/abstract.cfm?URI=oe-25-16-19529.

[58] René-Jean Essiambre and Robert W. Tkach. "Capacity Trends and Limits of Optical Communication Networks". In: *Proceedings of the IEEE* 100.5 (May 2012), pp. 1035–1055. DOI: 10.1109/jproc.2012.2182970.

[59] A. Ferrari et al. "GNPy: an open source application for physical layer aware open optical networks". In: *IEEE/OSA Journal of Optical Communications and Networking* 12.6 (2020), pp. C31–C40. DOI: 10.1364/JOCN.382906.

[60] A. Ferrari et al. "The GNPy Open Source Library of Applications for Software Abstraction of WDM Data Transport in Open Optical Networks". In: *2020 6th IEEE Conference on Network Softwarization (NetSoft)*. 2020, pp. 386–394. DOI: 10.1109/NetSoft48620.2020.9165313.

[61] Alessio Ferrari, Emanuele Virgillito, and Vittorio Curri. "Band-Division vs. Space-Division Multiplexing: A Network Performance Statistical Assessment". In: *J. Lightwave Technol.* 38.5 (Mar. 2020), pp. 1041–1049. URL: http://jlt.osa.org/abstract.cfm?URI=jlt-38-5-1041.

[62] Mark Filer, Hacene Chaouch, and Xiaoxia Wu. "Toward Transport Ecosystem Interoperability Enabled by Vendor-Diverse Coherent Optical Sources Over an Open Line System". In: *J. Opt. Commun. Netw.* 10.2 (Feb. 2018), A216–A224. DOI: 10.1364/JOCN.10.00A216. URL: http://jocn.osa.org/abstract.cfm?URI=jocn-10-2-A216.

[63] Mark Filer et al. "Multi-Vendor Experimental Validation of an Open Source QoT Estimator for Optical Networks". In: *J. of Lightwave Tech.* 36.15 (Aug. 2018), pp. 3073–3082. DOI: 10.1109/jlt.2018.2818406.

[64] E. Forestieri. "Evaluating the error probability in lightwave systems with chromatic dispersion, arbitrary pulse shape and pre- and postdetection filtering". In: *Journal of Lightwave Technology* 18.11 (2000), pp. 1493–1503. DOI: 10.1109/50.896209.

[65] W. Freude et al. "Quality metrics for optical signals: Eye diagram, Q-factor, OSNR, EVM and BER". In: *2012 14th International Conference on Transparent Optical Networks (ICTON)*. 2012, pp. 1–4. DOI: 10.1109/ICTON.2012.6254380.

[66] A. Galtarossa and C.R. Menyuk. *Polarization Mode Dispersion*. Optical and Fiber Communications Reports. Springer New York, 2006. ISBN: 9780387263076. URL: https://books.google.it/books?id=EuugmOUFvkgC.

[67] Miquel Garrich et al. "Open-Source Network Optimization Software in the Open SDN/NFV Transport Ecosystem". In: *J. Lightwave Technol.* 37.1 (Jan. 2019), pp. 75–88. URL: http://jlt.osa.org/abstract.cfm?URI=jlt-37-1-75.

[68] *GitHub repository of GNPy*. Version v2.0. DOI: 10.5281/zenodo.3458319. DOI: 10.5281/zenodo.3458319. URL: https://doi.org/10.5281/zenodo.3458319.

[69] J. P. Gordon and H. Kogelnik. "PMD fundamentals: Polarization mode dispersion in optical fibers". In: *Proceedings of the National Academy of Sciences* 97.9 (2000), pp. 4541–4550. ISSN: 0027-8424. DOI: 10.1073/pnas.97.9.4541. eprint: https://www.pnas.org/content/97/9/4541.full.pdf. URL: https://www.pnas.org/content/97/9/4541.

[70] Fernando P. Guiomar et al. "Hybrid Modulation Formats Enabling Elastic Fixed-Grid Optical Networks". In: *J. Opt. Commun. Netw.* 8.7 (July 2016), A92–A100. DOI: 10.1364/JOCN.8.000A92. URL: http://jocn.osa.org/abstract.cfm?URI=jocn-8-7-A92.

[71] Stephen Hardy. *Fujitsu contributes to TIP OOPT Phoenix 400G disaggregated transponder effort*. https://www.lightwaveonline.com/optical-tech/transport/article/14196679/fujitsu-contributes-to-tip-oopt-phoenix-400g-disaggregated-transponder-effort. 2021.

[72] Fabian N. Hauske et al. "Nonlinear Phase Noise Mitigation With Soft-Differential Decoding and Nonredundant Error Correction for Hybrid 10G/100G Transmission". In: *IEEE Photonics Technology Letters* 23.13 (2011), pp. 866–868. DOI: 10.1109/LPT.2011.2141127.

[73] Fabian N. Hauske et al. "On the Mitigation of the Differential Decoding Penalty in 100G PDM-QPSK Digital Coherent Receivers for Multirate WDM Transmission". In: *IEEE Photonics Technology Letters* 24.6 (2012), pp. 428–430. DOI: 10.1109/LPT.2011.2179932.

[74] Stephan Hellerbrand and Norbert Hanik. "Fast Implementation of the Split-Step Fourier Method using a Graphics Processing Unit". In: *Optical Fiber Communication Conference*. Optical Society of America, 2010, OTuD7. DOI: 10.1364/OFC.2010.OTuD7. URL: http://www.osapublishing.org/abstract.cfm?URI=OFC-2010-OTuD7.

[75] Infinera. *Open Optical Networking*. https://www.infinera.com/wp-content/uploads/Open-Optical-Networking-0279-SN-RevA-0121.pdf. [Online]. 2021.

[76] M. N. Islam. "Raman amplifiers for telecommunications". In: *IEEE Journal of Selected Topics in Quantum Electronics* 8.3 (2002), pp. 548–559. DOI: 10.1109/JSTQE.2002.1016358.

[77] P. Johannisson and E. Agrell. "Modeling of Nonlinear Signal Distortion in Fiber-Optic Networks". In: *Journal of Lightwave Technology* 32.23 (2014), pp. 4544–4552. DOI: 10.1109/JLT.2014.2361357.

[78] Pontus Johannisson and Magnus Karlsson. "Perturbation analysis of nonlinear propagation in a strongly dispersive optical communication system". In: *J. of Lightwave Tech.* 31.8 (2013), pp. 1273–1282.

[79] Valey Kamalov et al. "Lessons Learned From Open Line System Deployments". In: *Optical Fiber Communication Conference*. Optical Society of America, 2017, M2E.2. DOI: 10.1364/OFC.2017.M2E.2. URL: http://www.osapublishing.org/abstract.cfm?URI=OFC-2017-M2E.2.

[80] Magnus Karlsson and Henrik Sunnerud. "Effects of Nonlinearities on PMD-Induced System Impairments". In: *J. Lightwave Technol.* 24.11 (Nov. 2006), pp. 4127–4137. URL: http://jlt.osa.org/abstract.cfm?URI=jlt-24-11-4127.

[81] D. I. Kroushkov et al. "Simple Estimation of the XPM-Induced Phase Error Variance in Hybrid OOK-PSK Systems". In: *IEEE Photonics Technology Letters* 24.9 (2012), pp. 733–735. DOI: 10.1109/LPT.2012.2187332.

[82] J. Kundrát et al. "Physical-Layer Awareness: GNPy and ONOS for End-to-End Circuits in Disaggregated Networks". In: *2020 Optical Fiber Communications Conference and Exhibition (OFC)*. 2020, pp. 1–3.

[83] Jan Kundrát et al. "Opening up ROADMs: Let Us Build a Disaggregated Open Optical Line System". In: *J. Lightwave Technol.* 37.16 (Aug. 2019), pp. 4041–4051. URL: http://jlt.osa.org/abstract.cfm?URI=jlt-37-16-4041.

[84] Chiara Lasagni, Paolo Serena, and Alberto Bononi. "Modeling Nonlinear Interference With Sparse Raman-Tilt Equalization". In: *Journal of Lightwave Technology* 39.15 (2021), pp. 4980–4989. DOI: 10.1109/JLT.2021.3082287.

[85] Ferris Lipscomb. *400ZR Pluggable Modules Drive Down Cost-per-bit In Data Center Interconnects*. https://www.neophotonics.com/data-center-cost-per-bit/. [Online]. 2020.

[86] John Kerr LL.D. "XL. A new relation between electricity and light: Dielectrified media birefringent". In: *The London, Edinburgh, and Dublin Philosophical Magazine and Journal of Science* 50.332 (1875), pp. 337–348. DOI: 10.1080/14786447508641302. eprint: https://doi.org/10.1080/14786447508641302. URL: https://doi.org/10.1080/14786447508641302.

[87] Yann Loussouarn et al. "Single-Carrier and Multi-Carrier 400 Gbps Transmission With Multi-Rate Multi-Format Real-Time Transceiver Prototypes". In: *J. Lightwave Technol.* 37.2 (Jan. 2019), pp. 524–537. URL: http://jlt.osa.org/abstract.cfm?URI=jlt-37-2-524.

[88] C Manso et al. "TAPI-enabled SDN control for partially disaggregated multi-domain (OLS) and multi-layer (WDM over SDM) optical networks". In: *Journal of Optical Communications and Networking* 13.1 (2021), A21–A33.

[89] D. Marcuse, C. R. Manyuk, and P. K. A. Wai. "Application of the Manakov-PMD equation to studies of signal propagation in optical fibers with randomly varying birefringence". In: *Journal of Lightwave Technology* 15.9 (1997), pp. 1735–1746.

[90] Antonio Mecozzi and René-Jean Essiambre. "Nonlinear Shannon Limit in Pseudolinear Coherent Systems". In: *J. of Lightwave Tech.* 30.12 (June 2012), pp. 2011–2024. DOI: 10.1109/jlt.2012.2190582.

[91] Curtis R. Menyuk and Brian S. Marks. "Interaction of Polarization Mode Dispersion and Nonlinearity in Optical Fiber Transmission Systems". In: *J. Lightwave Technol.* 24.7 (July 2006), p. 2806. URL: http://jlt.osa.org/abstract.cfm?URI=jlt-24-7-2806.

[92] Paul Momtahan. *The Long Road to Open Optical Networks*. https://www.infinera.com/blog/the-long-road-to-open-optical-networks/tag/optical/. [Online]. 2021.

[93] R. Muñoz et al. "Transport Network Orchestration for End-to-End Multilayer Provisioning Across Heterogeneous SDN/OpenFlow and GMPLS/PCE Control Domains". In: *Journal of Lightwave Technology* 33.8 (2015), pp. 1540–1548. DOI: 10.1109/JLT.2015.2393634.

[94] S. Musetti and P. Serena. "Investigation of phase noise induced by cross channel nonlinear interference". In: *18th Italian National Conference on Photonic Technologies (Fotonica 2016)*. 2016, pp. 1–4. DOI: 10.1049/cp.2016.0879.

[95] Simone Musetti, Paolo Serena, and A. Bononi. "On the Accuracy of Split-Step Fourier Simulations for Wideband Nonlinear Optical Communications". In: *Journal of Lightwave Technology* PP (Oct. 2018), pp. 1–1. DOI: 10.1109/JLT.2018.2877384.

[96] A. Napoli et al. "Perspectives of multi-band optical communication systems". In: *OECC, 2018*.

[97] Antonio Napoli et al. "Towards multiband optical systems". In: *Photonic Networks and Devices*. Optical Society of America. 2018, NeTu3E–1.

[98] *ONOS (Open Network Operatimng System)*. https://opennetworking.org/onos/.

[99] *OpenConfig*. https://www.openconfig.net/.

[100] *OpenDaylight*. https://www.opendaylight.org/.

[101] *OpenROADM*. https://github.com/OpenROADM/OpenROADM_MSA_Public.

[102] *OptSim*. https://www.synopsys.com/photonic-solutions/rsoft-system-design-tools/system-network-optsim.html.

[103] S. Pachnicke et al. "Fast parallel simulation of fiber optical communication systems accelerated by a graphics processing unit". In: *2010 12th International Conference on Transparent Optical Networks*. 2010, pp. 1–4. DOI: 10.1109/ICTON.2010.5549002.

[104] Stephan Pachnicke et al. "Fast Analytical Assessment of the Signal Quality in Transparent Optical Networks". In: *J. Lightwave Technol.* 24.2 (Feb. 2006), p. 815. URL: http://jlt.osa.org/abstract.cfm?URI=jlt-24-2-815.

[105] R. Pastorelli et al. "Investigation of the Dependence of Non-Linear Interference on the Number of WDM Channels in Coherent Optical Networks". In: *European Conference and Exhibition on Optical Communication*. Optical Society of America, 2012, We.2.C.2. DOI: 10.1364/ECEOC.2012.We.2.C.2. URL: http://www.osapublishing.org/abstract.cfm?URI=ECEOC-2012-We.2.C.2.

[106] R. Pastorelli et al. “Optical control plane based on an analytical model of non-linear transmission effects in a self-optimized network”. In: *39th European Conference and Exhibition on Optical Communication (ECOC 2013)*. 2013, pp. 1–3.

[107] Rosanna Pastorelli. “Network Optimization Strategies and Control Plane Impacts”. In: *Optical Fiber Communication Conference*. OSA, 2015. DOI: 10.1364/ofc.2015.m2i.6.

[108] Rosanna Pastorelli et al. “Network Planning Strategies for Next-Generation Flexible Optical Networks”. In: *J. Opt. Commun. Netw.* 7.3 (Mar. 2015), A511–A525. DOI: 10.1364/JOCN.7.00A511. URL: http://jocn.osa.org/abstract.cfm?URI=jocn-7-3-A511.

[109] D.N. Payne. “Low-noise erbium-doped fibre amplifier operating at 1.54m”. English. In: *Electronics Letters* 23 (19 Sept. 1987), 1026–1028(2). ISSN: 0013-5194. URL: https://digital-library.theiet.org/content/journals/10.1049/el_19870719.

[110] D. Pilori et al. “FFSS: The fast fiber simulator software”. In: *2017 19th International Conference on Transparent Optical Networks (ICTON)*. 2017, We.B1.5.

[111] Dario Pilori et al. “Observing the effect of polarization mode dispersion on nonlinear interference generation in wide-band optical links”. In: *OSA Continuum* 2.10 (Oct. 2019), pp. 2856–2863. DOI: 10.1364/OSAC.2.002856. URL: http://www.osapublishing.org/osac/abstract.cfm?URI=osac-2-10-2856.

[112] P. Poggiolini. “The GN Model of Non-Linear Propagation in Uncompensated Coherent Optical Systems”. In: *Journal of Lightwave Technology* 30.24 (2012), pp. 3857–3879. DOI: 10.1109/JLT.2012.2217729.

[113] P. Poggiolini et al. “The GN-model of fiber non-linear propagation and its applications”. In: *IEEE / OSA JLT* 32.4 (2014), pp. 694–721.

[114] P. Poggiolini et al. “The LOGON strategy for low-complexity control plane implementation in new-generation flexible networks”. In: 2013, OW1H.3, OFC.

[115] P. Poggiolini and Y. Jiang. “Recent Advances in the Modeling of the Impact of Nonlinear Fiber Propagation Effects on Uncompensated Coherent Transmission Systems”. In: *Journal of Lightwave Technology* 35.3 (2017), pp. 458–480. DOI: 10.1109/JLT.2016.2613893.

[116] P. Poggiolini et al. “A Simple and Effective Closed-Form GN Model Correction Formula Accounting for Signal Non-Gaussian Distribution”. In: *Journal of Lightwave Technology* 33.2 (2015), pp. 459–473. DOI: 10.1109/JLT.2014.2387891.

[117] Pierluigi Poggiolini et al. *A Detailed Analytical Derivation of the GN Model of Non-Linear Interference in Coherent Optical Transmission Systems*. 2014. arXiv: 1209.0394 [physics.optics].

[118] Y. Pointurier. "Design of low-margin optical networks". In: *IEEE/OSA Journal of Optical Communications and Networking* 9.1 (2017), A9–A17. DOI: 10.1364/JOCN.9.0000A9.

[119] C. D. Poole and D. L. Favin. "Polarization-mode dispersion measurements based on transmission spectra through a polarizer". In: *Journal of Lightwave Technology* 12.6 (1994), pp. 917–929. DOI: 10.1109/50.296179.

[120] J.G. Proakis and M. Salehi. *Digital Communications*. McGraw-Hill, 2008. ISBN: 9781283387460. URL: https://books.google.it/books?id=ABSmAQAACAAJ.

[121] Chandrasekhara Venkata Raman. "A new radiation". In: *Indian Journal of Physics* 2 (1928), p. 387398.

[122] J. Renaudier et al. "Investigation on WDM Nonlinear Impairments Arising From the Insertion of 100-Gb/s Coherent PDM-QPSK Over Legacy Optical Networks". In: *IEEE Photonics Technology Letters* 21.24 (2009), pp. 1816–1818.

[123] Emilio Riccardi and Marco Schiano. "Optical Node Disaggregation Management and Interoperability". In: *Optical Fiber Communication Conference (OFC) 2020*. Optical Society of America, 2020, Th3A.3. DOI: 10.1364/OFC.2020.Th3A.3. URL: http://www.osapublishing.org/abstract.cfm?URI=OFC-2020-Th3A.3.

[124] Emilio Riccardi et al. "An Operator view on the Introduction of White Boxes into Optical Networks". In: *J. Lightwave Technol.* 36.15 (Aug. 2018), pp. 3062–3072. URL: http://jlt.osa.org/abstract.cfm?URI=jlt-36-15-3062.

[125] Ian Roberts et al. "Channel Power Optimization of WDM Systems Following Gaussian Noise Nonlinearity Model in Presence of Stimulated Raman Scattering". In: *J. Lightwave Technol.* 35.23 (Dec. 2017), pp. 5237–5249. URL: http://jlt.osa.org/abstract.cfm?URI=jlt-35-23-5237.

[126] S. Rommel et al. "Towards a Scaleable 5G Fronthaul: Analog Radio-over-Fiber and Space Division Multiplexing". In: *Journal of Lightwave Technology* 38.19 (2020), pp. 5412–5422. DOI: 10.1109/JLT.2020.3004416.

[127] N. Rossi, P. Ramantanis, and J.-C. Antona. "Nonlinear interference noise statistics in unmanaged coherent networks with channels propagating over different lightpaths". In: *2014 The European Conference on Optical Communication (ECOC)*. 2014, pp. 1–3. DOI: 10.1109/ECOC.2014.6964043.

[128] G. Saavedra et al. "Experimental Analysis of Nonlinear Impairments in Fibre Optic Transmission Systems up to 7.3 THz". In: *Journal of Lightwave Technology* 35.21 (2017), pp. 4809–4816. DOI: 10.1109/JLT.2017.2760138.

[129] Rasoul Sadeghi et al. "Multi Bands Network Performance Assessment for Different System Upgrades". In: *2020 IEEE Photonics Conference (IPC)*. 2020, pp. 1–2. DOI: 10.1109/IPC47351.2020.9252450.

[130] A. A. M. Saleh and J. M. Simmons. "All-Optical Networking—Evolution, Benefits, Challenges, and Future Vision". In: *Proceedings of the IEEE* 100.5 (2012), pp. 1105–1117. DOI: 10.1109/JPROC.2011.2182589.

[131] João Santos, Nelson Costa, and João Pedro. "On the Impact of Deploying Optical Transport Networks Using Disaggregated Line Systems". In: *J. Opt. Commun. Netw.* 10.1 (Jan. 2018), A60–A68. DOI: 10.1364/JOCN.10.000A60. URL: http://jocn.osa.org/abstract.cfm?URI=jocn-10-1-A60.

[132] S. J. Savory. "Approximations for the Nonlinear Self-Channel Interference of Channels With Rectangular Spectra". In: *IEEE Photonics Technology Letters* 25.10 (2013), pp. 961–964. DOI: 10.1109/LPT.2013.2255869.

[133] S. J. Savory. "Digital Coherent Optical Receivers: Algorithms and Subsystems". In: *IEEE Journal of Selected Topics in Quantum Electronics* 16.5 (2010), pp. 1164–1179. DOI: 10.1109/JSTQE.2010.2044751.

[134] Seb J. Savory et al. "Electronic compensation of chromatic dispersion using a digital coherent receiver". In: *Opt. Express* 15.5 (Mar. 2007), pp. 2120–2126. DOI: 10.1364/OE.15.002120. URL: http://www.opticsexpress.org/abstract.cfm?URI=oe-15-5-2120.

[135] Steven Searcy and Sorin Tibuleac. "Experimental study of cross-phase modulation reduction in hybrid systems with co-propagating 100G PM-QPSK and 10G OOK". In: *Opt. Express* 21.25 (Dec. 2013), pp. 31483–31491. DOI: 10.1364/OE.21.031483. URL: http://www.opticsexpress.org/abstract.cfm?URI=oe-21-25-31483.

[136] M. Secondini and E. Forestieri. "Analytical Fiber-Optic Channel Model in the Presence of Cross-Phase Modulation". In: *Photonics Technology Letters* 24.22 (Nov. 2012), pp. 2016–2019. DOI: 10.1109/lpt.2012.2217952.

[137] D. Semrau, R. I. Killey, and P. Bayvel. "The Gaussian Noise Model in the Presence of Inter-Channel Stimulated Raman Scattering". In: *Journal of Lightwave Technology* 36.14 (2018), pp. 3046–3055. DOI: 10.1109/JLT.2018.2830973.

[138] P. Serena and A. Bononi. "A Time-Domain Extended Gaussian Noise Model". In: *Journal of Lightwave Technology* 33.7 (2015), pp. 1459–1472. DOI: 10.1109/JLT.2015.2398873.

[139] P. Serena and A. Bononi. "An Alternative Approach to the Gaussian Noise Model and its System Implications". In: *Journal of Lightwave Technology* 31.22 (2013), pp. 3489–3499. DOI: 10.1109/JLT.2013.2284499.

[140] P. Serena et al. "Intra- Versus Inter-Channel PMD in Linearly Compensated Coherent PDM-PSK Nonlinear Transmissions". In: *Journal of Lightwave Technology* 29.11 (2011), pp. 1691–1700. DOI: 10.1109/JLT.2011.2144570.

[141] P. Serena et al. "Intra- Versus Inter-Channel PMD in Linearly Compensated Coherent PDM-PSK Nonlinear Transmissions". In: *Journal of Lightwave Technology* 29.11 (2011), pp. 1691–1700. DOI: 10.1109/JLT.2011.2144570.

[142] Andrea Sgambelluri et al. "Fully disaggregated ROADM white box with NETCONF/YANG control, telemetry, and machine learning-based monitoring". In: *Optical Fiber Communication Conference*. Optical Society of America. 2018, Tu3D–12.

[143] Muhammad Zubair Shafiq et al. "A First Look at Cellular Machine-to-Machine Traffic: Large Scale Measurement and Characterization". In: *SIGMETRICS Perform. Eval. Rev.* 40.1 (June 2012), pp. 65–76. ISSN: 0163-5999. DOI: 10.1145/2318857.2254767. URL: https://doi.org/10.1145/2318857.2254767.

[144] Behnam Shariati et al. "Learning From the Optical Spectrum: Failure Detection and Identification". In: *J. Lightwave Technol.* 37.2 (Jan. 2019), pp. 433–440. URL: http://jlt.osa.org/abstract.cfm?URI=jlt-37-2-433.

[145] A. Sheikh et al. "Dispersion Compensation FIR Filter With Improved Robustness to Coefficient Quantization Errors". In: *Journal of Lightwave Technology* 34.22 (2016), pp. 5110–5117. DOI: 10.1109/JLT.2016.2599276.

[146] M. Shtaif. "Analytical description of cross-phase modulation in dispersive optical fibers". In: *Opt. Lett.* 23.15 (Aug. 1998), pp. 1191–1193. DOI: 10.1364/OL.23.001191. URL: http://ol.osa.org/abstract.cfm?URI=ol-23-15-1191.

[147] Oleg Sinkin et al. "Optimization of the split-step Fourier method in modeling optical-fiber communication systems". In: *Journal of Lightwave Technology* 21 (Feb. 2003), pp. 61–. DOI: 10.1109/JLT.2003.808628.

[148] Z. Tao et al. "Simple Fiber Model for Determination of XPM Effects". In: *Journal of Lightwave Technology* 29.7 (2011), pp. 974–986. DOI: 10.1109/JLT.2011.2107728.

[149] Frederick Tappert. "Numerical solutions of the Korteweg-de Vries equation and its generalizations by the split-step Fourier method". In: *Nonlinear Wave Motion* 15 (1974), pp. 215–216.

[150] *Telecom Infra Project*. https://telecominfraproject.com/.

[151] Kathleen Tse. "Progress toward an Open, SDN-controlled Photonic Network". In: *Optical Fiber Communication Conference*. Optical Society of America, 2018, M2E.1. DOI: 10.1364/OFC.2018.M2E.1. URL: http://www.osapublishing.org/abstract.cfm?URI=OFC-2018-M2E.1.

[152] Francesco Vacondio et al. "On nonlinear distortions of highly dispersive optical coherent systems". In: *Opt. Express* 20.2 (Jan. 2012), pp. 1022–1032. DOI: 10.1364/OE.20.001022. URL: http://www.opticsexpress.org/abstract.cfm?URI=oe-20-2-1022.

[153] Blesson Varghese and Rajkumar Buyya. "Next generation cloud computing: New trends and research directions". In: *Future Generation Computer Systems* 79 (2018), pp. 849–861. ISSN: 0167-739X. DOI: https://doi.org/10.1016/j.future.2017.09.020. URL: https://www.sciencedirect.com/science/article/pii/S0167739X17302224.

[154] Alba P. Vela et al. "BER Degradation Detection and Failure Identification in Elastic Optical Networks". In: *J. Lightwave Technol.* 35.21 (Nov. 2017), pp. 4595–4604. URL: http://jlt.osa.org/abstract.cfm?URI=jlt-35-21-4595.

[155] Viavi. *Fiber in 5G Network*. https://comms.viavisolutions.com/White-Paper-Fiber-in-5G-Networks-vi106984. 2020.

[156] E. Virgillito et al. "Non-linear SNR degradation of mixed 10G/100G transmission over dispersion-managed networks". In: *ICTON*. 2020, We.C2.5.

[157] E. Virgillito et al. "Propagation Effects in Mixed 10G-100G Dispersion Managed Optical Links". In: *2019 21st International Conference on Transparent Optical Networks (ICTON)*. 2019, We.D1.5.

[158] Emanuele Virgillito et al. "Network Performance Assessment of C+L Upgrades vs. Fiber Doubling SDM Solutions". In: *Optical Fiber Communication Conference (OFC) 2020*. Optical Society of America, 2020, M2G.4. DOI: 10.1364/OFC.2020.M2G.4. URL: http://www.osapublishing.org/abstract.cfm?URI=OFC-2020-M2G.4.

[159] Emanuele Virgillito et al. "Observing and Modeling Wideband Generation of Non-Linear Interference". In: *2019 21st International Conference on Transparent Optical Networks (ICTON)*. IEEE. 2019, pp. 1–4.

[160] Emanuele Virgillito et al. "Single- vs. Multi-Band Optimized Power Control in C+L WDM 400G Line Systems". In: *Optical Fiber Communication Conference*. Optical Society of America. 2021, Accepted.

[161] Emanuele Virgillito et al. "Testing TIP Open Source Solutions in Deployed Optical Networks". In: *Optical Fiber Communication Conference*. Optical Society of America. 2021, Accepted.

[162] A. Viterbi. "Nonlinear estimation of PSK-modulated carrier phase with application to burst digital transmission". In: *IEEE Transactions on Information Theory* 29.4 (1983), pp. 543–551.

[163] *VPI Photonics*. https://www.vpiphotonics.com/index.php.

[164] Ping Kong Alexander Wai and C. R. Menyuk. "Polarization mode dispersion, decorrelation, and diffusion in optical fibers with randomly varying birefringence". English. In: *Journal of Lightwave Technology* 14.2 (Feb. 1996), pp. 148–157. ISSN: 0733-8724. DOI: 10.1109/50.482256.

[165] D. Wang et al. "Adaptive Chromatic Dispersion Compensation for Coherent Communication Systems Using Delay-Tap Sampling Technique". In: *IEEE Photonics Technology Letters* 23.14 (2011), pp. 1016–1018. DOI: 10.1109/LPT.2011.2151280.

[166] Glenn Wellbrock and Tiejun J. Xia. "How will optical transport deal with future network traffic growth?" In: *ECOC*. IEEE, Sept. 2014, pp. 1–3. DOI: 10.1109/ecoc.2014.6964248.

[167] Carol Wilson. *Nolle: In 2017, Cost Per Bit Exceeds Revenues*. https://www.lightreading.com/business-employment/business-transformation/nolle-in-2017-cost-per-bit-exceeds-revenues/d/d-id/729446.. [Online]. 2017.

[168] M. Winter, D. Setti, and K. Petermann. "Cross-Polarization Modulation in Polarization-Division Multiplex Transmission". In: *IEEE Photonics Technology Letters* 22.8 (2010), pp. 538–540. DOI: 10.1109/LPT.2010.2042164.

[169] Marcus Winter et al. "A Statistical Treatment of Cross-Polarization Modulation in DWDM Systems". In: *J. Lightwave Technol.* 27.17 (Sept. 2009), pp. 3739–3751. URL: http://jlt.osa.org/abstract.cfm?URI=jlt-27-17-3739.

[170] Peter J. Winzer and David T. Neilson. "From Scaling Disparities to Integrated Parallelism: A Decathlon for a Decade". In: *Journal of Lightwave Technology* 35.5 (2017), pp. 1099–1115. DOI: 10.1109/JLT.2017.2662082.

[171] Helen Xenos. *Updated: 800G – nothing but the facts*. https://www.ciena.com/insights/articles/800g-nothing-but-the-facts.html. [Online]. 2021.

[172] Chongjin Xie. "Impact of nonlinear and polarization effects in coherent systems". In: *Opt. Express* 19.26 (Dec. 2011), B915–B930. DOI: 10.1364/OE.19.00B915. URL: http://www.opticsexpress.org/abstract.cfm?URI=oe-19-26-B915.

[173] Chongjin Xie. "WDM coherent PDM-QPSK systems with and without inline optical dispersion compensation". In: *Opt. Express* 17.6 (Mar. 2009), pp. 4815–4823. DOI: 10.1364/OE.17.004815. URL: http://www.opticsexpress.org/abstract.cfm?URI=oe-17-6-4815.

[174] Chongjin Xie et al. "Open and disaggregated optical transport networks for data center interconnects

Invited

". In: *J. Opt. Commun. Netw.* 12.6 (June 2020), pp. C12–C22. DOI: 10.1364/JOCN.380721. URL: http://jocn.osa.org/abstract.cfm?URI=jocn-12-6-C12.

[175] Q. Zhang et al. "An efficient split-step optical fiber simulation package with global simulation accuracy control". In: *2013 IEEE/CIC International Conference on Communications in China (ICCC)*. 2013, pp. 158–164. DOI: 10.1109/ICCChina.2013.6671107.

[176] Qun Zhang and M. Imran Hayee. "Symmetrized Split-Step Fourier Scheme to Control Global Simulation Accuracy in Fiber-Optic Communication Systems". In: *J. Lightwave Technol.* 26.2 (Jan. 2008), pp. 302–316. URL: http://jlt.osa.org/abstract.cfm?URI=jlt-26-2-302.

[177] S. Zhang et al. "Performance investigation of the joint SPM compensation in a long-haul coherent dual-polarization QPSK system". In: *36th European Conference and Exhibition on Optical Communication*. 2010, pp. 1–3. DOI: 10.1109/ECOC.2010.5621436.

[178] T. Zhang et al. "A WDM Network Controller With Real-Time Updates of the Physical Layer Abstraction". In: *Journal of Lightwave Technology* 37.16 (2019), pp. 4073–4080. DOI: 10.1109/JLT.2019.2924397.

[179] X. Zhou. "An Improved Feed-Forward Carrier Recovery Algorithm for Coherent Receivers With M -QAM Modulation Format". In: *IEEE Photonics Technology Letters* 22.14 (2010), pp. 1051–1053. DOI: 10.1109/LPT.2010.2049644.

This Ph.D. thesis has been typeset by means of the TEX-system facilities. The typesetting engine was pdfLATEX. The document class was `toptesi`, by Claudio Beccari, with option `tipotesi=scudo`. This class is available in every up-to-date and complete TEX-system installation.